A Data-Assimilation Framework for Bubbly Flow Reconstruction Based on AOT-Nudging and Image Velocimetry

by

Lanyu Li

A thesis
presented to the University of Waterloo
in fulfillment of the
thesis requirement for the degree of
Doctor of Philosophy
in
Mechanical and Mechatronics Engineering

Waterloo, Ontario, Canada, 2026

© Lanyu Li 2026

Examining Committee Membership

The following served on the Examining Committee for this thesis. The decision of the Examining Committee is by majority vote.

External Examiner:	Dr. Rui Ni Associate Professor, Department of Mechanical Engineering, Johns Hopkins University
Supervisor:	Dr. Zhao Pan Associate Professor, Department of Mechanical and Mechatronics Engineering, University of Waterloo
Internal Member:	Dr. Andrea Scott Associate Professor, Department of Mechanical and Mechatronics Engineering, University of Waterloo
	Dr. Jean-Pierre Hickey Associate Professor, Department of Mechanical and Mechatronics Engineering, University of Waterloo
Internal-External Member:	Dr. Nasser Mohieddin Abukhdeir Associate Professor & Associate Chair, Department of Chemical Engineering, University of Waterloo

Author's Declaration

This thesis consists of material all of which I authored or co-authored: see Statement of Contributions included in the thesis. This is a true copy of the thesis, including any required final revisions, as accepted by my examiners.

I understand that my thesis may be made electronically available to the public.

Statement of Contributions

This thesis contains material adapted from one co-authored publication. The exception to sole authorship is as follows: Sect. 2.1.1 is partially adapted from

Li, Lanyu, and Zhao Pan. "Three-dimensional time-resolved Lagrangian flow field reconstruction based on constrained least squares and stable radial basis function." *Experiments in Fluids* 65.4 (2024): 57.

The work presented in this section was conducted under the supervision of Dr. Zhao Pan.

Abstract

Bubbly flows are common and important in nature and industry. For example, in lakes and oceans, bubbles affect methane emissions and oxygen exchange. In industry, bubbles in reactors affect reaction efficiency and operational safety. Many studies have attempted to reconstruct bubbly flows from experiments and investigate the bubble mechanism. However, bubbly-flow reconstruction remains challenging for several reasons. For example, bubbly flows are inherently multi-scale in time and space. Small and rapid interface dynamics (e.g., coalescence and breakup) are coupled with large-scale liquid motion, such as wakes and vortical structures. In many studies, it is also necessary to simultaneously resolve the bubble interface and the surrounding liquid-phase motion. Although both experimental and numerical methods are widely used to study bubbly flows, each approach has limitations. Experiments provide direct observations of real flows, but they are limited by spatial and temporal resolution, measurement noise, and optical accessibility. Numerical simulations can provide complete flow fields, but their accuracy depends on modeling assumptions, numerical discretization, initial and boundary conditions, and they require experimental validation.

In this thesis, a Data-Assimilation (DA) framework is proposed to synchronize numerical simulations with experimental observations for bubbly-flow reconstruction, simultaneously resolving bubble interfaces and liquid-phase velocities at the bubble scale. The experimental observations are obtained from image-based measurements, including image velocimetry for the liquid phase and bubble silhouette sequences for the gas–liquid interface. The simulation is performed using the Volume-of-Fluid (VoF) method. DA is achieved using the Azouani–Olson–Titi (AOT) nudging algorithm. In the AOT-nudging algorithm, penalty terms are embedded in the governing equations of the two-phase flow as source terms. These terms penalize discrepancies between the experimental observations and the simulations, thereby driving the simulation toward the true flow state. As a result, the reconstruction can be viewed as a simulation continuously corrected by the observations.

The proposed framework is validated using synthetic and experimental data. The validation considers bubbles rising in two dimensions (2D). The validation results show that the framework synchronizes the reconstructed bubble and liquid-phase kinematics with those from the ground truth, whereas the baseline simulation without DA deviates from the ground truth at an early stage. The framework can also reconstruct temporally and spatially resolved full-field flow states, which are difficult to obtain directly from experiments alone. A parameter study shows that the reconstruction accuracy depends on several DA parameters, providing practical guidance for parameter selection.

The thesis also develops an accompanying Uncertainty Quantification (UQ) method for the bubble interface and liquid-phase velocity. The uncertainty is estimated from the local observation–reconstruction mismatch and the measurement uncertainty. Synthetic noisy observations are used to show that the UQ is effective in bubbly-flow reconstruction: it can predict the spatial distribution and magnitudes of reconstruction errors.

Lastly, the AOT-nudging framework is extended and applied to a three-phase flow, enabling the use of inertial tracer particles to reconstruct bubbly flows. In the extended framework, the measured particle kinematics, such as velocities and accelerations, are used to infer a preliminary liquid-phase velocity based on a particle-inertia correction model. The inferred velocity nudges and updates the liquid-phase momentum equation. Next, the updated flow advects the reconstructed inertial particles. The reconstructed and observed particle locations are compared to nudge the reconstructed trajectories toward the observed ones. Using the latest reconstructed particle trajectories, the liquid-phase velocity is updated again. As a result, the DA algorithm treats inertial-particle trajectories, liquid-phase velocities, and bubble silhouettes as both observations and assimilated states. This allows the reconstructed three-phase flow to satisfy the governing equations while remaining consistent with the observations. Validations using synthetic data show that the solver can achieve accurate and physically consistent bubbly-flow reconstruction even when inertial tracer particles with high Stokes numbers are used.

In summary, this thesis proposes an AOT-nudging DA framework that provides a practical and extensible approach for simultaneous bubble-interface and liquid-phase flow reconstruction at the bubble scale, with integrated uncertainty quantification and inertial-particle tracking capabilities. The proposed framework can reconstruct bubbly flows from sparse observations with accuracy, robustness, completeness, and physical consistency. The framework can be readily extended to a wide range of multiphase-flow problems for which experiments or numerical simulations alone are difficult to apply.

Acknowledgements

I would like to express my sincere gratitude to my advisor, Prof. Zhao Pan, for his guidance and support throughout my M.A.Sc. and Ph.D. studies. I am especially grateful to him for giving me the opportunity to pursue my graduate studies at the University of Waterloo, which has had a profound impact on my academic and professional development. I also deeply appreciate his continued support, advice, and encouragement during my job search and career planning.

I would also like to thank Prof. Jean-Pierre Hickey and Prof. Serhiy Yarusevych for their instruction and support throughout my graduate studies. Their advice, particularly during my job search and transition from graduate studies to my professional career, has been greatly appreciated. I am also grateful to Prof. Elisabeth Larsson from Uppsala University for her valuable advice and insightful discussions.

I would like to thank my colleagues and friends, Apurav Tambe, Connor Pryce, Junrong Zhang, Kaveeshan Thurairajah, Maksym Veremchuk, Matthew Krmpotic, Dr. Nazmus Sakib, and Dr. Youchao Teng, for their friendship, support, and assistance throughout my graduate studies.

Lastly, I would like to acknowledge the Digital Research Alliance of Canada for providing high-performance computing resources and ChatGPT by OpenAI for assistance with proofreading and language editing.

Table of Contents

Examining Committee Membership ii

Author's Declaration iii

Statement of Contributions iv

Abstract v

Acknowledgements vii

List of Figures xii

List of Tables xiv

List of Abbreviations xv

List of Symbols xviii

1 Introduction 1

1.1 Motivation 1

1.2 Objectives 4

2 Background **5**
2.1 Experimental Reconstruction Methods . . . 5
2.1.1 Liquid-phase velocity reconstruction . . . 5
2.1.2 Bubble reconstruction . . . 9
2.1.3 Summary . . . 13
2.2 Numerical Simulation Methods . . . 14
2.3 Data Assimilation . . . 14
2.3.1 Overview . . . 14
2.3.2 Nudging algorithm . . . 16
2.3.3 AOT-nudging algorithm . . . 17
2.3.4 Factors that influence AOT convergence . . . 19
2.4 Summary . . . 21

3 Bubbly Flow Experiment **23**
3.1 Experiment Setup . . . 23
3.1.1 Quasi-2D water channel . . . 23
3.1.2 Operating conditions . . . 25
3.2 Bubble Image Processing . . . 26
3.3 Image-Based Velocimetry . . . 29
3.3.1 Particle image velocimetry . . . 29
3.3.2 Lagrangian particle tracking . . . 30
3.4 Summary . . . 34

4 AOT-Nudging in Bubbly Flow **35**
4.1 Introduction . . . 35
4.2 Methodology . . . 36
4.2.1 Governing equations . . . 37
4.2.2 Finite volume discretization . . . 38

4.2.3 AOT-nudging workflow . . . 40
4.3 Results and Discussion . . . 41
4.3.1 Reconstruction error metrics . . . 41
4.3.2 Validation based on synthetic data: setup . . . 43
4.3.3 Validation based on synthetic data: results . . . 46
4.3.4 Parameter sensitivity analysis . . . 56
4.3.5 Experimental validation: setup . . . 65
4.3.6 Experimental validation: results . . . 67
4.4 Conclusions . . . 74

5 Uncertainty Quantification **75**
5.1 Introduction . . . 75
5.2 Methodology . . . 77
5.2.1 General uncertainty bound . . . 77
5.2.2 Uncertainty of velocity . . . 78
5.2.3 Uncertainty of volume fraction . . . 81
5.3 Results and Discussion . . . 85
5.3.1 Error and uncertainty metrics . . . 85
5.3.2 Synthetic observation generation . . . 87
5.3.3 Validation results . . . 88
5.4 Conclusions . . . 98

6 AOT-Nudging with Inertial Particle Tracking **99**
6.1 Introduction . . . 99
6.2 Methodology . . . 101
6.2.1 Governing equations . . . 102
6.2.2 Particle force models . . . 103
6.2.3 Particle inertia correction . . . 104

6.2.4 Discretization . . . 105
6.2.5 AOT-nudging workflow . . . 107
6.3 Results and Discussion . . . 108
6.3.1 Validation setup . . . 108
6.3.2 Non-dimensional analysis . . . 109
6.3.3 Validation results . . . 112
6.4 Conclusions . . . 115

7 Conclusions and Future Work **118**
7.1 Conclusions . . . 118
7.2 Future Work . . . 120

References **122**

APPENDICES **160**

A Volume-of-Fluid Method **161**

B PIMPLE Algorithm **163**

C Derivation of Particle Response Time **165**

List of Figures

3.1 Quasi-2D water tank and clamping assembly 24

3.2 Workflow for generating observational data from the high-speed camera image sequence, with $t = 0.125$ s shown as an example 33

4.1 Initial and boundary conditions for the reference and AOT-nudging reconstruction cases 44

4.2 Lagrangian tracer initialization and trajectories in the 2D multi-bubble rise case 48

4.3 Comparison of bubble trajectories among the ground truth, baseline simulation, and AOT-nudging reconstruction 49

4.4 Ground truth and baseline simulation of velocity magnitude 50

4.5 Ground truth and AOT-nudging reconstruction of velocity magnitude . . . 51

4.6 Ground truth and AOT-nudging reconstruction of the volume-fraction field 52

4.7 Ground truth and AOT-nudging reconstruction of velocity-gradient magnitude 53

4.8 Ground truth and AOT-nudging reconstruction of the pressure field 54

4.9 Ground truth versus AOT-nudging reconstruction for the vorticity in a zoomed region 55

4.10 Time-varying reconstruction errors for different K_{vel} values 57

4.11 Time-varying reconstruction errors for different K_{vol} values 58

4.12 Time-varying reconstruction errors for different tracer seeding densities . . 59

4.13 Time-varying reconstruction errors for different observation frequencies . . 60

4.14 Time-varying reconstruction errors for different mesh spacings 61

4.15 Experimental measurement window and computational setup for the reconstruction . . . 66
4.16 Pre-processed images and reconstructed volume-fraction fields near bubble coalescence . . . 70
4.17 PIV observations and AOT-nudging velocity reconstruction near bubble coalescence . . . 71
4.18 LPT observations and AOT-nudging velocity reconstruction near bubble coalescence . . . 72
4.19 Zoomed comparison of PIV- and LPT-based AOT-nudging reconstructions near coalescence . . . 73

5.1 An illustration of residual-based velocity uncertainty . . . 78
5.2 A 1D illustration of the UQ model for the volume fraction . . . 82
5.3 A 2D illustration of residual-based volume-fraction uncertainty . . . 83
5.4 Synthetic velocity observation generation at $t = 0.1$ s . . . 88
5.5 Synthetic volume-fraction observation generation at $t = 0.1$ s . . . 89
5.6 Ground truth and AOT-nudging reconstruction of velocity magnitude . . . 92
5.7 Volume-fraction UQ results for noise level 1 at $t = 0.3$ s . . . 93
5.8 Volume-fraction UQ results for noise level 2 at $t = 0.35$ s . . . 94
5.9 Velocity UQ results for noise level 1 at $t = 0.3$ s . . . 95
5.10 Velocity UQ results for noise level 2 at $t = 0.35$ s . . . 96
5.11 Velocity E-versus-U comparison for different noise levels . . . 97

6.1 Initial and boundary conditions for the reference and AOT-nudging with inertial particle tracking reconstruction cases . . . 109
6.2 Inertial Lagrangian particle distribution and trajectories at $t = 0.2$ s . . . 110
6.3 Comparison of ground-truth and reconstructed particle trajectories . . . 113
6.4 Comparison of liquid-phase velocity magnitude fields at $t = 0.2$ s . . . 114
6.5 Comparison of liquid-phase velocity-gradient magnitude fields at $t = 0.2$ s . . . 115
6.6 Comparison of vorticity fields with tracer-particle locations at $t = 0.2$ s . . . 116

List of Tables

3.1 Image-acquisition parameters used in the quasi-2D bubbly-flow experiment 25
3.2 Operating conditions of the bubbly-flow experiment 27
3.3 Main parameters for PIV processing 31
3.4 Main parameters for LPT processing 32

4.1 Parameters used in the AOT-nudging sensitivity analysis 56

5.1 Synthetic observation noise parameters 87

List of Abbreviations

1D	One-dimensional or one dimension
2D	Two-dimensional or two dimensions
3D	Three-dimensional or three dimensions
3D-Var	Three-dimensional variational data assimilation
4D	Four-dimensional or four dimensions
4D-Var	Four-dimensional variational data assimilation
AOT	Azouani–Olson–Titi algorithm
ART	Algebraic Reconstruction Technique
AMR	Adaptive Mesh Refinement
BC	Boundary Condition
BFN	Back-and-Forth Nudging
BSD	Bubble Size Distribution
CFD	Computational Fluid Dynamics
CFL	Courant–Friedrichs–Lewy
CLAHE	Contrast–Limited Adaptive Histogram Equalization
CMOS	Complementary Metal–Oxide–Semiconductor
CSF	Continuum Surface Force
CVAT	Computer Vision Annotation Tool
DA	Data Assimilation
DNS	Direct Numerical Simulation
DoG	Difference of Gaussians
EnKF	Ensemble Kalman Filter
FDM	Finite Difference Method
FEM	Finite Element Method

FOV	Field of View
fps	Frames per second
FVM	Finite Volume Method
GCM	Global Climate Model
HFSB	Helium-Filled Soap Bubble
IC	Initial Condition
IMEX	Implicit–Explicit
KF	Kalman Filter
LDV	Laser Doppler Velocimetry
LES	Large Eddy Simulation
LPT	Lagrangian Particle Tracking
LS	Least Squares
MRG	Maxey–Riley–Gatignol equation
MULES	Multidimensional Universal Limiter for Explicit Solution
N–S	Navier–Stokes equation
NWP	Numerical Weather Prediction
OpenFOAM	Open-source Field Operation And Manipulation
OFAT	One-Factor-At-a-Time
PBM	Population Balance Model
PID	Proportional–Integral–Derivative
PIMPLE	PISO–SIMPLE algorithm
PISO	Pressure-Implicit with Splitting of Operators
PIV	Particle Image Velocimetry
PNG	Portable Network Graphics
ppp	Particles per pixel
PTV	Particle Tracking Velocimetry
RANS	Reynolds-Averaged Navier–Stokes
RBF	Radial Basis Function
RCM	Regional Climate Model
RHS	Right-Hand Side
ROI	Region of Interest
ROM	Reduced-Order Model
SIMPLE	Semi-Implicit Method for Pressure-Linked Equations

SIV	Schlieren Image Velocimetry
SPAV	Stochastic Particle Advection Velocimetry
STB	Shake-The-Box
Tomo-PIV	Tomographic Particle Image Velocimetry
TR	Time-Resolved
TR-LPT	Time-Resolved Lagrangian Particle Tracking
UQ	Uncertainty Quantification
VH	Visual Hull
VIC	Vortex-In-Cell
VoF	Volume-of-Fluid

List of Symbols

Accents, Subscripts, and Superscripts

$[\cdot]^*, [\cdot]^{**}$	Predicted and corrected quantities in a pressure-based CFD solver
$[\cdot]^n, [\cdot]^{n+1}$	Current and next time-step quantities
$[\cdot]_{\mathrm{P}}, [\cdot]_{\mathrm{N}}$	Cell-center and neighboring-cell quantities
$[\cdot]_{\mathrm{fc}}$	Face-centered quantity
$[\cdot]_{\mathrm{g}}, [\cdot]_{\mathrm{l}}$	Gas-phase and liquid-phase quantities
$[\cdot]_{\mathrm{p}}$	Particle-related quantity
$[\cdot]_{\mathrm{cen}}, [\cdot]_{\mathrm{tra}}$	Mesh-cell-center and tracer-location quantities
$[\cdot]^{\mathrm{grt}}$	Ground-truth quantity
$[\cdot]^{\mathrm{intp}}$	Interpolated quantity
$[\cdot]^{\mathrm{obs}}$	Observed quantity
$[\cdot]^{\mathrm{o}}, [\cdot]^{\mathrm{m}}$	Observation-space and mesh-space quantities
$[\cdot]^{\mathrm{rcs}}$	Reconstructed quantity
$[\cdot]_0$	Initial quantity
$\hat{[\cdot]}$	Estimated or assimilated quantity
$\overline{[\cdot]}$	Averaged quantity
$\tilde{[\cdot]}$	Reconstructed or approximated quantity
$\|\cdot\|_2$	Euclidean norm
$\|\cdot\|_F$	Frobenius norm

Roman Symbols

A_{b}	Projected bubble area	$[\mathrm{m}^2]$
A_{p}	Particle projected area	$[\mathrm{m}^2]$

$\mathrm{A}_{u,\mathrm{P}}, \mathrm{A}_{u,\mathrm{N}}$	Finite-volume matrix coefficients for velocity at cell P and neighboring cell N	
$\mathrm{A}_{\alpha,\mathrm{P}}, \mathrm{A}_{\alpha,\mathrm{N}}$	Finite-volume matrix coefficients for volume fraction at cell P and neighboring cell N	
$\boldsymbol{a}_{\mathrm{p}}$	Particle acceleration	$[\mathrm{m/s^2}]$
$\boldsymbol{a}_{\mathrm{p}}^{\mathrm{obs}}$	Observed particle acceleration	$[\mathrm{m/s^2}]$
$\boldsymbol{b}_{\mathrm{p}}$	Gravity–buoyancy contribution in the particle-response model	$[\mathrm{m/s^2}]$
b_α	Half-thickness of the synthetic interface-noise band	[cells]
C_{AM}	Added-mass coefficient	
C_D	Drag coefficient	
C_L	Lift coefficient	
c_x, c_y	Principal-point coordinates	[pixels]
$d(\boldsymbol{x})$	Signed-distance field	[m]
d_k, d_{k+1}	Signed-distance fields at two neighboring annotated frames	[m]
D_{b}	Bubble diameter	[m]
d_{p}	Particle diameter	[m]
d_{dist}	Minimum-distance criterion in particle tracking	[pixels]
E	Relative reconstruction error	
e_Q	Point-wise reconstruction error of a generic quantity Q	
E_u	Velocity reconstruction error	
E_α	Volume-fraction reconstruction error	
$\mathcal{E}$	Reconstruction error	
$\mathcal{E}_{L^2_{\mathrm{abs}}}$	Absolute L^2-norm reconstruction error	
$\mathcal{E}_{L^2_{\mathrm{rel}}}$	Relative L^2-norm reconstruction error	
$\boldsymbol{f}$	External body-force term per unit mass	$[\mathrm{m/s^2}]$
$\boldsymbol{f}_{\mathrm{grv}}$	Gravity force per unit volume	$[\mathrm{N/m^3}]$
$\boldsymbol{f}_{\mathrm{ten}}$	Surface-tension force per unit volume	$[\mathrm{N/m^3}]$
$\mathbf{F}$	Model evolution operator in a discrete dynamical system	
$F(\mathbf{v})$	Dynamical-system operator in the AOT-nudging formulation	
$\boldsymbol{F}_{AM}$	Added-mass force	[N]
$\boldsymbol{F}_B$	Buoyancy force	[N]
$\boldsymbol{F}_D$	Drag force	[N]

$\boldsymbol{F}_G$	Net gravity–buoyancy force	[N]
$\boldsymbol{F}_L$	Lift force	[N]
$\boldsymbol{F}_{\mathrm{BS}}$	Basset history force	[N]
$\boldsymbol{F}_{\mathrm{NUG,p}}$	Particle-trajectory nudging force	[N]
$\boldsymbol{F}_{\nabla p}$	Pressure-gradient force	[N]
f_x, f_y	Focal scales in the x- and y-directions	[pixels]
f_{acq}	Image-acquisition frequency	[Hz]
f_{ndg}	Nudging frequency	[Hz]
f_{obs}	Observation frequency	[Hz]
$f_{\mathrm{o_s}}$	Search-scale parameter in particle tracking	
$\boldsymbol{g}$	Gravitational acceleration vector	[m/s^2]
g	Magnitude of gravitational acceleration	[m/s^2]
G_σ	Gaussian kernel with standard deviation σ	
h	Observation resolution or characteristic interpolation length	[m]
$\boldsymbol{h}$	Position vector used in the modified pressure definition	[m]
$\mathbf{H}$	Observation operator in a discrete data-assimilation system	
$\mathbf{HbyA}$	Intermediate velocity-like field used in pressure correction	[m/s]
$H(\cdot)$	Heaviside step function	
$\mathbf{I}$	Identity tensor	
I_{DoG}	Difference-of-Gaussian filtered image intensity	
I_{raw}	Raw image intensity	
$\mathscr{I}$	Interpolation operator between mesh and observation spaces	
$\mathscr{I}_h$	AOT-nudging interpolation operator associated with observation resolution h	
$\mathscr{I}_{\boldsymbol{u},h}$	Velocity interpolation operator in AOT-nudging	
$\mathscr{I}_{\alpha,h}$	Volume-fraction interpolation operator in AOT-nudging	
$\mathscr{I}_{\mathrm{msh}\to\mathrm{tra}}$	Mesh-to-tracer interpolation operator	
$\mathscr{I}_{\mathrm{tra}\to\mathrm{msh}}$	Tracer-to-mesh interpolation operator	
K	Generic nudging gain or assimilation strength	
k	Discrete time-step index	
$\mathbf{K}$	Gain matrix in a discrete data-assimilation system	
K_{pos}	Particle-position nudging strength	
K_{vel}	Velocity nudging strength	

K_{vol}	Volume-fraction nudging strength	
L_{c}	Characteristic length scale	[m]
m_{p}	Particle mass	[kg]
N	Number of contour points on the bubble boundary	
N_{b}	Number of bubbles	
N_{eval}	Number of evaluation or sampling points	
N_x, N_y, N_z	Number of mesh cells in the x-, y-, and z-directions	
N_{frm}	Number of observation frames	
N_{pix}	Number of pixels in the image domain	
N_{p}	Number of tracer or inertial particles	
N_{tri}	Number of independent trials	
n_{corr}	Number of PIV outlier-correction passes	
n_{mp}	Number of multipass refinement passes in particle tracking	
$n_{\mathrm{mp,ti}}$	Number of initialization refinement passes in particle tracking	
n_{nei}	Number of neighboring particles used for local tracking consistency	
n_{outl}	Outlier-neighborhood size in particle tracking	
$n_{\mathrm{outl,iter}}$	Number of outlier-removal iterations in particle tracking	
$\boldsymbol{n}$	Unit normal vector	
$\boldsymbol{n}_{12}$	Unit vector connecting two interacting bubble centers	
$\boldsymbol{n}_u$	Particle-derived velocity nudging field	[m/s^2]
p	Pressure	[Pa]
p_{rgh}	Modified pressure excluding the hydrostatic component	[Pa]
I_{int}	Particle-detection intensity threshold	
$\mathrm{p}_{\mathrm{size}}$	Characteristic particle diameter used for particle detection	[pixels]
Q	Generic reconstructed quantity	
r	Radius of a spherical bubble or particle	[m]
$\boldsymbol{r}$	Residual vector between reconstruction and observation	
r_Q	Point-wise residual of a generic quantity Q	
$\boldsymbol{r}_u$	Velocity residual vector	
r_α	Volume-fraction residual	
R_{limit}	PIV correlation threshold	
r_ρ	Particle-to-fluid density ratio	
Re_{b}	Bubble Reynolds number	

$\mathrm{Re_p}$	Particle Reynolds number	
Re_ω	Vorticity Reynolds number	
s_c	Spatial calibration factor	[m/pixel]
$\boldsymbol{S}$	Strain-rate tensor	[s^{-1}]
$\boldsymbol{S}_\mathrm{fc}$	Face-area vector	[m^2]
$\mathrm{S}_{u,\mathrm{P}}$	Source term in the discretized velocity equation for cell P	
$\mathrm{S}_{\alpha,\mathrm{P}}$	Source term in the discretized volume-fraction equation for cell P	
t	Time	[s]
T_c	Characteristic time scale	[s]
t_k, t_{k+1}	Two neighboring time levels	[s]
u, v, w	Velocity components in the x-, y-, and z-directions	[m/s]
U	Uncertainty estimate	
$\boldsymbol{u}$	Velocity field	[m/s]
u_b	Bubble rising velocity	[m/s]
U_Q	Uncertainty estimate for a generic quantity Q	
u_ref	Reference velocity magnitude used for normalization	[m/s]
U_u	Velocity uncertainty estimate	
U_α	Volume-fraction uncertainty estimate	
$\boldsymbol{u}^{\mathrm{obs,f}}$	Inferred carrier-flow velocity observation	[m/s]
$\boldsymbol{u}_\mathrm{p}^\mathrm{obs}$	Observed particle velocity used in the inertial correction	[m/s]
$\boldsymbol{u}_0$	Reference or ground-truth velocity field	[m/s]
$\boldsymbol{u}_\mathrm{b}$	Bubble velocity	[m/s]
$\boldsymbol{u}_\mathrm{f}$	Carrier-flow velocity at the particle location	[m/s]
$\boldsymbol{u}_\mathrm{l}$	Liquid-phase velocity	[m/s]
$\boldsymbol{u}_\mathrm{rc}$	Relative compression velocity in the VoF equation	[m/s]
$\boldsymbol{u}_\mathrm{slip}$	Slip velocity between carrier flow and particle	[m/s]
u_slip	Slip-velocity magnitude	[m/s]
$\mathbf{U}_\mathrm{P}$	Discrete cell-centered velocity at cell P	[m/s]
$\mathbf{U}^*$	Predicted velocity field in the pressure–velocity iteration	[m/s]
$\mathbf{v}$	Assimilated solution in the AOT-nudging formulation	
$\mathbf{v}_0$	Initial assimilated solution	
$\boldsymbol{u}_\mathrm{p}$	Particle velocity	[m/s]
V_P	Volume of control volume of cell P	[m^3]

V_b	Bubble volume	[m^3]
V_p	Particle volume	[m^3]
W_m	Half-width of the moving-average smoothing window	
W_iw	PIV interrogation-window size	[pixels]
W_sw	PIV search-window size	[pixels]
x_c	Characteristic streamwise length	[m]
$\boldsymbol{x}$	Spatial coordinate vector	[m]
$\mathbf{x}_k$	Model state at time step k	
$\boldsymbol{x}_\mathrm{cen}$	Mesh-cell-center location	[m]
$\boldsymbol{x}_\mathrm{p}$	Particle position	[m]
$\boldsymbol{x}_\mathrm{p}^\mathrm{obs}$	Observed particle position	[m]
$\boldsymbol{x}_\mathrm{p}^\mathrm{rcs}$	Reconstructed particle position	[m]
$\boldsymbol{x}_\mathrm{tra}$	Tracer location	[m]
$\mathbf{z}_k$	Observation vector at time step k	
$\mathcal{N}(\mathrm{P})$	Set of neighboring cells of cell P	
ppp_eq	Equivalent particles per pixel	
Ca	Capillary number	
Eo	Eötvös number	
Fr	Froude number	
Mo	Morton number	
Re	Reynolds number	
St	Stokes number	
We	Weber number	
u_c	Characteristic velocity scale	[m/s]
L_plt	Plate spacing or channel-gap thickness	[m]
h_flm	Lubrication-film thickness on one side of a bubble	[m]
C_B	Bretherton wetting-film coefficient	
C_FS	Fairbrother–Stubbs wetting-film coefficient	
$\boldsymbol{x}_i, \overline{\boldsymbol{x}}_i$	Original and smoothed contour points	[m]
n_pnt	Tracer seeding density	[mm^{-2}]
ℓ_tra	Characteristic inter-tracer particle spacing	[m]
f_v	Vortex-shedding frequency	[Hz]
h_v	Transverse spacing between vortex rows	[m]

Sr	Strouhal number	
$\mathrm{Co}_{\mathrm{obs}}$	Observation Courant number	
$\mathrm{Co}_{\mathrm{obs}}^{\max}$	Maximum adopted observation Courant number	
$\lvert\boldsymbol{u}\rvert_{\max}$	Maximum velocity magnitude	[m/s]
$\Delta x_{\mathrm{px}}, \Delta y_{\mathrm{px}}$	Particle displacements in the image plane	[pixels]

Greek Symbols

α	Liquid volume fraction; $\alpha = 1$ in liquid and $\alpha = 0$ in gas	
α_0	Reference or ground-truth volume-fraction field	
α_{ref}	Reference volume fraction used for normalization	
$\alpha^{\mathrm{HO}}, \alpha^{\mathrm{UP}}$	High-order and upwind volume-fraction values in MULES	
$\alpha_{\mathrm{P}}, \alpha_{\mathrm{N}}$	Volume fractions of cell P and neighboring-cell N	
β	Saffman–Mei lift parameter	
γ_{c}	Gamma-correction parameter used in image processing	
γ_{SM}	Auxiliary Saffman–Mei lift parameter	
Γ	Gas–liquid interface	
$\Gamma^{\mathrm{grt}}, \Gamma^{\mathrm{obs}}$	Ground-truth and observed gas–liquid interfaces	
Γ_α^E	Boundary of the volume-fraction true-error region	
Γ_α^r	Boundary of the volume-fraction residual region	
Γ_α^U	Boundary of the volume-fraction uncertainty region	
δ_Q	Observation uncertainty bound for a generic quantity Q	
δ_u	Velocity observation uncertainty bound	[m/s]
δ_α	Interface-position uncertainty bound	[m]
δ_{BL}	Boundary-layer thickness	[m]
$\delta_{\mathrm{msh}\to\mathrm{tra}}^{\mathrm{intp}}$	Mesh-to-tracer interpolation-error bound	[m/s]
$\delta_{\mathrm{tra}\to\mathrm{msh}}^{\mathrm{intp}}$	Tracer-to-mesh interpolation-error bound	[m/s]
Δp	Pressure jump across the gas–liquid interface	[Pa]
Δt	Time-step size or frame interval	[s]
Δt_{obs}	Observation time interval	[s]
Δt_{out}	Dense-output time spacing	[s]
Δt_n	Particle-observation time interval at time step n	[s]
$\Delta\alpha$	Volume-fraction discrepancy used in AOT-nudging	
$\Delta\boldsymbol{u}$	Velocity discrepancy used in AOT-nudging	[m/s]

$\Delta x, \Delta y, \Delta z$	Mesh spacings in the x-, y-, and z-directions	[m]
$\Delta x_{\max}$	Maximum expected particle displacement	[pixels]
ϵ_E	Error threshold for volume-fraction uncertainty quantification	
ε_{blr}	Shape factor used for synthetic volume-fraction blurring	
ϵ_{r}	Residual threshold for volume-fraction uncertainty quantification	
ε	Observation error or approximation error	
ε_Q	Observation error of a generic quantity Q	
$\boldsymbol{\varepsilon}_u$	Velocity observation error	[m/s]
ε_α	Local interface-position error	[m]
ζ	Saffman–Mei lift correction factor	
$\boldsymbol{\eta}_{\text{msh}\to\text{tra}}$	Mesh-to-tracer interpolation error	[m/s]
$\boldsymbol{\eta}_{\text{tra}\to\text{msh}}$	Tracer-to-mesh interpolation error	[m/s]
κ	Interface curvature	[m^{-1}]
κ_{intp}	Ratio between interpolation-error bounds and the mesh-wise velocity residual	
λ_{c}	Temporal interpolation weight in signed-distance-field interpolation	
λ_{lmt}	MULES face-limiter coefficient	
λ_{v}	Streamwise vortex spacing	[m]
μ	Dynamic viscosity	[Pa s]
μ_{f}	Local carrier-flow dynamic viscosity	[Pa s]
μ_{g}	Gas dynamic viscosity	[Pa s]
μ_{l}	Liquid dynamic viscosity	[Pa s]
∇	Nabla operator	
ν	Kinematic viscosity	[m^2/s]
ν_{f}	Local carrier-flow kinematic viscosity	[m^2/s]
ν_{l}	Liquid kinematic viscosity	[m^2/s]
Ω	Bubble region or binary bubble-mask region	
Ω_{g}	Gas region	
Ω_{l}	Liquid region	
Ω_α^E	Volume-fraction true-error region	
Ω_α^r	Volume-fraction residual region	
Ω_α^U	Volume-fraction uncertainty region	
$\partial\Omega$	Boundary of the bubble or binary mask region	

ϕ_{p}	Particle volume fraction	
ϕ_{fc}	Corrected face flux after pressure correction	$[\mathrm{m}^3/\mathrm{s}]$
ψ, ψ_D	RBF-QR kernel and its derivative	
ρ	Density	$[\mathrm{kg}/\mathrm{m}^3]$
ρ_{f}	Local carrier-flow density	$[\mathrm{kg}/\mathrm{m}^3]$
ρ_{g}	Gas density	$[\mathrm{kg}/\mathrm{m}^3]$
ρ_{l}	Liquid density	$[\mathrm{kg}/\mathrm{m}^3]$
ρ_{p}	Particle density	$[\mathrm{kg}/\mathrm{m}^3]$
σ	Surface-tension coefficient	$[\mathrm{N}/\mathrm{m}]$
σ_u	Standard deviation of synthetic velocity-observation noise	$[\mathrm{m}/\mathrm{s}]$
σ_x	Metric position uncertainty	[mm]
$\sigma_{\mathrm{small}}, \sigma_{\mathrm{large}}$	Standard deviations of the small and large Gaussian kernels in the DoG filter	
τ	Dummy time variable in the Basset-history integral	[s]
$\boldsymbol{\tau}$	Deviatoric viscous stress tensor	[Pa]
τ_{p}	Particle response time	[s]
$\boldsymbol{\omega}$	Vorticity vector	$[\mathrm{s}^{-1}]$
ω_z	Out-of-plane vorticity component	$[\mathrm{s}^{-1}]$
$\hat{\boldsymbol{\omega}}$	Unit vector in the vorticity direction	
χ_α^E	Indicator of the volume-fraction true-error region	
χ_α^r	Indicator of the volume-fraction residual region	
χ_α^U	Indicator of the volume-fraction uncertainty region	
χ_{p}	Particle mass loading	

Chapter 1

Introduction

1.1 Motivation

A bubbly flow is a two-phase flow in which gas bubbles are dispersed or suspended in a continuous liquid phase. Bubbly flows are common in nature and industry. For example, beluga whales release bubbles to signal potential threats [1]. In lakes and oceans, bubbles influence methane emissions and gas exchange across the air-water interface [2, 3]. In ocean engineering, bubbles arise from cavitation in hydraulic machinery (e.g., [4–6]) and seismic air-gun operations for seabed geophysics (e.g., [7–9]). In nuclear reactors, understanding bubble behavior is important for heat management and operational safety (e.g., [10–12]). In chemical engineering, bubbles play an essential role in mixing and mass transfer in reactors (e.g., [13–15]).

Despite their ubiquity, some mechanisms of bubbly flows are still not fully understood because of their complex, multiscale, and strongly coupled nature. These mechanisms include bubble formation (e.g., [16–18]), rising (e.g., [19–21]), deformation (e.g., [22–26]), breakup (e.g., [24, 27, 28]), coalescence (e.g., [29–31]), and pinch-off (e.g., [32–34]). Some phenomena such as bubble interaction with turbulence (e.g., [22–26, 28, 35, 36]), interaction with structures or boundaries (e.g., [37–41]), gas holdup (e.g., [42, 43]), bubble size distribution (BSD) (e.g., [44, 45]), capillary or slug flow phenomena (e.g., [46–49]), and cavitation (e.g., [41, 50, 51]) remain active research topics.

To understand these phenomena, the bubbly flows should be studied at the bubble scale using time-resolved measurements. At this scale, the transient evolution of individual bubbles and the surrounding liquid response are resolved in space and time. There are four

major reasons for this. First, some important events may only occur at this scale, such as pinch-off (e.g., [32–34]). These processes involve rapid, localized interfacial motion. If they are observed only at a macroscopic scale or low temporal resolution, the underlying bubble dynamics are difficult to resolve. Second, many macroscopic bubbly-flow behaviors originate from mechanisms at the bubble scale. Examples include bubble-induced turbulence, mass transfer, and momentum transfer (e.g., [52–54]). Third, interface physics is inherently local. Important quantities such as curvature, surface-tension force, and interfacial shear are determined near the gas-liquid interface. These effects are hard to describe accurately by using averaged or global variables alone. Lastly, many closure models used in bubbly-flow simulations are derived from bubble-scale physics. For example, drag [55, 56], lift [57–59], breakup [60–63], and coalescence [61, 63, 64] models are often derived from bubble-scale studies. Therefore, bubble-scale analysis is needed to establish or improve closure models for large-scale simulations.

Researchers investigate bubbly flows through experiments and numerical simulations. Experiments are essential because they provide direct and trustworthy observations of real bubble behaviors. They are used to observe local bubble motion, interface evolution, and liquid-phase response at the bubble scale [65, 66]. They can also quantify key flow features for the development and validation of theoretical or numerical models (e.g., [67–70]). In addition, experiments can help develop scaling laws that connect single-bubble behavior to larger-scale bubbly-flow phenomena (e.g., [71, 72]).

However, experiments have limitations. The measurable quantities are restricted by optical access, camera resolution, frame rate, illumination quality, and tracer seeding conditions [73–75]. Moreover, many quantities of interest are difficult to measure directly, especially inside the flow area surrounded by many bubbles or near strongly deforming interfaces. Experimental data often contain noise, bias, and incomplete information [73, 75].

A numerical simulation solves the governing equations of the flow under prescribed physical assumptions and boundary conditions [76–78]. Compared with experiments, simulations can provide full flow-field data with high spatial and temporal resolution. They also allow specific mechanisms to be isolated, parameters to be varied systematically, and quantities that are difficult to measure experimentally to be evaluated (e.g., [77, 79, 80]). Different numerical methods have been developed for bubbly flows, depending on the target scale, ranging from macroscopic to microscopic scales [81, 82], and on the level of interface resolution, ranging from Eulerian-Eulerian models [56, 83, 84] to interface-capturing methods (e.g., [85–89]).

Although numerical simulations provide richer flow information than experiments, they have limitations. Their accuracy depends on the governing assumptions, closure models,

numerical discretization, mesh resolution, and boundary conditions (e.g., [90–92]). In many simulations, unresolved bubble-scale physics must be represented by empirical or semi-empirical closure models (e.g., [55–64, 78, 90, 93]). Even for interface-resolved simulations, modeling error, numerical diffusion, and uncertain initial or boundary conditions may still cause discrepancies from the real flow (e.g., [94–96]). As a result, simulations may provide a physically consistent flow field up to the given model, but not necessarily the true flow in the experiment.

Therefore, neither experiments nor numerical simulations alone are sufficient for complete bubbly-flow reconstruction. For this reason, experiments and simulations should be viewed as complementary rather than competing approaches. This complementarity motivates the use of data assimilation.

Data assimilation (DA) combines experimental observations with a numerical model to obtain an optimal estimate of the flow field [97–100]. The field is consistent with the measurements and the governing equations of the system. DA uses observations to correct the numerical solution and preserve physical consistency. DA could recover unobserved flow quantities, reduce uncertainty, and improve the accuracy of flow reconstruction. In bubbly flows, this is valuable because many quantities are hard to measure directly, and simulations alone may not reproduce the true flow observed in the experiments.

However, DA studies for bubbly flows are still limited. Existing studies have mainly focused on state or parameter estimation, such as estimating the gas holdup [101, 102], cavitation-flow velocity [103], gas injection velocity [104], inflow rate [102], bubble contact angle [104], cavitation bubble diameters [105], and shear modulus and viscosity in viscoelastic bubble cavitation [106], overlapped bubble detection from images [107], rather than simultaneous reconstruction of bubble interfaces and surrounding liquid-phase flow at the bubble scale. Some DA studies for multiphase systems have addressed subsurface flows [108–110], porous media flows [111–113], reservoir flows [114–116], pipeline stratified and slug flows [117], and free-surface flows [118–120]. These studies demonstrate the versatility of DA, but they also show that most applications still target macroscopic states, parameters, or history matching, rather than local bubble interfacial dynamics such as bubble deformation, coalescence, and breakup.

Moreover, many established assimilation methods remain computationally expensive. For example, the ensemble Kalman filter (EnKF) is widely used in multiphase flow problems [101, 103, 108, 116], but its performance is limited by updating the large covariance matrices in high-dimensional nonlinear systems [97, 98]. These computational demands and the complexity of multiphase flows have limited the direct assimilation of local bubble-scale interfacial dynamics. This gap motivates the present work with four research objectives.

1.2 Objectives

This research aims to advance bubbly-flow studies by developing a DA framework that combines experiments, numerical simulations, and uncertainty quantification for simultaneous bubble-interface and liquid-phase flow reconstruction at the bubble scale. The specific research objectives (O's) are:

- O1 Design and conduct quasi-2D bubbly flow experiments; acquire image-based measurements of bubble silhouettes and surrounding liquid-phase velocities; and develop a data-processing pipeline to extract observation data from the measurements.
- O2 Develop an accurate, robust, and efficient DA-based solver for bubbly-flow reconstruction; validate the solver using synthetic bubbly-flow data; and apply the solver to the experimental observations obtained in O1.
- O3 Develop and validate an uncertainty quantification (UQ) model for the bubbly-flow reconstruction framework in O2.
- O4 Extend the reconstruction framework in O2 to three-phase flows with inertial tracer particles; develop a corresponding DA solver and validate it using synthetic data.

The thesis is organized according to O1 – O4. Chap. 2 reviews the background on experimental techniques, numerical simulation, and DA. Chap. 3 addresses O1 by presenting the bubbly-flow experiment, data acquisition, and processing. Chap. 4 addresses O2 by developing and validating the proposed solver for bubbly flows. Chap. 5 addresses O3 by establishing and validating the UQ framework. Chap. 6 discusses O4 by extending the proposed solver to three-phase flow reconstruction. Lastly, Chap. 7 summarizes the main conclusions and future work.

Chapter 2

Background

This chapter reviews the background relevant to bubbly flow reconstruction. It focuses on three main components of the present work: experimental reconstruction methods, numerical simulation methods, and data assimilation (DA) techniques. First, Sect. 2.1 introduces the main experimental approaches used for bubbly flow reconstruction: Sect. 2.1.1 explains the Eulerian and Lagrangian descriptions in fluid mechanics and reviews liquid-phase velocity reconstruction methods; Sect. 2.1.2 reviews image-based methods for bubble reconstruction; Sect. 2.1.3 summarizes the main points of the experimental reconstruction literature. Next, Sect. 2.2 reviews numerical simulation methods for bubbly flows at different scales and with different levels of interface resolution. Then, Sect. 2.3 introduces the role of DA in combining experiments with numerical simulation. Sect. 2.3.1 reviews the general concept of DA. Sect. 2.3.2 reviews nudging-based assimilation methods. Sect. 2.3.3 introduces the Azouani–Olson–Titi algorithm as the DA method adopted in this thesis.

2.1 Experimental Reconstruction Methods

2.1.1 Liquid-phase velocity reconstruction

Image-based velocimetry is widely used in experimental fluid mechanics. These methods can be described from either an Eulerian or a Lagrangian perspective [121]. In the Eulerian perspective, the flow is analyzed within a fixed control volume, without tracking individual fluid parcels or bubbles. Typical techniques include Particle Image Velocimetry (PIV) [122–125], such as Stereo-PIV [126–128], Tomographic PIV (Tomo-PIV) [129, 130],

and micro-PIV [131], as well as Schlieren Image Velocimetry (SIV) [132, 133]. In the Lagrangian perspective, individual fluid parcels or bubbles are followed as they move through space and time. Lagrangian Particle Tracking (LPT) or Particle Tracking Velocimetry (PTV) is a typical technique based on the Lagrangian perspective. Common techniques include 2D-PTV, Shake-The-Box (STB)-PTV [134, 135], rainbow PTV [136–138], and plenoptic-PTV [139, 140]. Although both descriptions are fundamental in classical fluid mechanics [121, 141, 142], Eulerian approaches are more common in many practical applications. This preference may be related to the difficulty of tracking particles with high spatial and temporal resolution in 3D, the high data-processing cost of Lagrangian experiments [143], and the mathematical convenience of conservative laws in Eulerian descriptions [144, 145].

Recent developments in 3D, time-resolved, high-seeding density Lagrangian particle tracking (3D TR-LPT) [134, 135, 146] have highlighted the potential of the Lagrangian perspective. First, LPT provides an intuitive description of fluid motion by directly revealing particle trajectories and transport paths. Second, LPT could provide higher spatial resolution than typical Eulerian methods. LPT tracks individual particles without interrogation-window averaging. This makes it suitable for resolving localized flow features. Third, LPT naturally provides time-resolved trajectory information, which is valuable for analyzing transport pathways [147], particle residence times [148, 149], mixing, and Lagrangian flow structures [150, 151]. Therefore, in this chapter, Lagrangian reconstruction methods are emphasized.

Liquid-phase velocity reconstruction aims to recover particle trajectories, velocities, and differential flow quantities (e.g., velocity gradients and vortices [152–154]) from scattered particle measurements in the liquid phase of bubbly flows. Existing Lagrangian methods can be grouped into trajectory and velocity reconstruction, differential-quantity reconstruction, and comprehensive reconstruction strategies that combine multiple steps in a single framework.

Trajectory and velocity

Particle trajectory reconstruction is a central task in Lagrangian analysis. Common approaches approximate particle trajectories using polynomials or basis splines (B-splines), typically of second order [155], third order [134, 155–157], or fourth order [158]. Least-squares regression is often used to reduce the influence of noise in the particle coordinates [134, 155–157]. These methods are effective for smoothing noisy particle tracks, but they also face several limitations. Low-order functions may not capture strongly curved trajectories, whereas high-order functions may suffer from oscillations, known as Runge's

phenomenon. In addition, most existing methods use a fixed-order function throughout the reconstruction, which limits flexibility for trajectories with varying curvature. Another difficulty is that when only a small number of frames is available, the achievable smoothness is restricted.

Velocity reconstruction is commonly performed either by finite-difference methods or by differentiating a continuous trajectory function [134, 156, 157]. The simplest example is the first-order finite-difference method [159], which computes velocity from the displacement between two consecutive frames divided by the time interval.

Differential quantity

Differential quantities are derived from spatial derivatives of the velocity field. Common differential quantities include velocity gradients, strain-rate and rotation-rate tensors, and vortices [160–162]. These quantities provide information on local deformation, rotation, shear, and transport processes and are therefore important for characterizing complex flow structures. Methods for reconstructing differential flow quantities from Lagrangian data can be classified into mesh-based and meshless approaches. In mesh-based methods, such as Flowfit [157], Vortex-in-Cell+ [163], and Vortex-in-Cell# [164], scattered Lagrangian data are first projected onto an Eulerian mesh. Differential quantities are then computed on that mesh by finite-difference methods or spatial differentiation. While this strategy is convenient for applying established Eulerian operators, it introduces an additional data-conversion step. Because LPT data are typically irregularly distributed in space and time, whereas the target mesh is often structured, this projection may introduce approximation errors and reduce the spatial-localization advantages of Lagrangian measurement [165]. Moreover, differential quantities are not obtained directly at the particle locations, so a second interpolation step is often required to interpolate results back to the particle locations.

Meshless methods avoid this projection step and reconstruct flow quantities directly at the Lagrangian data points. These methods approximate the velocity field in each frame using continuous functions, typically polynomials [156, 166, 167] or Radial Basis Functions (RBFs) [168–174]. Differential quantities are then obtained from the spatial derivatives of the reconstructed velocity field. This approach is analogous to reconstructing velocity from trajectories by temporal differentiation.

Despite their advantages, both mesh-based and meshless approaches still face challenges. First, physical constraints are not always incorporated in a strict manner. Such constraints may arise from prior knowledge of the flow, for example, incompressibility or

boundary conditions [157, 164, 170–172]. Neglecting them may lead to unrealistic or inaccurate flow structures. Second, processing large LPT datasets can be computationally expensive and numerically unstable. The cost grows rapidly with the number of particles and frames, and some methods, especially global RBF-based methods, may suffer from instability if many data points are used without stabilization [168, 175]. Third, low-order polynomial or spline approximations may not be sufficient for strongly nonlinear flows. Lastly, there is often a mismatch between Lagrangian trajectory-based velocity reconstruction and Eulerian frame-based field reconstruction. The former follows directly from the kinematic definition of velocity, whereas the latter is often constrained by flow physics. If these two reconstructions are decoupled, the final result may be non-physical.

Comprehensive reconstruction

Several comprehensive reconstruction strategies have been proposed to recover multiple flow quantities in a coordinated manner. These methods typically begin by initializing particle trajectories, velocities, and accelerations from raw LPT data, and then use the initialized quantities for downstream analysis or data assimilation.

One example is the Trackfit–Flowfit framework introduced by Gesemann et al. [157]. Trackfit reconstructs particle trajectories, velocities, and accelerations along pathlines using cubic B-splines in time. Flowfit then takes the reconstructed Lagrangian quantities as input, projects them onto an Eulerian mesh using weighted cubic B-splines, and assimilates them by minimizing cost functions subject to physical constraints such as incompressibility and boundary conditions. This framework provides a systematic way to combine temporal and spatial reconstruction.

A meshless comprehensive strategy was proposed by Lüthi [156]. Their method reconstructs particle trajectories using localized cubic polynomials, differentiates them to obtain velocities and accelerations, and then fits the velocity field in each frame using piecewise linear polynomials. This avoids explicit projection to a global mesh, but it may not enforce incompressibility in a strict way.

Another meshless least-squares framework was developed by Bobrov et al. [167]. In this method, trajectories are reconstructed using weighted cardinal B-splines, velocities and accelerations are obtained by differentiation, and spatial derivatives are evaluated directly at scattered particle locations by a least-squares procedure. Pressure is then reconstructed using constraints from the Navier–Stokes and pressure Poisson equations.

A recent study [171] proposed a method that combines constrained least squares, stable RBFs, and the partition-of-unity method to reconstruct 3D time-resolved incompressible

flow fields from raw LPT data. Their framework reconstructs trajectories along particle pathlines in a Lagrangian step and then refines the velocity field in each frame in an Eulerian step under incompressibility constraints. By sharing the same RBF-based approximation coefficients in both steps, the temporal and spatial reconstructions remain consistent. This method links Lagrangian and Eulerian reconstruction in a unified framework. However, it still requires time-resolved input and cannot reconstruct pressure or acceleration from two-pulse LPT data.

2.1.2 Bubble reconstruction

Bubble reconstruction aims to recover the geometry, kinematics, and forces of bubbles from experiments. Compared with liquid-phase reconstruction, bubble reconstruction introduces additional challenges because the gas–liquid interface is moving, deforming, and may undergo topological changes such as breakup and coalescence. Existing work can be grouped into geometry reconstruction, kinematics reconstruction, force reconstruction, and simultaneous bubble–liquid reconstruction.

Geometry reconstruction

Bubble geometry reconstruction involves converting raw bubble images into silhouettes and extracting geometric quantities such as centroid, projected area, diameter, aspect ratio, and orientation. For (quasi-)2D bubbles [65, 176–178] and some axisymmetric 3D bubbles [179–181], a single camera may be sufficient to capture the projected bubble silhouette.

For fully 3D bubbles, advanced experimental setups and data-processing algorithms are required. One widely used method is the Visual Hull (VH) approach [182, 183], which has been applied in many bubble geometry reconstructions [22, 23, 25, 27, 35, 36, 66, 184–187]. In this method, binary silhouettes are extracted in each view, projected into 3D as generalized cones, and intersected to obtain the largest shape consistent with all views. The method is robust, naturally accommodates topology change, and scales to multiple simultaneously imaged bubbles. However, it may not recover concave regions that are not visible in any silhouette, which may lead to overestimated volumes.

Stereo vision [188–190] provides an alternative route to 3D geometry reconstruction. Two or more synchronized and calibrated cameras view the scene from different baselines. The 3D structure is obtained by triangulating image disparities. After rectification, features such as bubble edges or segmented boundaries are matched along epipolar lines. Stereo can recover fine local detail, but it requires sufficient image contrast and is sensitive to

specular reflections, refraction, and occlusion. It has been successfully applied in bubble-shape reconstruction [66, 191]. Similarly, virtual stereo methods [192, 193] create two virtual views with a single camera by using mirrors, prisms, or beam splitters. Because both views are recorded on the same sensor in a single exposure, synchronization issues are avoided. This is advantageous for rapidly moving bubbles or vibrating systems. However, the method requires careful optical alignment and calibration, and is sensitive to aberration and refraction effects.

Tomographic reconstruction has also been used for bubble geometry reconstruction [21, 185, 194–199]. In this approach, multiple synchronized and calibrated views are used to reconstruct a volumetric scalar field from the measured optical intensities through an inverse problem, for example, using the Algebraic Reconstruction Technique (ART) [200, 201]. The bubble interface is then extracted as an iso-surface of the reconstructed field. Compared with VH methods, tomography can recover concave structures, but it requires careful calibration and synchronization and is associated with high computational and experimental costs.

Other techniques have also been proposed. These include ray-tracing-based reconstruction [202, 203], physically constrained reconstruction [186], and machine-learning-based reconstruction [65, 203–208]. In addition to direct image-based reconstruction, analytical representations are often used to approximate bubble geometry. A bubble may be represented as a point cloud or connected pixel region [176–178], by circles or spheres [186, 209, 210], by ellipses or ellipsoids [22, 23, 25, 45, 66, 185, 191, 195, 207, 208, 211–215], or by more flexible spline-based descriptions [185, 202]. Although these geometric representations may oversimplify or distort the true interface geometry, they are useful because they provide compact descriptions of bubble shape.

Kinematic reconstruction

Bubble kinematics reconstruction focuses on bubble trajectories and velocities. Trajectories are usually represented by a sequence of bubble-centroid positions or by fitted trajectory functions [216]. The bubble centroid is typically computed as the geometric center. The simplest velocity estimate is obtained by tracking individual bubbles across frames and applying finite differences to the measured positions [48, 49, 65, 176–178, 192, 217–219]. Alternatively, when trajectories are approximated by continuous functions, bubble velocity can be obtained by temporal differentiation of the trajectory model [213]. These methods are effective for tracking bubble motion, but their accuracy depends on image quality, tracking robustness, and temporal resolution.

Force reconstruction

Bubble force reconstruction aims to estimate the forces acting on a bubble, including buoyancy, drag, lift, added mass, and pressure-gradient force. In most experimental studies, these forces are not measured directly at the bubble scale. Instead, they are inferred from bubble motion using prescribed models and assumptions, similar to those used in numerical simulations [17, 220, 221].

Buoyancy is a fundamental force in bubble motion. From Archimedes' principle [142, 222], it can be written as:

$$\mathbf{F}_B = -\rho_\mathrm{l} V_\mathrm{b} \mathbf{g},$$

where ρ_l is the liquid density, V_b is the bubble volume, and $\mathbf{g}$ is the gravitational acceleration. In experiments, this force is perhaps the easiest one to estimate because it depends mainly on bubble size and fluid density. However, its accuracy still depends on how well the bubble volume is reconstructed from the images.

Surface-tension force is associated with the local curvature and pressure balance across the gas–liquid interface. In bubble dynamics, it is commonly estimated through the Young–Laplace relation [223, 224],

$$\Delta p = \sigma \kappa,$$

where Δp is the pressure jump across the interface, σ is the surface tension coefficient, and κ is the local mean curvature. In experiments, surface tension is usually not measured directly as a force vector. It is inferred from the reconstructed bubble shape, local curvature, and the assumed pressure balance across the interface. The maximum bubble pressure method for surface tension measurement is based on the above idea [225–228]. The contribution of surface tension becomes important when the bubble is small or strongly deformed, for example, during growth, detachment, pinch-off, breakup, or coalescence. In this case, capillary effects strongly influence the interface evolution. As a result, the estimated surface-tension force is often sensitive to the accuracy of the reconstructed interface shape and to the modeling assumptions used to convert curvature or pressure difference into a force contribution.

Drag is the dominant hydrodynamic force opposing bubble motion. It is commonly modeled through a drag coefficient together with the liquid properties, bubble size, and the relative velocity between the bubble and the surrounding liquid [55, 187, 229–232]:

$$\mathbf{F}_D = \frac{1}{2} C_D \rho_\mathrm{l} A_\mathrm{b} |\mathbf{u}_\mathrm{l} - \mathbf{u}_\mathrm{b}| (\mathbf{u}_\mathrm{l} - \mathbf{u}_\mathrm{b}),$$

where C_D is the drag coefficient, $\mathbf{u}_\mathrm{l} - \mathbf{u}_\mathrm{b}$ is the relative velocity between the liquid and the bubble, and A_b is the projected area of the bubble in the direction of $\mathbf{u}_\mathrm{l} - \mathbf{u}_\mathrm{b}$. In general,

the total drag contains two main contributions: pressure drag and friction drag. The pressure drag is caused by the pressure difference between the upstream and downstream sides of the bubble, whereas the friction drag arises from viscous shear along the gas–liquid interface [230, 232–235]. In experimental bubble dynamics reconstruction, drag is rarely measured directly as a force. Instead, it is inferred from observed bubble motion by using empirical or semi-empirical drag correlations, such as those developed from terminal-rise experiments of single bubbles [55]. Consequently, the reconstructed drag force depends on the selected drag law and on the accuracy of the measured bubble velocity, bubble size, and surrounding liquid conditions.

Lift is modeled as a lateral force induced by liquid velocity gradients [58, 187, 229, 236–238]. It acts perpendicular to the main relative motion and is written as

$$\mathbf{F}_L = C_L \rho_\mathrm{l} V_\mathrm{b} \left(\mathbf{u}_\mathrm{l} - \mathbf{u}_\mathrm{b}\right) \times \left(\nabla \times \mathbf{u}_\mathrm{l}\right),$$

where C_L is the lift coefficient. This force can significantly alter the bubble trajectory, introducing lateral migration and interaction with vortical structures or nearby walls. In experiments, lift is inferred from the bubble trajectory with an assumed lift model. Its estimation is difficult because the lift coefficient depends not only on the local liquid shear, but also on bubble size, shape, orientation, and deformation [58, 229].

Added mass accounts for the fact that an accelerating bubble must also accelerate part of the surrounding liquid [213, 230, 239, 240]. Therefore, the effective inertia of the bubble is greater than that of the gas phase alone. A common form of the added-mass force is

$$\mathbf{F}_{AM} = C_{AM} \rho_\mathrm{l} V_\mathrm{b} \left(\frac{D\mathbf{u}_\mathrm{l}}{Dt} - \frac{d\mathbf{u}_\mathrm{b}}{dt} \right),$$

where C_{AM} is the added-mass coefficient and t is the time. For example, $C_{AM} = 1/2$ is often used for an isolated spherical bubble in an unbounded liquid [230, 239]. $D\boldsymbol{u}_\mathrm{l}/Dt$ is the material derivative of the carrier flow velocity, and $d\boldsymbol{u}_\mathrm{b}/dt$ is the time derivative of the bubble velocity along its trajectory. Some formulations also include the effect of a time-varying bubble volume, which becomes important when the bubble expands, contracts, or oscillates [213]. This force is therefore relevant when the bubble undergoes strong acceleration or oscillation. In experiments, added mass is challenging to measure directly.

The Basset force represents the viscous history effect associated with vorticity diffusion in the liquid boundary layer around the bubble [229, 240–243]. Unlike the other force terms, it depends on the time history of the relative motion between the bubble and the

liquid rather than only on the instantaneous state. A classical form of the Basset force is

$$\mathbf{F}_{BS} = 6r^2\sqrt{\pi\rho_{\mathrm{l}}\mu_{\mathrm{l}}}\int_0^t \frac{\frac{d}{d\tau}\left(\mathbf{u}_{\mathrm{l}} - \mathbf{u}_{\mathrm{b}}\right)}{\sqrt{t-\tau}}\,d\tau,$$

where r is the radius of a spherical bubble and τ is the integration time. This convolution form shows that the Basset force depends on the entire past acceleration history of the relative motion. Moreover, it could be relatively small compared to other forces such as buoyancy under some conditions and is usually ignored in many practical scenarios [229].

Simultaneous reconstruction

Many studies perform simultaneous measurements of bubbles and their surrounding liquid phase. Such measurements combine bubble imaging with liquid-phase diagnostics such as PIV [48, 65, 66, 177, 181, 184, 194, 209, 217, 229, 244, 245], LPT [21–23, 25–27, 36, 49, 187, 210, 211], and LDV [178, 246, 247]. This integration provides more complete information. It is useful for studying couplings in two-phase flows. Some important quantities, such as local slip velocity, cannot be measured from the bubble alone and must be inferred from the surrounding liquid motion. For this reason, simultaneous bubble–liquid reconstruction is especially relevant to bubbly flow reconstruction.

2.1.3 Summary

The above review shows that experimental reconstruction methods for bubbly flows can recover complementary information about both the liquid and gas phases. For the liquid phase, Lagrangian reconstruction methods provide trajectories, velocities, and higher-order differential quantities. However, they often rely on local interpolation or regression and may not enforce physical constraints. For the gas phase, bubble reconstruction methods range from simple silhouette extraction and analytical fits to advanced 3D reconstruction and machine-learning-based approaches. Bubble kinematics can be obtained through tracking and differentiation, whereas force reconstruction remains model-dependent and approximate. Simultaneous bubble–liquid measurements provide a more complete view of two-phase interaction, but they also increase experimental complexity. In general, existing experimental methods provide rich observational data, but they do not by themselves constitute a physically consistent reconstruction of the full bubbly-flow state.

2.2 Numerical Simulation Methods

Different numerical methods have been developed for bubbly-flow simulations, depending on the target spatial scale and the required interface resolution. At the macroscopic or industrial scale, the main interest is in averaged quantities, such as gas holdup, phase distribution, and pressure drop. Therefore, Eulerian–Eulerian or two-fluid models are commonly used [78, 83, 248, 249]. At the mesoscale, Eulerian–Lagrangian methods are often adopted when the liquid phase is treated as a continuum, but individual bubbles are tracked explicitly [250–253].

At the microscopic or bubble scale, the objective of the simulations is often to resolve local interfacial dynamics, such as deformation, breakup, and coalescence. This requires interface-tracking or interface-capturing. Interface-resolved methods can be classified into diffuse-interface and sharp-interface approaches. Diffuse-interface methods, such as the phase-field method [254, 255], represent the interface as a finite-thickness transition layer. The layer is represented by a smoothly varying phase indicator. The interface dynamics are governed by the Cahn–Hilliard equation [256, 257] or the Allen–Cahn equation [258, 259], coupled with the incompressible Navier–Stokes equations. These methods naturally handle large deformation, breakup, and coalescence. They also provide smooth interface normals and curvature. However, these methods require sufficient mesh resolution across the interface and may be sensitive to interface-width and model parameters.

Sharp-interface methods attempt to preserve the interface as a distinct boundary between the phases. Common approaches include front tracking [89, 260], the level-set method [88, 261–264], and the Volume-of-Fluid (VoF) method [86, 87, 265]. Front tracking provides accurate interface geometry but requires explicit interface management under topological changes. The level-set method offers a smooth implicit representation of the interface, but standard formulations are not strictly mass conservative. In the present work, the VoF method is adopted because it can preserve mass while handling large interface deformation and topological changes.

2.3 Data Assimilation

2.3.1 Overview

In the study of fluid mechanics, including bubbly flows, even when experiments and numerical simulations are performed for the same flow configuration, their results rarely

agree exactly. This discrepancy is inevitable because each approach is affected by different sources of uncertainty and error, as well as the resolution of the data.

Experimental measurements, such as those obtained from PIV or LPT, are limited by finite spatial and temporal resolution, systematic bias, and random noise. Spatial resolution depends on interrogation-window size, particle seeding density, optical quality, and pixel size, whereas temporal resolution depends on camera frame rate and illumination [73, 74]. Systematic errors may arise from time synchronization, misalignment, calibration inaccuracy, image distortion, or variation in illumination intensity [73, 75, 266–268]. As a result, experiments usually provide sparse and noisy observations, making it difficult to resolve rapidly evolving small-scale features, near moving interfaces in a large-scale bubbly flow reconstruction.

Numerical simulations are affected by different uncertainties, including discretization error, modeling error, and uncertainty in boundary and initial conditions [76]. Insufficient spatial or temporal resolution may lead to mesh-dependent solution or excessive numerical diffusion. In addition, errors in interface-capturing schemes, turbulence models, or subgrid closures may cause the computed flow to differ systematically from the true dynamics. Therefore, quantities such as local pressure, interfacial shear, or pinch-off dynamics require validation before they can be interpreted quantitatively.

Data assimilation (DA) provides a way to bridge this gap by systematically incorporating observational data into numerical simulations [97–99]. The major advantage is that DA combines the strengths of both approaches: simulations provide full flow-field information, while experiments provide direct reference to the real flow. This combination can improve reconstruction accuracy and robustness.

Common data-assimilation methods include sequential approaches, such as the Kalman Filter (KF) family, and variational approaches, such as 3D-Variational (3D-Var) [269, 270], 4D-Var [271, 272], and sequential variational [273] data assimilation methods. KFs update the system state as observations arrive [274–277]. Variational methods assimilate observations over a finite time window by minimizing a cost function [278, 279]. Although these methods are widely used, they require explicit treatment of uncertainty and may become computationally expensive in high-dimensional nonlinear systems. For such cases, lightweight alternatives are desirable. A representative example is nudging, which provides a simple and efficient assimilation strategy.

2.3.2 Nudging algorithm

Nudging, also known as Newtonian relaxation [97], is perhaps one of the simplest and most efficient DA methods. Related concepts also appear in control theory as state observers, asymptotic observers [280], or Luenberger observers [281], in control engineering as proportional feedback [282], and in nonlinear dynamics as data synchronization [283]. By introducing a feedback term into the governing equations, the numerical solution is driven toward the observations. This feedback term is proportional to the mismatch between the computed state and the measured data.

In discrete time, the nudging algorithm for a linear system is written as

$$\hat{\mathbf{x}}_{n+1} = \mathbf{F}\hat{\mathbf{x}}_n + \mathbf{K}\big(\mathbf{z}_n - \mathbf{H}\hat{\mathbf{x}}_n\big), \tag{2.1}$$

where $\hat{\mathbf{x}}_n$ is the model state at time step n, and $\mathbf{z}_n$ is the observation vector, typically obtained from measurements. The operator $\mathbf{F}$ is the model evolution operator, so that $\hat{\mathbf{x}}_{n+1} = \mathbf{F}\hat{\mathbf{x}}_n$ represents the discrete system dynamics. The operator $\mathbf{H}$ is the observation operator. It maps the model state to the observation space. Therefore, $\mathbf{H}\hat{\mathbf{x}}_n$ is the model-predicted observation corresponding to $\hat{\mathbf{x}}_n$. The term $\mathbf{z}_n - \mathbf{H}\hat{\mathbf{x}}_n$ is the innovation, namely the discrepancy between the measurement and the model prediction. $\mathbf{K}$ is the gain that determines how strongly this discrepancy is fed back into the model state.

Equation (2.1) represents a family of DA methods, from the classic nudging to KFs. A successful DA method aims to reduce the discrepancy between the estimated and true states as observations are assimilated. In standard nudging, $\mathbf{K}$ is a constant scalar or a constant diagonal matrix. In a KF, the gain is determined from the predicted-state and observation-error covariances to balance model and observational uncertainty. Although this adaptive gain can improve estimation accuracy, it also makes the KFs expensive, especially for large nonlinear systems. This is because KFs require repeated covariance propagation, matrix updates, and the manipulation or inversion of large covariance matrices.

Nudging has been widely used in meteorology, oceanography, and fluid mechanics [283–286]. Its main advantages are simplicity, sequential implementation, and relatively low computational cost. Unlike variational methods, nudging does not require repeated optimization over a full assimilation window. Unlike KFs, it does not require propagation of uncertainty covariances and manipulation of large matrices. These features make nudging particularly attractive for high-dimensional problems.

Several extensions of standard nudging have been proposed. Spectral nudging [287] applies feedback only to selected spatial modes and has been widely used in Numerical

Weather Prediction (NWP) and turbulence studies [283, 288, 289]. Back-and-Forth Nudging (BFN) [290] combines forward and backward integration to improve finite-window reconstruction. However, for nonlinear systems, these methods generally may not provide a guaranteed convergence result. In addition, their practical convergence may depend on empirical tuning.

2.3.3 AOT-nudging algorithm

The Azouani–Olson–Titi (AOT) algorithm [291, 292] is a nudging-based DA method for dissipative dynamical systems. For such a system, the AOT-nudging algorithm can be written as

$$\frac{d\mathbf{v}}{dt} = F(\mathbf{v}) + K\,\mathscr{I}_h(\mathbf{u}-\mathbf{v})\,, \tag{2.2}$$

with the initial condition

$$\mathbf{v}(\mathbf{x},0) = \mathbf{v}_0(\mathbf{x}), \tag{2.3}$$

where $\mathbf{u}$ is the reference, or true, solution, $\mathbf{v}$ is the assimilated solution, $F(\mathbf{v})$ represents the original system dynamics, $K > 0$ is the nudging strength or gain, and $\mathscr{I}_h$ is a linear interpolant associated with the observation resolution h. Here, $\mathscr{I}_h(\mathbf{u}-\mathbf{v})$ represents the mismatch between the observed state and the corresponding component of the assimilated solution.

The role of the interpolant $\mathscr{I}_h$ is essential in the AOT-nudging algorithm. Rather than requiring full-field observations, the algorithm uses only coarse observations, such as nodal values, low Fourier modes, and local averages of the state. In a dissipative system with sufficient observation resolution h, the AOT-nudging algorithm can drive $\mathbf{v}$ toward $\mathbf{u}$ asymptotically, and in many cases exponentially [292]. Although the AOT-nudging algorithm resembles classical nudging in mathematical expression, the explicit use of the interpolant $\mathscr{I}_h$ distinguishes it and enables rigorous mathematical analysis of convergence.

The AOT-nudging algorithm is motivated by the phenomenon that a dissipative dynamical system possesses a finite number of determining modes, nodes, or functionals that govern its long-term behavior [292]. These determining quantities are related to the concept of a global attractor, which is a bounded set toward which all trajectories of the system evolve as time tends to infinity [293]. If a sufficient number of these determining quantities is observed, then the full state of the system can, in principle, be recovered.

AOT-nudging inherits the main advantages of standard nudging, including its sequential nature, conceptual simplicity, and relatively low computational cost. Compared with standard nudging, a distinctive feature of AOT-nudging is the inclusion of an interpolation

operator that maps scattered low-resolution observations onto the numerical grid where the full state lives. This feature makes AOT-nudging especially suitable for practical situations in which the observation locations do not match the numerical mesh. Under appropriate conditions, AOT-nudging yields exponential convergence of the nudged solution toward the reference solution [292].

The AOT-nudging algorithm was first developed within a rigorous theoretical framework for dissipative systems. As emphasized by Azouani et al. [292], exponential convergence requires two key properties of the underlying dynamical system: (i) global well-posedness, including existence, uniqueness, and continuous dependence on the initial condition; and (ii) the existence of a global attractor, which guarantees that the system evolves toward a bounded set of long-time states. With these conditions, AOT-nudging can be analyzed rigorously as an observer for dissipative dynamics, under a theoretical framework.

Rigorous convergence analysis has been established for the Navier–Stokes equations in 2D [294–299] and 3D [300], as well as for related equations such as the vorticity–stream-function form [301]. The behavior of AOT-nudging solutions for the Navier–Stokes equations has also been examined from several perspectives. These include statistical downscaling in 2D flows [302], higher-order synchronization [303], and derivation of uniform-in-time error bounds [304–307]. Other studies considered discrete-in-time observations, spectral filtering, and nudging windows [308, 309]. In turbulence modeling, AOT-nudging has also been analyzed for the Navier–Stokes-α equations [310] and the 3D Leray-α model [311].

Beyond the classical Navier–Stokes system, AOT-nudging has been extended to a broad range of dissipative systems. For example, convergence has been proved for the Chafee–Infante reaction–diffusion equation, which exhibits bifurcation and multiple steady states [291]. In the subcritical surface quasi-geostrophic equation, AOT-nudging has been shown to converge with blurred-in-time observations [312] and even with only boundary temperature or buoyancy observations [313]. AOT-nudging has also been analyzed for 2D and 3D Bénard convection [111, 314, 315], 2D magnetohydrodynamics [316], and the 3D Brinkman–Forchheimer–extended Darcy model for porous-media flow [317]. These extensions demonstrate that AOT-nudging is applicable to a wide class of dissipative systems.

Some studies have extended AOT-nudging analysis and implementation under numerical frameworks. For instance, Zauner et al. [318] incorporated AOT-nudging into unsteady Reynolds-averaged Navier–Stokes simulations of flow past a square cylinder at $Re = 22{,}000$. Using finite-element methods, Gardner et al. [301] applied AOT-nudging to laminar flow over a vertical flat plate at $Re = 50$ and 100, while Larios et al. [319] and Rebholz and Zerfas [320] studied 2D channel flow past a circular cylinder over a range of Reynolds numbers. AOT-nudging has also been coupled with spectral and pseudo-spectral methods

in the vorticity–stream-function formulation to analyze the effect of observation types on convergence [298, 321, 322].

Beyond the Navier–Stokes equations, AOT-nudging has also been numerically tested in other dissipative systems. Examples include the 1D Allen–Cahn equation with moving observations [323], the 1D Kuramoto–Sivashinsky equation [324–326], 2D Bénard convection [327], large-scale atmospheric and oceanic models [328, 329], and the 3D primitive equations [330]. These numerical studies further support the flexibility of AOT-nudging in practical settings.

The AOT-nudging algorithm has also been applied to parameter identification. Pachev et al. [325] used AOT-nudging to recover both the state and a scalar parameter in the 1D Kuramoto–Sivashinsky equation, demonstrating the possibility of simultaneous state and parameter estimation. Carlson et al. [331] proved and tested AOT-nudging for estimating unknown viscosity in the 2D Navier–Stokes equations using sparse observations. They showed that the convergence of the viscosity estimate and the flow-state reconstruction occurred at the same exponential rate. Similarly, Carlson et al. [332] applied AOT-nudging to infer unknown non-dimensional parameters in the 3D Lorenz system using only partial observations.

AOT-nudging has also been integrated with a variety of numerical schemes. As noted by Altaf et al. [327], AOT-nudging can be coupled with standard discretization frameworks such as spectral, finite-difference, and finite-element methods, as long as the numerical discretization is finer than the observational resolution. Zerfas et al. [333] developed a reduced-order-model DA framework for the 2D and 3D Navier–Stokes equations with no-slip boundaries, and applied it to cylinder-flow problems at moderate Reynolds numbers using DNS data as observations. Moreover, they proposed an adaptive nudging strategy based on the predicted kinetic-energy error. Their results showed that reduced-order models can be significantly improved while maintaining computational efficiency. Antil et al. [334] integrated AOT-nudging into residual neural networks and demonstrated accurate reconstruction for the Lorenz-63 and Lorenz-96 systems at relatively low computational cost. In addition, AOT-nudging has also been combined with Galerkin and finite-element methods [304, 306, 307, 319, 320].

2.3.4 Factors that influence AOT convergence

The convergence of AOT depends on several factors, including the nudging strength, the type of observed variables, the spatial distribution of observations, the density of observations, and the observational noise. When the nudging strength is large, the feedback

term enforces consistency with the observations and may accelerate convergence. If the nudging strength is too small, the correction is weak and convergence may be slow [292]. Other studies reached similar conclusions and further showed that the effect of the nudging strength depends on other factors, such as observation placement and numerical stability constraints. For example, Franz et al. [322] showed that the choice of the nudging strength is influenced by both the observation arrangement and the Courant–Friedrichs–Lewy (CFL) number. They also reported that moving observers often require a larger nudging strength than stationary ones, and that fast-moving observers generally favor a stronger nudging strength.

The choice of observed variables is another important factor. Most AOT-nudging studies for the Navier–Stokes equations use all velocity components as observations [292, 297, 310, 321]. Alternative variables, such as vorticity and stream function, have also been considered [301, 322]. By contrast, pressure is usually not used directly [292], likely because it does not satisfy an explicit evolution equation in the same way as velocity. Several studies have shown that partial observations may still be sufficient for convergence. For example, in the 2D Navier–Stokes equations [295], 2D Bénard convection [314, 315], and the 3D Leray-α turbulence model [311], observing only selected velocity components was enough to recover the full state. In a 2D magnetohydrodynamic system, convergence was obtained using complete or partial observations of velocity and magnetic field, although velocity-only or magnetic-only observations remained inconclusive [316]. In other dissipative systems, temperature-only observations have also been shown to be sufficient, for example in 3D porous-media convection and planetary geostrophic models [111, 335]. In the 3D surface quasi-geostrophic equation, even time-averaged observations can lead to convergence [313].

The spatial distribution of observations also affects AOT-nudging performance. Uniformly distributed stationary observations are the most common setting in both theoretical and computational studies [292, 321]. However, moving or mobile observations may improve efficiency. For example, Larios and Victor [323] showed, in the 1D Allen–Cahn equation, that moving sensors placed in dynamically important regions can improve observation efficiency. Since such regions are generally not known in advance, practical strategies are still needed. Franz et al. [322] compared stationary and moving observations with random, periodic, and Lagrangian motion. They found that mobile observers usually outperform stationary ones, with random motion giving the fastest convergence, although random motion is difficult to implement experimentally. Lagrangian observers performed worst among the moving strategies considered in their study, likely because their motion was too slow to provide sufficient spatial coverage. Similarly, Biswas et al. [298] found that observations moving through a subdomain can accelerate convergence over the whole domain.

The density or spatial resolution of observations is important. If too few observations

are available, the solution may become inaccurate or unstable; if too many are used, the computational cost increases. The original analysis of Azouani et al. [292] showed that the observational resolution must be sufficiently high to achieve exponential convergence. A computational study of the 2D Navier–Stokes equations by Gesho et al. [321] further demonstrated that observation density and the nudging strength interact strongly: higher spatial resolution allows a broader admissible range of nudging strengths while preserving stability. Their study also suggested that nodal observations may be significantly sparser than theoretical estimates while still remaining effective. Although the original theory assumes observations over the whole domain [292], later work showed that locally concentrated observations may still lead to convergence under suitable conditions, provided that the local resolution is sufficiently high and the nudging strength is chosen properly [298].

Observation errors are inevitable in practice. Bessaih et al. [296] analyzed AOT-nudging convergence under Gaussian observational noise and showed that the asymptotic reconstruction error is bounded by the variance of the noise, with the bound also depending on the spatial resolution of the observations. Foias et al. [299] considered systematic observational errors in the 2D Navier–Stokes equations and derived explicit uniform error bounds. By contrast, Celik and Olson [297] focused again on Gaussian noise, which is unbounded and therefore more difficult to treat than deterministic bounded errors. They pointed out that outlier removal may be necessary, since Gaussian noise can push observations outside any physically realizable trajectory. They further showed that the AOT-nudging reconstruction error remains bounded by the noise variance if the grid spacing and nudging time interval are sufficiently small. Although these bounds are rigorous, they may be conservative in practical applications. Other studies examined AOT-nudging under noisy observations and different numerical or observational settings [321, 324, 327, 332], and collectively they indicate that AOT-nudging can remain effective even in the presence of observational noise.

2.4 Summary

This chapter reviews the background relevant to bubbly-flow reconstruction in three areas: (i) experimental techniques, (ii) numerical simulation, and (iii) DA. For experiments, simultaneous reconstruction of bubble geometry and the surrounding liquid phase is valuable because the two are coupled. The review emphasizes the Lagrangian techniques for the liquid phase reconstruction. These methods provide particle-resolved transport information, making them suited to resolving localized liquid motion near bubbles.

The numerical-simulation review shows that different methods are available depending

on the scale of interest and the required level of interface resolution. For the present study, interface-resolved simulation is needed so that local interfacial dynamics, deformation, breakup, and coalescence can be captured directly. Among the available interface-resolved methods, the VoF method is chosen because it provides mass conservation and can accommodate large interface deformation and topological changes.

DA provides a principled way to reconstruct a flow field that is consistent with both the measurements and the governing equations. The AOT-nudging algorithm is chosen because it is designed for dissipative systems and can incorporate sparse and scattered observations through interpolation. The interpolant is central to the rigorous convergence analyses established for AOT-nudging. In addition, the literature shows that AOT-nudging is compatible with a wide range of numerical discretizations and remains effective under different observation types, spatial resolutions, and noise levels. These properties make AOT-nudging a promising approach for addressing the current gap in bubbly-flow DA.

Chapter 3

Bubbly Flow Experiment

This chapter presents the quasi-2D bubbly-flow experiment and its data processing. The experiment is designed to provide two synchronized observation streams from the same high-speed image sequences: liquid-phase velocity observations obtained by image velocimetry and bubble-interface observations obtained from bubble silhouettes.

The chapter is organized as follows. Sect. 3.1 describes the quasi-2D water channel, tracer particles, optical arrangement, image-acquisition system, bubble-generation system, and operating conditions. Sect. 3.2 describes the bubble-image processing workflow used to obtain bubble masks and observations. Sect. 3.3 describes the tracer-image pre-processing and image velocimetry workflow. Lastly, Sect. 3.4 summarizes the observation outputs from the experiment.

3.1 Experiment Setup

3.1.1 Quasi-2D water channel

A vertical quasi-2D water channel was constructed from a glass tank, acrylic panels, 3D-printed modular clamping frames, and support components. As illustrated in Fig. 3.1, the outer glass tank, shown in gray, has dimensions of 250 mm × 250 mm × 300 mm and a wall thickness of 5 mm. Two acrylic panels, shown in green, each of thickness 2 mm, are installed inside the tank to define the measurement channel. A gap of 2.2 mm is maintained between the two panels by custom 3D-printed supports, shown in blue and red, positioned at the top and bottom of the tank. These supports are fixed by external clamping frames

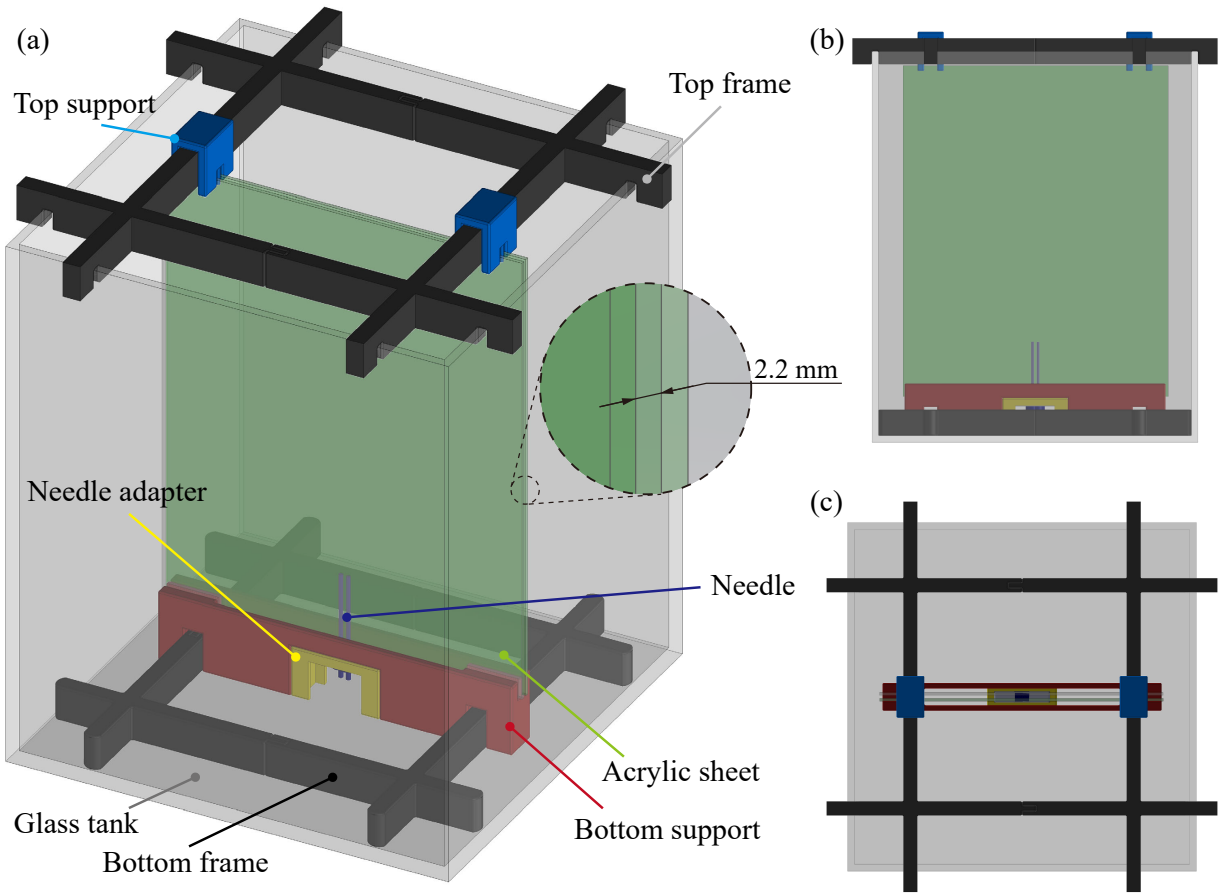


Figure 3.1: Quasi-2D water tank and clamping assembly. (a) Trimetric, (b) front, and (c) top views showing the tank, acrylic sheets, top and bottom frames, gap supports, gas-injection needles, and needle adapter.

(shown in black). At the bottom of the tank, a 3D-printed needle adapter, shown in yellow, is used to hold the gas-injection needles in a fixed position.

The measurement plane is illuminated by six continuous-wave 532 nm, 5 mW, Class 3B lasers aligned with the mid-plane of the gap, with three lasers positioned on each side. The laser intensity is assumed to follow a Gaussian profile across the sheet thickness, decreasing to 13.5% of its peak value at the boundaries of an effective sheet thickness of approximately 4 mm. A high-speed CMOS camera is placed normal to the front acrylic sheet to image the illuminated plane. The camera records image sequences at a resolution of $1,024 \times 1,024$ pixels. The frame rate is set to 2,000 frames per second (fps), and the exposure time is

1/3,000 s. The resulting field of view is 40 mm × 40 mm in the physical plane. The same raw image sequence is used for both bubble observation extraction and particle tracking. This ensures that the two observation channels are synchronized in time and registered on the same image plane. Parameters for the image acquisition are summarized in Tab. 3.1.

Table 3.1: Image-acquisition parameters used in the quasi-2D bubbly-flow experiment.

Parameter	Value	Unit
Camera resolution	1,024×1,024	pixels
Frame rate	2,000	Hz
Exposure time	1/3,000	s
Field of view	40×40	mm^2
Laser wavelength	532	nm
Laser-sheet thickness	~ 4	mm

3.1.2 Operating conditions

Two columns of bubbles are generated by injecting air through syringe spargers mounted at the bottom of the tank. Air is supplied to the larger needle by a precision syringe pump at a controlled volumetric flow rate, with a nominal gas flow rate of $800\,\mathrm{mL\,h^{-1}}$. Air is injected manually through the smaller needle, without a constant flow rate.

The working fluid is distilled water at a temperature of approximately 20 °C. The density and dynamic viscosity of water are $\rho_\mathrm{l} = 998.2\,\mathrm{kg\,m^{-3}}$ and $\mu_\mathrm{l} = 1.002 \times 10^{-3}\,\mathrm{Pa\,s}$, respectively. The surface tension coefficient at the water–air interface is $\sigma = 7.2 \times 10^{-2}\,\mathrm{N\,m^{-1}}$. The water is seeded with spherical plastic tracer particles with a diameter of 38 µm and a density of $1.05\,\mathrm{g\,cm^{-3}}$. The effective tracer seeding density is 0.0128 ppp.

The bubble-generation assembly consists of two needles with inner diameters of 1.37 and 1.19 mm, and corresponding outer diameters of 2.11 and 1.65 mm, respectively. The distance between the needles is 5 mm. Under the operating condition, the generated bubbles have an equivalent diameter of about 3 mm. This size is larger than the 2.2 mm gap thickness of the tank. As a result, the bubbles are flattened by the gap and appear as quasi-2D silhouettes in the recorded images. The gap is treated as the nominal plate spacing. Its full-field uniformity and manufacturing tolerance are not quantified. This limitation is acknowledged as a possible source of model error. The free surface is located above the measurement window so that the bubble trajectories of interest remain within the optical field of view. The operating conditions are summarized in Tab. 3.2.

Since the bubble and liquid motions are confined between two plates, it is necessary to assess the influence of the wall boundary layers. Based on the laminar flat-plate boundary-layer estimate [336],

$$\delta_{\mathrm{BL}} \approx 5\sqrt{\nu_{\mathrm{l}} x_{\mathrm{c}}/u_{\mathrm{c}}}, \tag{3.1}$$

where $u_{\mathrm{c}} \approx 0.5\,\mathrm{m\,s^{-1}}$ is a characteristic liquid velocity, $\nu_{\mathrm{l}} \approx 1.0 \times 10^{-6}\,\mathrm{m^2\,s^{-1}}$ is the kinematic viscosity of water, and $x_{\mathrm{c}} \approx 20\,\mathrm{mm}$ is a representative streamwise length comparable to half of the measurement window. The boundary-layer thickness developing on one acrylic sheet is then estimated to be $\delta_{\mathrm{BL}} \approx 1\,\mathrm{mm}$. This value is approximately half of the gap thickness. Therefore, the boundary layers developing from the two acrylic sheets may overlap. They may influence the bubble and tracer dynamics. This influence will be discussed in Sect. 4.3.6.

For a bubble moving through a narrow gap, the film thickness between the bubble and each acrylic sheet can be estimated using classical wetting-film scalings. Two commonly used estimates are the Bretherton [337–339] and Fairbrother–Stubbs scaling [340],

$$\frac{h_{\mathrm{flm}}}{L_{\mathrm{plt}}/2} = C_{\mathrm{B}}\mathrm{Ca}^{2/3}, \qquad \frac{h_{\mathrm{flm}}}{L_{\mathrm{plt}}/2} = C_{\mathrm{FS}}\mathrm{Ca}^{1/2}, \qquad \mathrm{Ca} = \frac{\mu_{\mathrm{l}} u_{\mathrm{c}}}{\sigma},$$

where h_{flm} is the film thickness on one side of the bubble, L_{plt} is the plate spacing, $\sigma = 0.072\,\mathrm{N\,m^{-1}}$ is the air–water surface tension, and $C_{\mathrm{B}} \approx 1.34$ and $C_{\mathrm{FS}} \approx 0.5$. Using the parameters in (3.1), the capillary number is $\mathrm{Ca} \approx 6.9 \times 10^{-3}$. The Bretherton scaling gives

$$h_{\mathrm{flm}} \approx 5.0 \times 10^{-5}\,\mathrm{m},$$

whereas the Fairbrother–Stubbs scaling gives

$$h_{\mathrm{flm}} \approx 4.2 \times 10^{-5}\,\mathrm{m}.$$

Both estimates indicate a film thickness of order $O(10)$ μm. The result suggests that the bubble is separated from each acrylic sheet by a thin lubrication film. Although tracers could be trapped within this film, no such trapped tracers are observed in the experiments.

3.2 Bubble Image Processing

Bubble observations are generated from the high-speed image sequence through an image-processing workflow. This workflow has three purposes. First, it pre-processes the raw images for downstream image velocimetry. Second, it generates frame-wise bubble masks

Table 3.2: Operating conditions of the quasi-2D bubbly-flow experiment.

Parameter	Value	Unit
Working fluid	Water	–
Fluid temperature	20	°C
Plate spacing	2.2	mm
Liquid height	250	mm
Gas type	Air	–
Gas flow rate	800	$\mathrm{mL\,h^{-1}}$
Number of needles	2	–
Needle inner diameter	1.37 & 1.19	mm
Needle spacing	5	mm
Typical bubble diameter	3–4	mm
Effective seeding density	0.0128	ppp

for image velocimetry. Third, it constructs smooth, mesh-aligned bubble observations for downstream DA. The workflow begins with raw images and manually annotated bubble silhouettes and proceeds through image pre-processing, temporal interpolation, spatial down-sampling, and data export.

First, the raw image sequence is pre-processed to enhance tracer and bubble visibility. The raw images are stored in `.raww` format as `uint16` data with little-endian byte order. A median background model is constructed from the first 200 images. The model is used to remove stationary illumination patterns, stains, reflections, and fixed camera noise. For each frame, the positive part of the background-subtracted image is used as the tracer signal. A Difference-of-Gaussians (DoG) filter [341] is then applied to enhance tracer particles:

$$I_{\mathrm{DoG}} = G_{\sigma_{\mathrm{small}}} * I_{\mathrm{raw}} - G_{\sigma_{\mathrm{large}}} * I_{\mathrm{raw}},$$

where I_{raw} is the input raw image, G_σ is a Gaussian kernel with standard deviation $G_{\sigma_{\mathrm{small}}} = 0.75$ and $G_{\sigma_{\mathrm{large}}} = 3.20$, and $*$ denotes convolution. This operation enhances small tracer-scale features while suppressing large-scale background variations. The enhanced signal is then globally rescaled to 8-bit PNG using percentile-based limits, with lower and upper percentiles of 0.30 and 99.20, respectively. After rescaling, a gamma correction with $\gamma_{\mathrm{c}} = 0.60$ is applied to brighten weak tracer signals. Last, Contrast-Limited Adaptive Histogram Equalization (CLAHE) is used to improve local contrast. It helps reveal faint tracers without excessively amplifying noise. In this work, the CLAHE clip limit is 3.5, and the tile-grid size is 8×8 pixels. The processed images (see Fig. 3.2 (b) as an example) are then

exported as PNG images for downstream analysis.

Second, a set of bubble masks is manually annotated in the Computer Vision Annotation Tool (CVAT) for the pre-processed images. In each image, every bubble is represented as a polygon with more than 20 control points. This number of control points provides sufficient geometric detail to represent the irregular bubble shapes. Two processing streams are then constructed from these annotations. The first stream preserves the original annotation polygons and is used as a mask for image velocimetry. The second stream generates smoother bubble silhouettes as observational data for DA.

In the first stream, each annotated frame is converted directly into a binary bubble mask (see Fig. 3.2 (d)). Next, the mask is dilated outward by 10 pixels. For storage as an 8-bit image, bubble and background pixels are assigned values of 255 and 0, respectively. This stream is used to mask bubble regions, including reflections and glares near bubble boundaries, during particle detection and tracking.

In the second stream, smoother bubble-observation products are generated from the same CVAT annotations (see Fig. 3.2 (e)). For each bubble, the outer boundary is extracted and smoothed by repeated moving-average filtering along the closed contour. If the ordered boundary points are denoted by $\{\mathbf{x}_i\}_{i=1}^{N}$, then one pass of the moving-average smoothing can be written as

$$\bar{\mathbf{x}}_i = \frac{1}{2W_m + 1} \sum_{j=-W_m}^{W_m} \mathbf{x}_{i+j},$$

where periodic indexing is used along the closed contour and $2W_m + 1$ is the smoothing-window size. In this work, the moving-average smoothing uses a window of 11 points and 3 passes. This operation suppresses small jagged variations in the annotated boundary while preserving the overall bubble shape. The smoothed contour is then rasterized back to a binary mask. To generate a conservative bubble observation for reconstruction, the smoothed mask is eroded inward by 3 pixels. This inward erosion is introduced because the visible bubble edge typically occupies a boundary band of about 6 pixels.

Next, the smooth bubble silhouettes are interpolated in time to construct a high-frequency sequence. A signed-distance-field interpolation is applied. For a binary bubble mask Ω, the signed-distance field $d(\mathbf{x})$ is defined as

$$d(\mathbf{x}) = \begin{cases} -\min\limits_{\mathbf{y}\in\partial\Omega} \|\mathbf{x} - \mathbf{y}\|, & \mathbf{x} \in \Omega, \\ \min\limits_{\mathbf{y}\in\partial\Omega} \|\mathbf{x} - \mathbf{y}\|, & \mathbf{x} \notin \Omega, \end{cases}$$

where $\partial\Omega$ is the bubble boundary. Thus, the bubble interface is represented by the zero level set $d(\mathbf{x}) = 0$. For each output time, the two neighboring masks are first converted

into signed-distance fields and then linearly interpolated in time:

$$d(\mathbf{x}, t) = (1 - \lambda_c)\, d_k(\mathbf{x}) + \lambda_c\, d_{k+1}(\mathbf{x}), \qquad \lambda_c = \frac{t - t_k}{t_{k+1} - t_k},$$

where d_k and d_{k+1} are the signed-distance fields at two neighboring times t_k and t_{k+1}, respectively. The interpolated field is then thresholded back to a binary mask at the zero level set.

Lastly, after temporal interpolation, the bubble masks are cropped and down-sampled to match the mesh resolution in reconstruction (see Fig. 3.2 (f)). The masks are first resized to 240×240 pixels using bilinear interpolation and then re-binarized by thresholding. The resized masks are then embedded in the computational domain together with the buffer zones. The binary masks are converted to volume-fraction observations, with $\alpha^{\text{obs}} = 0$ in the bubble region and $\alpha^{\text{obs}} = 1$ in the liquid region. In addition, buffer zones are introduced around the observed region to separate the observation window from the outer computational domain. The buffer sizes are 60 cells on the left, right, and bottom, and 120 cells at the top (see Fig. 4.15 (b)). The final output is a mesh-aligned, lower-spatial-resolution but high-frequency sequence of binary volume-fraction observations.

3.3 Image-Based Velocimetry

In the previous section, two types of bubble-related data were generated: (i) polygon-based binary bubble masks for image velocimetry and (ii) mesh-based bubble observations for DA. In this section, the liquid-phase velocity observations are extracted from the pre-processed image sequence using two image-velocimetry methods: Particle Image Velocimetry (PIV) and Lagrangian Particle Tracking (LPT). PIV provides spatially averaged velocity fields on interrogation windows, while LPT provides scattered particle-resolved velocity observations from individual tracer trajectories. These two types of velocity data are then used as liquid-phase observations in the AOT-nudging DA framework.

3.3.1 Particle image velocimetry

For PIV, the pre-processed image sequence generated in Sect. 3.2 is used as the input. Since the acquisition frequency is $2,000$ Hz, the time interval between two consecutive frames is

$$\Delta t = \frac{1}{2,000} = 5 \times 10^{-4} \text{ s}.$$

The spatial calibration is $s_c = 40/1,024$ mm/pixel. The PIV code [342] excludes regions inside bubbles from the cross-correlation using the bubble masks.

A masked cross-correlation is performed for each frame. The interrogation window is a square with 49×49 pixels. The search window size is chosen based on the maximum expected particle displacement between two consecutive frames. With a maximum liquid velocity of $|\boldsymbol{u}|_{\max} \approx 0.6$ m/s, a frame interval of $\Delta t = 5 \times 10^{-4}$ s, and a spatial calibration of 40 mm/1,024 pixels, the maximum expected displacement is

$$\Delta x_{\max} = \frac{|\boldsymbol{u}|_{\max} \Delta t}{40 \times 10^{-3}/1024} \approx 7.68 \text{ pixels}.$$

For an interrogation window size of 49 pixels, the search window should exceed the interrogation window by twice this displacement, which gives

$$W_{\text{sw}} \approx 49 + 2 \times 7.68 = 64.36 \text{ pixels}.$$

Accordingly, the minimum search-window size is 65 pixels and the effective overlap ratio is 50%. Furthermore, only windows with a valid liquid-region fraction greater than 0.75 are accepted. For each interrogation window, the particle displacement is determined by maximizing the masked normalized correlation coefficient over all admissible displacements within the search region. Next, sub-pixel refinement is applied around the correlation peak by fitting a parabola separately in the horizontal and vertical directions. After the displacement field is obtained, a local iterative outlier removal is applied three times to remove spurious vectors. In each iteration, a vector is identified as spurious if its correlation coefficient is below the prescribed threshold or if it deviates from the mean of its four-neighbor vectors. Such vectors are then replaced by the local neighbor average.

The PIV fields are then converted into high-frequency velocity observations for DA. Each PIV vector field is associated with the midpoint time of its corresponding image pair and is then temporally interpolated to the DA output times, creating a high-frequency output sequence over $0 \leq t \leq 0.25$ s. The outputs have 8,001 frames, corresponding to a temporal interval of 3.125×10^{-5} s. These velocity fields (see Fig. 3.2 (c1)) provide the liquid-phase velocity observations used by DA. The parameters used in the PIV are summarized in Tab. 3.3.

3.3.2 Lagrangian particle tracking

For LPT, the liquid-phase tracer particle motion is reconstructed from the pre-processed images using the open-source MATLAB package PART2TRACK [343]. The PNG images

Table 3.3: Main parameters used in the PIV processing.

Parameter	Symbol	Value	Unit
Image resolution	–	$1,024 \times 1,024$	pixels
Frame rate	f_{acq}	$2,000$	Hz
Frame interval	Δt	5×10^{-4}	s
Spatial calibration	s_{c}	$40/1,024$	mm/pixel
Interrogation window	W_{iw}	49	pixels
Search window	W_{sw}	65	pixels
Overlap ratio	–	50	%
Minimum liquid-region fraction	–	0.75	–
Correlation threshold	R_{limit}	0.75	–
Sub-pixel refinement	–	enabled	–
Iterative outlier removal passes	n_{corr}	3	–
High-frequency output time range	–	$0 \leq t \leq 0.25$	s
Number of high-frequency output times	–	$8,001$	–
High-frequency output time interval	Δt_{out}	3.125×10^{-5}	s

generated in Sect. 3.2 are used as the input. In addition, the bubble masks are applied, and the particle detection is performed only in the liquid phase of each frame.

After masking, candidate tracers are identified frame by frame. The detection uses a characteristic particle diameter $\mathrm{p}_{\mathrm{size}} = 3$ pixels and an intensity threshold $I_{\mathrm{int}} = 68$. Sub-pixel localization is enabled through Gaussian interpolation, so that the detected particle centers are refined to sub-pixel accuracy.

Next, the particles are linked across time to form trajectories. PART2TRACK is run in the time-resolved mode with a history-matching strategy. In the history matching, candidate links are evaluated according to their consistency with the recent motion history of each particle. The matching process uses the search-scale parameter $f_{\mathrm{o_s}} = 13$ to control the size of the candidate search region for frame-to-frame linking. Besides, a local-neighborhood parameter $n_{\mathrm{nei}} = 14$ defines the number of surrounding particles to assess local motion consistency. In addition, the time-resolved initialization stage includes a minimum-distance $d_{\mathrm{dist}} = 4.5$ pixels, together with $n_{\mathrm{mp,ti}} = 2$ initialization refinement passes. A further multipass refinement stage, controlled by $n_{\mathrm{mp}} = 2$, is then applied to improve the trajectory linking. Together, these parameters are used to maintain local trajectory consistency while limiting mismatches in regions of complex motion.

During tracking, inconsistent matches are removed using a neighborhood-based outlier

Table 3.4: Main parameters used in the LPT processing.

Parameter	Symbol	Value	Unit
Image resolution	–	$1,024 \times 1,024$	pixels
Frame rate	f_{acq}	$2,000$	Hz
Frame interval	Δt	5×10^{-4}	s
Spatial calibration	s_{c}	$40/1,024$	mm/pixel
Characteristic particle diameter	$\mathrm{p}_{\mathrm{size}}$	3	pixels
Detection intensity threshold	I_{int}	68	gray level
Gaussian sub-pixel interpolation	–	enabled	–
Tracking mode	–	time-resolved	–
Tracking method	–	history matching	–
Search-scale parameter	$f_{\mathrm{o_s}}$	13	–
Local-neighborhood size	n_{nei}	14	particles
Minimum-distance criterion	d_{dist}	4.5	pixels
Initialization refinement passes	$n_{\mathrm{mp,ti}}$	2	–
Multipass refinement passes	n_{mp}	2	–
Outlier-neighborhood size	n_{outl}	14	particles
Noise parameter	–	0.25	–
Outlier-removal iterations	$n_{\mathrm{outl,iter}}$	4	–
Minimum retained trajectory length	–	5	frames

removal. The outlier removal uses $n_{\mathrm{outl}} = 14$ neighboring particles, a threshold of 2.1, and an assumed noise level of 0.25. The outlier removal is repeated $n_{\mathrm{outl,iter}} = 4$ times. After tracking, only tracers that are present for at least 5 frames are retained. This filtering step removes short or poorly resolved trajectories.

Particle velocities are obtained from the reconstructed image-space displacements using the spatial calibration and frame interval. The LPT shares the same frame rate and spatial calibration factor as those in PIV. Therefore, if Δx_{px} and Δy_{px} denote the particle displacements in pixels, the planar velocity components are

$$u = \frac{\Delta x_{\mathrm{px}}\, s_{\mathrm{c}}}{\Delta t}, \qquad v = \frac{\Delta y_{\mathrm{px}}\, s_{\mathrm{c}}}{\Delta t}.$$

The output of PART2TRACK is a scattered set of tracer positions and velocity vectors (see Fig. 3.2 (c2)). The parameters used in the LPT are summarized in Tab. 3.4.

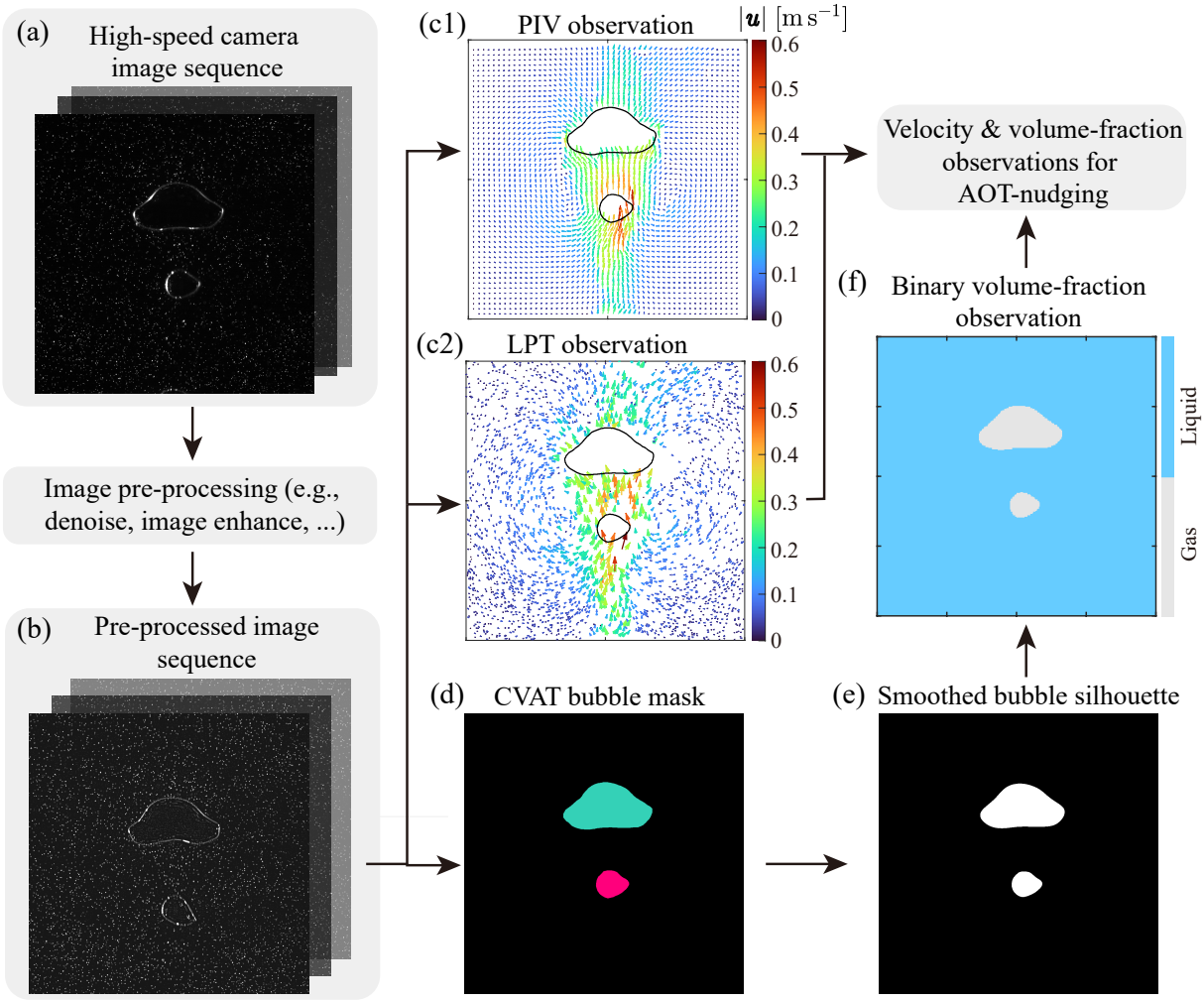


Figure 3.2: Workflow for generating observational data from the high-speed camera image sequence, with $t = 0.125$ s shown as an example. (a) High-speed camera image sequence. The images are first pre-processed. (b) Pre-processed image sequence. From the pre-processed images, two types of velocity observations are generated: (c1) PIV observation and (c2) LPT observation, both colored by velocity magnitude and overlaid with bubble outlines. In parallel, the bubble geometry is extracted through (d) a CVAT bubble mask, followed by (e) a smoothed bubble silhouette, and then converted to (f) a binary volume-fraction observation. The velocity observations in (c1) and (c2), together with the volume-fraction observation in (f), are used as inputs for AOT-nudging.

3.4 Summary

The quasi-2D bubbly-flow experiment provides two synchronized observation streams from the same image sequences. The first stream consists of liquid-phase velocity observations obtained using PIV and LPT, including gridded PIV velocity fields and scattered LPT tracer positions and velocities. The second stream is a bubble observation set obtained from bubble image processing. Both observation streams are subsequently used as inputs to the DA framework.

This quasi-2D experiment provides a practical configuration for validating the AOT-nudging framework. The confined geometry enables simultaneous visualization of the bubbles and tracer particles over the controlled measurement region, while reducing the complexity and computational cost associated with 3D measurements and reconstruction.

The boundary layers between two acrylic sheets reduce both the bubble-rise and tracer velocities, introducing a model error in the quasi-2D reconstruction. In addition, the tracer velocity is influenced by its position across the gap, producing a depthwise velocity gradient. This velocity gradient appears as an observation error in reconstruction. These experimental and modeling limitations make the reconstruction challenging and therefore provide a useful test of the robustness of the AOT-nudging framework (see Sect. 4.3.5).

Chapter 4

AOT-Nudging in Bubbly Flow

4.1 Introduction

In this chapter, an AOT-nudging DA framework is proposed to reconstruct bubbles with their ambient flows simultaneously. The AOT-nudging algorithm is suitable for dynamic systems in which perturbations are damped by intrinsic dissipation (i.e., viscosity) [344]. This characteristic aligns with common bubbly flows. Although inviscid bubbly flows have been studied [345–347], in most practical scenarios, bubbles are dispersed in viscous fluids.

The VoF method [86, 87, 265] is chosen to represent the interface of two phases through a phase-fraction scalar, the volume fraction. The scalar gives the fraction of one phase in each computational cell. The transport equation of the volume fraction is solved as an additional governing equation, together with the continuity and Navier–Stokes equations. The interface is then computed from this volume-fraction field.

The VoF method has several advantages. A major advantage of VoF is that it is inherently mass conservative, which is important in long-time simulations of moving and deforming bubbles. The method can also handle large interface deformation, breakup, and coalescence without explicitly tracking interface connectivity. In addition, VoF is computationally efficient on finite-volume and unstructured meshes. Compared with the level-set method [88, 261–264], VoF avoids the need for additional mass-conservation correction. Compared with front-tracking [89, 260], it avoids the complexity of marker management when the interface changes topology. VoF is also available in many open-source and commercial CFD platforms, which facilitate coupling with turbulence models, mesh adaptivity, and DA algorithms. The VoF framework is implemented in OpenFOAM [348].

Prior research has demonstrated the efficacy of AOT-nudging in scalar transport problems such as Bénard convection [314, 315]. In Bénard convection, the temperature is analogous to the volume fraction field in VoF. These studies suggest that AOT-nudging could be applied to VoF simulations. However, the two cases differ in three important respects. First, temperature varies continuously and smoothly throughout the domain, whereas the volume-fraction field is nominally binary with a sharp transition across a few interfacial cells. Second, the volume-fraction field determines the local density and viscosity and influences the surface-tension force and interface topology. Third, the thermal diffusion in Bénard convection is physical, whereas diffusion of the VoF field is numerical and should be minimized to preserve a sharp interface. These characteristics may make AOT-nudging in bubbly flows more challenging than in Bénard convection and motivate the investigation presented in this thesis.

An AOT-nudging bubbly flow solver is created and validated in this chapter. In this solver, the AOT-nudging algorithm is integrated into the momentum and volume fraction transport equations via feedback control terms. Sparse velocity observations are interpolated onto the computational mesh and assimilated through the momentum equation. The volume-fraction observations are also assimilated via interpolation. The solver estimates the flow quantities including velocity, velocity gradient, and bubble geometry, under the constraints of mass and momentum conservation.

This chapter is organized as follows. Sect. 4.1 introduces the VoF framework and its implementation in OpenFOAM for bubbly-flow reconstruction. Sect. 4.2 presents the proposed AOT-nudging formulation, including the governing equations, finite-volume discretization, and the DA workflow. Sect. 4.3 presents the validation and performance of the proposed solver through synthetic and experimental data reconstruction, and parameter-sensitivity analysis. Sect. 4.4 summarizes the main findings of this chapter.

4.2 Methodology

The Volume-of-Fluid (VoF) method is a sharp interface-capturing method. In VoF, the gas–liquid interface is represented implicitly by a phase volume-fraction field rather than being tracked explicitly by interface markers. The volume fraction α is transported by solving an advection equation, with $\alpha = 1$ and $\alpha = 0$ representing the pure phases and $0 < \alpha < 1$ identifying the interface cells. The interface can be identified from the spatial distribution of α, commonly using an iso-surface such as $\alpha = 0.5$. Across the interface, α

changes rapidly, and its gradient $\nabla\alpha$ provides the local interface-normal direction

$$\boldsymbol{n} = \frac{\nabla\alpha}{\|\nabla\alpha\|},$$

so that the interface is locally perpendicular to $\nabla\alpha$. Therefore, VoF captures the motion and deformation of a sharp interface through the evolution of the volume-fraction field and naturally accommodates interface breakup and coalescence.

4.2.1 Governing equations

In OpenFOAM, the standard incompressible two-phase VoF solver is called `interFoam`. The governing equations solved by this solver are

$$\begin{aligned} \nabla \cdot \boldsymbol{u} &= 0, \\ \frac{\partial(\rho\boldsymbol{u})}{\partial t} + \nabla \cdot (\rho\boldsymbol{u}\boldsymbol{u}) &= -\nabla p_{\mathrm{rgh}} + \nabla \cdot (\mu\nabla\boldsymbol{u}) + \nabla\boldsymbol{u} \cdot \nabla\mu \\ &\quad + \sigma\kappa\nabla\alpha - \boldsymbol{g} \cdot \boldsymbol{h}\nabla\rho, \\ \frac{\partial\alpha}{\partial t} + \nabla \cdot (\alpha\boldsymbol{u}) + \nabla \cdot [\boldsymbol{u}_{\mathrm{rc}}\alpha(1-\alpha)] &= 0, \end{aligned} \tag{4.1}$$

where $\boldsymbol{u}$ is the velocity field shared by the two phases, and α is the volume fraction, with $\alpha = 1$ in liquid and $\alpha = 0$ in gas. The modified pressure is defined as $p_{\mathrm{rgh}} = p - \rho\,\boldsymbol{g}\cdot\boldsymbol{h}$, where p is the pressure, $\boldsymbol{g}$ is the gravitational acceleration vector, and $\boldsymbol{h}$ is the position vector. This definition removes the hydrostatic contribution from the pressure field and improves numerical stability in gravity-driven two-phase flows. The effective density ρ and dynamic viscosity μ are evaluated from the volume fraction by $\rho = \rho_{\mathrm{l}}\alpha + \rho_{\mathrm{g}}(1-\alpha), \mu = \mu_{\mathrm{l}}\alpha + \mu_{\mathrm{g}}(1-\alpha)$, where the subscripts $[\cdot]_{\mathrm{l}}$ and $[\cdot]_{\mathrm{g}}$ denote the liquid and gas phases, respectively. The parameter σ is the surface tension coefficient, and κ is the interface curvature. The additional compression term $\nabla \cdot [\boldsymbol{u}_{\mathrm{rc}}\alpha(1-\alpha)]$ numerically maintains a sharp gas–liquid interface. In VoF, the diffusion of the volume-fraction field near bubble interfaces is purely numerical. It does not have a prescribed physical length scale. Its characteristic length scale is associated with the local mesh spacing and the numerical discretization. To address the diffusion issue, $\boldsymbol{u}_{\mathrm{rc}}$ is introduced as a relative compression velocity aligned with the interface normal. Because the factor $\alpha(1-\alpha)$ is nonzero only in interfacial cells, this term acts only near the interface. Its role is to counteract the numerical diffusion caused by the advection discretization. Thus, it helps maintain a thin interface. Further details of the VoF formulation are given in Appx. A.

To assimilate measurements into simulations, AOT-nudging terms are introduced to both the momentum equation and the transport of volume fraction equation in (4.1):

$$
\begin{aligned}
\nabla \cdot \boldsymbol{u} &= 0, \\
\frac{\partial(\rho \boldsymbol{u})}{\partial t} + \nabla \cdot (\rho \boldsymbol{u}\boldsymbol{u}) &= -\nabla p_{\mathrm{rgh}} + \nabla \cdot (\mu \nabla \boldsymbol{u}) \\
&\quad + \nabla \boldsymbol{u} \cdot \nabla \mu + \sigma \kappa \nabla \alpha \\
&\quad - \boldsymbol{g} \cdot \boldsymbol{h} \nabla \rho + K_{\mathrm{vel}} \left[\mathscr{I}_{\boldsymbol{u},h}(\boldsymbol{u}^{\mathrm{obs}}) - \mathscr{I}_{\boldsymbol{u},h}(\boldsymbol{u}) \right], \\
\frac{\partial \alpha}{\partial t} + \nabla \cdot (\alpha \boldsymbol{u}) + \nabla \cdot [\boldsymbol{u}_{\mathrm{rc}} \alpha (1-\alpha)] &= K_{\mathrm{vol}} \left[\mathscr{I}_{\alpha,h}(\alpha^{\mathrm{obs}}) - \mathscr{I}_{\alpha,h}(\alpha) \right],
\end{aligned}
\tag{4.2}
$$

where K_{vel} and K_{vol} are nudging coefficients for velocity and volume fraction, respectively; they control the strength of assimilation. $\mathscr{I}_h$ is the interpolation operator with an equivalent grid spacing h. It transfers data between the mesh and observational points, ensuring compatibility between scattered tracer locations and the computational grid. $[\cdot]^{\mathrm{obs}}$ denotes an observed quantity, obtained either from the reference simulation in synthetic validation or from experimental measurements. $K_{\mathrm{vel}} \left[\mathscr{I}_{\boldsymbol{u},h}(\boldsymbol{u}^{\mathrm{obs}}) - \mathscr{I}_{\boldsymbol{u},h}(\boldsymbol{u}) \right]$ and $K_{\mathrm{vol}} \left[\mathscr{I}_{\alpha,h}(\alpha^{\mathrm{obs}}) - \mathscr{I}_{\alpha,h}(\alpha) \right]$ are the AOT-nudging terms. The interpolant $\mathscr{I}_h$ can be nearest or linear interpolation [292]. Other interpolants such as radial basis functions [168, 169, 172, 174] could also be applied to improve the nudging accuracy.

As shown in (4.2), the pressure is not governed by a transport equation, and the velocities are constrained by the continuity equation. A segregated solver can decouple pressure and velocity, and solve the incompressible N-S equations iteratively. This work adopts the PIMPLE (PISO [349] + SIMPLE [350, 351]) algorithm [352]. The solver `interFoam` in OpenFOAM [348] utilizes the PIMPLE algorithm for an incompressible transient Newtonian two-phase flow.

4.2.2 Finite volume discretization

The AOT-nudging terms are implemented as explicit feedback source terms. In the momentum equation, the nudging term can be interpreted as an artificial forcing that drives the solution toward the observations. In this work, they are explicitly discretized. This section details the finite volume discretization for the AOT-nudging terms in the new solver. The decoupling of pressure and velocity is the same as in the standard OpenFOAM two-phase flow solver: the volume fraction is updated first, then the momentum and pressure are advanced within PIMPLE.

Transport of volume fraction

The transport of α is solved first to initialize and transport the interface, using the AOT-nudging form (4.2):

$$\frac{\partial \alpha}{\partial t} + \nabla \cdot (\alpha \boldsymbol{u}) + \nabla \cdot [\alpha(1-\alpha)\, \boldsymbol{u}_{\mathrm{rc}}] = K_{\mathrm{vol}} \left[\mathscr{I}_{\alpha,h}(\alpha^{\mathrm{obs}}) - \mathscr{I}_{\alpha,h}(\alpha) \right], \tag{4.3}$$

Applying the FVM over a control volume V_{P} and a time step Δt, and linearizing the convective and compressive fluxes in the standard OpenFOAM manner, yields:

$$\mathrm{A}^{\mathrm{n}}_{\alpha,\mathrm{P}}\, \alpha^{\mathrm{n+1}}_{\mathrm{P}} \;=\; - \sum_{N \in \mathcal{N}(\mathrm{P})} \mathrm{A}^{\mathrm{n}}_{\alpha,\mathrm{N}}\, \alpha^{\mathrm{n}}_{\mathrm{N}} \;+\; \mathrm{S}^{\mathrm{n}}_{\alpha,\mathrm{P}}, \tag{4.4}$$

where $\mathcal{N}(\mathrm{P})$ denotes the set of neighbor cells of P; the subscripts $[\cdot]_{\mathrm{P}}$ and $[\cdot]_{\mathrm{N}}$ represent the cell and its neighbors, respectively; the superscript $[\cdot]^{\mathrm{n}}$ denotes the current time step, and the next time step is $[\cdot]^{\mathrm{n+1}}$. $\alpha^{\mathrm{n+1}}_{\mathrm{P}}$ and $\alpha^{\mathrm{n}}_{\mathrm{N}}$ are discretized volume fractions. The coefficients $\mathrm{A}^{\mathrm{n}}_{\alpha}$ collect the time term and the linearized flux contributions from both the physical advection $\alpha\boldsymbol{u}$ and the compressive term $\alpha(1-\alpha)\boldsymbol{u}_{\mathrm{rc}}$. The source $\mathrm{S}^{\mathrm{n}}_{\alpha}$ contains two parts: (i) the explicit AOT contribution

$$\mathrm{S}^{\mathrm{n}}_{\alpha,\mathrm{P}}\big|_{\mathrm{AOT}} \;=\; K_{\mathrm{vol}} \Big(\mathscr{I}_{\alpha,h}(\alpha^{\mathrm{obs}}) - \mathscr{I}_{\alpha,h}(\alpha) \Big)^{\mathrm{n}}_{\mathrm{P}},$$

assembled at cell centers using the same interpolation operator as in (4.2) (nearest-neighbor in this work; see Sect. 4.2.3); and (ii) the Multi-dimensional Universal Limiter for Explicit Solution (MULES) boundedness correction. A MULES limiter [353, 354] is used to enforce $0 \le \alpha \le 1$ by restricting the high-order anti-diffusive contribution at each face. In its standard form, MULES blends an upwind value α^{UP} with a high-order value α^{HO} using a face limiter $\lambda_{\mathrm{lmt}} \in [0,1]$. In the limiter, $\lambda_{\mathrm{lmt}} \to 0$ recovers strictly bounded but diffusive upwind transport, whereas $\lambda_{\mathrm{lmt}} \to 1$ restores the unbounded high-order flux.

Because experimental bubble silhouettes provide direct phase information, after solving (4.4), the observations in pure-phase regions with nearest interpolation are enforced:

$$\alpha^{\mathrm{n+1}}_{\mathrm{P}} \;=\; \begin{cases} 0, & \mathbf{x}_{\mathrm{P}} \in \Omega^{\mathrm{obs}}_{\mathrm{g}}, \\ 1, & \mathbf{x}_{\mathrm{P}} \in \Omega^{\mathrm{obs}}_{\mathrm{l}}, \end{cases} \tag{4.5}$$

where $\Omega^{\mathrm{obs}}_{\mathrm{g}}$ and $\Omega^{\mathrm{obs}}_{\mathrm{l}}$ are observation domains of pure gas and pure liquid, respectively.

Once α is updated, mixture properties are recomputed as

$$\rho^{*} \;=\; \rho_{\mathrm{l}}\alpha + \rho_{\mathrm{g}}(1-\alpha), \qquad \mu^{*} \;=\; \mu_{\mathrm{l}}\alpha + \mu_{\mathrm{g}}(1-\alpha), \qquad \kappa^{*} \;=\; -\nabla\cdot\left(\frac{\nabla\alpha}{\|\nabla\alpha\|}\right). \tag{4.6}$$

They will be used in the subsequent N-S equations.

Momentum equations

Based on (4.2), the N-S equation is linearized and discretized as a momentum predictor at time step n, written as

$$\mathrm{A}^{\mathrm{n}}_{u,\mathrm{P}}\,\mathbf{U}^{*}_{\mathrm{P}} \;=\; -\sum_{N\in\mathcal{N}(P)} \mathrm{A}^{\mathrm{n}}_{u,\mathrm{N}}\,\mathbf{U}^{*}_{\mathrm{N}} \;+\; \mathrm{S}^{\mathrm{n}}_{u,\mathrm{P}} \;-\; \nabla p^{\mathrm{n}}_{\mathrm{rgh},\mathrm{P}}, \tag{4.7}$$

where $\mathrm{A}^{\mathrm{n}}_{u}$ collects the temporal, convective, and diffusive contributions formed with the updated (ρ^{*},μ^{*}), and $\mathrm{S}^{\mathrm{n}}_{u}$ gathers body forces. $\mathbf{U}^{\mathrm{n+1}}_{\mathrm{P}}$ and $\mathbf{U}^{\mathrm{n}}_{\mathrm{N}}$ are discretized velocities. The body forces include gravity via p_{rgh}, surface tension via $\sigma\kappa^{*}\nabla\alpha$, and the explicit AOT-nudging forcing for velocity. The superscript $[\cdot]^{*}$ indicates the prediction. Equation (4.7) does not enforce incompressibility. Then, a pressure Poisson equation is assembled from the predicted field:

$$\nabla\cdot\left(\tfrac{1}{\mathrm{A}^{\mathrm{n}}_{u}}\nabla p^{*}_{\mathrm{rgh}}\right) \;=\; \nabla\cdot\,\mathbf{HbyA}^{*}, \qquad \mathbf{HbyA}^{*}_{\mathrm{P}} \;=\; \frac{-\sum \mathrm{A}^{\mathrm{n}}_{u,\mathrm{N}}\,\mathbf{U}^{*}_{\mathrm{N}} + \mathrm{S}^{\mathrm{n}}_{u,\mathrm{P}}}{\mathrm{A}^{\mathrm{n}}_{u,\mathrm{P}}}. \tag{4.8}$$

As in practice, $\mathbf{HbyA}^{*}$ is assembled at cell centers by (4.8) and interpolated to faces. Therefore, in (4.7) and (4.8), the N-S equations are discretized.

4.2.3 AOT-nudging workflow

After discretization, the original solver embeds the AOT-nudging algorithm at each time step in the following loop:

1. Interpolation: mesh → observations. For each observation location $\mathbf{x}^{\mathrm{obs}}_{j}$ at tracer j, the nearest mesh values from the previous time step are sampled to obtain $\mathbf{u}(\mathbf{x}^{\mathrm{obs}}_{j})$ and $\alpha(\mathbf{x}^{\mathrm{obs}}_{j})$. In this work, nearest interpolation is used for all observation–mesh transfers.

2. Discrepancy calculation. Compute the discrepancies at the observation points:

$$\Delta\mathbf{u}_{j} = \mathbf{u}^{\mathrm{obs}}_{j} - \mathbf{u}(\mathbf{x}^{\mathrm{obs}}_{j}), \qquad \Delta\alpha_{j} = \alpha^{\mathrm{obs}}_{j} - \alpha(\mathbf{x}^{\mathrm{obs}}_{j}).$$

3. Interpolation: observations → mesh. Map these discrepancies back to the mesh by assigning to each cell center $\mathbf{x}^{\mathrm{m}}_{i}$ the value from its nearest observation point. This yields cell-wise discrepancy fields $\Delta\mathbf{u}(\mathbf{x}^{\mathrm{m}}_{i})$ and $\Delta\alpha(\mathbf{x}^{\mathrm{m}}_{i})$.

4. Assembly of the AOT-nudging terms. Form the explicit nudging sources based on the cell-wise discrepancies:

$$\mathrm{S}^{\mathrm{n}}_{u,\mathrm{P}}\big|_{\mathrm{AOT}} = K_{\mathrm{vel}}\,\Delta\mathbf{u}(\mathbf{x}^{\mathrm{m}}_{\mathrm{P}}), \qquad \mathrm{S}^{\mathrm{n}}_{\alpha,\mathrm{P}}\big|_{\mathrm{AOT}} = K_{\mathrm{vol}}\,\Delta\alpha(\mathbf{x}^{\mathrm{m}}_{\mathrm{P}}),$$

   and add them to the right-hand side of (4.4) and (4.7), respectively.

5. Volume-fraction correction. The MULES logic is retained in the transport of volume fraction equation. After enforcing the pure-phase observations through (4.5) and adding the AOT-nudging source, (4.4) is solved with MULES. The updated volume fraction field is then used to refresh the mixture properties (ρ, μ, κ) before entering the pressure–velocity loop.

6. PIMPLE loop. After the phase-fraction update, the solver advances the momentum and pressure fields through the standard PIMPLE algorithm. At each iteration, a momentum predictor is solved, the pressure Poisson equation (4.8) is assembled and solved, the face fluxes are corrected, and the cell-centered velocity field is updated accordingly. This pressure–velocity coupling is repeated until the specified convergence tolerances or iteration limits are reached. During these inner corrections, the mixture properties and explicit AOT-nudging source terms remain fixed within the current time step. The full discrete formulation is presented in Appx. B.

With this procedure, both α and $\boldsymbol{u}$ are nudged toward the observations while preserving boundedness, enforcing discrete continuity, and maintaining a sharp interface through the compressive term and MULES algorithm.

4.3 Results and Discussion

4.3.1 Reconstruction error metrics

To quantify reconstruction quality, the reconstructed fields f^{rcs} are compared with the reference (i.e., ground-truth) fields f^{grt} through discrete sampling-based error metrics. In this work, both the velocity and volume-fraction errors are evaluated at the same fixed and uniform sampling locations. At each selected evaluation time, the reconstructed and reference fields are sampled at these locations, and the resulting discrepancies are used to define time-dependent error metrics.

Let $\{\boldsymbol{x}_i\}_{i=1}^{N_{\text{eval}}}$ denote the evaluation points, where N_{eval} is the total number of points. At time t_k, the reconstructed and reference velocities sampled at these points are

$$\boldsymbol{u}_i^{\text{rcs}}(t_k) = \boldsymbol{u}^{\text{rcs}}(\boldsymbol{x}_i, t_k) \text{ and } \boldsymbol{u}_i^{\text{grt}}(t_k) = \boldsymbol{u}^{\text{grt}}(\boldsymbol{x}_i, t_k),$$

respectively. The point-wise velocity discrepancy is defined as

$$\mathbf{e}_i^{(\boldsymbol{u})}(t_k) = \boldsymbol{u}_i^{\text{rcs}}(t_k) - \boldsymbol{u}_i^{\text{grt}}(t_k).$$

The corresponding discrete absolute L^2 norm error is

$$\mathcal{E}_{L^2_{\text{abs}}}^{(\boldsymbol{u})}(t_k) = \left(\sum_{i=1}^{N_{\text{eval}}} \left\| \mathbf{e}_i^{(\boldsymbol{u})}(t_k) \right\|_2^2 \right)^{1/2}.$$

The relative velocity error is defined using a reference velocity $|\boldsymbol{u}|_{\text{ref}}$:

$$\mathcal{E}_{L^2_{\text{rel}}}^{(\boldsymbol{u})}(t_k) = \frac{1}{|\boldsymbol{u}|_{\text{ref}}} \left(\frac{1}{N_{\text{eval}}} \sum_{i=1}^{N_{\text{eval}}} \left\| \mathbf{e}_i^{(\boldsymbol{u})}(t_k) \right\|_2^2 \right)^{1/2}, \tag{4.9}$$

where $|\boldsymbol{u}|_{\text{ref}}$ denotes the reference velocity, taken as the average of the maximum rising velocities of the bubbles:

$$|\boldsymbol{u}|_{\text{ref}} \approx \frac{1}{N_{\text{b}}} \sum_{i=1}^{N_{\text{b}}} \max_t |\boldsymbol{u}_{\text{b},i}(t)|,$$

where N_{b} is the number of bubbles, $\boldsymbol{u}_{\text{b},i}(t)$ is the instantaneous rising velocity of bubble i, and $\max_t |\boldsymbol{u}_{\text{b},i}(t)|$ is the maximum rising velocity attained by that bubble over the observation period.

For the volume-fraction field, the same evaluation points are used. Let

$$\alpha_i^{\text{rcs}}(t_k) = \alpha^{\text{rcs}}(\mathbf{x}_i, t_k) \text{ and } \alpha_i^{\text{grt}}(t_k) = \alpha^{\text{grt}}(\mathbf{x}_i, t_k),$$

denote the reconstructed and reference liquid volume fractions sampled at the evaluation points. The point-wise discrepancy is defined as

$$e_i^{(\alpha)}(t_k) = \alpha_i^{\text{rcs}}(t_k) - \alpha_i^{\text{grt}}(t_k).$$

The corresponding discrete absolute error in a L^2 sense is

$$\mathcal{E}_{L^2_{\text{abs}}}^{(\alpha)}(t_k) = \left(\sum_{i=1}^{N_{\text{eval}}} \left(e_i^{(\alpha)}(t_k) \right)^2 \right)^{1/2}.$$

The relative volume-fraction error is defined using a reference value α_{ref}:

$$\mathcal{E}^{(\alpha)}_{L^2_{\mathrm{rel}}}(t_k) = \frac{1}{\alpha_{\mathrm{ref}}} \left(\frac{1}{N_{\mathrm{eval}}} \sum_{i=1}^{N_{\mathrm{eval}}} \left(e_i^{(\alpha)}(t_k) \right)^2 \right)^{1/2}. \tag{4.10}$$

For each reconstruction setting, time histories of these errors are reported over the reconstruction interval. These diagnostics quantify how well the reconstructed liquid-phase velocity field and volume-fraction field reproduce the ground truth. They also provide a consistent basis for comparison across different nudging parameters, observation densities, and nudging frequencies.

4.3.2 Validation based on synthetic data: setup

The proposed framework is validated using synthetic observations generated from a high-resolution reference simulation. The reference case solves the incompressible, isothermal Navier–Stokes equations with a VoF interface-capturing scheme under gravity acting in the $-y$ direction. The flow consists of six bubbles rising in an initially quiescent 2D column (see Fig. 4.1).

The computational domain of the reference simulation is 2D with width 20 mm, height 50 mm, and numerical thickness 1×10^{-3} m in z. In the z direction, it is a single cell with `empty` boundary conditions. Water fills the column up to 48 mm, leaving a 2 mm air headspace at the top. A uniform Cartesian mesh with $\Delta x = \Delta y = 1 \times 10^{-4}$ m discretizes the domain, giving $N_x = 200$, $N_y = 500$, $N_z = 1$.

The time step is calculated based on the Courant number. The maximum Courant number for the fluid flow and interface is set to 0.1. The observation interval is selected such that the bubble displacement between two consecutive observations does not exceed one cell width:

$$|\boldsymbol{u}|_{\max} \Delta t_{\mathrm{obs}} \leq \Delta x. \tag{4.11}$$

With $|\boldsymbol{u}|_{\max} = 0.6\,\mathrm{m\,s^{-1}}$ and $\Delta x = \Delta y = 1 \times 10^{-4}$ m, this requires

$$\Delta t_{\mathrm{obs}} \leq \frac{\Delta x}{|\boldsymbol{u}|_{\max}} = 1.67 \times 10^{-4}\,\mathrm{s},$$

or equivalently $f_{\mathrm{obs}} \geq 6$ kHz. Therefore, $\Delta t_{\mathrm{obs}} = 1 \times 10^{-4}$ s is chosen in validation.

For the boundary and initial conditions, see Fig. 4.1 (a). The top boundary is open to the atmosphere: the volume fraction uses `inletOutlet` with air on backflow, which

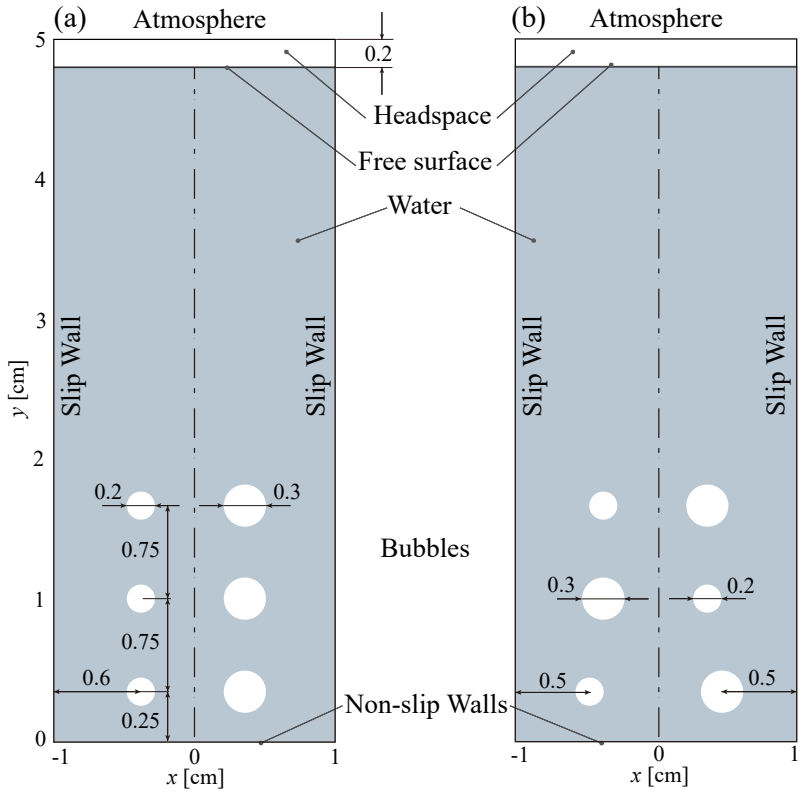


Figure 4.1: Initial and boundary conditions for the reference solution and the AOT-nudging reconstruction. The subfigure (a) shows the reference case, and the subfigure (b) shows the initial and boundary conditions used in the AOT-nudging reconstruction. In both cases, the bubble centers are arranged symmetrically with respect to the centerline. In the reference solution, the upper two bubbles are initialized with an upward vertical velocity of $0.01\,\mathrm{m\,s^{-1}}$. In the AOT-nudging reconstruction case, the liquid phase and all bubbles are initially at rest. All units are in centimeters.

means that `inletValue = 0`, `pressureInletOutletVelocity` for velocity, and p_{rgh} uses `totalPressure`. The bottom wall is `noSlip`; the side walls use `slip` to emulate a laterally wide tank. On solid walls, α is `zeroGradient` and p_{rgh} is `fixedFluxPressure`. Front and back planes are `empty` (i.e., 2D). Initially, $\alpha = 1$ in water and $\alpha = 0$ in the headspace. Six circular gas volumes (radii 1 mm to 1.5 mm) are placed in the liquid and released to rise.

For a representative bubble diameter $d = 2.5\,\mathrm{mm}$ and reference liquid-phase velocity

$|\boldsymbol{u}|_{\text{ref}} = 0.5\,\text{m}\,\text{s}^{-1}$, the Reynolds, Weber, Capillary, Eötvös, and Morton numbers are

$$\begin{aligned} \text{Re} &= \frac{\rho_\text{l}\,|\boldsymbol{u}|_{\text{ref}}\,d}{\mu_\text{l}} \approx 1.25\times10^{3}, \quad \text{We} = \frac{\rho_\text{l}\,|\boldsymbol{u}|^2_{\text{ref}}\,d}{\sigma} \approx 8.66, \\ \text{Ca} &= \frac{\mu_\text{l}\,|\boldsymbol{u}|_{\text{ref}}}{\sigma} \approx 6.96\times10^{-3}, \quad \text{Eo} = \frac{(\rho_\text{l}-\rho_\text{g})gd^2}{\sigma} \approx 0.85, \\ \text{Mo} &= \frac{g\mu_\text{l}^4(\rho_\text{l}-\rho_\text{g})}{\rho_\text{l}^2\sigma^3} \approx 2.65\times10^{-11} \end{aligned} \tag{4.12}$$

The Reynolds number indicates that the bubble motion is well above the creeping-flow regime and is approaching the turbulent flows. It can generate irregular wakes. The Weber number shows that inertial effects are strong enough to deform the interface, but not so large as to cause severe distortion or breakup. The small Capillary number indicates that viscous deformation of the interface is limited. The Eötvös number implies that the bubble shape is expected to remain close to spherical or mildly ellipsoidal. The small Morton number confirms that the surface tension remains important, and strongly deformed bubble shapes are less likely at this bubble size. In summary, the present bubble regime is characterized by inertia-dominated motion while still being strongly influenced by surface tension. The bubbles are expected to rise with noticeable wakes while remaining moderately deformed. Their shapes are consistent with nearly spherical to mildly ellipsoidal bubbles [355–357].

Synthetic observational data are generated in two streams: (i) velocity observations derived from Lagrangian tracer particles and (ii) image-based bubble silhouettes extracted from the phase field. For the velocity observations, the sampling locations evolve in time and therefore form Lagrangian trajectories, as illustrated in Fig. 4.2. At the initial frame, $N_\text{p} = 800$ massless tracers are seeded in the liquid phase and then transported using ParaView's `particleTracer`, producing trajectories over 4,001 frames. The tracer trajectories (see Fig. 4.2) illustrate that the particles remain randomly distributed throughout the liquid region and sample the evolving recirculating motion around the rising bubbles. The velocity observations are obtained by interpolating the liquid velocity field $\boldsymbol{u}_\text{l} = (u, v)$ to the instantaneous tracer positions, yielding sparse Lagrangian samples at locations $\{\mathbf{x}_i(t)\}_{i=1}^{N_\text{p}}$ in the liquid phase. The observation window is limited to 0.4 s because, beyond this time, no bubbles remain within the region below $y = 4$ cm.

Figure 4.2 illustrates the initialization and evolution of the Lagrangian tracers used to generate the liquid-phase velocity observations. The tracers are initially seeded randomly in the liquid phase and are advected by the bubble-induced flow. As the bubbles rise, deform, and interact, the surrounding liquid develops wakes, recirculation zones, and localized

high-shear regions. These movements cause the tracer trajectories to become curved and nonuniform, leading to a nonuniform distribution of observed velocities.

To compare the tracer density with image-based measurements, an equivalent particles-per-pixel (ppp) value is defined as

$$\mathrm{ppp}_{\mathrm{eq}} = \frac{N_{\mathrm{p}}}{N_{\mathrm{pix}}}, \tag{4.13}$$

where N_{p} is the number of tracer particles and N_{pix} is the number of pixels in the image domain. For the present ground-truth dataset, $\mathrm{ppp}_{\mathrm{eq}} = 0.008$. Here, $\mathrm{ppp}_{\mathrm{eq}}$ is an equivalent measure obtained by treating each in-plane computational cell as an image pixel. It changes with reconstruction resolution even when the number of tracer observations is unchanged. This equivalent seeding density is below values commonly reported in modern experiments, which are approximately 0.1 ppp for STB-LPT [134] and 0.05 ppp for Tomo-PIV [129, 130].

For generating volume-fraction observations, at each t_k the volume-fraction field $\alpha(\mathbf{x}, t_k)$ is thresholded at $\alpha = 0.5$ to form volume-fraction observations, which are integrated across the thin z direction to obtain a 2D silhouette. The bubble images only capture the silhouette below $y = 4$ cm, excluding the headspace and bubbles above $y = 4$ cm. The mask is rasterized on an image grid with a pixel pitch matching the mesh.

The AOT-nudging reconstruction is performed on a mesh with $N_x = 100$, $N_y = 250$, and $N_z = 1$, corresponding to an equivalent tracer density of 0.032 ppp. At this resolution, the thinnest inter-bubble liquid film is not fully resolved. This limitation could be alleviated in future work using Adaptive Mesh Refinement (AMR) to locally refine the film region. Except for the time step, initial conditions, and mesh resolution, the physical properties and numerical settings are kept consistent with those of the ground-truth simulation. The nudging strengths for the velocity and volume-fraction fields are set to $K_{\mathrm{vel}} = 100$ and $K_{\mathrm{vol}} = 100$, respectively.

A baseline simulation is also conducted using the same mesh, physical parameters, and numerical settings as the AOT-nudging case. However, no observational data are assimilated, and its initial conditions are the same as the ground truth.

4.3.3 Validation based on synthetic data: results

The validation results are presented in Figs. 4.3 – 4.9. Figure 4.3 compares the bubble trajectories obtained from the ground truth, the baseline simulation, and the AOT-nudging reconstruction. The baseline simulation exhibits increasing deviations in bubble

trajectories and outlines as the bubbles rise, deform, and interact, even when accurate initial conditions were employed. In contrast, the AOT-nudging reconstruction follows the ground-truth trajectories and outlines closely throughout the observed region. Even after bubble coalescence, their trajectories and shapes remain consistent with those in the ground truth. This agreement indicates that the AOT-nudging reconstruction captures both the motion of individual bubbles and the associated topological changes.

Figures 4.4 and 4.5 compare the velocity magnitude $|\boldsymbol{u}|$ obtained from the ground truth, the baseline simulation, and the AOT-nudging reconstruction. Without DA, the baseline simulation progressively deviates from the ground truth as errors in the bubble positions and wake structures accumulate. Consequently, the associated jets, vortices, and bubble-induced wakes become displaced or misrepresented. By contrast, the AOT-nudging reconstruction reproduces the dominant high- and low-velocity flow structures at the correct locations. It also captures the principal wake and vortices throughout the observation period. Although volume-fraction observations (i.e., bubble silhouette and free-surface observations) are unavailable above $y = 4\,\mathrm{cm}$, the reconstructed velocity field and free surface remain more consistent with the ground truth than those of the baseline simulation. This comparison shows that the velocity observations, together with the volume-fraction observations, provide sufficient constraints to correct the evolving two-phase flow and reduce its deviations from the ground truth.

Figures 4.6, 4.7, and 4.8 illustrate the volume-fraction field, velocity-gradient magnitude, and pressure field, respectively. The reconstructed volume-fraction field recovers the bubble locations, shapes, and interface topology while maintaining sharp and coherent gas–liquid interfaces. The reconstructed velocity-gradient field captures the high-gradient regions near the interfaces and in the bubble wakes. Although some small-scale gradient peaks are smoothed because of the coarse mesh, nearest interpolation, and numerical diffusion, their dominant locations and overall spatial organization remain consistent with the ground truth. Similarly, the reconstructed pressure field reproduces the dominant pressure variations associated with bubble wakes, interface deformation, and the free surface. This agreement is obtained despite the absence of volume-fraction observations above $y = 4\,\mathrm{cm}$, sparse and random tracer distribution, the reconstruction mesh containing only 25% of the cells used in the ground-truth simulation, and the use of inaccurate initial conditions and large time steps.

Figure 4.9 shows the spanwise vorticity ω_z in a local region (i.e., $-1 \leq x \leq 0$ cm and $2.5 \leq y \leq 3.5$ cm) where two bubbles approach and coalesce. The ground-truth field contains opposite-direction vortical structures along the bubble flanks and in the surrounding wake, reflecting shear layers and vortices. The AOT-nudging reconstruction recovers the locations, signs, and spatial organization of these vortical structures. This agreement

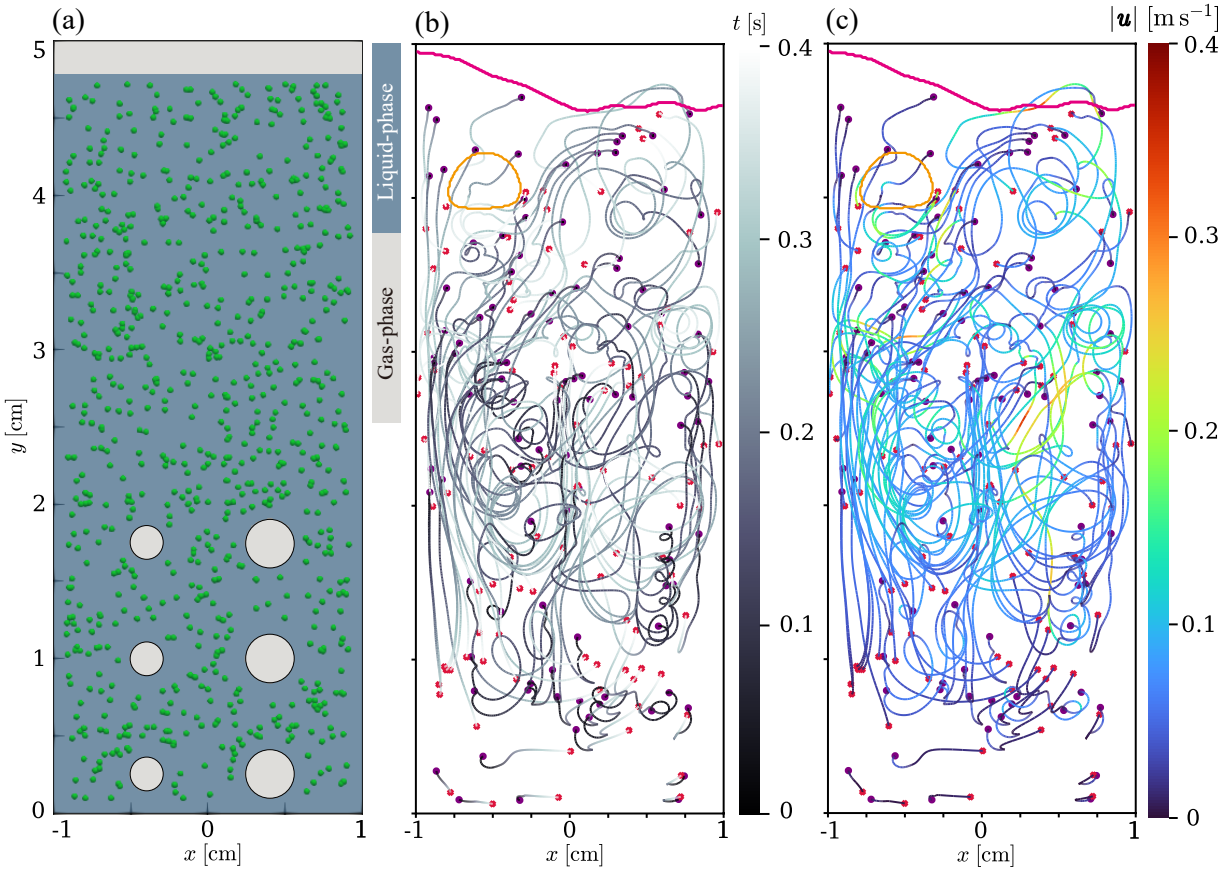


Figure 4.2: Lagrangian tracer initialization and trajectories in the 2D multi-bubble rise case. (a): initial tracer distribution at $t = 0$, where tracers are seeded only in the liquid phase and denoted by green dots. (b) and (c): tracer trajectories over $0 \leq t \leq 0.4$ s, colored by the time and the instantaneous liquid-phase velocity magnitude $|\boldsymbol{u}|$, respectively. In (b) and (c), the initial and end positions of particles are denoted by purple and red dots, respectively. The bubble outlines and free surfaces at the last time are denoted by orange and pink curves, respectively. One hundred out of 800 particles are shown for visualization.

is notable because the tracers are sparse in this region, showing the ability to recover dynamically important flow structures even when observational coverage is incomplete.

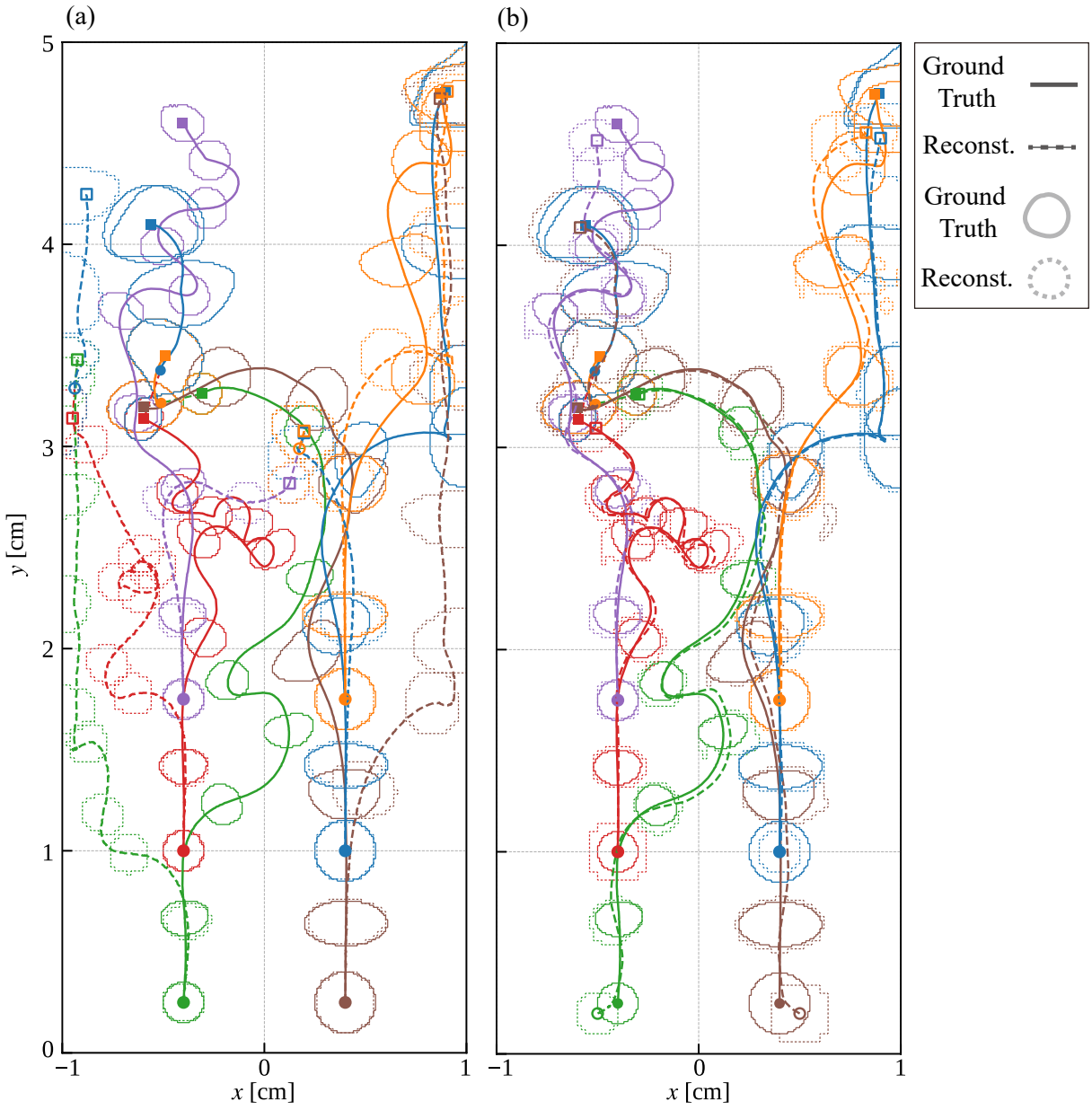


Figure 4.3: Comparison of bubble trajectories and outlines among the ground truth, baseline simulation, and AOT-nudging reconstruction. (a) Trajectories and outlines of the ground truth vs. baseline simulation; (b) Trajectories and outlines of the ground truth vs. the AOT-nudging reconstruction. The colors identify different trajectories and outlines of bubbles.

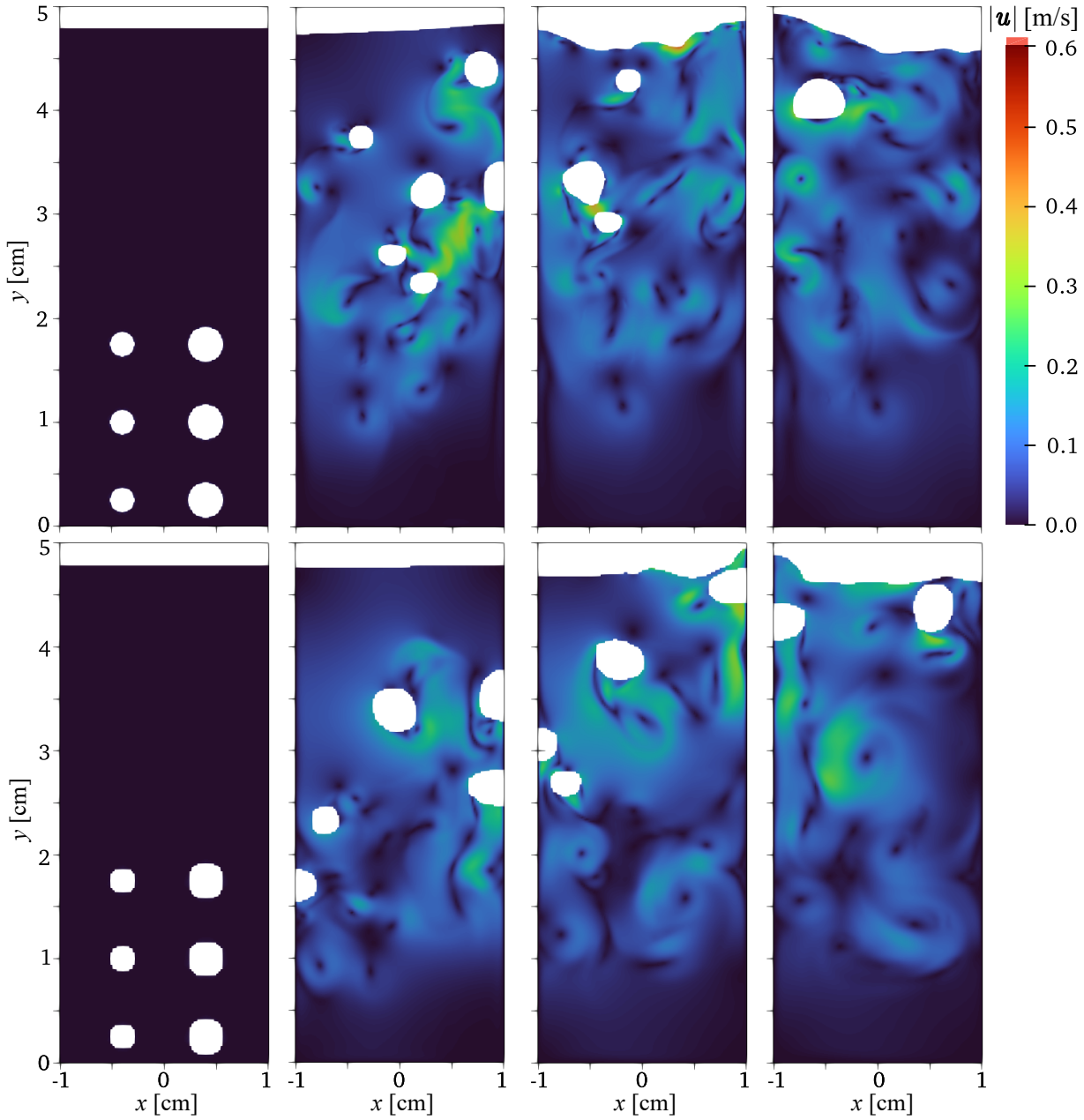


Figure 4.4: Comparison of the velocity magnitude $|\boldsymbol{u}|$ between the ground truth (upper row) and the baseline simulation without DA (lower row). Columns from left to right correspond to $t = 0.001$, 0.2, 0.3, and 0.4 s.

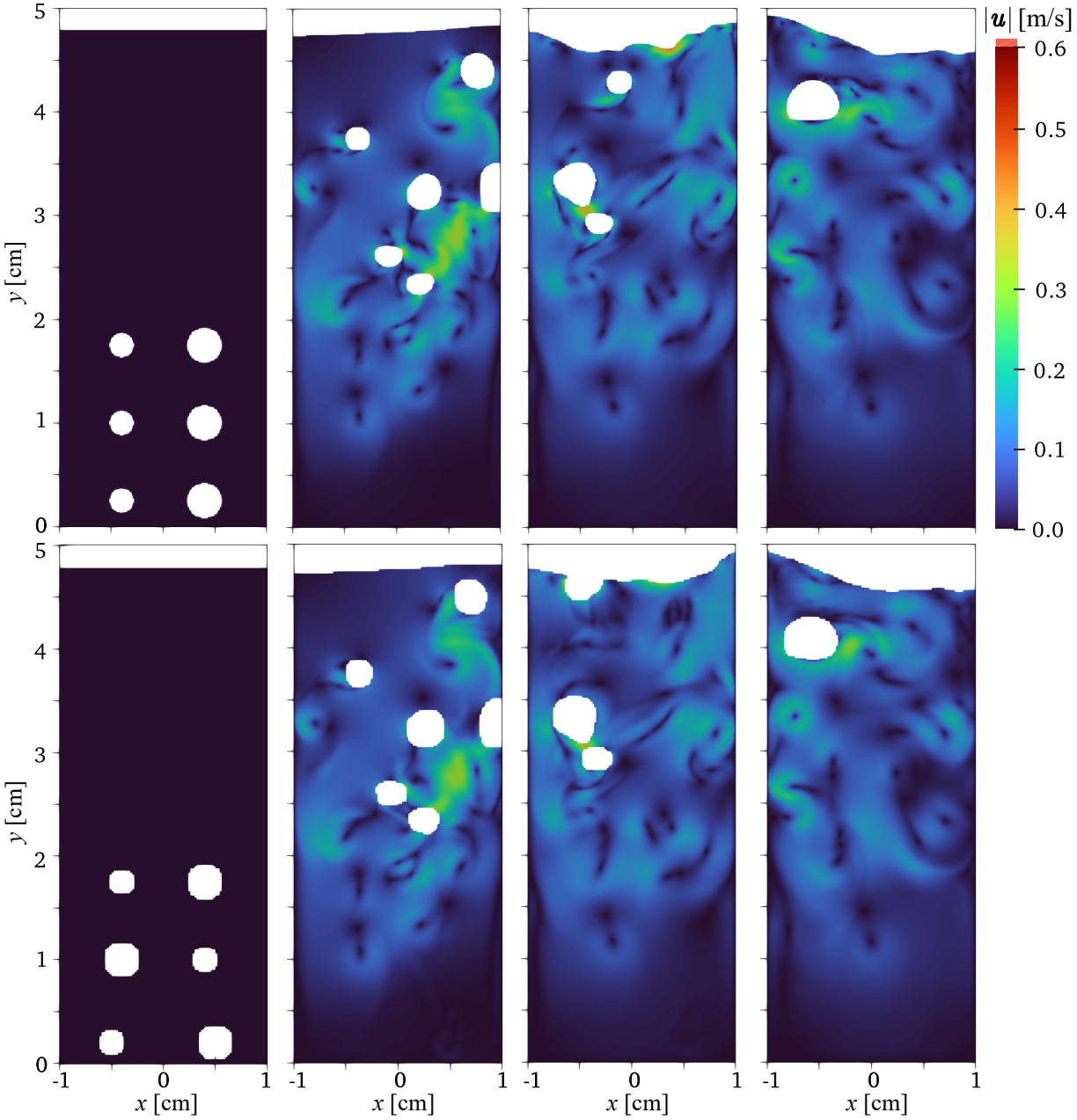


Figure 4.5: Comparison of the velocity magnitude $|\boldsymbol{u}|$ between the ground truth (upper row) and the AOT-nudging reconstruction (lower row). Columns from left to right correspond to $t = 0.001$, 0.2, 0.3, and 0.4 s.

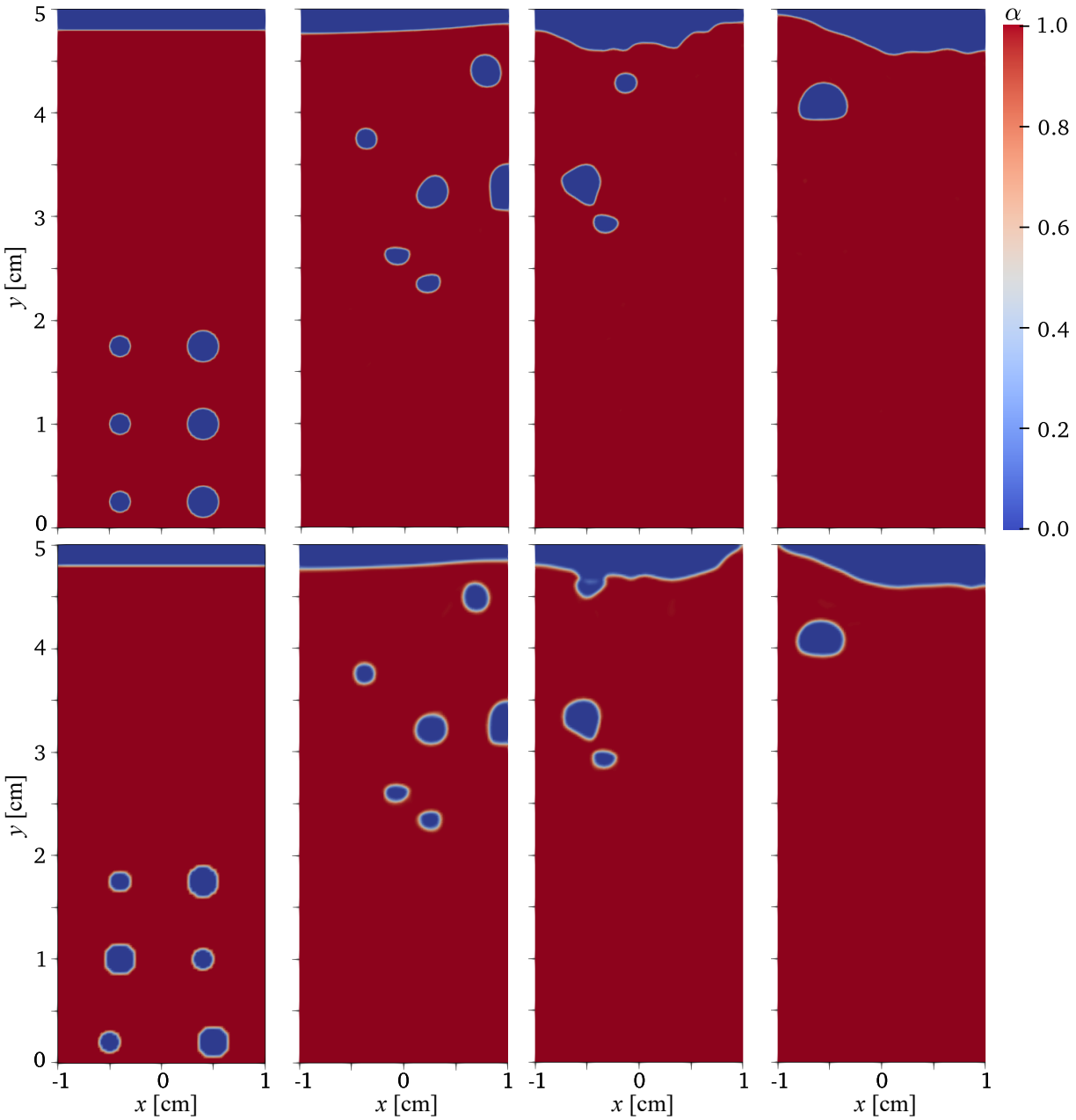


Figure 4.6: Comparison of the volume-fraction field α between the ground truth (upper row) and the AOT-nudging reconstruction (lower row). Columns from left to right correspond to $t = 0.001$, 0.2, 0.3, and 0.4 s.

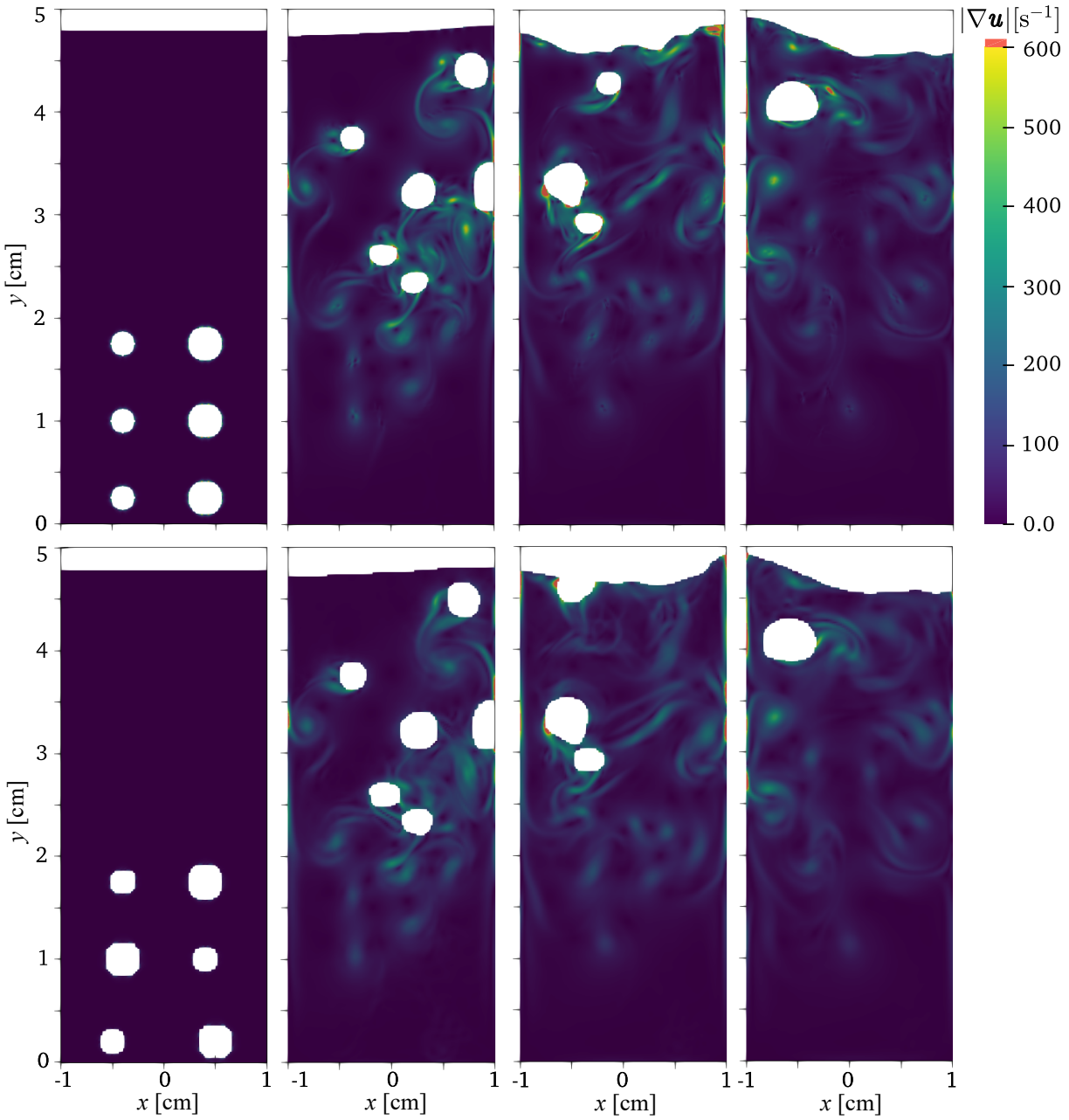


Figure 4.7: Comparison of the velocity-gradient magnitude $|\nabla \boldsymbol{u}|$ between the ground truth (upper row) and the AOT-nudging reconstruction (lower row). Columns from left to right correspond to $t = 0.001$, 0.2, 0.3, and 0.4 s.

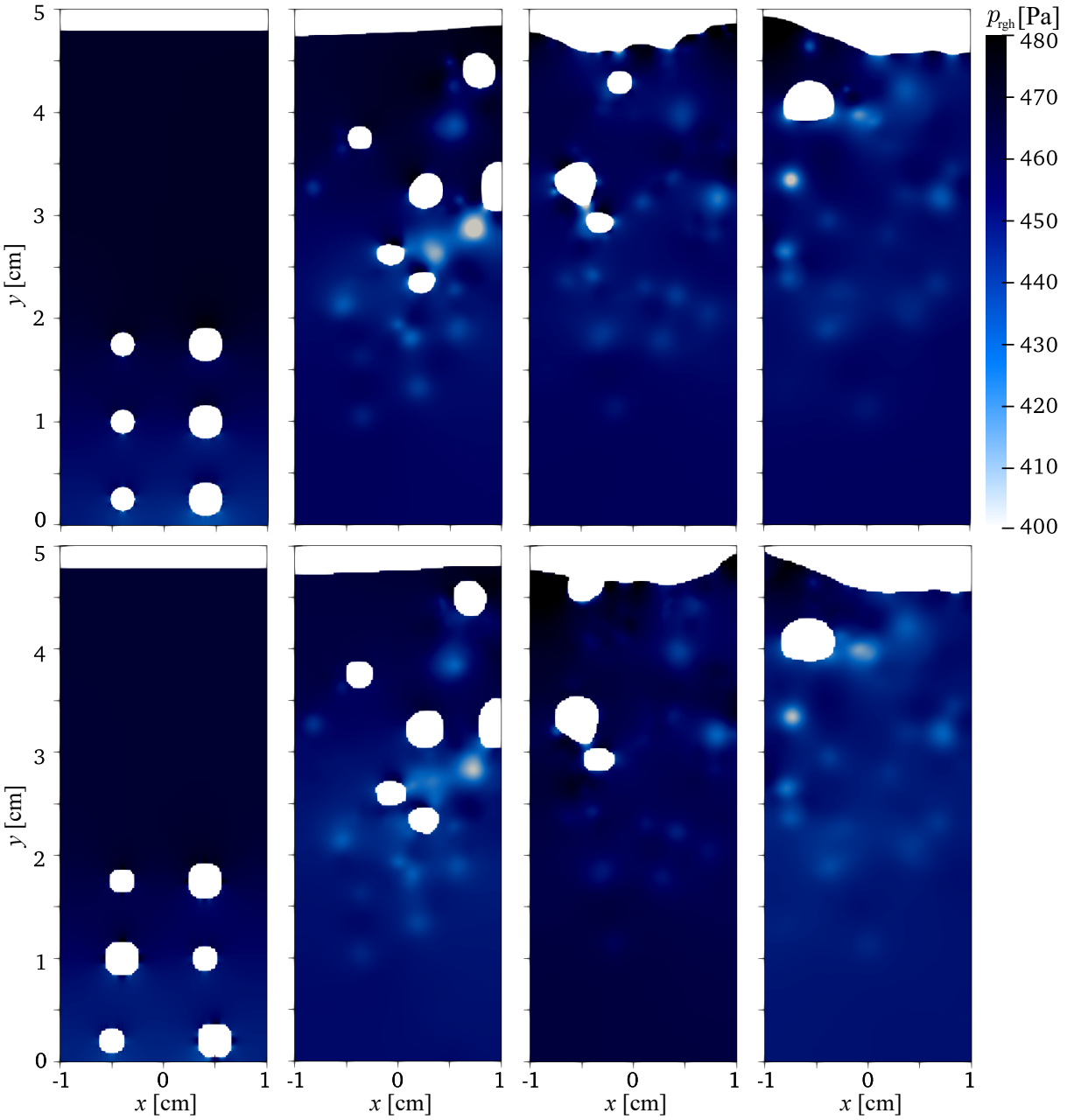


Figure 4.8: Comparison of the pressure field between the ground truth (upper row) and the AOT-nudging reconstruction (lower row). Columns from left to right correspond to $t = 0.001$, 0.2, 0.3, and 0.4 s.

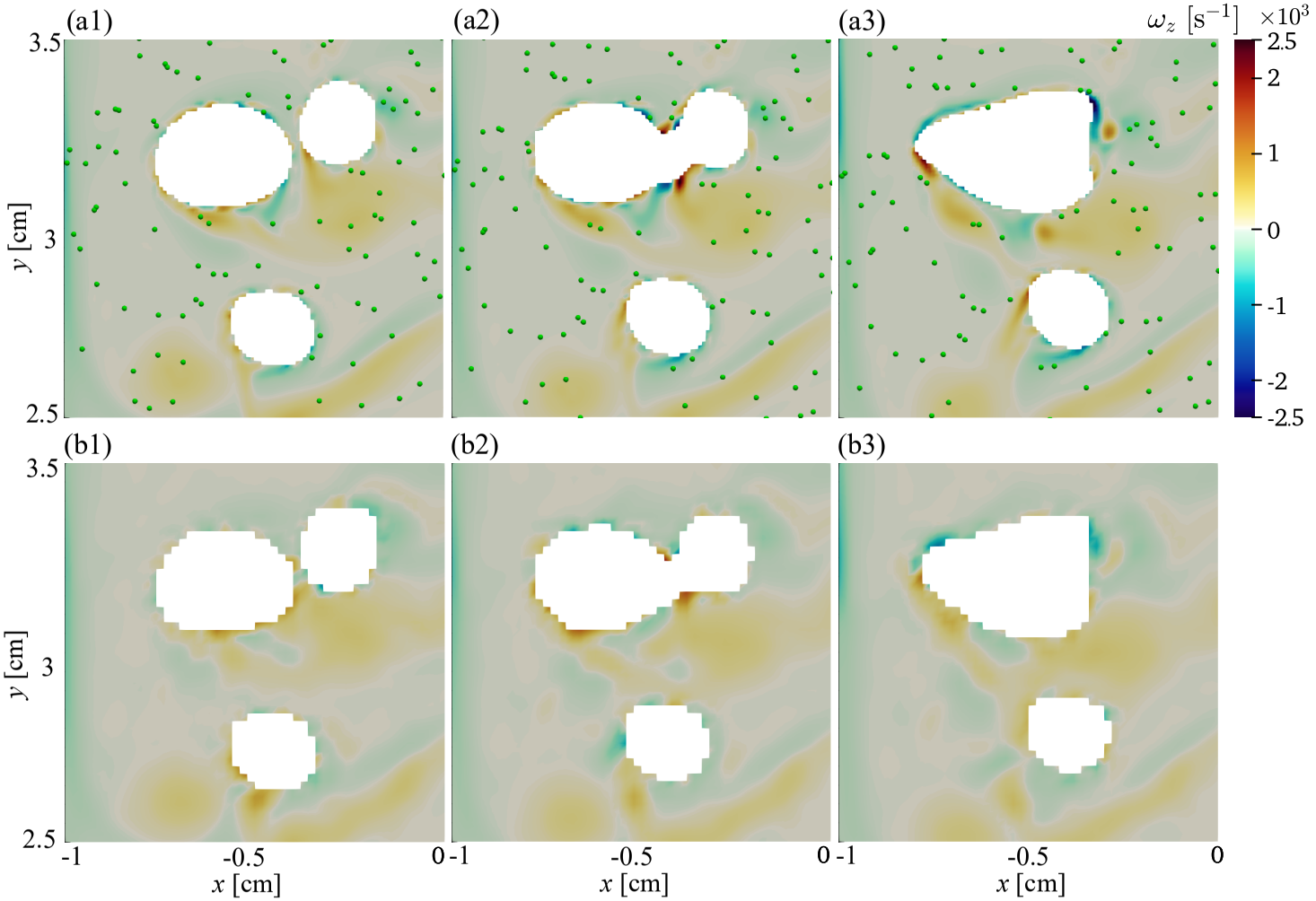


Figure 4.9: Zoomed comparison of the vorticity ω_z between the ground truth and the AOT-nudging reconstruction near the bubble coalescence region. The ground truth is shown in the upper row, and the AOT-nudging reconstruction in the bottom row. Columns from left to right correspond to $t = 0.275$, 0.280, and 0.285 s. In the upper row, the tracer-particle positions used to generate the liquid-phase velocity observations are also overlaid.

In summary, the AOT-nudging reconstruction improves the recovery of the bubble motion and liquid-phase flow relative to the baseline simulation. It reproduces the bubble trajectories, interface evolution, velocities, velocity gradients, pressure, and vortical structure of the ground truth despite a coarse mesh, large time steps, and inaccurate initial conditions, as well as sparse observations. In particular, the reconstruction does not require the initial velocity and volume-fraction fields to exactly match the observations in the first frame. The AOT-nudging terms can progressively correct the initial discrepancies as observations are assimilated. The robustness of the reconstruction to noisy synthetic observations is examined in Chap. 5.

4.3.4 Parameter sensitivity analysis

This section examines the sensitivity of AOT-nudging performance to five parameters: (1) the velocity nudging strength K_{vel}, (2) the volume-fraction nudging strength K_{vol}, (3) the tracer seeding density n_{pnt}, (4) the observation frequency f_{obs}, and (5) the mesh spacing Δx. The objective is to identify parameter trends and ranges that yield accurate reconstruction while maintaining numerical stability. The sensitivity is assessed using the time histories of the relative volume-fraction error $\mathcal{E}^{(\alpha)}_{L^2_{\mathrm{rel}}}(t)$ and the relative velocity error $\mathcal{E}^{(u)}_{L^2_{\mathrm{rel}}}(t)$. The reference values $|\boldsymbol{u}|_{\mathrm{ref}} \approx 0.5\ \mathrm{m\,s^{-1}}$ and $\alpha_{\mathrm{ref}} = 1$ are used to normalize the velocity and volume-fraction errors, respectively.

A One-Factor-At-A-Time (OFAT) analysis is performed: each parameter is varied independently, while the remaining parameters are fixed at their baseline values. The parameter settings are summarized in Tab. 4.1.

Table 4.1: Parameters varied in the sensitivity analysis and their baseline values.

Parameter	Baseline	Variation	Unit
K_{vel}	100	1, 5, ..., 5000, 10000	–
K_{vol}	100	1, 5, ..., 500, 1000	–
n_{pnt}	1	0.125, 0.25, 0.5, 1, 2	$\mathrm{mm^{-2}}$
f_{obs}	10	1.25, 2.5, 5, 10, 20	kHz
Δx	0.2	0.4, 0.267, 0.2, 0.133, 0.1	mm

Figure 4.10 shows the sensitivity of reconstruction to the velocity nudging strength K_{vel}, which varies from 1 to 10,000. As K_{vel} increases from small to moderate values, the velocity error decreases. In addition, the volume-fraction error also becomes smaller than

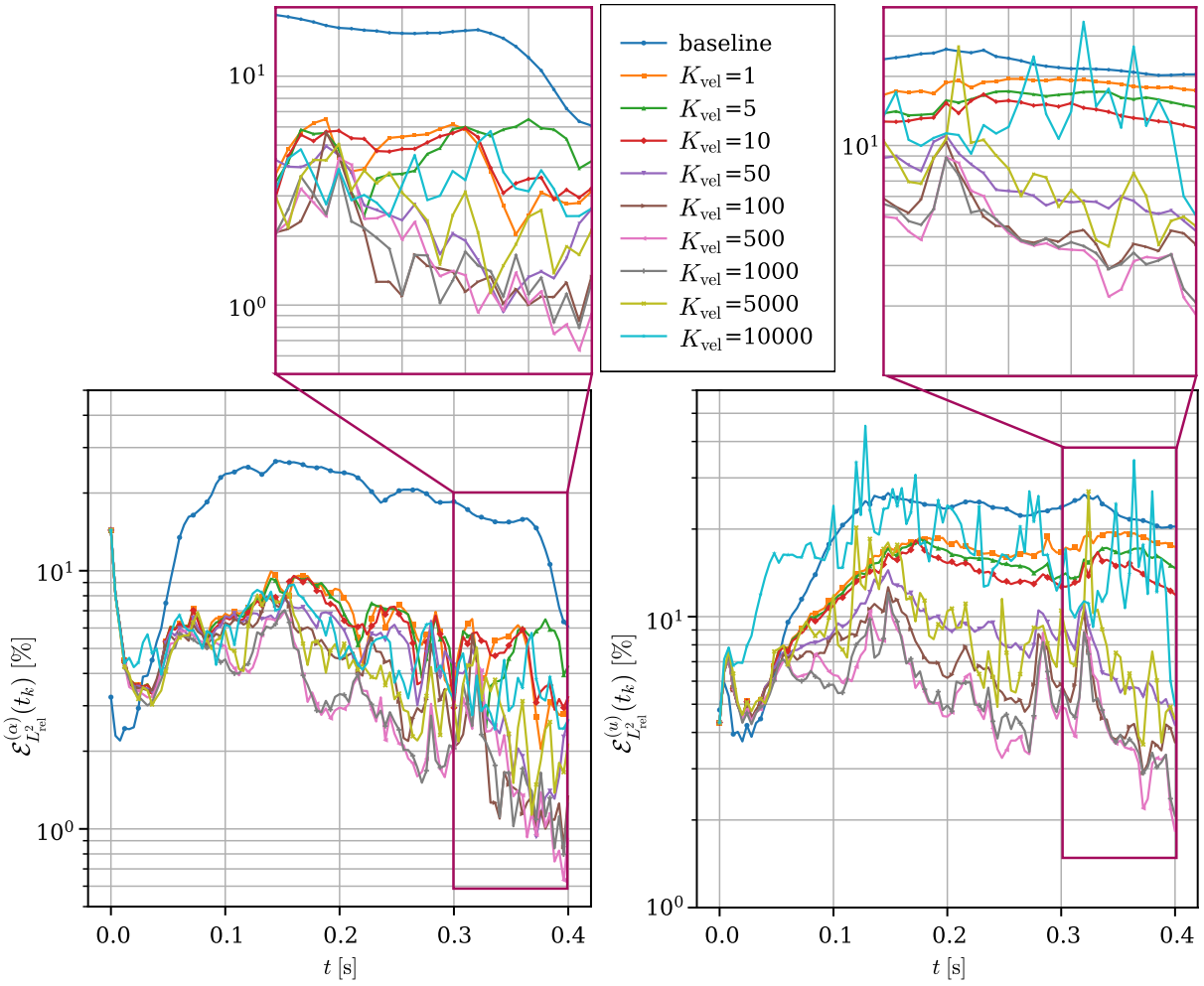


Figure 4.10: Time histories of the reconstruction errors for different values of the velocity nudging strength K_{vel}. The left panel shows the volume-fraction error $\mathcal{E}^{(\alpha)}_{L^2_{\mathrm{rel}}}(t)$, and the right panel shows the velocity error $\mathcal{E}^{(u)}_{L^2_{\mathrm{rel}}}(t)$. The baseline simulation is included for comparison. Insets enlarge the later-time region to highlight the differences among cases.

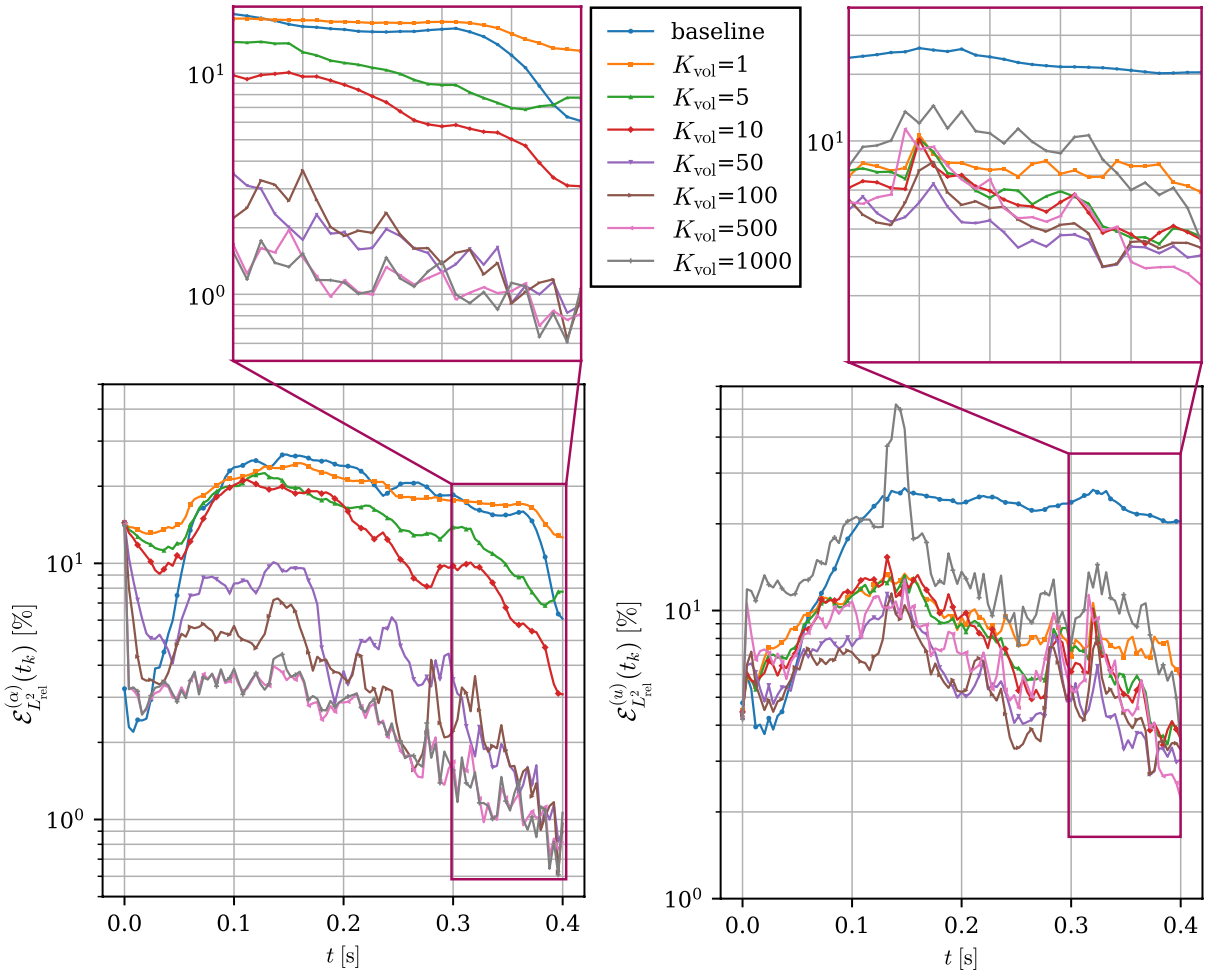


Figure 4.11: Time histories of the reconstruction errors for different values of the volume-fraction nudging strength K_{vol}. The left panel shows the volume-fraction error $\mathcal{E}^{(\alpha)}_{L^2_{\mathrm{rel}}}(t)$, and the right panel shows the velocity error $\mathcal{E}^{(u)}_{L^2_{\mathrm{rel}}}(t)$. The baseline simulation is included for comparison. Insets enlarge the later-time region to highlight the differences among cases.

that in the baseline simulation. However, excessively large values such as $K_{\mathrm{vel}} = 10,000$ produce stronger fluctuations in the bubble interfaces and larger velocity errors than those in moderate-strength cases. For cases that have strengths larger than $K_{\mathrm{vel}} = 10,000$, the reconstruction fails (not shown in the figures). This behavior indicates that a moderate-to-large value of K_{vel} improves the liquid-phase flow correction and benefits the volume

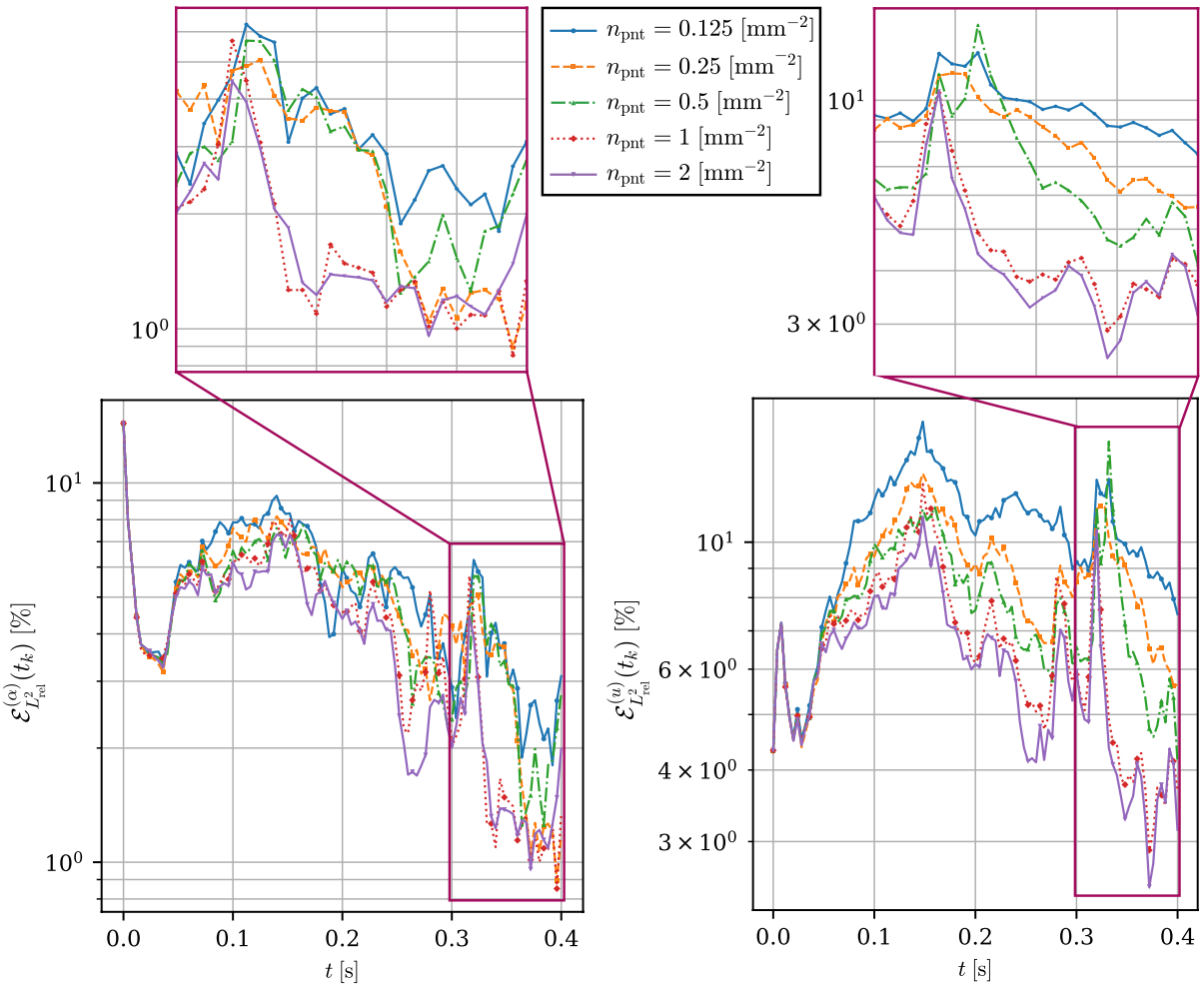


Figure 4.12: Time histories of the reconstruction errors for different tracer seeding densities n_{pnt} [mm^{-2}]. The left panel shows the relative volume-fraction error $\mathcal{E}^{(\alpha)}_{L^2_{\mathrm{rel}}}(t)$, and the right panel shows the relative velocity error $\mathcal{E}^{(u)}_{L^2_{\mathrm{rel}}}(t)$. The insets enlarge the later-time region to highlight the effect of tracer seeding density on the reconstruction accuracy.

fraction reconstruction, but an overly large value reduces numerical stability.

Figure 4.11 shows the sensitivity of the reconstruction to the volume-fraction nudging strength K_{vol}, varied from 1 to 1000. In general, increasing K_{vol} from small to moderate values reduces both the volume-fraction and velocity errors relative to the baseline case, indicating that interface correction contributes to the overall reconstruction performance.

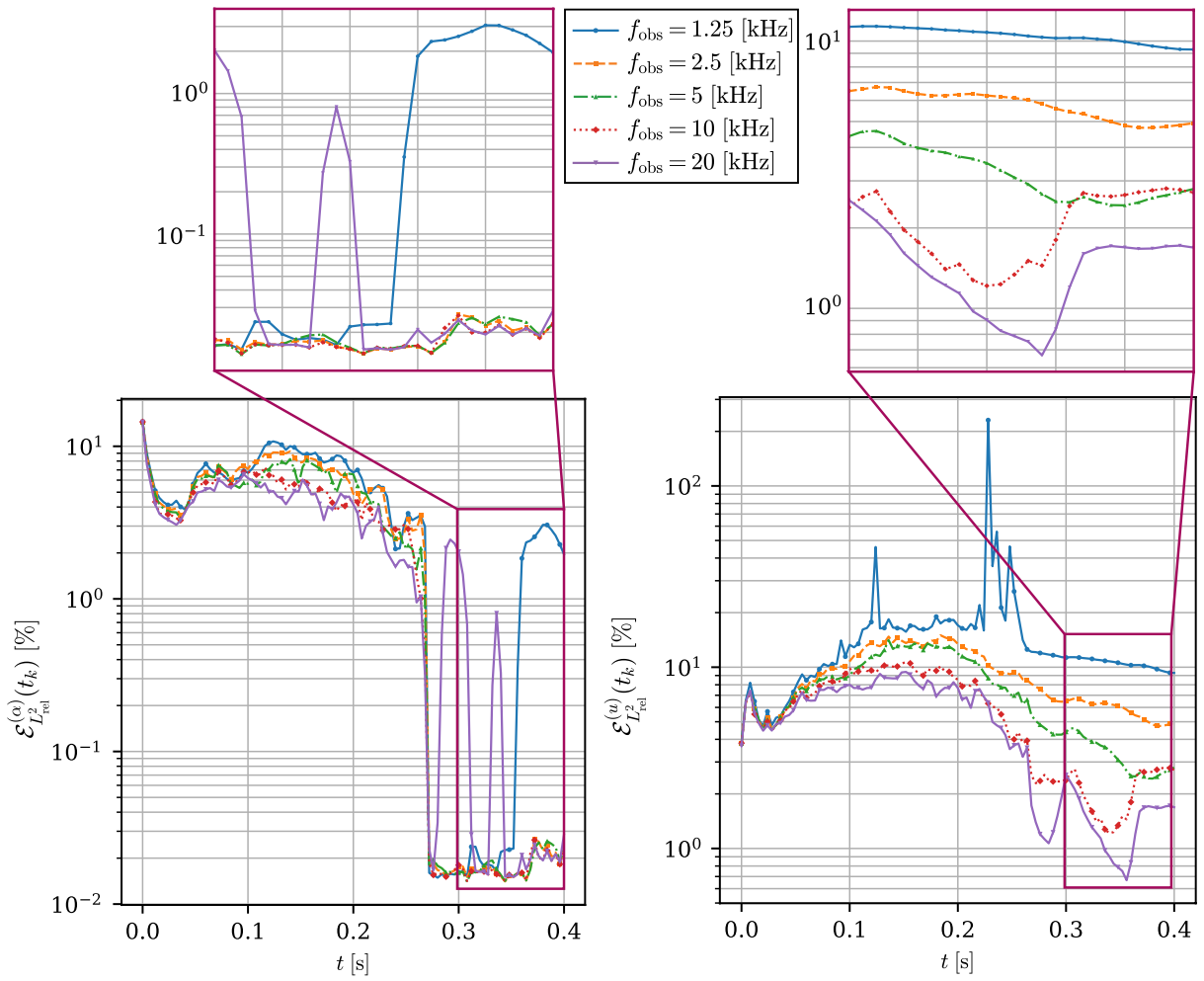


Figure 4.13: Time histories of the reconstruction errors for different observation frequencies f_{obs} [kHz]. The left panel shows the relative volume-fraction error $\mathcal{E}^{(\alpha)}_{L^2_{\mathrm{rel}}}(t)$, and the right panel shows the relative velocity error $\mathcal{E}^{(u)}_{L^2_{\mathrm{rel}}}(t)$. The insets enlarge the later-time region to highlight the effect of observation frequency on the reconstruction accuracy.

This coupled response is expected because the volume-fraction field directly affects the momentum equation through the local density, viscosity, and surface-tension terms (see (4.6)). Among the tested cases, moderate-to-large values such as $K_{\mathrm{vol}} = 50$, 100, and 500 provide low errors in both fields while maintaining stable behavior. However, the largest value, $K_{\mathrm{vol}} = 1000$, produces a spike in the velocity error and exhibits numerical instability.

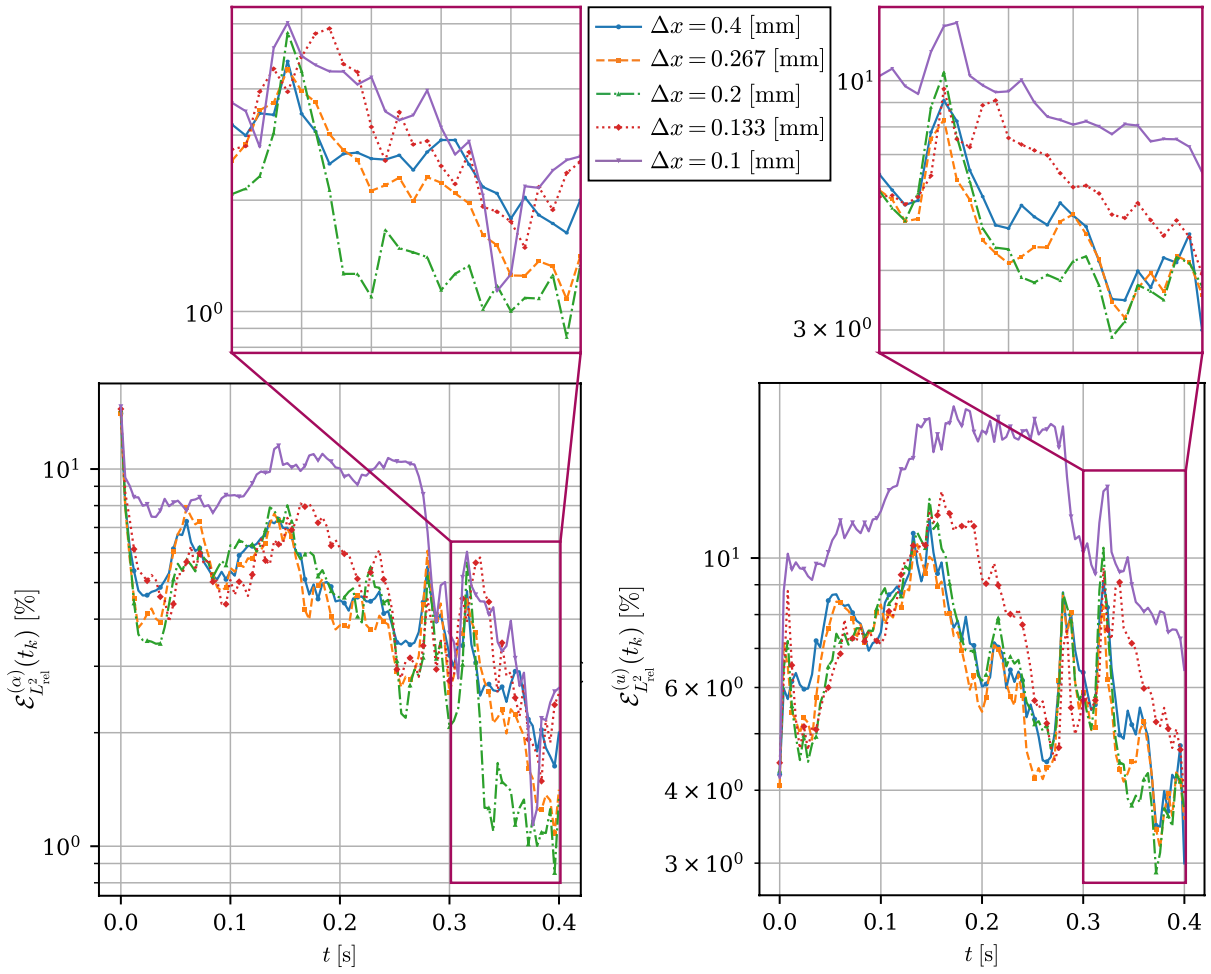


Figure 4.14: Time histories of the reconstruction errors for different mesh spacings Δx [mm]. The left panel shows the relative volume-fraction error $\mathcal{E}^{(\alpha)}_{L^2_{\mathrm{rel}}}(t)$, and the right panel shows the relative velocity error $\mathcal{E}^{(u)}_{L^2_{\mathrm{rel}}}(t)$. The insets enlarge the later-time region to highlight the effect of mesh spacing on the reconstruction accuracy.

Thus, increasing K_{vol} is beneficial up to a certain threshold, whereas excessively strong volume-fraction nudging can impose the correction too aggressively and amplify numerical instability.

The trends in Figs. 4.10 and 4.11 are consistent with the AOT-nudging literature (e.g., [292, 322]), which shows that the nudging parameter must be sufficiently large to achieve ef-

fective reconstruction. However, an excessively large nudging strength can introduce overly aggressive corrections, leading to instability. Physically, K_{vel} and K_{vol} define characteristic relaxation rates, with corresponding correction time scales $1/K_{\mathrm{vel}}$ and $1/K_{\mathrm{vol}}$. These time scales can be compared with the observation time interval and the characteristic flow time scales, such as bubble-rise or capillary time scales. If the nudging time scale is too long, the observations are incorporated too slowly and the reconstruction converges weakly. If it is too short, the correction becomes overly aggressive and may introduce numerical stiffness, overshoot, or conflict with the observations. From a practical standpoint, K_{vel} and K_{vol} should be selected as large as possible while remaining below the threshold at which unstable behavior emerges.

Figure 4.12 shows the effect of the tracer seeding density n_{pnt} on the reconstruction. The tested values are 0.125, 0.25, 0.50, 1.00, and 2.00 mm^{-2}. Overall, increasing n_{pnt} reduces the reconstruction errors, with a more pronounced improvement in the velocity field than in the volume-fraction field. In particular, the cases with $n_{\mathrm{pnt}} = 1.00$ and 2.00 mm^{-2} produce noticeably lower velocity errors throughout the assimilation window, whereas the volume-fraction error changes only moderately.

This trend is expected because the tracers provide direct observations of the liquid-phase velocity. A higher seeding density improves the spatial coverage of the liquid region, reduces interpolation gaps between observation locations, and strengthens the local correction applied to the momentum equation. By contrast, the volume-fraction field benefits from the tracer observations only indirectly through its coupling with the velocity field. Consequently, further increases in n_{pnt} yield diminishing improvements in the volume-fraction reconstruction.

Figure 4.13 shows the effect of the observation frequency f_{obs}, varied from 1.25 to 20 kHz. The results show a strong sensitivity of both error measures to this parameter. The lowest frequency, $f_{\mathrm{obs}} = 1.25$ kHz, produces the largest errors. As f_{obs} increases from 2.5 to 20 kHz, both errors decrease monotonically. These results show that frequent nudging limits the growth of reconstruction errors between consecutive updates. When the observation interval is large, the nonlinear flow evolution amplifies the mismatch before the next correction is applied.

Figure 4.14 shows the sensitivity of the reconstruction to the mesh spacing Δx, varied from 0.4 to 0.1 mm. The reconstruction quality is not uniform across the tested meshes. The coarsest and finest meshes, $\Delta x = 0.4$ and 0.1 mm, produce larger errors than the intermediate meshes, whereas $\Delta x = 0.267$ and 0.2 mm provide the best overall reconstruction performance. This non-monotonic trend shows that simply decreasing the mesh spacing does not necessarily improve the AOT-nudging reconstruction.

This non-monotonic behavior can be interpreted in terms of the compatibility between the mesh spacing and observation frequency. A coarse mesh, such as $\Delta x = 0.4\,\mathrm{mm}$, under-resolves the bubble interface, deformation, and wake structures. Conversely, reducing Δx while keeping the observation frequency fixed increases the observation Courant number,

$$\mathrm{Co}_{\mathrm{obs}} = \frac{|\boldsymbol{u}|_{\max}\Delta t_{\mathrm{obs}}}{\Delta x} = \frac{|\boldsymbol{u}|_{\max}}{f_{\mathrm{obs}}\Delta x}.$$

$\mathrm{Co}_{\mathrm{obs}}$ is analogous to the Courant number used by MULES, which measures the interface displacement between consecutive updates. A conservative limit of $\mathrm{Co}_{\mathrm{obs}}^{\max} = 0.5$, motivated by the accurate explicit MULES, is used here [358–360]. The corresponding compatibility condition is

$$\Delta x \geq \frac{|\boldsymbol{u}|_{\max}}{\mathrm{Co}_{\mathrm{obs}}^{\max} f_{\mathrm{obs}}}, \qquad \mathrm{Co}_{\mathrm{obs}}^{\max} = 0.5. \tag{4.14}$$

For $\Delta x = 0.2\,\mathrm{mm}$, $0.133\,\mathrm{mm}$, and $0.1\,\mathrm{mm}$, using $|\boldsymbol{u}|_{\max} = 0.6\,\mathrm{m\,s^{-1}}$ and $f_{\mathrm{obs}} = 10\,\mathrm{kHz}$, the corresponding observation Courant numbers are

$$\mathrm{Co}_{\mathrm{obs}} = 0.30,\ 0.45,\ 0.60,$$

respectively. The first two meshes satisfy the adopted compatibility condition, whereas the finest mesh exceeds the limit, leading to inaccurate reconstruction.

A scale analysis further clarifies the effects of mesh spacing and tracer density shown in Figs. 4.12 and 4.14. Using flow past a circular cylinder as an order-of-magnitude analogy for the bubble wake, the present case with $\mathrm{Re} \approx 1.25 \times 10^3$ is assigned a Strouhal number $\mathrm{Sr} \approx 0.25$ [361]. For $D_{\mathrm{b}} = 2.5\,\mathrm{mm}$ and $|\boldsymbol{u}|_{\mathrm{ref}} = 0.5\,\mathrm{m\,s^{-1}}$, the vortex-shedding frequency and streamwise vortex spacing are estimated as

$$f_{\mathrm{v}} = \frac{\mathrm{Sr}\,|\boldsymbol{u}|_{\mathrm{ref}}}{D_{\mathrm{b}}} = 50\,\mathrm{Hz}, \qquad \lambda_{\mathrm{v}} = \frac{|\boldsymbol{u}|_{\mathrm{ref}}}{f_{\mathrm{v}}} = \frac{D_{\mathrm{b}}}{\mathrm{Sr}} = 10\,\mathrm{mm}.$$

For a von Kármán vortex street, $h_{\mathrm{v}}/\lambda_{\mathrm{v}} \approx 0.28$ [362], giving a transverse vortex-row spacing of $h_{\mathrm{v}} \approx 2.8\,\mathrm{mm}$. Thus, the relevant wake scales are $O(1)$ mm in the transverse direction and $O(10)$ mm in the streamwise direction.

The ground-truth mesh spacing, $\Delta x = 0.1\,\mathrm{mm}$, provides approximately 25, 28, and 100 cells across D_{b}, h_{v}, and λ_{v}, respectively. The reconstruction mesh spacings $\Delta x = 0.267\,\mathrm{mm}$, $0.200\,\mathrm{mm}$, $0.133\,\mathrm{mm}$, and $0.100\,\mathrm{mm}$ provide approximately 9.4, 12.5, 18.8, and 25 cells across the bubble diameter, respectively. The two coarser meshes contain fewer than 20 cells across the bubble diameter and under-resolve the interface deformation and wake

structures. By contrast, the two finer meshes approach or exceed 20 cells per diameter and provide sufficient numerical resolution of these features. This is consistent with interface-resolved bubble simulations, which commonly employ at least 20 cells per diameter to capture the principal bubble and wake dynamics [363–368].

For a 2D random tracer distribution, the characteristic inter-particle spacing is estimated from the tracer density as

$$\ell_{\mathrm{p}} \approx n_{\mathrm{pnt}}^{-1/2}.$$

For $n_{\mathrm{pnt}} = 0.125$, 0.25, 0.50, 1.00, and 2.00 mm^{-2}, the corresponding characteristic spacings are $\ell_{\mathrm{p}} \approx 2.83\,\mathrm{mm}$, $2.00\,\mathrm{mm}$, $1.41\,\mathrm{mm}$, $1.00\,\mathrm{mm}$, and $0.71\,\mathrm{mm}$, respectively. For a bubble-scale structure with $D_{\mathrm{b}} = 2.5\,\mathrm{mm}$, these values correspond to approximately 0.9, 1.3, 1.8, 2.5, and 3.5 tracer samples across the structure. Based on Fig. 4.12, 2.5 samples across a bubble-scale structure appear to provide a practical threshold for constraining the wake dynamics. Below this threshold, the velocity error increases noticeably, whereas increasing the sampling from 2.5 to 3.5 points produces only limited additional improvement. This observation is consistent with the criterion based on the Nyquist sampling theorem, which requires at least two samples across the smallest wavelength to be resolved [369]. Because the tracer locations are randomly distributed and interpolation is required, slightly more than two samples are needed in practice.

In summary, the parameter study shows that the AOT-nudging reconstruction is accurate and stable when the parameters are chosen within intermediate ranges. Moderate-to-large values of K_{vel} and K_{vol} improve the reconstruction, whereas excessively large strengths can introduce numerical oscillations and reduce stability. Increasing the tracer seeding density improves velocity reconstruction and indirectly benefits the volume-fraction field. Increasing the observation frequency is almost always beneficial because it limits error growth between consecutive updates. This suggests that time-resolved experiments with high tracer seeding density have strong potential to further improve DA performance. The present tests also show that useful reconstruction is still possible with relatively low spatial and temporal observation resolution. Lastly, the mesh spacing is governed by both numerical and physical considerations. The mesh resolution should be selected according to the observation frequency and the Courant number. For the volume-fraction field, the mesh spacing must be sufficiently small to resolve the bubble diameter, interface curvature, and deformation. For the velocity field, it must also resolve the wake and vortical length scales and the transverse vortex spacing.

4.3.5 Experimental validation: setup

The proposed framework is examined using the experimental data from Chap. 3. The experimental data are incorporated into the solver in the same way as in the synthetic validation. The observations are provided in two channels: one liquid-phase velocity observation channel from PIV or LPT, and one volume-fraction channel from the bubble images (see Sect. 3.2).

The geometry of the computational setup of the AOT-nudging reconstruction is shown in Fig. 4.15. The orange square denotes the experimental observation window. It corresponds to the 40 mm×40 mm field of view of the high-speed camera. This observed region is embedded in a larger computational domain with buffer zones. The buffer zones provide a transition region between the observation window and the numerical boundaries. With these zones, the flow can evolve without being overly constrained by the outer boundaries. Above the observed water column, a headspace layer is included together with a free surface and an open atmospheric top boundary.

The reconstruction is performed on a uniform unstructured mesh. The computational domain covers -30 mm $\leq x \leq 30$ mm and -10 mm $\leq y \leq 60$ mm, with a thickness of 2 mm. The domain is discretized using $N_x = 360$, $N_y = 420$, and $N_z = 1$ cells, giving a uniform in-plane cell size of $\Delta x = \Delta y \approx 1.67 \times 10^{-4}$ m. A uniform mesh grading is used in all directions. The front and back planes are treated as `empty` boundaries, so the reconstruction is carried out in the $x - y$ plane. The left, right, and bottom boundaries are slip walls.

The reconstruction is carried out over $0 \leq t \leq 0.25$ s. The camera frame rate is 2,000 Hz, and the raw image sequence contains 501 frames. The observational data are interpolated in time before assimilation (see Sect. 3.2), and the effective observation frequency becomes 32,000 Hz, corresponding to 8,001 frames over the same time interval.

The same fluid properties and operating conditions described in Chap. 3 are used in the reconstruction. For a representative experimental bubble diameter $D_\mathrm{b} = 3$ mm and the reference liquid-phase velocity $|\boldsymbol{u}|_\mathrm{ref} = 0.5\,\mathrm{m\,s^{-1}}$, the non-dimensional numbers defined in (4.12) become

$$\mathrm{Re} \approx 1.49 \times 10^3, \qquad \mathrm{We} \approx 10.4, \qquad \mathrm{Ca} \approx 6.96 \times 10^{-3},$$
$$\mathrm{Eo} \approx 1.22, \qquad \mathrm{Mo} \approx 2.65 \times 10^{-11}.$$

These values indicate that the dynamics of the rising 2D bubbles in the experiment are similar to those in the synthetic data validation (see Sect. 4.3.2).

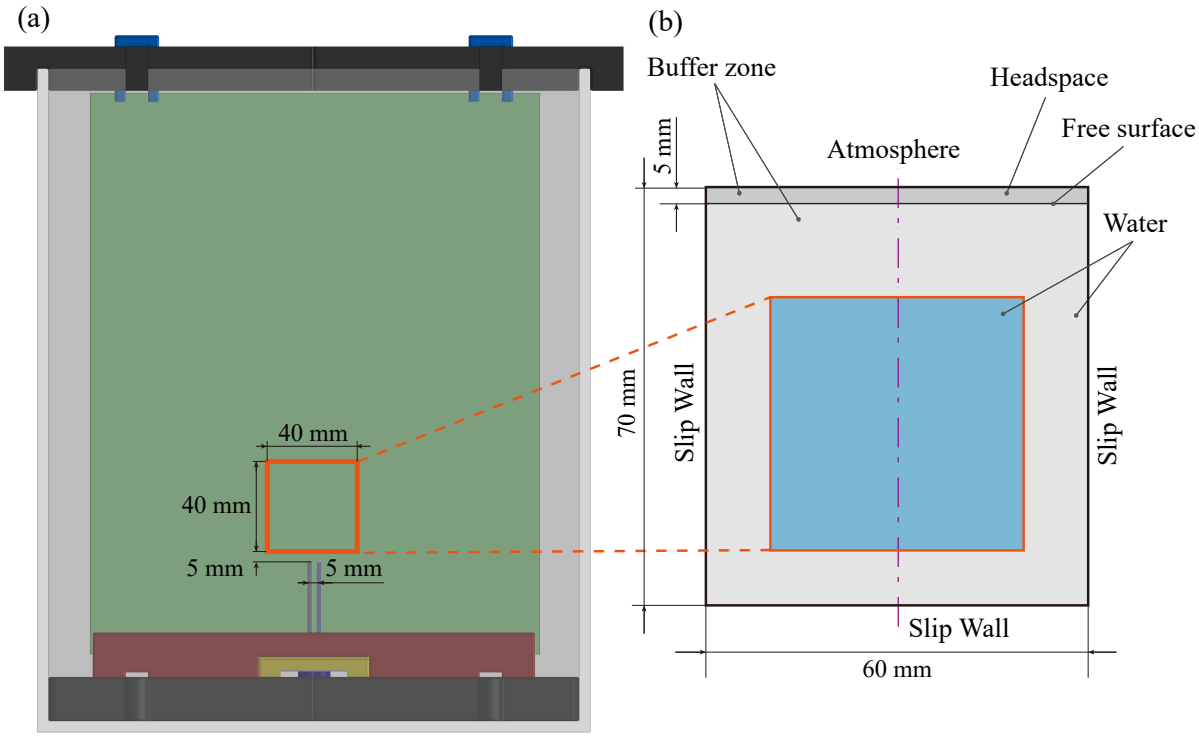


Figure 4.15: Experimental measurement window and computational setup for the AOT-nudging reconstruction. (a) Front view of the quasi-2D water channel, showing the 40 mm×40 mm measurement window recorded by the camera. (b) Computational domain and boundary conditions used in the reconstruction. The orange square denotes the observation window corresponding to the experimental field of view, and the surrounding region is the buffer zone. The top boundary is open to the atmosphere, with a headspace layer above the free surface.

It should be noted that the experimental dataset is 2D in terms of the measured bubble interfaces and velocity fields, while the underlying flow is still influenced by 3D wall effects from the no-slip front and back walls. Because these depthwise effects are not explicitly resolved, the reconstruction should be interpreted as a 2D flow constrained by observations that contain 3D wall influences. This mismatch introduces model error into the reconstruction. Therefore, the AOT-nudging algorithm compensates for the resulting model error. A full 3D simulation with no-slip front and back walls would reduce this model mismatch and the required nudging strength, potentially leading to improved reconstruction quality.

4.3.6 Experimental validation: results

Figures 4.16 – 4.19 show the experimental validation results. Figure 4.16 focuses on the reconstructed volume-fraction field near the coalescence event. It compares the pre-processed camera images with the AOT-nudging reconstruction at $t = 0.1690$, 0.1695, and 0.1700 s. These times span the short interval immediately before and after coalescence. At $t = 0.1690$ s, the two bubbles are separated by a visible gap (see Fig. 4.16 (a1)). As the bubbles approach each other, the gap becomes thinner and forms a narrow liquid film between the two interfaces. By $t = 0.1700$ s, the film has ruptured, the two interfaces have connected, and the bubble topology has changed to a merged bubble (see Fig. 4.16 (a3)). The reconstructed volume-fraction fields remain consistent with the measured bubble silhouettes throughout this process. At $t = 0.1695$ s, it is difficult to determine from the measured silhouettes whether coalescence has already occurred (see Fig. 4.16 (a2)). The reconstruction reflects this transitional state through a locally smeared volume-fraction field in the region between the two bubbles.

Figures 4.17 and 4.18 compare the velocity observations (upper rows) and the corresponding AOT-nudging reconstructions (lower rows) obtained from PIV and LPT data, respectively, at $t = 0.1690$, 0.1695, and 0.1700 s. The PIV data are smooth because each velocity vector is obtained through spatial correlation and implicit averaging over a finite interrogation window. In contrast, the LPT data exhibit stronger local velocity variations because they are derived from individual tracers. Consequently, LPT data retain high-speed vectors, especially near the coalescence and jet regions. In addition, some tracers appear dim in the wake of bubble A because of reduced image quality, preventing the LPT algorithm from resolving their trajectories. This results in missing tracer observations in the downstream region of bubble A. In contrast, PIV is less sensitive to this limitation, and removed vectors are supplemented by interpolation (see Sect. 3.3.1).

As shown in the lower rows of Figs. 4.17 and 4.18, despite the different spatial sampling characteristics of PIV and LPT, both reconstructions recover the dominant liquid-flow structures, including the central upward jet between bubbles A and C, the counter-rotating vortices on either side of the jet, and the S-shaped jet trapping bubble C, contributing to the oscillation induced by the leading bubble A. In the quasi-2D experiment, the liquid velocity varies across the gap because of the boundary layers along the acrylic sheets. Tracers near the walls move more slowly than those near the mid-plane, creating a strong depthwise velocity gradient that cannot be resolved by the planar measurement. Consequently, some measured vectors deviate from the in-plane velocity and appear as measurement errors or isolated spurious vectors. In PIV, such vectors are removed and refilled by interpolation, which produces a smoother velocity field but may smear localized velocity gradients. In

LPT, unreliable trajectories (e.g., short trajectories and trajectories associated with dim particles) are discarded, leading to even sparser observations in key regions, such as the wake of bubble A. By combining observations with the governing equations, AOT-nudging supplements the sparse or missing velocities and suppresses noisy or inconsistent velocities. The performance of the reconstruction under noisy observations is examined further in Chap. 5.

Figure 4.19 provides a zoomed comparison of the PIV- and LPT-based AOT-nudging reconstructions near the coalescence region. Although direct velocity observations are sparse or unavailable in this region at $t = 0.169375$ and 0.169625 s, both reconstructions recover a high-speed flow near the upper-left side of bubble A and within the thin liquid film between bubbles A and B. The former promotes rapid motion and deformation of the bubble tip, while the latter is consistent with liquid drainage from the inter-bubble region and the approaching coalescence event. These local high-speed flows generate high velocity gradients and shear stresses near bubble interfaces. When sufficiently intense, such stresses may damage live particles (e.g., microorganisms and cells [370, 371]). Furthermore, these localized flow features are mostly inferred by the AOT-nudging from the available observations and governing equations. In addition, the reconstruction provides spatiotemporally refined velocity fields and interfaces beyond the measurements since $t = 0.169375$ and 0.169625 s are not available in the image sequence.

In Fig. 4.19, the recovery of these local jets may be attributed mainly to two factors. First, the accurate volume-fraction observations constrain the instantaneous bubble geometry and interface motion. Second, the AOT-nudging algorithm uses the available observations to constrain the resolved large-scale flow structures, while the governing equations reconstruct unresolved or unobserved features at smaller spatial and temporal scales.

As shown in Fig. 4.19, over the whole time window, the asymmetric velocity distribution near the liquid film between bubbles A and B emerges. This can be interpreted as the combined effect of bubble movement and surface-tension-driven interface motion. On the left side of the film, these contributions act in aligned directions and produce a high-speed flow. On the right side, they act in opposing directions and partially cancel, resulting in lower velocities. Because the PIV and LPT data differ within the thin liquid film, the corresponding reconstructed velocity fields also exhibit differences.

At the coalescence instant $t = 0.1695$ s, the PIV- and LPT-based velocity observations in Fig. 4.19 lead to slightly different velocity reconstructions. The LPT-based reconstruction predicts a high-speed flow on the right side of bubble B, which is absent from the PIV-based result. In PIV, velocity observations are available in this region and constrain the reconstructed flow, whereas the LPT observations are missing, allowing AOT-nudging

to infer the velocity field. The different local velocity fields also produce distinct high-speed flows near bubble B. For PIV, the high-speed flow is near the lower part of bubble B and may promote its rotation, which is observed later in the video sequence. For LPT, the high-speed flow is near the liquid film, facilitating film drainage and coalescence. These local differences also lead to slight differences in the bubble outlines.

The reconstructed bubble outlines differ from the observations near coalescence at $t = 0.1695$ s, as indicated by the blue and pink contours in Figs. 4.17, 4.18, and 4.19 (a2) and (b2). Three factors may account for these differences. First, the instantaneous coalescence state is difficult to determine from the image at this time, unlike the separated pre-coalescence state at $t = 0.1690$ s and the post-coalescence state at $t = 0.1700$ s. Because the instantaneous interface state is ambiguous in the image, the reconstructed interface is constrained by its temporal evolution, velocity observations, and governing equations. Second, the observed bubble outlines are manually annotated using CVAT and consequently contain uncertainty in their position and smoothness. A spatially irregular contour or one that is temporally inconsistent with adjacent frames may introduce an instantaneous shape that cannot be fully corrected within a short nudging interval. The reconstructed interface therefore remains influenced by its preceding evolution and does not follow an isolated observed contour exactly. Lastly, the interface evolution is jointly constrained by the volume-fraction and velocity observations. The PIV- and LPT-based cases have different local velocity fields, resulting in different interface shapes. These results suggest that AOT-nudging does not simply reproduce the observed contours but reconstructs a spatially smooth and temporally consistent evolution of the bubble interface.

In summary, the experimental validation demonstrated that the proposed AOT-nudging method can utilize synchronized bubble silhouette and liquid-phase velocity observations from real bubbly-flow experiments for reconstruction. At the measured instants, the reconstructed bubble interfaces and liquid-velocity fields remain consistent with the camera images and the PIV or LPT data. The method also supplements sparse velocities and corrects inconsistent velocities beyond observed regions and times, i.e., achieving spatiotemporal super-resolution with smoothing. During the rapid coalescence event, it reconstructs smooth and physically consistent intermediate interface and flow states that are not directly available from the images. Although the PIV- and LPT-based reconstructions exhibit local differences because of their distinct spatial resolutions and sampling characteristics, both recover the dominant flow features such as jet, wake, recirculation, thin-film flow, and bubble-topology evolution.

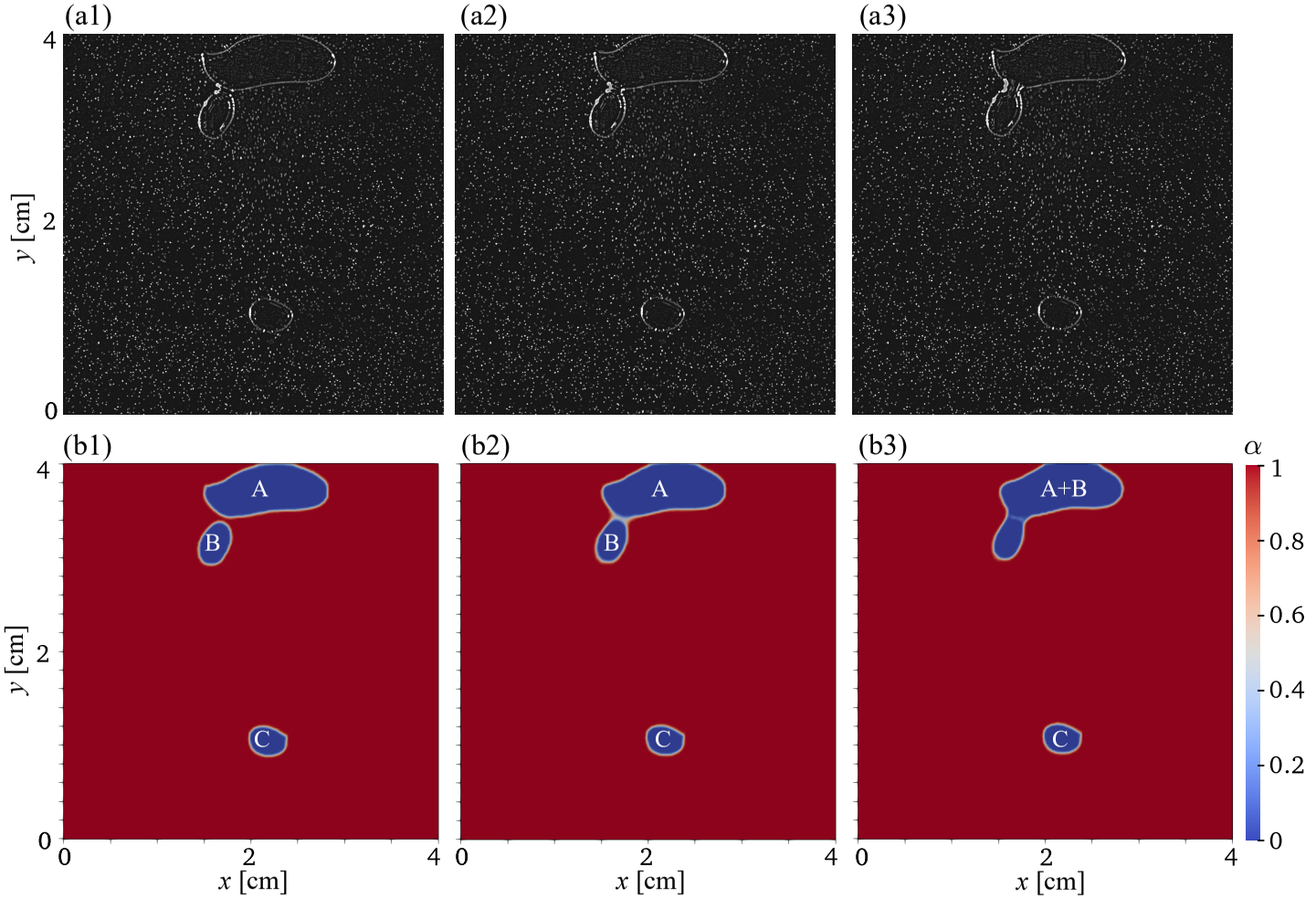


Figure 4.16: Bubble coalescence illustrated by pre-processed images and reconstructed volume-fraction fields. The upper row shows the pre-processed images used for image velocimetry at $t = 0.1690$, 0.1695, and 0.1700 s, from left to right. These three instants are immediately before and after the coalescence event. The lower row shows the corresponding volume-fraction fields reconstructed by AOT-nudging at the same three instants.

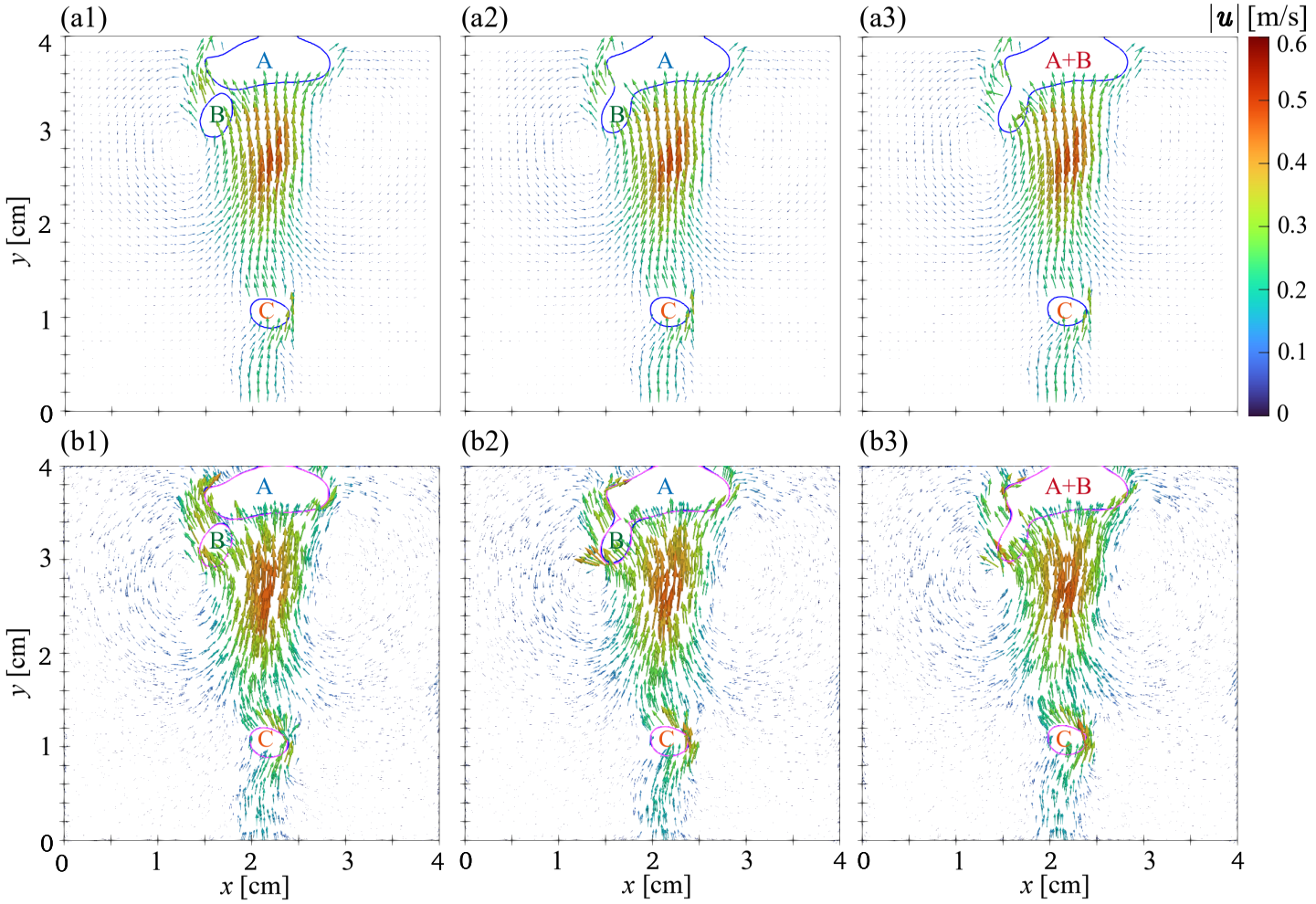


Figure 4.17: PIV observations and the corresponding AOT-nudging reconstruction near bubble coalescence. The upper row shows the PIV velocity fields at $t = 0.1690$, 0.1695, and 0.1700 s, from (a1) to (a3), while the lower row shows the corresponding reconstructed fields at the same instants. The vectors are colored by the velocity magnitude $|\boldsymbol{u}|$. The blue lines denote the observed bubble outlines, whereas the pink lines denote the reconstructed bubble interfaces extracted from the contour $\alpha = 0.5$.

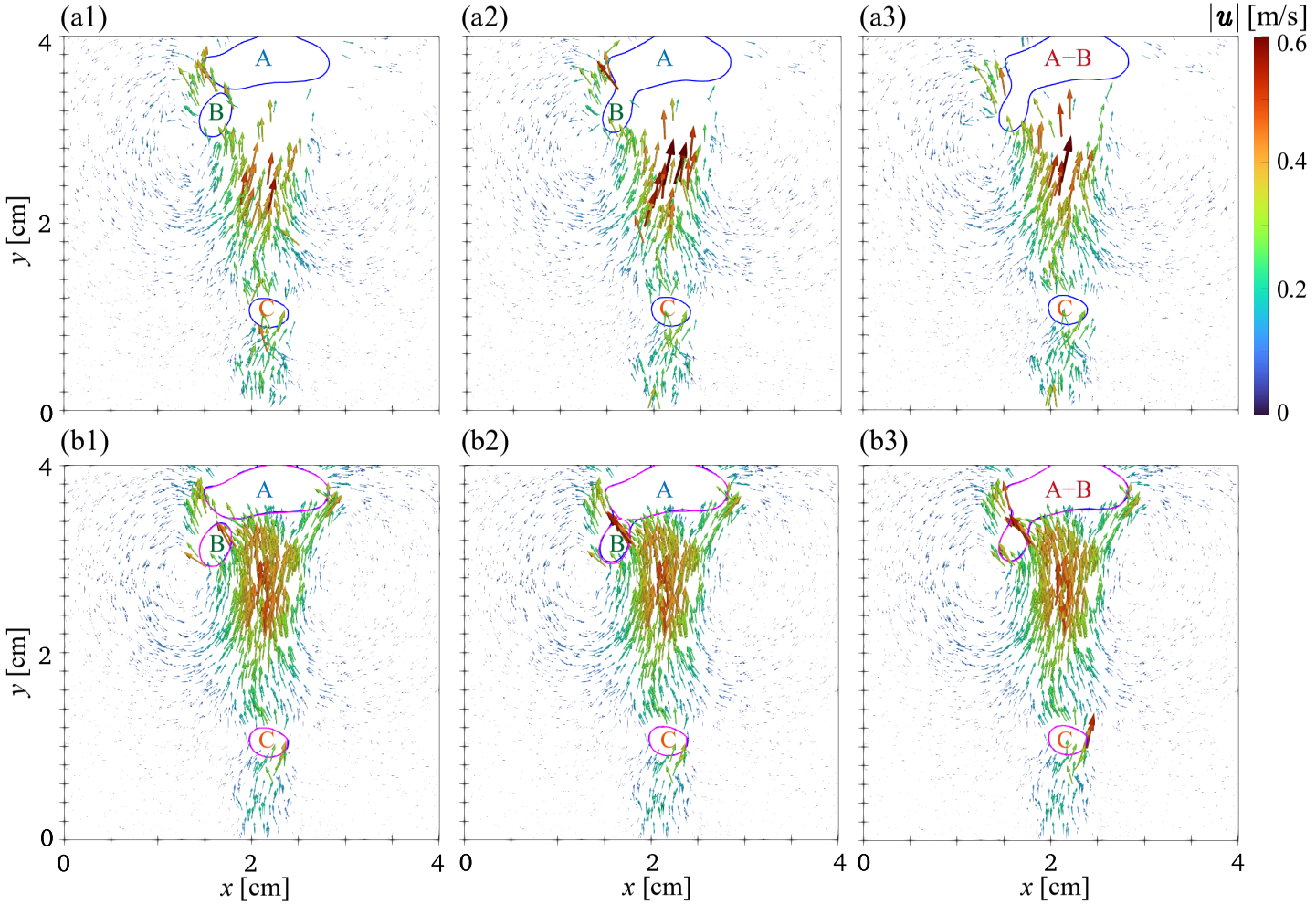


Figure 4.18: LPT observations and the corresponding AOT-nudging reconstruction near bubble coalescence. The upper row shows the LPT velocity fields at $t = 0.1690$, 0.1695, and 0.1700 s, from (a1) to (a3), while the lower row shows the corresponding reconstructed fields at the same instants. The vectors are colored by the velocity magnitude $|\boldsymbol{u}|$. The blue lines denote the observed bubble outlines, whereas the pink lines denote the reconstructed bubble interfaces extracted from the contour $\alpha = 0.5$.

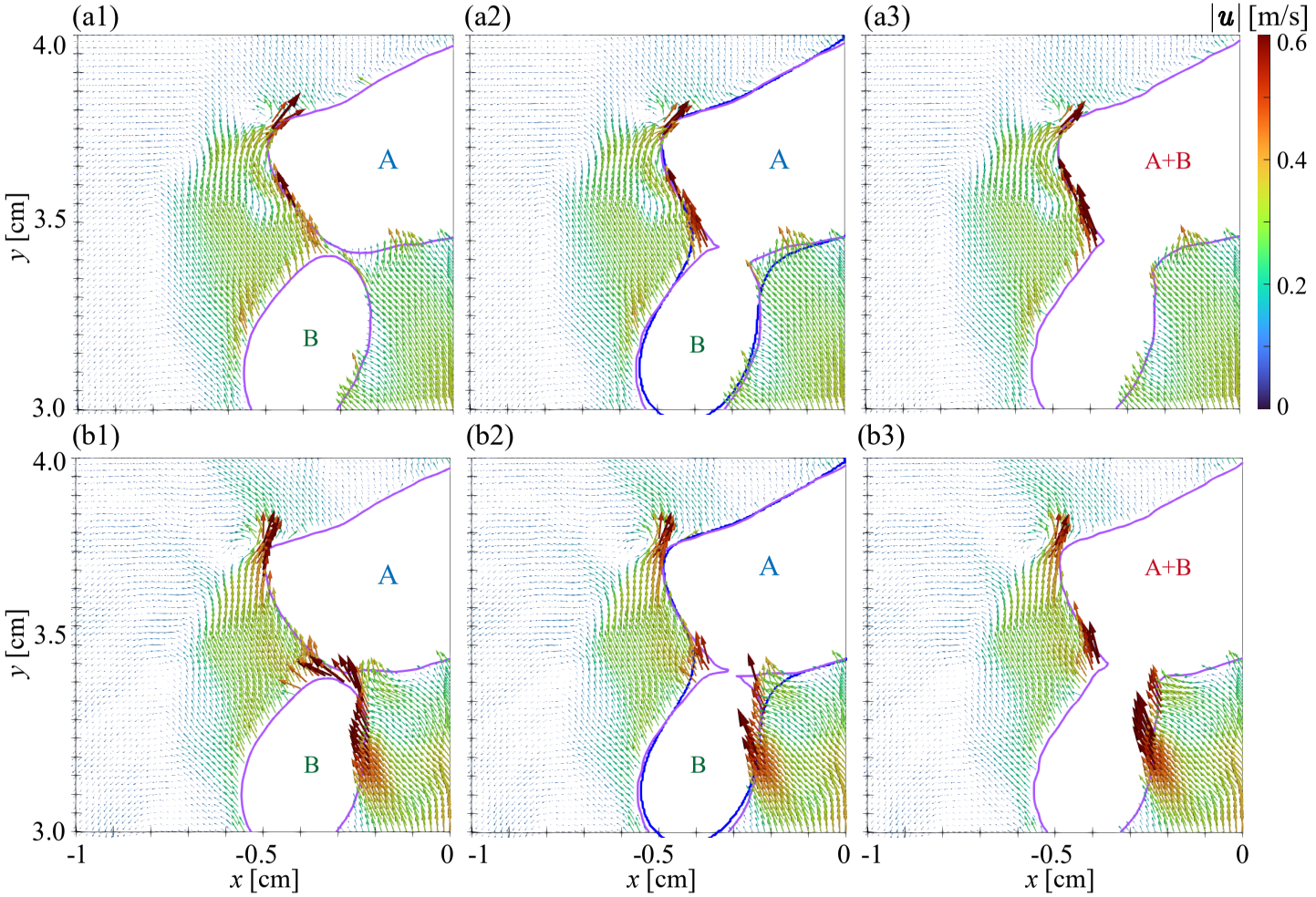


Figure 4.19: Zoomed comparison of the PIV- and LPT-based AOT-nudging velocity reconstructions near coalescence. The upper and lower rows correspond to PIV and LPT observations, respectively, at t = 0.169375, 0.169500, and 0.169625 s from left to right. The vectors are colored by $|\boldsymbol{u}|$. The blue lines show the observed bubble outlines, and the pink lines show the reconstructed $\alpha = 0.5$ contours. Observations are unavailable at the first and last instants; these intermediate states are reconstructed by AOT-nudging.

4.4 Conclusions

This chapter developed an AOT-nudging DA framework for reconstructing bubbly flows, addressing Obj. O2. The method was implemented in a VoF-based OpenFOAM solver by assimilating liquid-phase velocity observations through the momentum equation and bubble-silhouette observations through the transport of volume-fraction equation.

Validation based on synthetic data showed that the AOT-nudging reconstruction recovered the bubble trajectories, interface shapes, liquid-phase velocity, velocity gradients, pressure field, and vortical structures despite inaccurate initial conditions, a coarse mesh, and incomplete observations. Compared with the baseline simulation, it reduced errors in both bubble motion and liquid-phase kinematics. The parameter study showed that effective reconstruction requires moderate-to-strong nudging strengths, high tracer seeding density and observation frequency, and a mesh resolution that is compatible with nudging strength and observation frequency.

Experimental validation using bubble silhouettes, PIV, and LPT observations demonstrated that the framework can reconstruct realistic bubbly-flow dynamics. Both PIV- and LPT-based reconstructions recovered the jets, wakes, recirculation vortices, and bubble-topology changes during coalescence, while also providing physically consistent intermediate states that were not directly captured by the camera images.

In summary, the proposed framework combines sparse experimental observations with the governing equations or constraints (e.g., conservation of mass and momentum) to reconstruct dynamically consistent, spatiotemporal super-resolution/interpolation bubble and liquid-phase fields. These results provide the foundation for the uncertainty quantification and the three-phase flow extensions developed in the following chapters.

Chapter 5

Uncertainty Quantification

5.1 Introduction

Uncertainty Quantification (UQ) characterizes the level of confidence in a reconstructed field. For image-based velocimetry, many UQ models have been developed. In Particle Image Velocimetry (PIV), velocity uncertainty is estimated using *a priori* or *a posteriori* approaches [75]. This velocity uncertainty can also be propagated to derived quantities, such as vorticity and pressure. An *a priori* approach estimates uncertainty from theoretical models or calibration information. An *a posteriori* approach estimates the local and instantaneous uncertainty from the measured data. For PIV, *a posteriori* methods can be further classified into indirect and direct methods [75]. Indirect methods infer uncertainty from the uncertainty surface or from cross-correlation signal-to-noise metrics [372–375]. Direct methods estimate uncertainty from information extracted from the particle images or from the correlation plane [376–378]. Comparative studies show that direct methods are useful for estimating the local instantaneous uncertainty of individual velocity vectors, while indirect methods are suitable when empirical calibration information or systematic error is of interest [75].

UQ has also been developed for Lagrangian Particle Tracking (LPT). For example, in volumetric LPT, the uncertainty of reconstructed particle positions can be obtained by propagating uncertainty through the measurement chain [379]. This chain includes particle-image localization uncertainty, re-projection uncertainty, camera calibration uncertainty, and uncertainty propagation through the volumetric reconstruction process. The velocity uncertainty is then estimated from the reconstructed particle-position uncertainty. For time-resolved LPT, polynomial trajectory filtering can be combined with local confidence

intervals [380]. This approach provides uncertainty estimates for particle position, velocity, and acceleration along each trajectory.

For simultaneous bubbly-flow experiments, as discussed in Sect. 2.1.2, UQ is complicated by bubble interfaces and optical distortion. In gas–liquid systems, refraction, reflection, shadowing, and sampling effects caused by bubbles can introduce external uncertainty. These bubble-induced effects introduce additional uncertainty beyond the intrinsic uncertainty of PIV or LPT. For example, bubble-induced light distortion and sampling uncertainty were studied by Liu et al. [381]. Using ray-optics modeling and Monte Carlo synthetic PIV images, they showed that bubble-induced light distortion can degrade particle images and increase velocity uncertainty.

Some studies have addressed uncertainty in multiphase-flow simulations. In these studies, Bayesian and physics-informed UQ approaches have been widely applied [382–385]. These approaches estimate uncertainty in closure models, model parameters, or predicted flow quantities. Reported applications include bubbly-flow quantities such as void fraction, liquid-phase velocity, and gas-phase velocity.

In Data Assimilation (DA), UQ is treated differently depending on whether the method is stochastic or deterministic. In stochastic DA methods, uncertainty is part of the formulation. Examples include Kalman filters, particle filters, and Bayesian smoothers [97–100]. In these methods, the reconstructed state is accompanied by an uncertainty estimate. This estimate may be given by an analysis of covariance, an ensemble spread, or *a posteriori* probability distribution for the reconstructed quantities.

In deterministic DA methods, uncertainty is treated differently. For example, variational methods calculate *a posteriori* uncertainty from the Hessian of the cost function [97, 98], where the background and observation error covariance matrices are used to weight the cost function. For the AOT-nudging algorithm, feedback terms are added to the governing equations to drive the numerical solution toward the observations [292]. However, this deterministic feedback procedure does not directly provide a probability distribution, an ensemble spread, or a confidence interval for the reconstructed quantities. Therefore, a separate UQ framework is required to assess the reliability of AOT-nudging reconstructions.

This chapter is organized as follows. Sect. 5.2.1 derives a general uncertainty bound for reconstructed quantities in AOT-nudging. Sect. 5.2.2 and 5.2.3 apply UQ to the liquid velocity field $\boldsymbol{u}$ and the volume-fraction field α, respectively. Sect. 5.3 validates the proposed UQ framework using synthetic bubbly-flow test cases with known ground truth. Sect. 5.4 summarizes the main findings of this chapter.

5.2 Methodology

5.2.1 General uncertainty bound

The general UQ quantities are evaluated point-wise at the nudging times t_k. Let Q denote a generic reconstructed quantity. An observation is modeled as

$$Q^{\text{obs}} = Q^{\text{grt}} + \varepsilon_Q, \qquad \|\varepsilon_Q\| \leq \delta_Q, \tag{5.1}$$

where ε_Q is the observation error and δ_Q is an observation error bound. The superscripts $[\cdot]^{\text{grt}}$, $[\cdot]^{\text{obs}}$, and $[\cdot]^{\text{rcs}}$ denote the ground-truth, observed, and reconstructed fields, respectively. For a vector field, such as velocity $\boldsymbol{u}$, $\|\cdot\|$ represents the Euclidean norm. For a scalar field, such as volume fraction α, $\|\cdot\|$ reduces to the absolute value.

At a nudging time t_k and based on (5.1), the point-wise observation can be modeled as an independent error superposed on the ground truth:

$$Q^{\text{obs}}(\mathbf{x}, t_k) = Q^{\text{grt}}(\mathbf{x}, t_k) + \varepsilon_Q(\mathbf{x}, t_k), \qquad \|\varepsilon_Q(\mathbf{x}, t_k)\| \leq \delta_Q(\mathbf{x}, t_k), \tag{5.2}$$

where $\mathbf{x}$ denotes the coordinates of a point. The residual between the reconstruction and the observation is defined as

$$r_Q(\mathbf{x}, t_k) = Q^{\text{rcs}}(\mathbf{x}, t_k) - Q^{\text{obs}}(\mathbf{x}, t_k). \tag{5.3}$$

The point-wise reconstruction error is

$$e_Q(\mathbf{x}, t_k) = Q^{\text{rcs}}(\mathbf{x}, t_k) - Q^{\text{grt}}(\mathbf{x}, t_k). \tag{5.4}$$

Substituting (5.2) and (5.3) into (5.4) gives

$$e_Q(\mathbf{x}, t_k) = r_Q(\mathbf{x}, t_k) + \varepsilon_Q(\mathbf{x}, t_k). \tag{5.5}$$

Applying the Euclidean norm and triangle inequality to (5.5) leads to

$$\begin{aligned} \|e_Q(\mathbf{x}, t_k)\| &= \|r_Q(\mathbf{x}, t_k) + \varepsilon_Q(\mathbf{x}, t_k)\| \\ &\leq \|r_Q(\mathbf{x}, t_k)\| + \|\varepsilon_Q(\mathbf{x}, t_k)\| \\ &\leq \|r_Q(\mathbf{x}, t_k)\| + \delta_Q(\mathbf{x}, t_k). \end{aligned} \tag{5.6}$$

Therefore, the generic uncertainty of Q is defined as

$$U_Q(\mathbf{x}, t_k) = \|r_Q(\mathbf{x}, t_k)\| + \delta_Q(\mathbf{x}, t_k), \tag{5.7}$$

and the reconstruction error should be bounded by the uncertainty, i.e., $\|e_Q(\mathbf{x}, t_k)\| \leq U_Q(\mathbf{x}, t_k)$. The uncertainty in (5.7) is fully computable. The residual r_Q is obtained from the local difference between the reconstructed field and the observation. The bound δ_Q is prescribed by the uncertainty of the image-based measurement.

5.2.2 Uncertainty of velocity

Based on (5.7), Fig. 5.1 illustrates the derivation of the velocity uncertainty. Since the velocity residual is evaluated on the mesh while observations are available only at tracer locations, interpolation $\mathscr{I}_{\boldsymbol{u},h}$ between the mesh and tracers introduces an additional error that must be included in the uncertainty estimate.

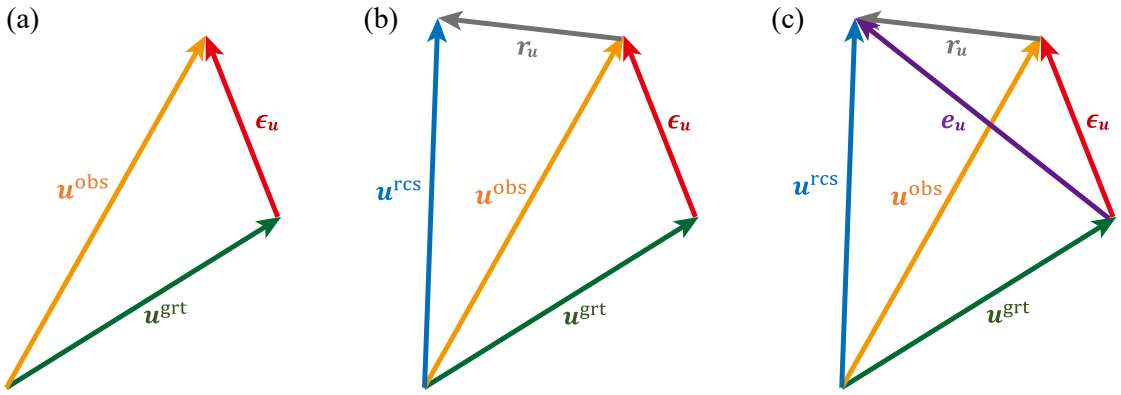


Figure 5.1: An illustration of the residual-based uncertainty model for velocity. (a) The observed velocity $\boldsymbol{u}^{\text{obs}}$ differs from the ground-truth velocity $\boldsymbol{u}^{\text{grt}}$ by the observation error $\boldsymbol{\varepsilon_u}$. (b) The AOT-nudging residual $\boldsymbol{r_u}$ is the difference between the observed and reconstructed velocities. (c) The reconstruction error is related to the residual, observation error, and observation error bound, giving $|\boldsymbol{e_u}| \leq |\boldsymbol{r_u}| + |\boldsymbol{\varepsilon_u}| \leq |\boldsymbol{r_u}| + \delta_{\boldsymbol{u}}$.

With nearest interpolation, the reconstructed velocity at the tracer location is written as

$$\boldsymbol{u}^{\text{rcs}}(\mathbf{x}_{\text{tra}}, t_k) = \mathscr{I}_{\text{msh}\to\text{tra}}(\boldsymbol{u}^{\text{rcs}}(t_k))\,|_{\mathbf{x}_{\text{tra}}} + \boldsymbol{\eta}_{\text{msh}\to\text{tra}}(\mathbf{x}_{\text{tra}}, t_k), \tag{5.8}$$

where $\mathbf{x}_{\text{cen}}$ is the center of the nearest cell to a tracer, $\mathbf{x}_{\text{tra}}$ is the tracer location, and $\mathscr{I}_{\text{msh}\to\text{tra}}(\boldsymbol{u}^{\text{rcs}}(t_k))\,|_{\mathbf{x}_{\text{tra}}}$ is the mesh-to-tracer interpolation that can map the reconstructed velocity field $\boldsymbol{u}^{\text{rcs}}(t_k)$ at the center of a mesh cell to the tracer $\mathbf{x}_{\text{tra}}$; $\boldsymbol{u}^{\text{rcs}}(t_k)$ can be directly accessed from the AOT-nudging reconstruction; $\boldsymbol{\eta}_{\text{msh}\to\text{tra}}$ denotes the mesh-to-tracer interpolation error. If $\mathscr{I}_{\text{msh}\to\text{tra}}$ is a nearest (piecewise constant) interpolation, as used in this work, then

$$\mathscr{I}_{\text{msh}\to\text{tra}}(\boldsymbol{u}^{\text{rcs}}(t_k))\,|_{\mathbf{x}_{\text{tra}}} = \boldsymbol{u}^{\text{rcs}}(\mathbf{x}_{\text{cen}}, t_k). \tag{5.9}$$

Substituting (5.9) into (5.8) leads to

$$\boldsymbol{u}^{\text{rcs}}(\mathbf{x}_{\text{tra}}, t_k) = \boldsymbol{u}^{\text{rcs}}(\mathbf{x}_{\text{cen}}, t_k) + \boldsymbol{\eta}_{\text{msh}\to\text{tra}}(\mathbf{x}_{\text{tra}}, t_k). \tag{5.10}$$

The interpolation error can be estimated by a first-order Taylor expansion at the tracer:

$$\|\boldsymbol{\eta}_{\text{msh}\to\text{tra}}(\mathbf{x}_{\text{tra}},t_k)\| \le \delta^{\text{intp}}_{\text{msh}\to\text{tra}}(\mathbf{x}_{\text{tra}},t_k) \approx \|\nabla \boldsymbol{u}^{\text{rcs}}(\mathbf{x}_{\text{tra}},t_k)\|_F \, \|\mathbf{x}_{\text{tra}}-\mathbf{x}_{\text{cen}}\|, \tag{5.11}$$

where $\delta^{\text{intp}}_{\text{msh}\to\text{tra}}(\mathbf{x}_{\text{tra}},t_k)$ is an upper bound of the interpolation error; $\nabla \boldsymbol{u}^{\text{rcs}}(\mathbf{x}_{\text{tra}},t_k)$ is the reconstructed velocity gradient at $\mathbf{x}_{\text{tra}}$; $\|\cdot\|_F$ denotes the Frobenius norm; and $\|\mathbf{x}_{\text{tra}}-\mathbf{x}_{\text{cen}}\|$ is the distance between the tracer and the cell center.

Similar to (5.9) and (5.10), with the nearest interpolation, the velocity observation on the mesh can be written as

$$\begin{aligned}\boldsymbol{u}^{\text{obs}}(\mathbf{x}_{\text{cen}},t_k) &= \mathscr{I}_{\text{tra}\to\text{msh}}\big(\boldsymbol{u}^{\text{obs}}(t_k)\big)\,|_{\mathbf{x}_{\text{cen}}} + \boldsymbol{\eta}_{\text{tra}\to\text{msh}}(\mathbf{x}_{\text{cen}},t_k)\\ &= \boldsymbol{u}^{\text{obs}}(\mathbf{x}_{\text{tra}},t_k) + \boldsymbol{\eta}_{\text{tra}\to\text{msh}}(\mathbf{x}_{\text{cen}},t_k),\end{aligned} \tag{5.12}$$

where the interpolation error is bounded by

$$\|\boldsymbol{\eta}_{\text{tra}\to\text{msh}}(\mathbf{x}_{\text{cen}},t_k)\| \le \delta^{\text{intp}}_{\text{tra}\to\text{msh}}(\mathbf{x}_{\text{cen}},t_k).$$

This interpolation error bound can also be estimated similarly to (5.11).

Equations (5.10) and (5.12) allow the tracer-wise residual to be calculated when using the residual of velocities on the mesh based on (5.3) when Q represents the velocity $\boldsymbol{u}$:

$$\begin{aligned}\boldsymbol{r}_{\boldsymbol{u}}(\mathbf{x}_{\text{tra}},t_k) &= \boldsymbol{u}^{\text{rcs}}(\mathbf{x}_{\text{tra}},t_k) - \boldsymbol{u}^{\text{obs}}(\mathbf{x}_{\text{tra}},t_k)\\ &= \big(\boldsymbol{u}^{\text{rcs}}(\mathbf{x}_{\text{cen}},t_k) + \boldsymbol{\eta}_{\text{msh}\to\text{tra}}(\mathbf{x}_{\text{tra}},t_k)\big)\\ &\quad - \big(\boldsymbol{u}^{\text{obs}}(\mathbf{x}_{\text{cen}},t_k) - \boldsymbol{\eta}_{\text{tra}\to\text{msh}}(\mathbf{x}_{\text{cen}},t_k)\big)\\ &= \boldsymbol{r}_{\boldsymbol{u}}(\mathbf{x}_{\text{cen}},t_k) + \boldsymbol{\eta}_{\text{msh}\to\text{tra}}(\mathbf{x}_{\text{tra}},t_k) + \boldsymbol{\eta}_{\text{tra}\to\text{msh}}(\mathbf{x}_{\text{cen}},t_k),\end{aligned} \tag{5.13}$$

where the residual of velocities on the mesh $\boldsymbol{r}_{\boldsymbol{u}}(\mathbf{x}_{\text{cen}},t_k)$ can be directly accessed through the AOT-nudging reconstruction. Next, the observation model in (5.2) can be adapted when it is evaluated at tracer locations:

$$\boldsymbol{u}^{\text{obs}}(\mathbf{x}_{\text{tra}},t_k) = \boldsymbol{u}^{\text{grt}}(\mathbf{x}_{\text{tra}},t_k) + \boldsymbol{\varepsilon}_{\boldsymbol{u}}(\mathbf{x}_{\text{tra}},t_k), \tag{5.14}$$

assuming the experimental error is bounded, i.e., $\|\boldsymbol{\varepsilon}_{\boldsymbol{u}}(\mathbf{x}_{\text{tra}},t_k)\| \le \delta_{\boldsymbol{u}}(\mathbf{x}_{\text{tra}},t_k)$. Isolating $\boldsymbol{u}^{\text{rcs}}(\mathbf{x}_{\text{tra}},t_k)$ from (5.13) and $\boldsymbol{u}^{\text{grt}}(\mathbf{x}_{\text{tra}},t_k)$ from (5.14), the tracer-wise reconstruction error and uncertainty can be computed by applying the triangle inequality, leading to an upper bound for $\boldsymbol{\mathcal{E}}_{\boldsymbol{u}}(\mathbf{x}_{\text{tra}},t_k)$ as an uncertainty:

$$\begin{aligned}\boldsymbol{\mathcal{E}}_{\boldsymbol{u}}(\mathbf{x}_{\text{tra}},t_k) &= \|\boldsymbol{u}^{\text{rcs}}(\mathbf{x}_{\text{tra}},t_k) - \boldsymbol{u}^{\text{grt}}(\mathbf{x}_{\text{tra}},t_k)\|\\ &= \|\boldsymbol{r}_{\boldsymbol{u}}(\mathbf{x}_{\text{cen}},t_k) + \boldsymbol{\eta}_{\text{msh}\to\text{tra}}(\mathbf{x}_{\text{tra}},t_k) + \boldsymbol{\eta}_{\text{tra}\to\text{msh}}(\mathbf{x}_{\text{cen}},t_k) + \boldsymbol{\varepsilon}_{\boldsymbol{u}}(\mathbf{x}_{\text{tra}},t_k)\|\\ &\le \|\boldsymbol{r}_{\boldsymbol{u}}(\mathbf{x}_{\text{cen}},t_k)\| + \delta_{\boldsymbol{u}}(\mathbf{x}_{\text{tra}},t_k) + \delta^{\text{intp}}_{\text{msh}\to\text{tra}}(\mathbf{x}_{\text{tra}},t_k) + \delta^{\text{intp}}_{\text{tra}\to\text{msh}}(\mathbf{x}_{\text{cen}},t_k)\\ &= U_{\boldsymbol{u}}(\mathbf{x}_{\text{tra}},t_k).\end{aligned} \tag{5.15}$$

The relative contribution of the interpolation errors can be characterized by

$$\kappa_{\text{intp}}(\mathbf{x}_{\text{tra}}, t_k) = \frac{\delta^{\text{intp}}_{\text{msh}\to\text{tra}}(\mathbf{x}_{\text{tra}}, t_k) + \delta^{\text{intp}}_{\text{tra}\to\text{msh}}(\mathbf{x}_{\text{cen}}, t_k)}{\|\boldsymbol{r}_{\boldsymbol{u}}(\mathbf{x}_{\text{cen}}, t_k)\|}. \tag{5.16}$$

Substituting (5.16) into (5.15) leads to

$$U_{\boldsymbol{u}}(\mathbf{x}_{\text{tra}}, t_k) = (1 + \kappa_{\text{intp}}(\mathbf{x}_{\text{tra}}, t_k)) \, \|\boldsymbol{r}_{\boldsymbol{u}}(\mathbf{x}_{\text{cen}}, t_k)\| + \delta_{\boldsymbol{u}}(\mathbf{x}_{\text{tra}}, t_k). \tag{5.17}$$

In (5.17), the first term on the Right-Hand Side (RHS) represents the uncertainty associated with the AOT-nudging residual and the interpolation errors. The mesh-wise residual $\|\boldsymbol{r}_{\boldsymbol{u}}(\mathbf{x}_{\text{cen}}, t_k)\|$ can be directly obtained from the AOT-nudging algorithm. The factor κ_{intp} accounts for the interpolation errors introduced when the velocity is interpolated between tracers and mesh-cell centers. This factor can be computed based on (5.11) using local velocity gradients and the distances between the tracers and the mesh-cell centers:

$$\begin{aligned} &\delta^{\text{intp}}_{\text{msh}\to\text{tra}}(\mathbf{x}_{\text{tra}}, t_k) + \delta^{\text{intp}}_{\text{tra}\to\text{msh}}(\mathbf{x}_{\text{cen}}, t_k) \\ &\qquad \approx \|\nabla \boldsymbol{u}^{\text{rcs}}(\mathbf{x}_{\text{tra}}, t_k)\|_F \, \|\mathbf{x}_{\text{tra}} - \mathbf{x}_{\text{cen}}\| + \|\nabla \boldsymbol{u}^{\text{rcs}}(\mathbf{x}_{\text{cen}}, t_k)\|_F \, \|\mathbf{x}_{\text{cen}} - \mathbf{x}_{\text{tra}}\|. \end{aligned} \tag{5.18}$$

The second term on the RHS of (5.17), $\delta_{\boldsymbol{u}}(\mathbf{x}_{\text{tra}}, t_k)$, represents the prescribed uncertainty of the velocity measurement.

The factor κ_{intp} can be estimated through a characteristic scaling analysis. After AOT-nudging has converged, the mesh-wise velocity residual is assumed to be dominated by the tracer-to-mesh interpolation error:

$$\|\boldsymbol{r}_{\boldsymbol{u}}(\mathbf{x}_{\text{cen}}, t_k)\| \approx \delta^{\text{intp}}_{\text{tra}\to\text{msh}}(\mathbf{x}_{\text{cen}}, t_k). \tag{5.19}$$

Substituting (5.19) into (5.16) gives

$$\kappa_{\text{intp}} \approx 1 + \frac{\delta^{\text{intp}}_{\text{msh}\to\text{tra}}}{\delta^{\text{intp}}_{\text{tra}\to\text{msh}}}. \tag{5.20}$$

At sufficiently high seeding density, the characteristic tracer-to-cell distance is comparable to the mesh size Δx, leading to

$$\delta^{\text{intp}}_{\text{msh}\to\text{tra}} \approx \delta^{\text{intp}}_{\text{tra}\to\text{msh}},$$

and (5.20) gives $\kappa_{\text{intp}} \approx 2$. The corresponding velocity uncertainty is:

$$U_{\boldsymbol{u}} \approx 3\|\boldsymbol{r}_{\boldsymbol{u}}\| + \delta_{\boldsymbol{u}}. \tag{5.21}$$

At low seeding density, the characteristic tracer spacing ℓ_{tra} is larger than Δx, so that

$$\delta^{\mathrm{intp}}_{\mathrm{msh}\to\mathrm{tra}} \sim \|\nabla \boldsymbol{u}\|_F \Delta x, \qquad \delta^{\mathrm{intp}}_{\mathrm{tra}\to\mathrm{msh}} \sim \|\nabla \boldsymbol{u}\|_F \ell_{\mathrm{tra}}.$$

Equation (5.20) then becomes

$$\kappa_{\mathrm{intp}} \approx 1 + \frac{\Delta x}{\ell_{\mathrm{tra}}} \approx 1 \qquad \text{for } \ell_{\mathrm{tra}} \gg \Delta x,$$

and the uncertainty can be approximated as

$$U_{\boldsymbol{u}} \approx 2\|\boldsymbol{r}_{\boldsymbol{u}}\| + \delta_{\boldsymbol{u}}. \tag{5.22}$$

Equations (5.21) and (5.22) provide a practical approximation for the AOT-nudging reconstruction at a converged state. Since the present seeding density is low, (5.22) is adopted and assessed in Sect. 5.3.

5.2.3 Uncertainty of volume fraction

The uncertainty in the reconstructed volume fraction on the mesh is estimated from (i) the AOT-nudging residual of volume fraction fields and (ii) the uncertainty in the observations of the bubble geometry and position. The point-wise quantities defined in Sect. 5.2.1 are specified here as the volume fraction on the mesh. Since the true bubble interface is unavailable in practice, a bubble interface uncertainty is proposed, and its region is supposed to enclose the true bubble interface.

A volume-fraction observation model is introduced following (5.2). Let $\Omega_g^{\mathrm{grt}}(t_k)$ and $\Gamma^{\mathrm{grt}}(t_k) = \partial\Omega_g^{\mathrm{grt}}(t_k)$ denote the ground-truth gas region and its gas–liquid interface, respectively. Similarly, let $\Omega_g^{\mathrm{obs}}(t_k)$ and $\Gamma^{\mathrm{obs}}(t_k) = \partial\Omega_g^{\mathrm{obs}}(t_k)$ denote the observed gas interface region and its interface, respectively. The outward unit normal vector on the ground-truth interface is denoted by $\boldsymbol{n}^{\mathrm{grt}}(\mathbf{x}, t_k)$. The observed gas-liquid interface is assumed to deviate from the ground-truth interface inward and outward along the normal direction:

$$\Gamma^{\mathrm{obs}}(t_k) = \left\{ \mathbf{x} + \varepsilon_\alpha(\mathbf{x}, t_k)\boldsymbol{n}^{\mathrm{grt}}(\mathbf{x}, t_k) : \mathbf{x} \in \Gamma^{\mathrm{grt}}(t_k) \right\}, \qquad |\varepsilon_\alpha(\mathbf{x}, t_k)| \le \delta_\alpha, \tag{5.23}$$

where $\varepsilon_\alpha(\mathbf{x}, t_k)$ is the local interface-position error and δ_α is the prescribed bound on the interface-position error. δ_α can be estimated based on the width of the bubble interface from images.

Based on (5.3), the mesh-wise volume-fraction residual is defined as

$$r_\alpha(\mathbf{x}_{\mathrm{cen}}, t_k) = \alpha^{\mathrm{rcs}}(\mathbf{x}_{\mathrm{cen}}, t_k) - \alpha^{\mathrm{obs}}(\mathbf{x}_{\mathrm{cen}}, t_k), \tag{5.24}$$

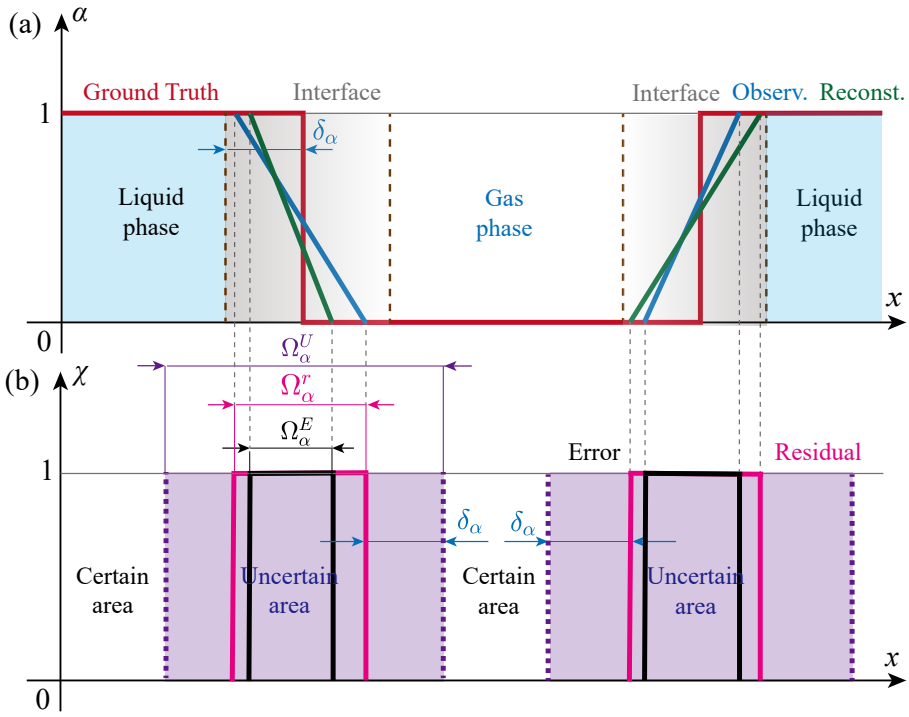


Figure 5.2: A 1D illustration of the UQ model for the volume fraction. (a) The red, blue, and green curves denote the ground-truth, observed, and reconstructed volume fraction. The observation uncertainty is represented by an inward/outward displacement of the ground-truth interface, bounded by δ_α. (b) The black, magenta, and purple regions represent the true error region Ω_α^E, the residual uncertain region Ω_α^r obtained from the AOT-nudging residual, and the uncertainty region Ω_α^U obtained by expanding the residual region Ω_α^r inward and outward by the prescribed bound δ_α. A reliable uncertainty estimate should make Ω_α^U enclose Ω_α^E.

where $\mathbf{x}_{\text{cen}}$ is the center of a mesh cell, $\alpha^{\text{obs}}(\mathbf{x}_{\text{cen}}, t_k)$ and $\alpha^{\text{rcs}}(\mathbf{x}_{\text{cen}}, t_k)$ are the observed and reconstructed volume fractions at time t_k, respectively. $r_\alpha(\mathbf{x}_{\text{cen}}, t_k)$ from (5.24) can be directly accessed from the AOT-nudging reconstruction. The sign of r_α indicates whether the reconstructed field locally underestimates or overestimates the observed volume-fraction field. However, for the volume-fraction UQ, the sign or magnitude of this mismatch is less meaningful than the location and geometry of the interface of the bubble. Therefore, the residual is converted into a spatial indicator χ_α^r by taking its absolute value and applying a threshold:

$$\chi_\alpha^r(\mathbf{x}_{\text{cen}}, t_k) = H\left(|r_\alpha(\mathbf{x}_{\text{cen}}, t_k)| - \epsilon_{\text{r}}\right), \tag{5.25}$$

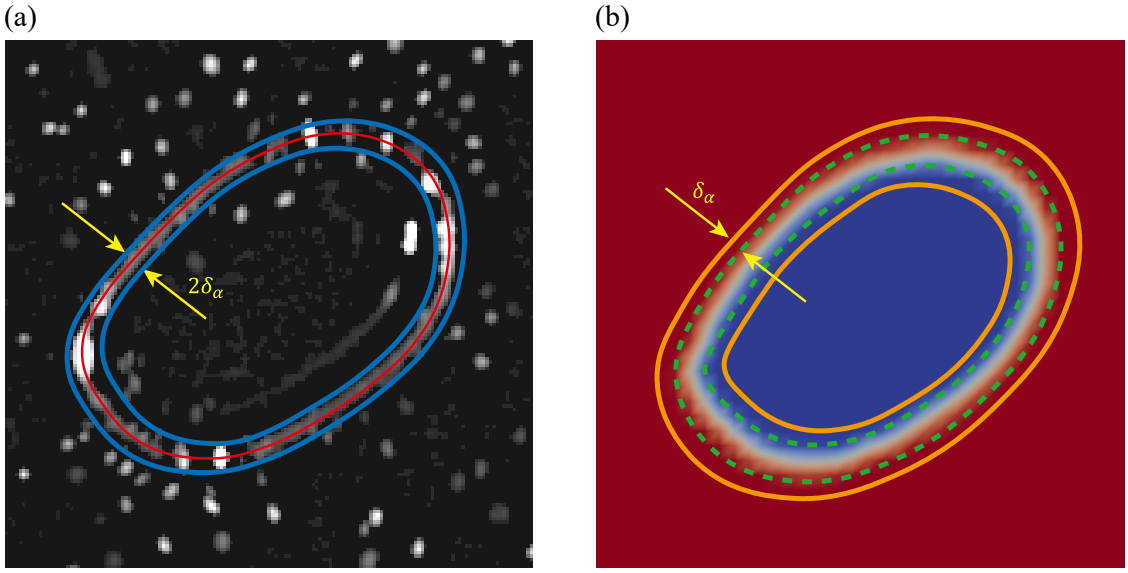


Figure 5.3: A 2D illustration of the residual-based uncertainty model for the volume fraction. (a) A bubble image from a high-speed camera. The red curve represents the ground-truth bubble interface Γ^{grt}. The two blue curves bound the possible locations of the observed interface obtained by displacing Γ^{grt} inward and outward by δ_α. (b) The volume-fraction field in the reconstruction. The blue and red regions denote the gas and liquid phases, respectively. The two green dashed curves bound the residual region, which identifies discrepancies between the observed and reconstructed interfaces. The uncertainty region is obtained by expanding the inner and outer boundaries of the residual region by δ_α, as indicated by the orange curves. Ideally, the observed band should enclose the ground-truth bubble interface. The residual region should in turn enclose the observed band, and its expansion by δ_α defines the uncertainty region. Therefore, the uncertainty region is expected to enclose the ground-truth bubble interface.

where $H(\cdot)$ is the Heaviside step function, and ϵ_{r} is a small threshold used to remove numerical round-off residuals. Thus, $\chi_\alpha^r = 1$ marks cells in which the residual exceeds the prescribed threshold, whereas $\chi_\alpha^r = 0$ marks cells in which the residual is below the threshold. The nonzero support in (5.25) defines the residual region and its boundary:

$$\Omega_\alpha^r(t_k) = \{\mathbf{x}_{\mathrm{cen}} : \chi_\alpha^r(\mathbf{x}_{\mathrm{cen}}, t_k) = 1\}, \qquad \Gamma_\alpha^r(t_k) = \partial\Omega_\alpha^r(t_k). \tag{5.26}$$

Cells inside Ω_α^r are interpreted as cells with non-zero residual. This residual may arise from numerical diffusion or weak AOT-nudging near the reconstructed bubble interfaces,

as well as from inaccurate bubble-boundary detection during image processing, which may shift or blur the observed interface away from its true location or width. Cells outside Ω_α^r are treated as certain (i.e., zero-residual) because the observed and reconstructed volume fractions agree within the prescribed threshold. In practice, these zero-residual cells are usually located either entirely inside the bubble or entirely outside it, away from the gas–liquid interface.

Next, to formulate the uncertainty of the reconstructed volume fraction, the residual region in (5.26) is expanded inward and outward from the residual boundaries $\Gamma_\alpha^r(t_k)$, by the uncertainty bound of the observed interface (i.e., δ_α). Therefore, the uncertainty region is defined as

$$\Omega_\alpha^U(t_k) = \left\{ \mathbf{x}_{\text{cen}} : \min_{\mathbf{x}\in\Omega_\alpha^r(t_k)} \|\mathbf{x}_{\text{cen}} - \mathbf{x}\|_2 \le \delta_\alpha \right\}. \tag{5.27}$$

where $\min \|\cdot\|_2$ is the shortest Euclidean distance between two points, Ω_α^U represents the possible uncertainty area caused by both observation and reconstruction. The corresponding boundary of the uncertainty region is

$$\Gamma_\alpha^U(t_k) = \partial\Omega_\alpha^U(t_k).$$

Cells inside Ω_α^U are treated as uncertain cells for the reconstructed volume fraction, while cells outside Ω_α^U are treated as certain ones. Ideally, the true bubble interface should lie within Ω_α^U.

In practice, the true bubble interface is unknown. If the interface-uncertainty region encloses the erroneous interface regions caused by observation and reconstruction, it is expected to contain the true bubble interface. Thus, it provides a reliable estimate of the true bubble interface.

To validate the uncertainty in (5.27), following (5.4), the true reconstruction error of the volume fraction is defined as the difference between the reconstructed and ground-truth fields:

$$e_\alpha(\mathbf{x}_{\text{cen}}, t_k) = \alpha^{\text{rcs}}(\mathbf{x}_{\text{cen}}, t_k) - \alpha^{\text{grt}}(\mathbf{x}_{\text{cen}}, t_k), \tag{5.28}$$

where $\alpha^{\text{grt}}(\mathbf{x}_{\text{cen}}, t_k)$ is the ground-truth of the volume fraction field. The scalar error field in (5.28) is converted into a spatial error indicator χ_α^E by applying a threshold:

$$\chi_\alpha^E(\mathbf{x}_{\text{cen}}, t_k) = H\left(|e_\alpha(\mathbf{x}_{\text{cen}}, t_k)| - \epsilon_E\right),$$

where ϵ_E is the prescribed error threshold. Thus, $\chi_\alpha^E = 1$ identifies cells where the magnitude of the true volume-fraction error exceeds ϵ_E, while $\chi_\alpha^E = 0$ indicates that the local

error is negligible and is assigned a zero value. The nonzero support of χ_α^E is the true error region with a boundary:

$$\Omega_\alpha^E(t_k) = \left\{ \mathbf{x}_{\text{cen}} : \chi_\alpha^E(\mathbf{x}_{\text{cen}}, t_k) = 1 \right\}, \qquad \Gamma_\alpha^E(t_k) = \partial\Omega_\alpha^E(t_k). \tag{5.29}$$

Thus, Ω_α^E represents the mesh cells where the reconstructed bubble geometry differs from the ground truth by more than the threshold.

Therefore, based on (5.27) and (5.29), a reliable uncertainty estimate should enclose the true error region:

$$\Omega_\alpha^E(t_k) \subseteq \Omega_\alpha^U(t_k), \tag{5.30}$$

where Ω_α^E is the true error region and Ω_α^U is the reconstruction uncertainty region. This means that cells with true volume-fraction reconstruction error are enclosed by the reconstruction uncertainty region, especially near the gas–liquid interface. The derivation of the volume-fraction uncertainty is illustrated in 1D and 2D in Figs. 5.2 and 5.3, respectively.

5.3 Results and Discussion

5.3.1 Error and uncertainty metrics

This section validates the proposed UQ framework using synthetic test cases for which the ground-truth fields are known. Because the exact fields are available, the true reconstruction error can be evaluated directly and compared with the proposed uncertainty estimates.

For α and $\boldsymbol{u}$, the validation objective is to assess whether the residual-based uncertainty bounds in (5.22) and (5.27) provide reliable upper bounds for the true reconstruction errors in (5.15) and (5.29). The volume-fraction error is evaluated at mesh-cell centers, whereas the velocity error is evaluated at tracer locations.

Independent trials are performed to reduce the influence of random noise on the error and uncertainty metrics. Let $q = 1, \ldots, N_{\text{tri}}$ denote the trial index. For the velocity field, let j represent the index of a tracer sample. For the trial q, the relative velocity error is defined as

$$E_{u,j}^q(\mathbf{x}_{\text{tra}}, t_k) = \frac{\left\| \boldsymbol{u}_j^{\text{rcs},q}(\mathbf{x}_{\text{tra}}, t_k) - \boldsymbol{u}_j^{\text{grt},q}(\mathbf{x}_{\text{tra}}, t_k) \right\|}{|\boldsymbol{u}|_{\text{ref}}} \times 100\%,$$

where $|\boldsymbol{u}|_{\text{ref}}$ is the reference velocity for normalization. The relative velocity uncertainty for trial q is defined as

$$U_{u,j}^{q}(\mathbf{x}_{\text{tra}}, t_k) = \frac{2\left\|\boldsymbol{u}_j^{\text{rcs},q}(\mathbf{x}_{\text{cen}}, t_k) - \boldsymbol{u}_j^{\text{obs},q}(\mathbf{x}_{\text{cen}}, t_k)\right\| + \delta_u}{|\boldsymbol{u}|_{\text{ref}}} \times 100\%,$$

where $\mathbf{x}_{\text{cen}}$ denotes the center of the mesh cell associated with tracer j, and $\boldsymbol{u}_j^{\text{rcs},q}(\mathbf{x}_{\text{cen}}, t_k) - \boldsymbol{u}_j^{\text{obs},q}(\mathbf{x}_{\text{cen}}, t_k)$ is the residual at the mesh-cell center corresponding to the tracer j in trial q, which can be directly accessed from the AOT-nudging reconstruction. Then, the trial-averaged velocity error and uncertainty are defined as

$$\overline{E}_{u,j}(\mathbf{x}_{\text{tra}}, t_k) = \frac{1}{N_{\text{tri}}}\sum_{q=1}^{N_{\text{tri}}} E_{u,j}^{q}(\mathbf{x}_{\text{tra}}, t_k), \qquad \overline{U}_{u,j}(\mathbf{x}_{\text{tra}}, t_k) = \frac{1}{N_{\text{tri}}}\sum_{q=1}^{N_{\text{tri}}} U_{u,j}^{q}(\mathbf{x}_{\text{tra}}, t_k). \tag{5.31}$$

For the volume-fraction field and trial q, the relative volume-fraction error at mesh cell j is defined as

$$E_{\alpha,j}^{q}(\mathbf{x}_{\text{cen}}, t_k) = \frac{\left|\alpha_j^{\text{rcs},q}(\mathbf{x}_{\text{cen}}, t_k) - \alpha_j^{\text{grt},q}(\mathbf{x}_{\text{cen}}, t_k)\right|}{\alpha_{\text{ref}}} \times 100\%,$$

where α_{ref} is the reference volume fraction for normalization. The corresponding relative volume-fraction uncertainty is defined as

$$U_{\alpha,j}^{q}(\mathbf{x}_{\text{cen}}, t_k) = \frac{\left|\alpha_j^{\text{rcs},q}(\mathbf{x}_{\text{cen}}, t_k) - \alpha_j^{\text{obs},q}(\mathbf{x}_{\text{cen}}, t_k)\right|}{\alpha_{\text{ref}}} \times 100\%.$$

Then, the trial-averaged volume-fraction error and uncertainty are

$$\overline{E}_{\alpha,j}(\mathbf{x}_{\text{cen}}, t_k) = \frac{1}{N_{\text{tri}}}\sum_{q=1}^{N_{\text{tri}}} E_{\alpha,j}^{q}(\mathbf{x}_{\text{cen}}, t_k), \qquad \overline{U}_{\alpha,j}(\mathbf{x}_{\text{cen}}, t_k) = \frac{1}{N_{\text{tri}}}\sum_{q=1}^{N_{\text{tri}}} U_{\alpha,j}^{q}(\mathbf{x}_{\text{cen}}, t_k). \tag{5.32}$$

Lastly, the true error and uncertainty regions are denoted by $\Omega_\alpha^E(t_k)$ and $\Omega_\alpha^U(t_k)$, respectively. The comparison is then made between these two regions rather than only between point-wise scalar values. A reliable uncertainty estimate should make $\Omega_\alpha^U(t_k)$ enclose most of $\Omega_\alpha^E(t_k)$, especially near the bubble interface where bubble-size and bubble-location errors are concentrated.

5.3.2 Synthetic observation generation

Synthetic observations are generated based on the same reference simulation used in Sect. 4.3.2. The AOT-nudging reconstruction settings are the same as those in Sect. 4.3.2. For the noisy velocity observations, the reference velocity field is first sampled at the tracer locations at each observed frame. Independent zero-mean Gaussian noise is then superposed on each velocity component at tracer locations to generate synthetic velocity observations. The noise level is controlled by the standard deviation σ_u. With increasing σ_u, the observed tracer velocities deviate more from the reference values.

For the volume-fraction observations, the perturbation is applied to the gas–liquid interface. The Gaussian blurring is applied with a shape factor $\varepsilon_{\mathrm{blr}}$ within an interface band. The noise level is also controlled by the band half-thickness b_α.

Four noise levels are considered, as listed in Tab. 5.1. For each noise level, five independent trials, i.e., $N_{\mathrm{tri}} = 5$, are generated. The reported errors and uncertainties are obtained by averaging them over all trials using (5.31) and (5.32). The reference velocity and volume fraction used for normalization are $|\boldsymbol{u}|_{\mathrm{ref}} = 0.5$ m s^{-1} and $\alpha_{\mathrm{ref}} = 1$, respectively. The thresholds for volume fraction residual and error are $\epsilon_r = \epsilon_E = 0.0001$. In addition, the prescribed velocity uncertainty δ_u is taken to be equal to σ_u.

Figures 5.4 and 5.5 illustrate the generation of synthetic velocity and volume-fraction observations at these noise levels, respectively. Figure 5.4 indicates the ground-truth tracer velocity field and the corresponding noisy velocity observations at $t = 0.1$ s. As the noise level increases, the measured velocity field deviates more from the reference field. Figure 5.5 shows the ground-truth volume-fraction field and the blurred volume-fraction observations. The perturbation is localized near the bubble interfaces. As the noise level increases, the interface becomes wider and smoother, and the observed volume-fraction field deviates more from the ground truth field.

Table 5.1: Noise parameters used for the synthetic velocity and volume-fraction observations.

Noise level	σ_u [m/s]	b_α [cells]	$\varepsilon_{\mathrm{blr}}$
1	0.001	1	0.8
2	0.005	2	1.2
3	0.01	3	1.8
4	0.1	4	2.2

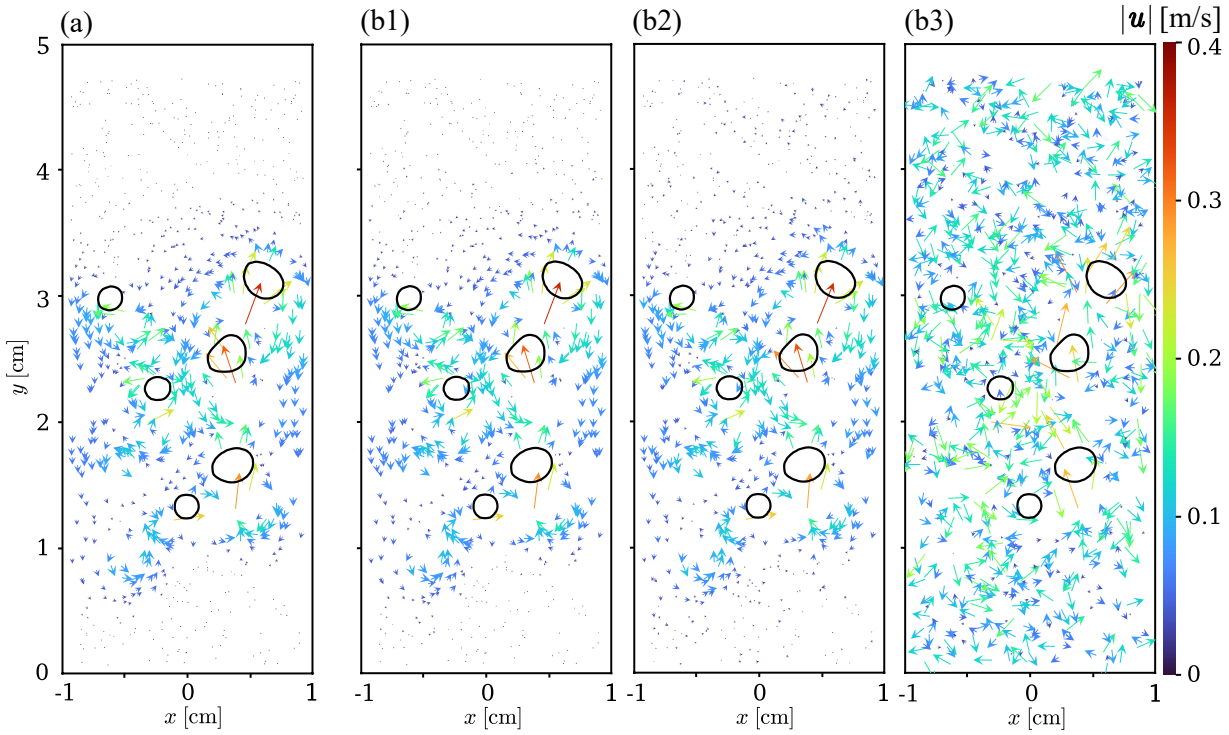


Figure 5.4: Generation of synthetic velocity observations at $t = 0.1$ s. Subfigure (a) shows the ground-truth tracer velocity field. Subfigures (b1) – (b3) show the corresponding noisy tracer velocity observations for noise levels 2, 3, and 4 in Tab. 5.1. Noise level 1 is not shown because it is virtually identical to the ground truth. Solid black curves indicate the bubble outlines. Velocity vectors are colored by their magnitude.

5.3.3 Validation results

Validation results are presented in Figs. 5.6 – 5.11. Figure 5.6 compares the ground-truth velocity magnitude with the AOT-nudging reconstruction obtained from noisy velocity observations (noise level 4). The reconstructed field captures the bubble-induced wakes and recirculation structures and agrees well with the ground truth across the selected times. This shows that the AOT-nudging method can recover the dominant flow structures even when the velocity observations are noisy.

Compared with the reconstruction using noise-free data in Fig. 4.5, the reconstruction based on noisy data as shown in Fig. 5.6 still preserves the major flow structures (e.g., the wakes, recirculation, and bubble kinematics). High noise in velocity observations introduces

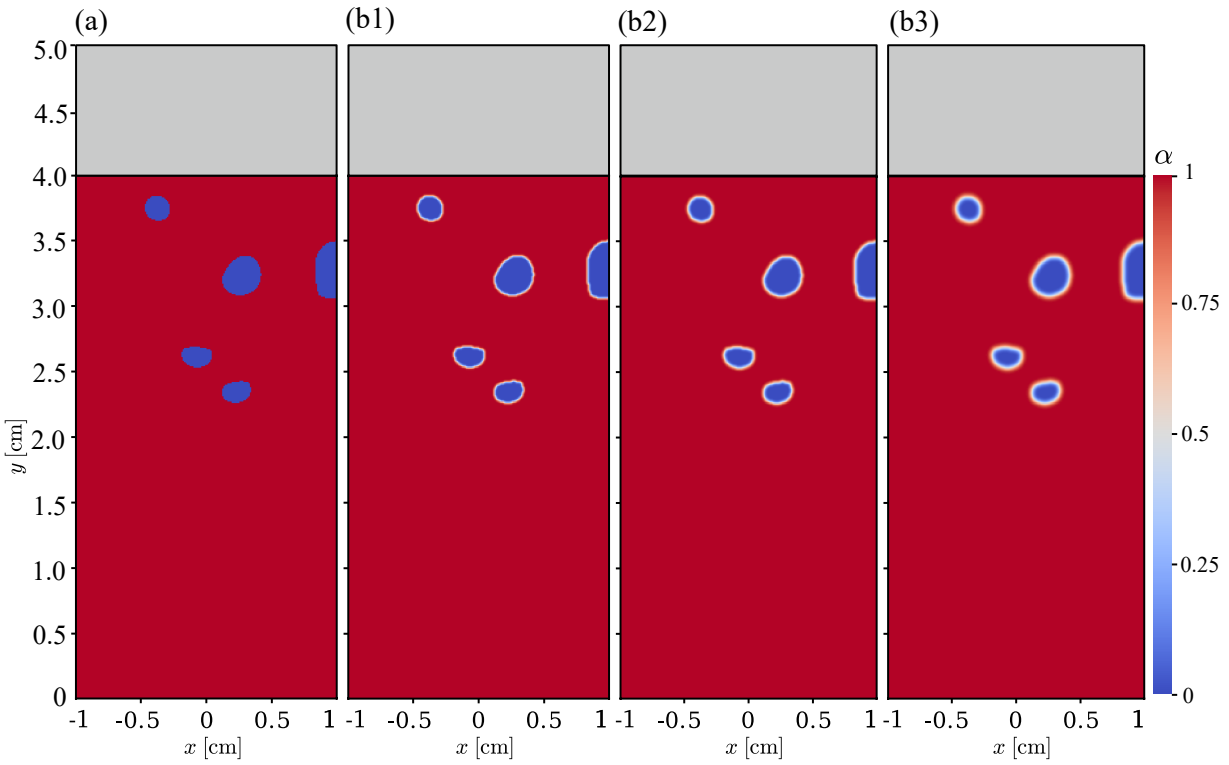


Figure 5.5: Generation of synthetic volume-fraction observations at $t = 0.1$ s. Subfigure (a) shows the ground-truth volume-fraction field, which has sharp gas–liquid interfaces. Subfigures (b1) – (b3) show noisy observations for noise levels 2, 3, and 4 in Tab. 5.1. No volume fraction observations are available in the gray area (i.e., $y \geq 4$ cm).

slight localized reconstruction error in the wake and low-speed regions, without altering the main flow structures. This agreement suggests that the AOT-nudging reconstruction is robust to random noise in both the volume-fraction and velocity observations.

The volume-fraction UQ results are shown in Figs. 5.7 and 5.8. The two figures correspond to noise levels 1 and 2 in Tab. 5.1, respectively. Each figure shows the trial-averaged true reconstruction error $\overline{E}_\alpha$, the trial-averaged uncertainty estimate $\overline{U}_\alpha$, and the enclosure map of the error region. In Figs. 5.7 (a) and 5.8 (a), the reconstruction error $\overline{E}_\alpha$ is mainly concentrated near the bubble interfaces. This is expected because the synthetic volume-fraction error is introduced near the gas–liquid interface. The uncertainty estimate $\overline{U}_\alpha$ shows a similar spatial distribution, as shown in Figs. 5.7 (b) and 5.8 (b). Large uncertainty surrounds the bubble boundaries, but away from the observed interface, $\overline{U}_\alpha$ is

close to zero. This indicates that the UQ model correctly identifies the regions where the reconstructed volume fraction is less reliable. In Figs. 5.7 (c) and 5.8 (c), almost all of the error region is enclosed by the uncertainty region. This means that $\overline{U}_\alpha$ provides a useful point-wise indicator of the true volume-fraction reconstruction error.

The velocity UQ results are shown in Figs. 5.9 and 5.10. These figures correspond to noise levels 1 and 2 in Tab. 5.1. Each figure compares the averaged true relative velocity reconstruction error on the mesh, the averaged true relative reconstruction error at tracer locations, the averaged uncertainty estimate $\overline{U}_{\boldsymbol{u}}$, and the difference map $\overline{U}_{\boldsymbol{u}} - \overline{E}_{\boldsymbol{u}}$. The difference map visualizes the local conservativeness or underestimation of the uncertainty estimate. Positive values, shown in green, mean that $\overline{U}_{\boldsymbol{u}}$ is larger than $\overline{E}_{\boldsymbol{u}}$. For an ideal UQ model, $\overline{U}_{\boldsymbol{u}} - \overline{E}_{\boldsymbol{u}}$ should be slightly positive.

In the subfigures (a) and (b) of Figs. 5.9 and 5.10, the reconstruction error $\overline{E}_{\boldsymbol{u}}$ is primarily located in bubble-influenced regions. Large values of $\overline{E}_{\boldsymbol{u}}$ appear near bubble wakes, recirculation, and regions with strong velocity gradients. These regions are sensitive to observation noise and tracer sparsity. As shown in Figs. 5.9 (c) and 5.10 (c), the uncertainty field $\overline{U}_{\boldsymbol{u}}$ captures the same spatial distribution of error: high uncertainty appears in the same regions where the velocity error is high. This indicates that the UQ model can identify the main regions of unreliable velocity reconstruction.

The difference maps (i.e., $\overline{U}_{\boldsymbol{u}} - \overline{E}_{\boldsymbol{u}}$) in Figs. 5.9 (d) and 5.10 (d) further illustrate the performance of the uncertainty estimate. At the low noise level, the subfigure shows a light green color, indicating that $\overline{U}_{\boldsymbol{u}}$ is slightly above $\overline{E}_{\boldsymbol{u}}$. Therefore, (5.22) is an accurate and relatively sharp estimate. As the noise level increases, the $\overline{U}_{\boldsymbol{u}} - \overline{E}_{\boldsymbol{u}}$ maps become dark green and more positive, showing that $\overline{U}_{\boldsymbol{u}}$ increasingly exceeds $\overline{E}_{\boldsymbol{u}}$ and therefore becomes more conservative. Overall, these results indicate that (5.22) provides an accurate velocity uncertainty estimate at low noise levels and a reliable conservative bound as the observation noise increases.

Figure 5.11 compares the true relative velocity error with the corresponding uncertainty estimate for noise levels 1 – 3. The upper row shows the tracer-wise quantities averaged over the five trials, whereas the lower row includes all individual tracer samples without trial averaging. In all cases, most points lie above and close to the diagonal, indicating that the uncertainty estimate generally bounds the true error while remaining reasonably sharp. The individual samples in Fig. 5.11 (b1) – (b3) exhibit broader scatter than the trial-averaged results in Fig. 5.11 (a1) – (a3). This is attributed to the trial-to-trial variations in the imposed noise. For noise levels 1, 2, and 3, 4.43%, 1.34%, and 0.89% of the individual points, respectively, fall below the diagonal, indicating that underestimation occurs rarely. These localized underestimations may be attributed to (i) the use of

a one-standard-deviation observation uncertainty δ_u, rather than a $3\delta_u$ bound, and (ii) errors introduced by the nearest interpolation. From (a1) and (b1) to (a3) and (b3), both $E_{\boldsymbol{u}}$ and $U_{\boldsymbol{u}}$ generally increase with the local velocity-gradient magnitude $\|\nabla \boldsymbol{u}\|_F$, since high-gradient regions are sensitive to sparse sampling and interpolation errors. A plateau is observed at small $E_{\boldsymbol{u}}$, where $U_{\boldsymbol{u}}$ remains nearly constant as the true error approaches zero. This plateau results from the prescribed observation uncertainty δ_u, which reflects a noise floor in the UQ model. Reducing the observation error would lower this floor. Overall, the uncertainty estimate remains relatively accurate at low-to-moderate noise levels in observation and becomes conservative as the noise level increases.

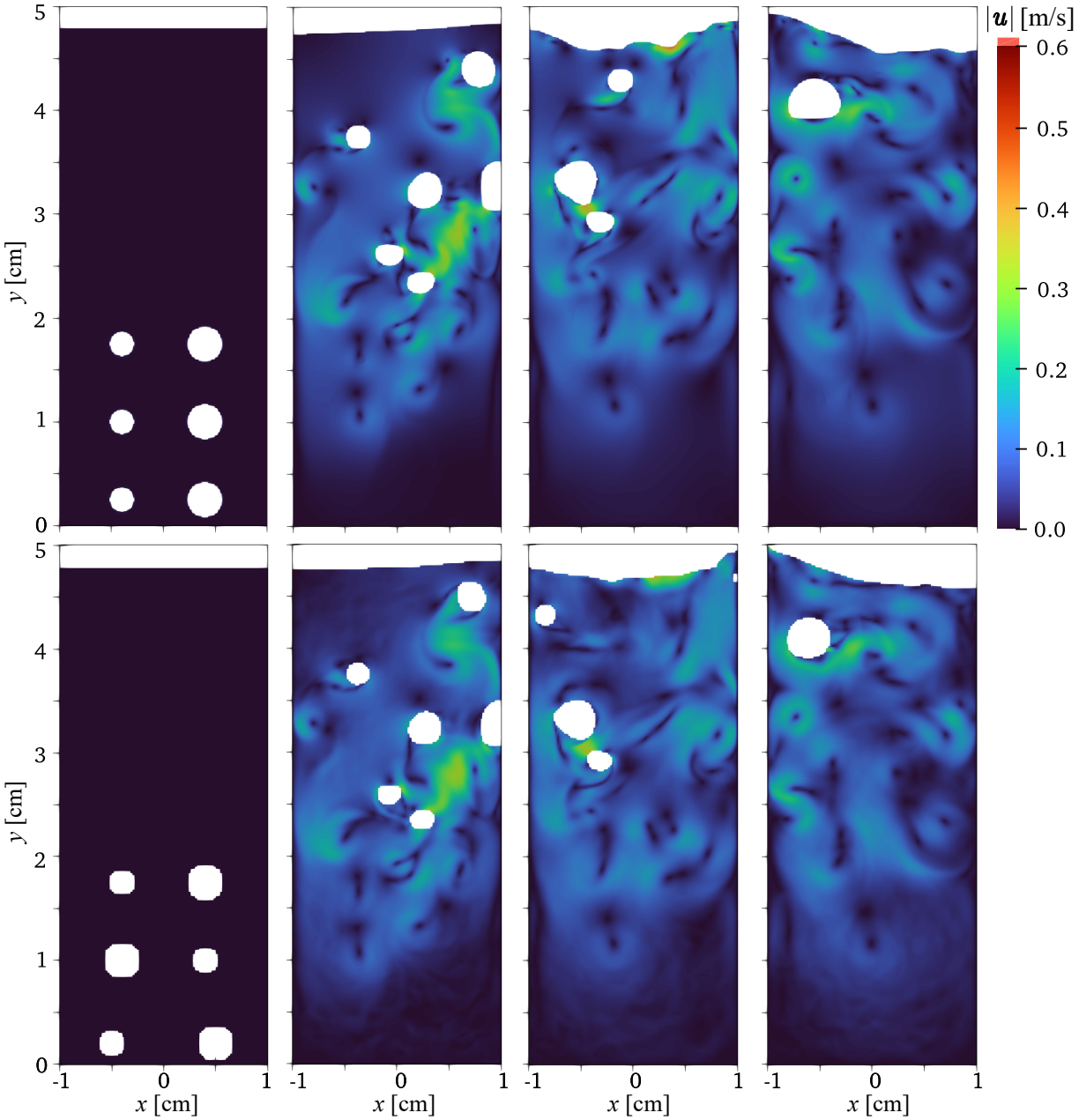


Figure 5.6: Velocity magnitude and bubble-induced circulation in the UQ case. The upper row shows the ground-truth velocity magnitude, and the lower row shows the AOT-nudging reconstruction obtained using noisy observations from noise level 4. Columns from left to right correspond to $t = 0.001$, 0.2, 0.3, and 0.4 s. The field is colored by $|\boldsymbol{u}|$.

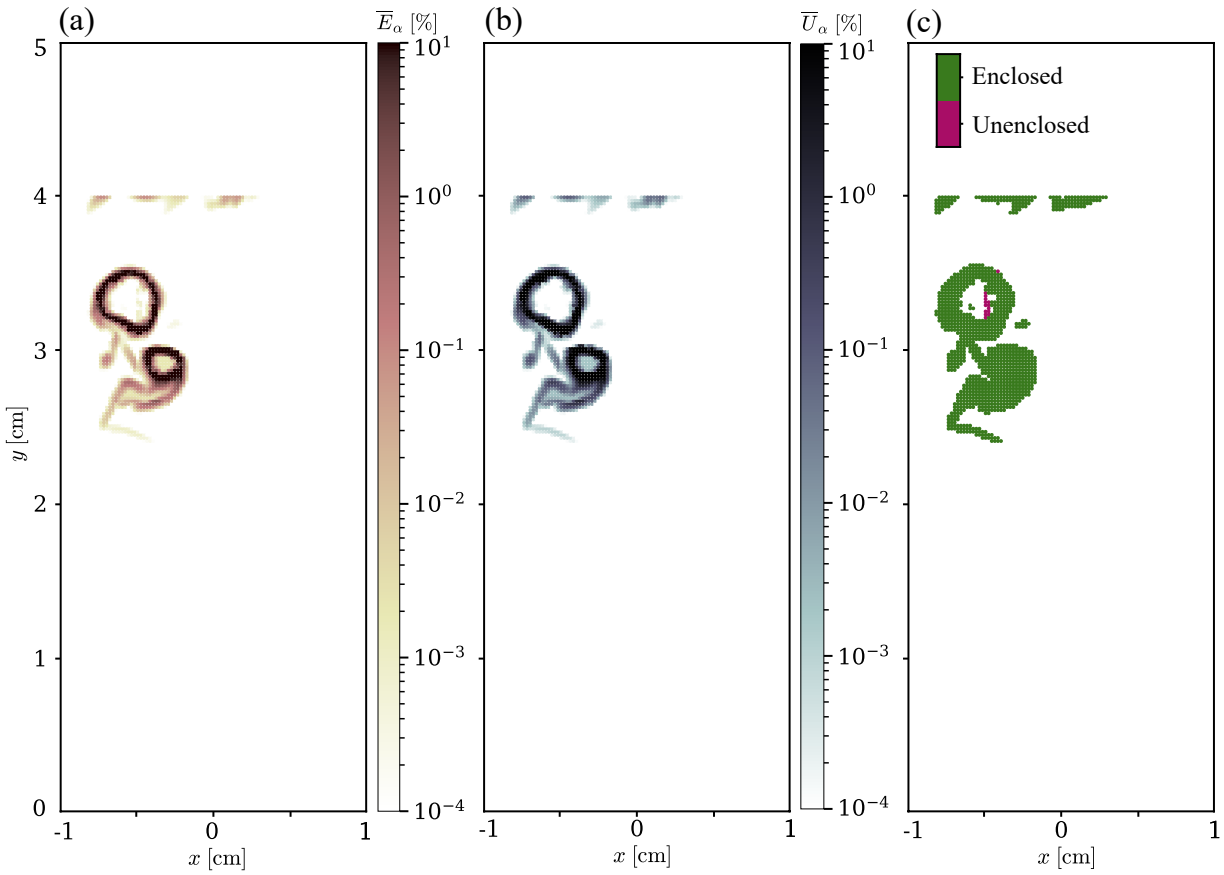


Figure 5.7: Averaged volume-fraction UQ results for noise level 1 at $t = 0.3$ s. From left to right: averaged true reconstruction error $\overline{E}_\alpha$, averaged uncertainty estimate $\overline{U}_\alpha$ around the observed interface, and the corresponding enclosure map of the error region. In the enclosure map, green denotes error pixels enclosed by the uncertainty region, and magenta denotes unenclosed error pixels.

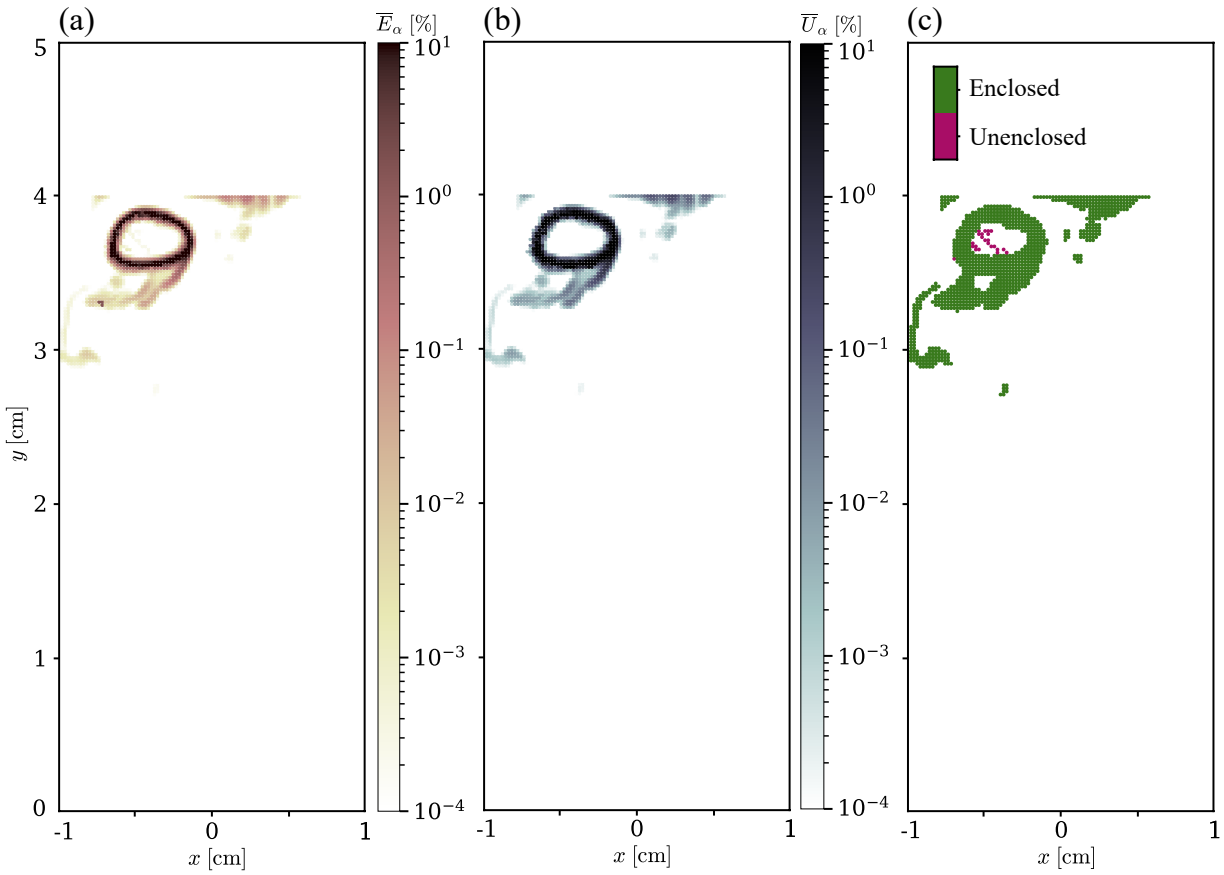


Figure 5.8: Averaged volume-fraction UQ results for noise level 2 at $t = 0.35$ s. From left to right: averaged true reconstruction error $\overline{E}_\alpha$, averaged uncertainty estimate $\overline{U}_\alpha$ around the observed interface, and the corresponding enclosure map of the error region. In the enclosure map, green denotes error pixels enclosed by the uncertainty region, and magenta denotes unenclosed error pixels.

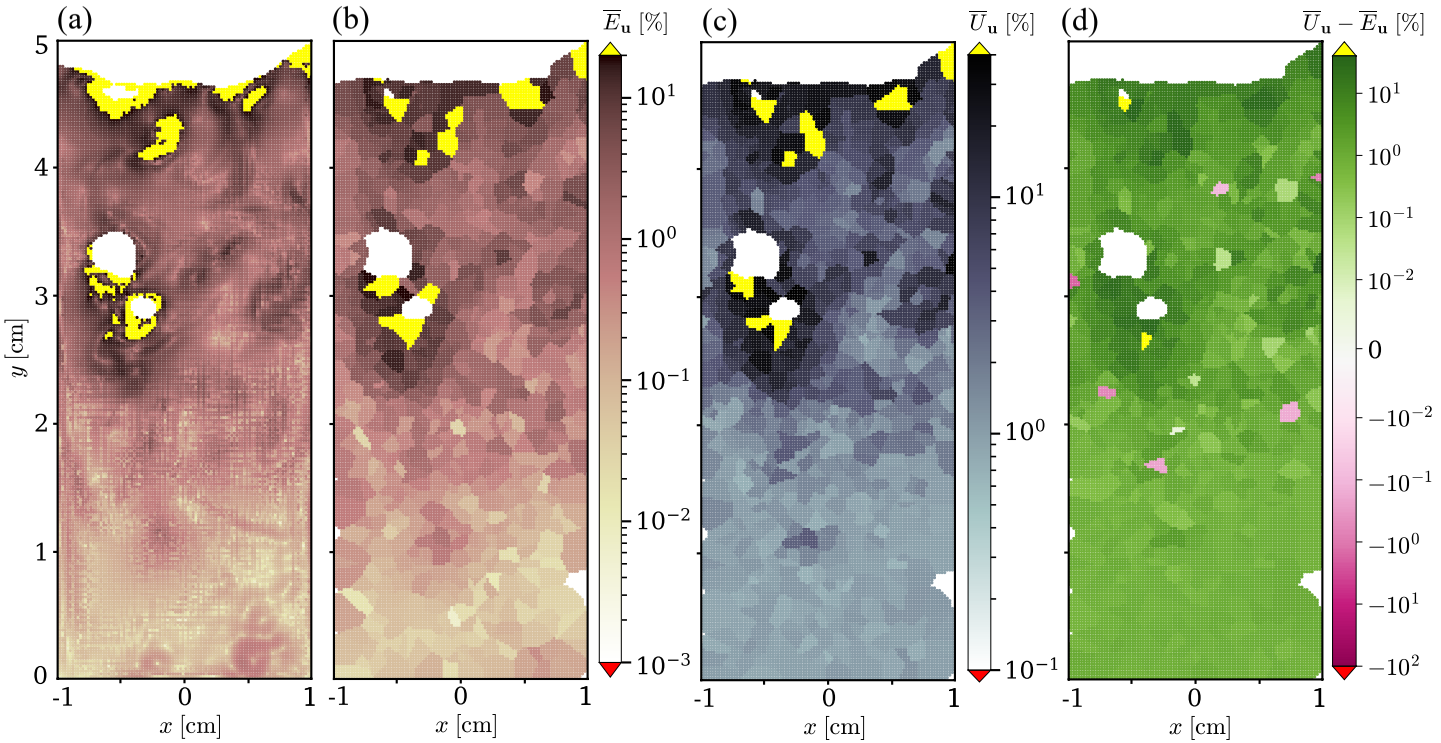


Figure 5.9: Averaged velocity UQ results for noise level 1 at $t = 0.3$ s. From left to right, subfigures (a) – (d) show the averaged true relative reconstruction error $\overline{E}_{\boldsymbol{u}}$ on the mesh, the averaged true relative reconstruction error $\overline{E}_{\boldsymbol{u}}$ at tracers, the averaged uncertainty estimate $\overline{U}_{\boldsymbol{u}}$, and the difference map $\overline{U}_{\boldsymbol{u}} - \overline{E}_{\boldsymbol{u}}$, respectively. In subfigure (d), green indicates $\overline{U}_{\boldsymbol{u}} > \overline{E}_{\boldsymbol{u}}$, and magenta indicates $\overline{U}_{\boldsymbol{u}} < \overline{E}_{\boldsymbol{u}}$.

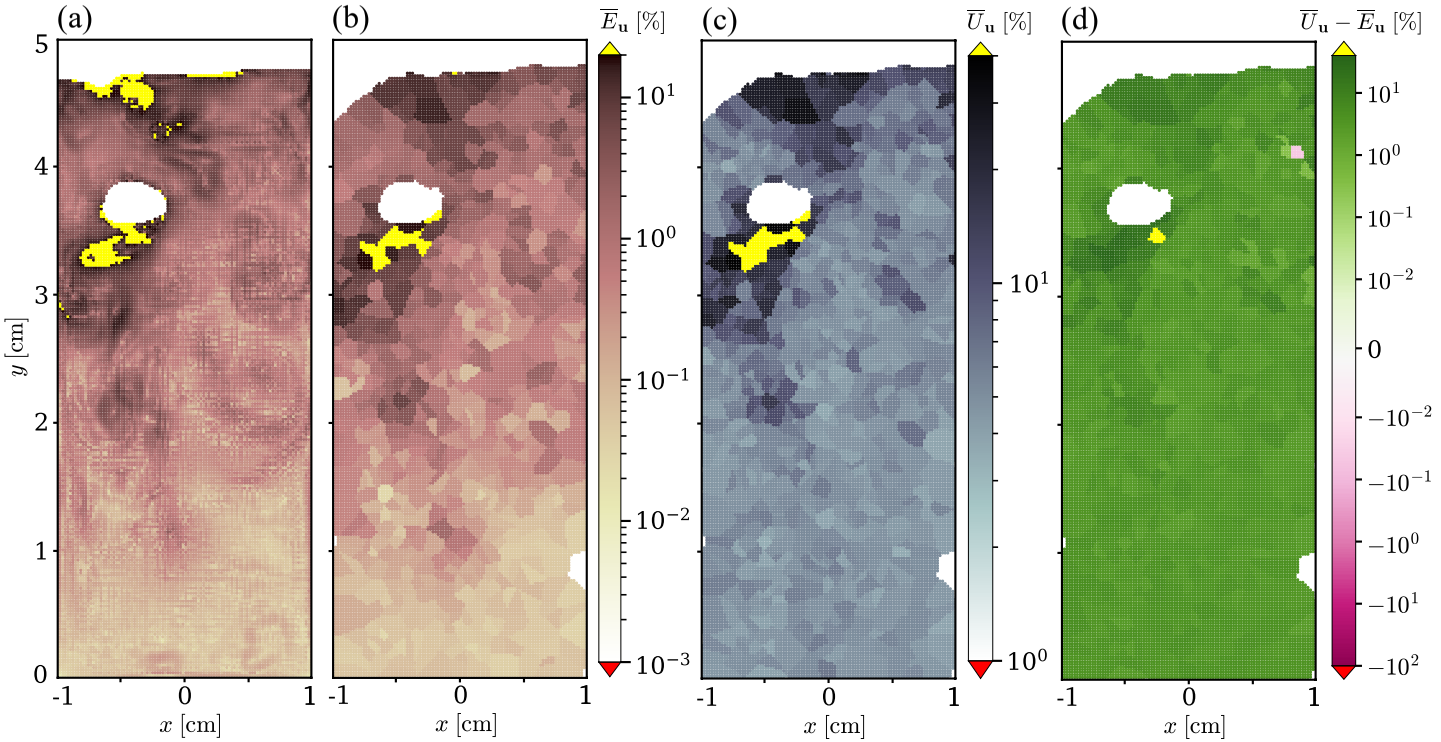


Figure 5.10: Averaged velocity UQ results for noise level 2 at $t = 0.35$ s. From left to right, subfigures (a) – (d) show the averaged true relative reconstruction error $\overline{E}_{\boldsymbol{u}}$ on the mesh, the averaged true relative reconstruction error $\overline{E}_{\boldsymbol{u}}$ at tracers, the averaged uncertainty estimate $\overline{U}_{\boldsymbol{u}}$, and the difference map $\overline{U}_{\boldsymbol{u}} - \overline{E}_{\boldsymbol{u}}$, respectively. In subfigure (d), green indicates $\overline{U}_{\boldsymbol{u}} > \overline{E}_{\boldsymbol{u}}$, and magenta indicates $\overline{U}_{\boldsymbol{u}} < \overline{E}_{\boldsymbol{u}}$.

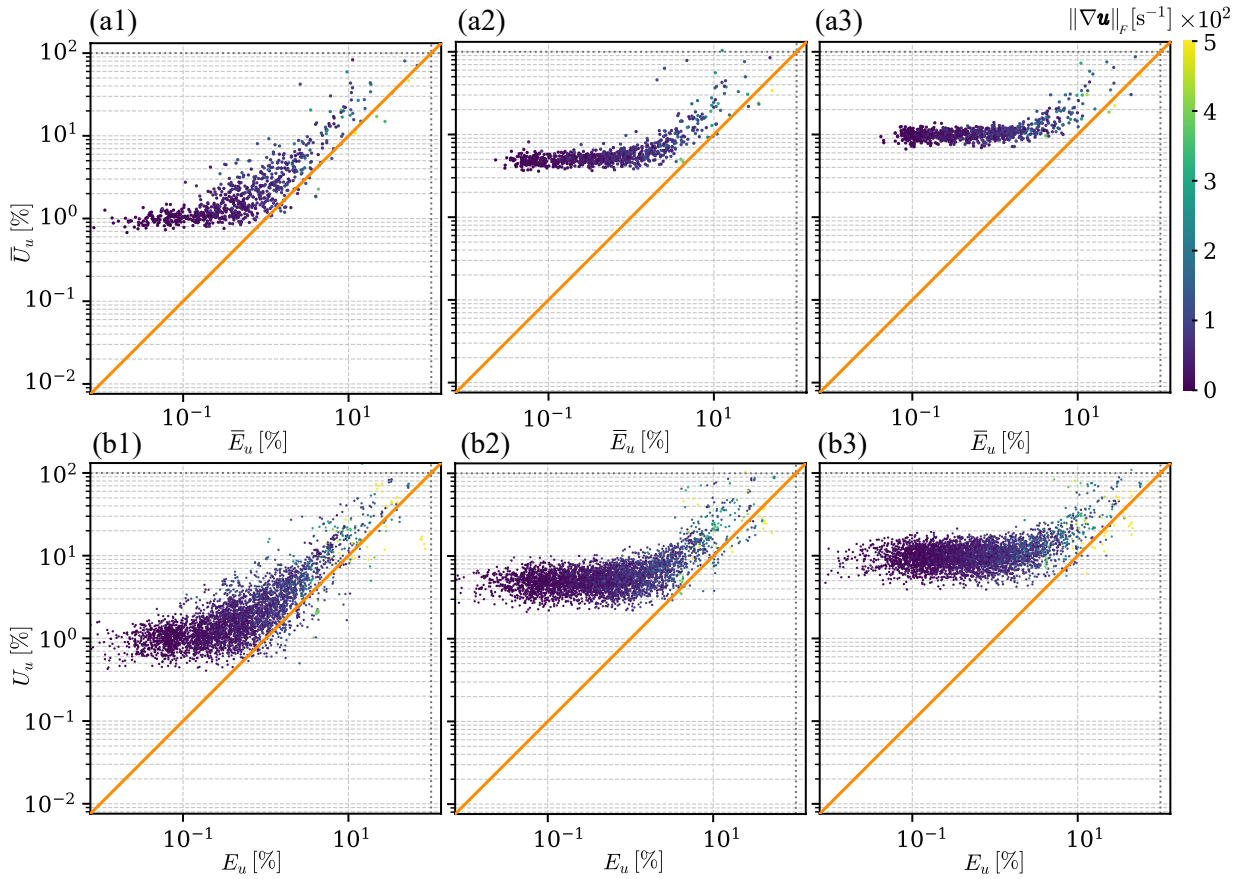


Figure 5.11: Comparison between the true relative velocity error and the uncertainty estimate at $t = 0.4$ s. Subfigures (a1) – (a3) show the trial-averaged quantities $\overline{E}_{\boldsymbol{u}}$ and $\overline{U}_{\boldsymbol{u}}$, whereas subfigures (b1) – (b3) show all individual tracer samples from the five trials without averaging. Columns 1 – 3 correspond to noise levels 1, 2, and 3, respectively. Each point represents a tracer location, and its color denotes the local velocity-gradient magnitude $\|\nabla \boldsymbol{u}\|_F$. The orange diagonal denotes $\overline{U}_{\boldsymbol{u}} = \overline{E}_{\boldsymbol{u}}$ or $U_{\boldsymbol{u}} = E_{\boldsymbol{u}}$; points above the diagonal indicate conservative uncertainty estimates, whereas points below it indicate local underestimation.

5.4 Conclusions

This chapter developed a residual-based UQ model for AOT-nudging reconstruction of bubbly flows. The proposed uncertainty estimates are derived using the triangle inequality and first-order Taylor approximations. The estimates are computable from the reconstruction residuals (i.e., the AOT-nudging terms), prescribed observation-error bounds, and, for the velocity field, interpolation errors from mapping data between tracer locations and mesh cells.

For the volume-fraction field, the uncertainty is represented by a spatial region obtained by expanding the residual region according to the prescribed interface-position uncertainty. The residual region is defined by the nonzero support of the thresholded observation–reconstruction residual and therefore identifies the mesh cells in which the observed and reconstructed bubble interfaces differ. Expanding this region inward and outward accounts for uncertainty in the measured interface position.

For the velocity field, the uncertainty is estimated from the local velocity residual (i.e., the momentum AOT-nudging terms), the prescribed velocity-observation uncertainty, and the interpolation error introduced by nearest interpolation. The UQ model further suggests that replacing nearest interpolation with a more accurate interpolation scheme could reduce both the interpolation-induced uncertainty and the reconstruction error, particularly in regions with strong velocity gradients. Consequently, for a prescribed reconstruction accuracy, improved interpolation may reduce the spatial density of observations required.

Synthetic validation showed that the proposed UQ model captures the main spatial distributions of the true reconstruction errors. The volume-fraction uncertainty is concentrated near the gas–liquid interfaces and encloses most of the true interface-error region. The velocity uncertainty is large in bubble wakes, recirculation, and regions with strong velocity gradients, where sparse sampling and interpolation errors are most significant. At low noise levels, the velocity uncertainty remains accurate and sharp; as the observation noise increases, it becomes conservative. Overall, the proposed framework identifies the regions of reduced reconstruction reliability and quantifies the effect of observation uncertainty on the reconstructed bubbly-flow fields.

Chapter 6

AOT-Nudging with Inertial Particle Tracking

6.1 Introduction

In real experiments, tracer particles do not always follow the fluid motion exactly. The density, finite size, and finite response time of tracers can produce a non-zero slip velocity relative to the carrier fluid. The dynamics of a small spherical inertial particle can be described by the Maxey–Riley–Gatignol equation [386, 387]. This equation includes the effects of drag, buoyancy, pressure gradient, added mass, and history forces. In practice, this full equation is simplified to a particle response time model in the Stokes regime. The response time depends on the particle size, particle density, and fluid viscosity, while its importance relative to the surrounding flow is characterized by the Stokes number. Therefore, accurate tracer measurements require particles that are sufficiently small and close in density to the carrier fluid [73, 125, 388–390].

Tracer fidelity has long been recognized as an important concern in image velocimetry. Conventional PIV/LPT tracers are typically micron-sized particles selected to follow the carrier-fluid motion with limited slip [389, 391, 392]. For larger-scale gas-flow experiments, Helium-Filled Soap Bubbles (HFSB) have also been used as tracers [393–395]. They make it possible to use sub-millimeter tracers while maintaining acceptable response characteristics. However, even nearly neutrally buoyant tracers can show non-negligible slip in accelerated or strongly sheared regions. In such cases, unsteady forces may become important for accurate flow tracking [390, 394, 395].

Several PIV studies quantify or correct inertial particle effects. The first group of studies focuses on particle response-time evaluation. For example, Ragni et al. [392] measured particle response across a shock wave using a single-exponential decay model. In addition, Chen et al. [396] modeled particle relaxation across shock waves while considering compressibility and rarefaction effects. The resulting response-time estimates were then used to assess PIV measurement fidelity and guide tracer selection.

A second group of studies uses numerical simulations and synthetic images to analyze tracer inertia bias. For example, Burns et al. [397] combined Large Eddy Simulation (LES), particle tracking, synthetic image generation, and PIV processing to examine how particle inertia and PIV processing parameters affect the measured velocity field. Martins et al. [398] combined LES with particle tracking to analyze the bias caused by particle lag and intermittent particle seeding. Aultman et al. [399] studied the influence of particle lag on hypersonic turbulent statistics using Direct Numerical Simulation (DNS) data. These studies show that PIV bias can arise from both tracer inertia and measurement-processing choices, such as interrogation window size and image resolution.

A third group of studies develops models to correct tracer-inertia bias in measured velocities. For example, Koike et al. [400] proposed a correction method based on the Stokes drag law. In this method, the measured particle velocity is corrected using a particle-response model to better represent the carrier-flow velocity. Kalagotla et al. [401] proposed a deep-learning-based tracer-inertia bias corrector for shock-wave PIV measurements. Their method uses synthetic PIV data to train a neural network. The neural network corrects tracer inertia bias. These studies demonstrate that tracer inertia effects can be estimated or compensated. However, these approaches either employ open-loop corrections without DA feedback or have not been demonstrated for multiphase-flow reconstruction.

Recent LPT/PTV reconstruction studies move beyond the ideal-tracer assumption. Zhou et al. [402] proposed Stochastic Particle Advection Velocimetry (SPAV). In SPAV, measured particle tracks are compared with particles advected by the reconstructed velocity field. SPAV uses a particle-advection model and can account for inertial particle effects, such as drag. It also accounts for localization and tracking uncertainty in the particle-position measurements. Similarly, Zhou and Grauer [403] developed a reconstruction framework for inertial Lagrangian tracks. Their method couples the carrier-flow equations with particle-transport equations. By doing this, the flow field and unknown particle properties, such as particle size and density, can be estimated together from LPT data. More recently, Zhou and Grauer [404] further investigated the joint estimation of flow fields and particle properties from Lagrangian data. They showed that particle inertia, measurement noise, and seeding density strongly affect the reconstruction quality of the

carrier-flow field. These studies show that inertial particles should not always be treated as direct fluid-velocity probes. Instead, their trajectories can be interpreted through a particle-dynamics observation model. However, these methods are mainly developed for single-phase or general particle-laden flow reconstruction. Romanò [405] reconstructed the background fluid velocity from the trajectories of a few large, density-mismatched particles with different Stokes numbers. This method interpolates the particle velocity in a phase space defined by particle properties and position, and then evaluates the limit $\mathrm{St} \to 0$ to recover the underlying fluid flow.

These considerations and gaps motivate the present chapter. When particle positions are used as the primary observations for data assimilation, finite particle inertia cannot be ignored. The tracked particle motion needs to be converted into information about the underlying liquid-phase motion. If this conversion assumes that particles are perfect tracers, the inferred liquid velocity may be biased in regions where particle slip is important. Therefore, an inertial correction is needed to obtain a reliable estimate of the liquid-phase kinematics from particle trajectories.

This chapter extends the AOT-nudging framework in Chap. 4 to a liquid-gas-solid flow, i.e., a three-phase flow. A new AOT-nudging solver explicitly tracks dispersed inertial tracer particles. In this three-phase system, a dilute population of solid particles is transported by the liquid-gas carrier flow. Unlike the solver presented in Chap. 4, the present solver tracks the dispersed inertial particles directly within the simulation. The resulting particle trajectories provide localized kinematic information in the liquid phase.

This chapter is organized as follows. Sect. 6.2 presents the methodology of the proposed AOT-nudging solver with inertial particle tracking. Sect. 6.3 presents the validation results for a two-dimensional bubble-rise case with inertial tracer particles. Sect. 6.4 summarizes the main findings of this chapter.

6.2 Methodology

The solver extends the AOT-nudging solver developed in Chap. 4. The main extensions are Lagrangian particle tracking (see Sects. 6.2.1 and 6.2.2), an inertial-particle correction (see Sect. 6.2.3), and a particle-based observation nudging pathway (see Sect. 6.2.5). The carrier-flow equations remain based on the incompressible two-phase VoF formulation (see Sect. 4.2.1 and Appx. A).

6.2.1 Governing equations

The Eulerian carrier flow is governed by the AOT-nudging VoF equations [86, 87, 292]:

$$\begin{aligned}
\nabla \cdot \boldsymbol{u} &= 0, \\
\frac{\partial(\rho \boldsymbol{u})}{\partial t} + \nabla \cdot (\rho \boldsymbol{u}\boldsymbol{u}) &= -\nabla p_{\mathrm{rgh}} + \nabla \cdot (\mu \nabla \boldsymbol{u}) + \nabla \boldsymbol{u} \cdot \nabla \mu \\
&\quad + \sigma \kappa \nabla \alpha - \boldsymbol{g} \cdot \boldsymbol{h} \nabla \rho \\
&\quad + K_{\mathrm{vel}} \left[\mathscr{I}_{\boldsymbol{u},h}(\boldsymbol{u}^{\mathrm{obs,f}}) - \mathscr{I}_{\boldsymbol{u},h}(\boldsymbol{u}) \right], \\
\frac{\partial \alpha}{\partial t} + \nabla \cdot (\alpha \boldsymbol{u}) + \nabla \cdot [\boldsymbol{u}_{\mathrm{rc}} \alpha (1-\alpha)] &= K_{\mathrm{vol}} \left[\mathscr{I}_{\alpha,h}(\alpha^{\mathrm{obs}}) - \mathscr{I}_{\alpha,h}(\alpha) \right],
\end{aligned} \tag{6.1}$$

where $\boldsymbol{u}$ is the carrier-flow velocity and α is the volume fraction. The density ρ, viscosity μ, modified pressure p_{rgh}, interface curvature κ, compression velocity $\boldsymbol{u}_{\mathrm{rc}}$, velocity nudging strength K_{vel}, volume-fraction nudging strength K_{vol}, and the interpolants $\mathscr{I}_{\boldsymbol{u},h}$ and $\mathscr{I}_{\alpha,h}$ follow the same definitions in Sect. 4.2.1. The field α^{obs} is obtained from bubble-image observations, which is the same as that in Sect. 4.2.1. The field $\boldsymbol{u}^{\mathrm{obs,f}}$ is the inferred liquid-phase velocity observation obtained from particle trajectories, as described in Sect. 6.2.3.

The particle motion is governed by a simplified Maxey–Riley–Gatignol equation [386, 387] with a particle-trajectory nudging term:

$$\frac{d\boldsymbol{x}_{\mathrm{p}}}{dt} = \boldsymbol{u}_{\mathrm{p}}, \tag{6.2a}$$

$$m_{\mathrm{p}} \frac{d\boldsymbol{u}_{\mathrm{p}}}{dt} = \boldsymbol{F}_G + \boldsymbol{F}_D + \boldsymbol{F}_{AM} + \boldsymbol{F}_{\nabla p} + \boldsymbol{F}_L + \underbrace{m_{\mathrm{p}} K_{\mathrm{pos}} \left(\boldsymbol{x}_{\mathrm{p}}^{\mathrm{obs}} - \boldsymbol{x}_{\mathrm{p}} \right)}_{\boldsymbol{F}_{\mathrm{NUG,p}}}, \tag{6.2b}$$

where $\boldsymbol{x}_{\mathrm{p}}$, $\boldsymbol{u}_{\mathrm{p}}$, and m_{p} are the particle position, velocity, and mass, respectively. The physical forces are net gravity-buoyancy force $\boldsymbol{F}_G$, drag $\boldsymbol{F}_D$, added mass $\boldsymbol{F}_{AM}$, pressure-gradient force $\boldsymbol{F}_{\nabla p}$, and shear-induced lift $\boldsymbol{F}_L$; K_{pos} is the particle-position nudging strength. The vectors $\boldsymbol{x}_{\mathrm{p}}^{\mathrm{obs}}$ and $\boldsymbol{x}_{\mathrm{p}}$ are the observed and reconstructed particle positions, respectively. The term $\boldsymbol{F}_{\mathrm{NUG,p}}$ is a numerical particle-trajectory nudging force. It reduces the mismatch between observed and reconstructed particle trajectories. This term is not a physical force. It is a numerical feedback term used to keep the reconstructed particle trajectories consistent with the observed trajectories. In addition, particle rotation and Basset history force are not considered in this thesis.

6.2.2 Particle force models

Particle force models in (6.2b) are based on the assumption that each particle is spherical, with diameter d_p, density ρ_p, volume $V_\mathrm{p} = \pi d_\mathrm{p}^3/6$, projected area $A_\mathrm{p} = \pi d_\mathrm{p}^2/4$, and mass $m_\mathrm{p} = \rho_\mathrm{p} V_\mathrm{p}$ [386, 387, 406]. The gravity-buoyancy force is modeled as

$$\boldsymbol{F}_G = (\rho_\mathrm{p} - \rho_\mathrm{f}) V_\mathrm{p} \boldsymbol{g},$$

where ρ_f is the local carrier flow density at the particle position [386, 406]. This term represents the net effect of particle weight and fluid buoyancy.

The drag force is modeled as

$$\boldsymbol{F}_D = \frac{1}{2} \rho_\mathrm{f} C_D A_\mathrm{p} \|\boldsymbol{u}_\mathrm{f} - \boldsymbol{u}_\mathrm{p}\| (\boldsymbol{u}_\mathrm{f} - \boldsymbol{u}_\mathrm{p}),$$

where $\boldsymbol{u}_\mathrm{f}$ is the carrier velocity sampled at the particle position [386, 389, 407]. The drag coefficient is evaluated from the Schiller-Naumann model [407]:

$$C_D = \begin{cases} \dfrac{24}{\mathrm{Re}_\mathrm{p}} \left(1 + 0.15 \mathrm{Re}_\mathrm{p}^{0.687}\right), & \mathrm{Re}_\mathrm{p} < 1000, \\ 0.44, & \mathrm{Re}_\mathrm{p} \geq 1000, \end{cases} \qquad \mathrm{Re}_\mathrm{p} = \frac{\rho_\mathrm{f} d_\mathrm{p} \|\boldsymbol{u}_\mathrm{f} - \boldsymbol{u}_\mathrm{p}\|}{\mu_\mathrm{f}},$$

where Re_p is the particle Reynolds number and μ_f is the local carrier dynamic viscosity.

The added-mass force accounts for the inertia of the fluid displaced by the accelerating particle:

$$\boldsymbol{F}_{AM} = C_{AM} \rho_\mathrm{f} V_\mathrm{p} \left(\frac{D\boldsymbol{u}_\mathrm{f}}{Dt} - \frac{d\boldsymbol{u}_\mathrm{p}}{dt} \right),$$

with $C_{AM} = 1/2$ for an isolated spherical particle in an unbounded fluid under the classical potential-flow approximation [386, 387, 406, 408]. $D\boldsymbol{u}_\mathrm{f}/Dt$ is the material derivative of the carrier flow velocity, and $d\boldsymbol{u}_\mathrm{p}/dt$ is the time derivative of the particle velocity along its trajectory. The added-mass force is important when the surrounding flow is strongly unsteady or when the particle and fluid densities are comparable.

The pressure-gradient force is [386, 387, 409]

$$\boldsymbol{F}_{\nabla p} = -V_\mathrm{p} \nabla p.$$

It represents the direct action of the carrier pressure gradient on the particle.

The shear-induced lift force is modeled using the Saffman-Mei model [410, 411]:

$$\boldsymbol{F}_L = C_L \rho_\mathrm{f} \nu_\mathrm{f}^{1/2} d_\mathrm{p}^2 \|\boldsymbol{S}\|^{1/2} \left[(\boldsymbol{u}_\mathrm{f} - \boldsymbol{u}_\mathrm{p}) \times \hat{\boldsymbol{\omega}} \right],$$

where ν_f is the local kinematic viscosity of the carrier flow, $\boldsymbol{S}$ is the strain-rate tensor, $\boldsymbol{\omega} = \nabla \times \boldsymbol{u}_\mathrm{f}$, and $\hat{\boldsymbol{\omega}} = \boldsymbol{\omega}/\|\boldsymbol{\omega}\|$. The coefficient C_L is evaluated from the particle and vorticity Reynolds numbers:

$$\mathrm{Re}_\mathrm{p} = \frac{\rho_\mathrm{f} d_\mathrm{p} \|\boldsymbol{u}_\mathrm{f} - \boldsymbol{u}_\mathrm{p}\|}{\mu_\mathrm{f}}, \qquad \mathrm{Re}_\omega = \frac{\rho_\mathrm{f} d_\mathrm{p}^2 \|\boldsymbol{\omega}\|}{\mu_\mathrm{f}}.$$

Then,

$$\beta = \frac{1}{2}\frac{\mathrm{Re}_\omega}{\mathrm{Re}_\mathrm{p}}, \qquad \gamma_\mathrm{SM} = 0.3314\sqrt{\beta}, \qquad \zeta = (1-\gamma_\mathrm{SM})\exp(-0.1\mathrm{Re}_\mathrm{p}) + \gamma_\mathrm{SM}.$$

The Saffman-Mei lift coefficient is

$$C_L = \frac{3}{2\pi\sqrt{\mathrm{Re}_\omega}} \begin{cases} 6.46\zeta, & \mathrm{Re}_\mathrm{p} < 40, \\ 0.34\sqrt{\beta \mathrm{Re}_p}, & \mathrm{Re}_\mathrm{p} \geq 40. \end{cases}$$

This term affects particle motion in sheared regions, such as bubble wakes and near-wall flows.

6.2.3 Particle inertia correction

In (6.1), $\boldsymbol{u}^{\mathrm{obs,f}}$ is not directly available since the particles are inertial and their velocities do not necessarily equal the local liquid-phase velocity. Therefore, $\boldsymbol{u}^{\mathrm{obs,f}}$ must be inferred from the kinematics of particles using a particle-response model. A correction model is adapted from [400] to infer the liquid-phase velocity, where the liquid-phase velocity can be calculated from the particle velocity using a correction term based on the particle response-time model.

For a spherical particle in the Stokes-drag regime, the particle response time is modeled as [73, 388, 389]

$$\tau_\mathrm{p} = \frac{\rho_\mathrm{p} d_\mathrm{p}^2}{18\mu_\mathrm{f}}. \tag{6.3}$$

The derivation of (6.3) can be found in Appx. C. For ideal tracers, the observed particle velocity can be used directly as the local liquid-velocity observation without using (6.3):

$$\boldsymbol{u}_\mathrm{p}^{\mathrm{obs,f}} = \boldsymbol{u}_\mathrm{p}^{\mathrm{obs}}. \tag{6.4}$$

Equation (6.4) is valid only when the particle response time is much shorter than the characteristic flow time scale [73, 388–390].

For inertial particles, the particle velocity differs from the local liquid velocity. The inferred liquid velocity is approximated using a simplified particle response model. This model is derived from the Maxey–Riley–Gatignol equation [386, 387] by retaining the Stokes drag and net gravity-buoyancy terms, neglecting added mass, pressure-gradient, lift, and history forces [73, 386–390, 412]:

$$\boldsymbol{a}_{\mathrm{p},n}^{\mathrm{obs}} \approx \frac{\boldsymbol{u}_{\mathrm{p},n}^{\mathrm{obs,f}} - \boldsymbol{u}_{\mathrm{p},n}^{\mathrm{obs}}}{\tau_{\mathrm{p}}} + \boldsymbol{b}_{\mathrm{p}}, \tag{6.5}$$

where $\boldsymbol{b}_{\mathrm{p}}$ is the gravity-buoyancy contribution, and n is the time step. Rearranging (6.5) gives the inferred liquid-phase velocity:

$$\boldsymbol{u}_{\mathrm{p},n}^{\mathrm{obs,f}} \approx \boldsymbol{u}_{\mathrm{p},n}^{\mathrm{obs}} + \tau_{\mathrm{p}} \left(\boldsymbol{a}_{\mathrm{p},n}^{\mathrm{obs}} - \boldsymbol{b}_{\mathrm{p}} \right), \tag{6.6}$$

where the observed particle velocity and acceleration are reconstructed from consecutive observed positions using the backward Euler method:

$$\boldsymbol{u}_{\mathrm{p},n}^{\mathrm{obs}} = \frac{\boldsymbol{x}_{\mathrm{p},n}^{\mathrm{obs}} - \boldsymbol{x}_{\mathrm{p},n-1}^{\mathrm{obs}}}{\Delta t_n}, \qquad \boldsymbol{a}_{\mathrm{p},n}^{\mathrm{obs}} = \frac{\boldsymbol{u}_{\mathrm{p},n}^{\mathrm{obs}} - \boldsymbol{u}_{\mathrm{p},n-1}^{\mathrm{obs}}}{\Delta t_n}, \tag{6.7}$$

and the gravity-buoyancy contribution is

$$\boldsymbol{b}_{\mathrm{p}} = \left(1 - \frac{\rho_{\mathrm{f}}}{\rho_{\mathrm{p}}} \right) \boldsymbol{g}.$$

From (6.6), the particle velocity is corrected by an acceleration-dependent response term and a gravity-buoyancy term before it is used as a liquid-velocity observation.

Equation (6.6) can be interpreted through its asymptotic behavior with respect to the particle response time and the gravity-buoyancy imbalance. For a neutrally buoyant particle, $\boldsymbol{b}_{\mathrm{p}} = \boldsymbol{0}$, and the correction is determined only by the inertial term $\tau_{\mathrm{p}} \boldsymbol{a}_{\mathrm{p}}^{\mathrm{obs}}$. However, even for a neutrally buoyant particle, a large particle diameter can increase the response time because $\tau_{\mathrm{p}} \propto d_{\mathrm{p}}^2$, leading to a finite velocity lag. When the particle density differs from that of the carrier fluid, the gravity-buoyancy contribution appears explicitly through $\boldsymbol{b}_{\mathrm{p}}$. In this case, the particle may settle or rise due to the density mismatch even when the liquid is quiescent.

6.2.4 Discretization

The Eulerian carrier-flow discretization follows the finite-volume procedure introduced in Sect. 4.2.2. The volume-fraction equation is solved first. The mixture properties are

then updated from the new volume-fraction field. The momentum predictor and pressure-correction steps are solved within the PIMPLE loop. The main difference in this chapter is that the Eulerian velocity-nudging term is built from particle-position observations instead of direct velocity observations.

At an observation time t_n, the inferred particle-based liquid velocity $\boldsymbol{u}_{\mathrm{p},n}^{\mathrm{obs,f}}$ is obtained from (6.6). The reconstructed velocity is obtained by sampling the reconstructed velocity field at the observed particle location, i.e., $\boldsymbol{u}\big(\boldsymbol{x}_{\mathrm{p},n}^{\mathrm{obs}}\big)$. Thus, the particle-wise velocity discrepancy is

$$\Delta\boldsymbol{u}_{\mathrm{p},n} = \boldsymbol{u}_{\mathrm{p},n}^{\mathrm{obs,f}} - \boldsymbol{u}\big(\boldsymbol{x}_{\mathrm{p},n}^{\mathrm{obs}}\big)\,. \tag{6.8}$$

This discrepancy is transferred to the mesh using the same observation-to-mesh interpolation strategy as in Sect. 4.2.3. Based on (6.8), the cell-centered velocity nudging correction is

$$\boldsymbol{n}_{u,\mathrm{P}}^{n} = K_{\mathrm{vel}}\Delta\boldsymbol{u}_{\mathrm{P},n}, \tag{6.9}$$

where $\Delta\boldsymbol{u}_{\mathrm{P},n}$ is the velocity discrepancy $\Delta\boldsymbol{u}_{\mathrm{p},n}$ mapped from particle p to the cell P, using the interpolants $\mathscr{I}_{\boldsymbol{u},h}$.

With (6.9), the momentum predictor becomes

$$\mathrm{A}_{u,\mathrm{P}}^{\mathrm{n}}\mathbf{U}_{\mathrm{P}}^{*} = -\sum_{N\in\mathcal{N}(\mathrm{P})}\mathrm{A}_{u,\mathrm{N}}^{\mathrm{n}}\mathbf{U}_{\mathrm{N}}^{*} + \mathrm{S}_{u,\mathrm{P}}^{\mathrm{n}} + \rho_{\mathrm{P}}\boldsymbol{n}_{u,\mathrm{P}}^{n} - \nabla p_{\mathrm{rgh,P}}^{\mathrm{n}},$$

where $\mathrm{A}_{u}^{\mathrm{n}}$ contains the temporal, convective, and diffusive coefficients. The source term $\mathrm{S}_{u,\mathrm{P}}^{\mathrm{n}}$ contains the standard body force contributions, including gravity and surface tension. The additional term $\rho_{\mathrm{P}}\boldsymbol{n}_{u,\mathrm{P}}^{\mathrm{n}}$ is the particle-derived nudging source. After the momentum predictor is assembled, the pressure Poisson equation and velocity correction are solved with the same PIMPLE procedure as in Sect. 4.2.3.

The Lagrangian particle equations are advanced explicitly. For each particle,

$$\boldsymbol{u}_{\mathrm{p}}^{n+1} = \boldsymbol{u}_{\mathrm{p}}^{n} + \frac{\Delta t}{m_{\mathrm{p}}}\left(\boldsymbol{F}_{G}^{n} + \boldsymbol{F}_{D}^{n} + \boldsymbol{F}_{AM}^{n} + \boldsymbol{F}_{\nabla p}^{n} + \boldsymbol{F}_{L}^{n} + \boldsymbol{F}_{\mathrm{NUG,p}}^{n}\right), \tag{6.10}$$

$$\boldsymbol{x}_{\mathrm{p}}^{n+1} = \boldsymbol{x}_{\mathrm{p}}^{n} + \Delta t\,\boldsymbol{u}_{\mathrm{p}}^{n}. \tag{6.11}$$

The carrier-flow quantities required by the force models are sampled at the particle position. The particle-level nudging force is activated only when particle observations are available. The dispersed solid phase is assumed to be dilute. Therefore, physical two-way momentum coupling from the particles to the carrier flow is neglected. The particle observations nevertheless influence the carrier flow numerically through the AOT-nudging term.

6.2.5 AOT-nudging workflow

The solver procedure at the time step t_n is summarized as follows.

1. Infer liquid-phase velocity observations from particle kinematics. Reconstruct the observed particle velocity and acceleration from consecutive particle positions using (6.7). Use (6.6) to infer $\boldsymbol{u}_{\mathrm{p},n}^{\mathrm{obs,f}}$ for inertial particles.
2. Assemble velocity discrepancy. Sample the reconstructed velocity at the observed particle locations. Compute the particle-wise velocity discrepancy from (6.8). Transfer this discrepancy to the mesh and formulate the velocity-nudging field $\boldsymbol{n}_u^n$.
3. Assemble volume-fraction discrepancy. Compute the volume-fraction discrepancy between the observed and simulated volume fraction fields. Transfer this discrepancy to the mesh and form the volume-fraction nudging source, as in Sect. 4.2.3.
4. Solve the volume-fraction equation. Solve the VoF transport equation with the volume-fraction AOT-nudging source. Enforce boundedness using the MULES algorithm and update the mixture properties ρ, μ, and κ, as in Chap. 4.
5. Solve the momentum and pressure equations. Add the velocity-nudging field to the momentum predictor and solve the PIMPLE loop. This step updates the carrier-flow velocity and pressure while enforcing incompressibility.
6. Update the Lagrangian particle trajectories. Sample the updated carrier-flow fields at particle locations. Integrate the particle motion equations using (6.10) and (6.11).

The observation system contains two sources of observations. Bubble-silhouette observations provide the gas-liquid interface location and are converted into volume-fraction observations for the VoF solver, using the same procedure as in Chap. 4. Particle-position observations, instead of velocity observations used in Chap. 4, provide Lagrangian information about the liquid motion. For inertial particles, the observed particle motion is first corrected using the particle-response model before it is used for velocity nudging.

The coupling between these observations and the numerical solver is achieved through both Eulerian and Lagrangian pathways. From an Eulerian perspective, the volume-fraction observations correct the interface evolution, while the particle-derived liquid-velocity observations correct the carrier-flow momentum equation. From a Lagrangian perspective, the simulated particles are advanced by the reconstructed carrier flow and directly nudged toward the observed particle positions. Thus, the carrier flow affects particle motion via the physical force model, and particle observations feed back to the carrier flow via AOT-nudging.

6.3 Results and Discussion

This section presents the validation results for a 2D bubble-rise case with inertial tracer particles in a bubble column. The validation uses particles with St ≈ 1, for which the particle response time is comparable to the characteristic bubble-flow time scale. Therefore, the particles cannot be assumed to behave as ideal passive tracers.

The validation is based on synthetic observations generated from a ground-truth simulation. Three solutions are compared: the ground-truth solution, the baseline simulation without DA, and the AOT-nudging reconstruction.

6.3.1 Validation setup

The synthetic observations are generated from the ground-truth simulation, similar to that in Sect. 4.3.2. Bubble silhouettes are extracted from the ground-truth volume-fraction field and used as observations. Tracer particle positions are sampled from the ground-truth particle trajectories at prescribed observation times and used as Lagrangian observations. The volume-fraction observations are available only below $y = 4.5$ cm. The tracers are modeled as inertial spherical particles with density $\rho_\mathrm{p} = 1,380$ kg/m^3 and diameter $d_\mathrm{p} = 255.5$ μm. The nudging strengths are $K_\mathrm{vel} = 200$ and $K_\mathrm{vol} = 200$, and the particle-position nudging strength is $K_\mathrm{pos} = 10^6$. Compared with the ground truth, the AOT-nudging reconstruction starts from different bubble sizes and positions and with zero initial bubble-rise velocity, as shown in Fig. 6.1. The baseline simulation shares the same initial conditions as the ground truth. All other numerical settings are the same as those used in Sect. 4.3.2.

Figure 6.2 shows the initial tracer distribution and the ground-truth particle trajectories used to generate the synthetic observations. At the initial state, the particles are randomly distributed throughout the liquid phase while avoiding the gas regions. As the bubbles rise, the particles are advected into the bubble-induced recirculation zones and wake structures. The time-colored trajectories in Fig. 6.2 (b) show that the particle paths organize into curved pathlines around the bubbles in the wake. The velocity-colored trajectories in Fig. 6.2 (c) show that the highest particle speeds occur near the upper bubble and in the immediately surrounding liquid. A gradual downward migration of particles is also observed, caused by the particle density being greater than the carrier-fluid density.

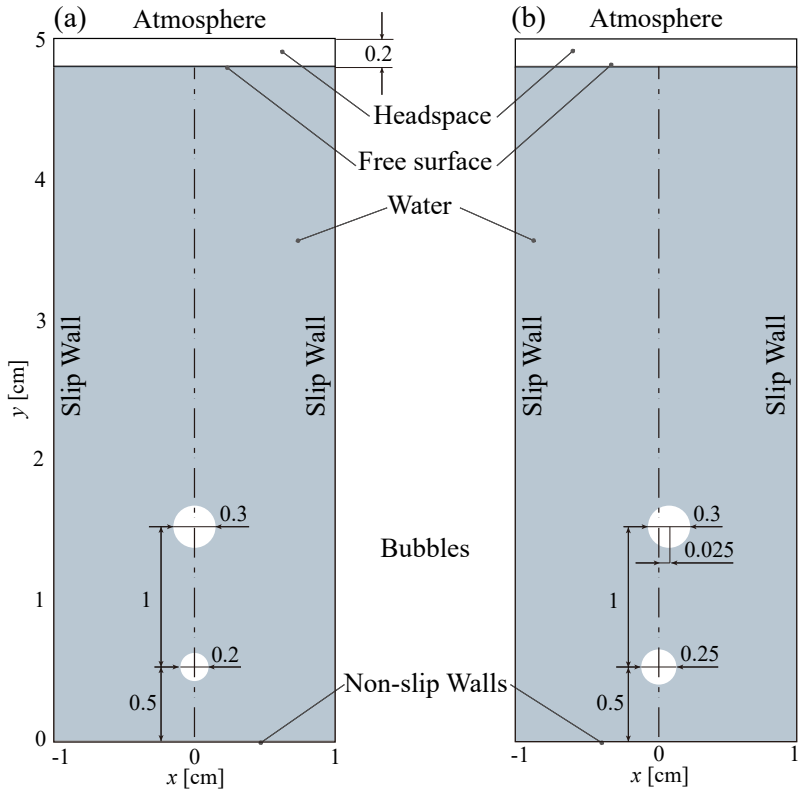


Figure 6.1: Initial and boundary conditions for the reference solution and the AOT-nudging with inertial particle tracking reconstruction. The left panel (a) shows the reference case, and the right panel (b) shows the initial and boundary conditions used in the AOT-nudging reconstruction with inertial particle tracking. In both cases, the bubble centers are arranged symmetrically with respect to the centerline. In the reference solution, the upper bubble has an upward vertical velocity of $0.02\,\mathrm{m\,s^{-1}}$, whereas in the AOT-nudging reconstruction case, the liquid phase and all bubbles are initially at rest. All units are in centimeters.

6.3.2 Non-dimensional analysis

To identify the dominant particle-force balances, several non-dimensional parameters are evaluated. The characteristic length and velocity are chosen from the bubble-induced carrier flow, with $L_\mathrm{c} = D_\mathrm{b} = 2$ mm and $u_\mathrm{c} = u_\mathrm{b} \approx 0.4$ m s^{-1}. D_b is the bubble diameter and u_b is the mean of the maximum bubble rising velocity. Thus, the characteristic bubble-

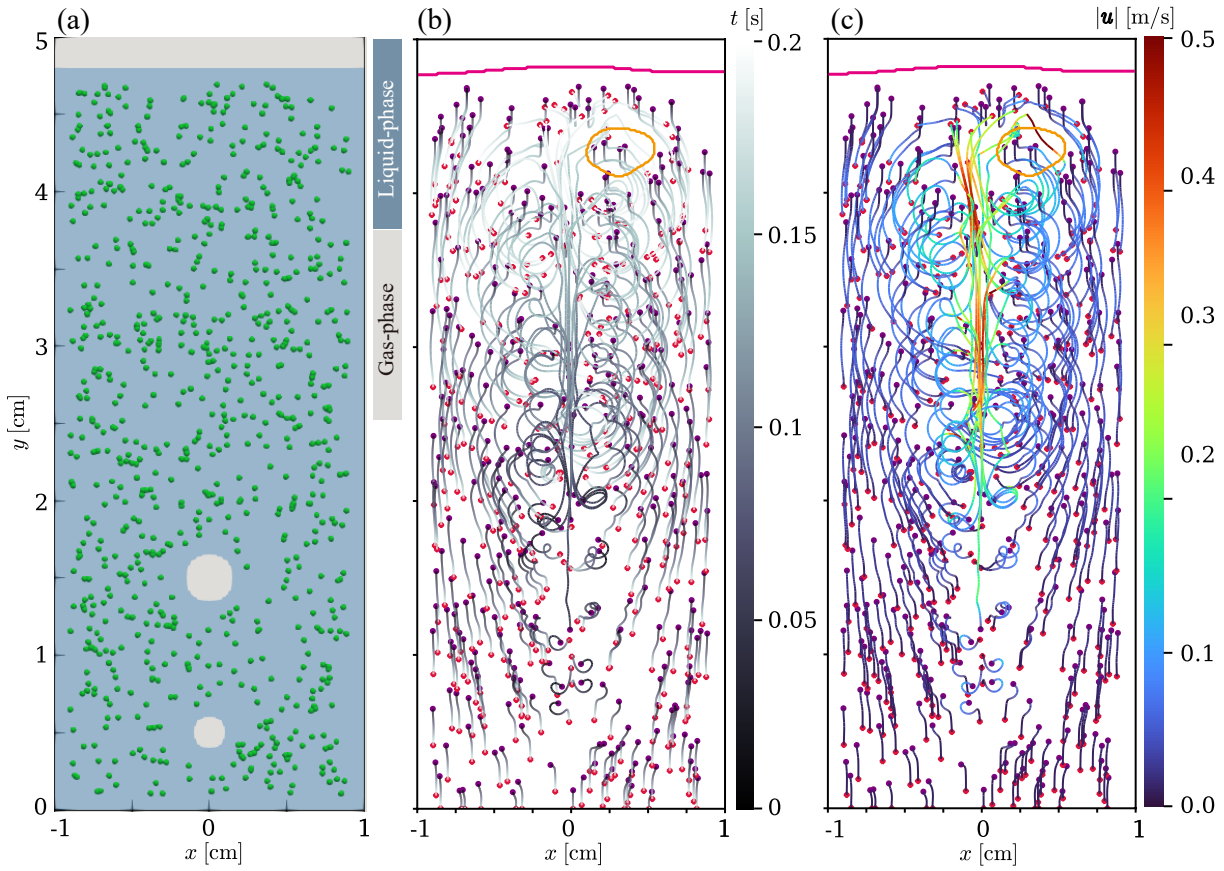


Figure 6.2: Inertial Lagrangian tracer initialization and trajectories in the 2D bubble rise case. (a) Initial tracer-particle distribution in the liquid phase. (b) Particle trajectories over $0 \leq t \leq 0.2$ s, colored by time. (c) The same trajectories colored by tracer velocity magnitude $|\boldsymbol{u}|$. In (b) and (c), the initial and end positions of particles are denoted by purple and red dots, respectively; the bubble outlines and free surface are illustrated by orange and pink curves, respectively.

flow time scale is

$$T_{\mathrm{c}} = \frac{L_{\mathrm{c}}}{u_{\mathrm{c}}} = \frac{D_{\mathrm{b}}}{u_{\mathrm{c}}} = \frac{2 \times 10^{-3}}{0.4} = 5.0 \times 10^{-3} \text{ s}.$$

Using $\mu_{\mathrm{f}} = \rho_{\mathrm{f}} \nu_{\mathrm{f}} = 998 \times 10^{-6} \approx 9.98 \times 10^{-4}$ Pa $\cdot$ s, the particle response time from (6.3) is $\tau_{\mathrm{p}} \approx 5.0 \times 10^{-3}$ s. The bubble-scale Stokes number is

$$\mathrm{St} = \frac{\tau_{\mathrm{p}}}{T_{\mathrm{c}}} \approx \frac{5.0 \times 10^{-3}}{5.0 \times 10^{-3}} = 1.$$

$\mathrm{St} \approx 1$ indicates that the particle response time is comparable to the bubble-flow time scale. Therefore, particle inertia is not negligible, and the particles cannot be treated as ideal passive tracers at this scale.

The density ratio is

$$r_\rho = \frac{\rho_\mathrm{p}}{\rho_\mathrm{f}} \approx \frac{1380}{998} \approx 1.38.$$

This value shows that gravity-buoyancy effects are present but moderate. It also indicates that the added-mass effect may influence the particle motion in unsteady regions.

The particle Reynolds number is evaluated using a representative slip velocity $u_\mathrm{slip} = |\boldsymbol{u}_\mathrm{f} - \boldsymbol{u}_\mathrm{p}| = 0.1$ m s^{-1}:

$$\mathrm{Re}_\mathrm{p} = \frac{\rho_\mathrm{f} d_\mathrm{p} |\boldsymbol{u}_\mathrm{f} - \boldsymbol{u}_\mathrm{p}|}{\mu_\mathrm{f}} = \frac{\rho_\mathrm{f} d_\mathrm{p} u_\mathrm{slip}}{\mu_\mathrm{f}} \approx 25.4.$$

$\mathrm{Re}_\mathrm{p} = 25.4$ suggests that the particles are in a low-to-moderate Reynolds-number regime, where the viscous drag remains the dominant particle force. The bubble Reynolds number is

$$\mathrm{Re}_\mathrm{b} = \frac{\rho_\mathrm{f} u_\mathrm{b} D_\mathrm{b}}{\mu_\mathrm{f}} \approx 800. \tag{6.12}$$

This value is consistent with inertial bubble motion accompanied by wake formation and recirculation. The Froude number is

$$\mathrm{Fr} = \frac{u_\mathrm{c}}{\sqrt{g L_\mathrm{c}}} = \frac{u_\mathrm{c}}{\sqrt{g D_\mathrm{b}}} \approx 3.5, \tag{6.13}$$

and it shows that inertial effects are strong at the bubble scale, although buoyancy remains the driving mechanism of the flow.

The Faxén correction [413] scales with $d_\mathrm{p}^2/(24 D_\mathrm{b}^2) = 6.5 \times 10^{-4}$, where $d_\mathrm{p} = 0.2555$ mm and $D_\mathrm{b} = 2$ mm. This indicates that finite-size spatial averaging is negligible. The Faxén correction may become important in the bubble wake, near the gas-liquid interface, or within thin liquid films, where the characteristic length scale of the velocity variation is smaller than D_b. However, the representative particle Reynolds number is $\mathrm{Re}_\mathrm{p} \approx 25.4$, so the creeping-flow assumptions in the classical Faxén correction are not strictly satisfied. Therefore, the Faxén term is neglected in the present particle model.

In summary, the estimates show that drag is the primary force governing particle response. The value $\mathrm{St} \approx 1$ indicates that inertial effects are important. The values $\mathrm{Re}_b \approx 800$ and $\mathrm{Fr} \approx 3.5$ indicate a bubble-driven flow with inertial motion, wake formation, and recirculation. Therefore, an inertial-particle correction is needed before particle observations are used for velocity nudging.

6.3.3 Validation results

Validation results are shown in Figs. 6.3 – 6.6. Figure 6.3 compares the ground-truth and reconstructed Lagrangian particle trajectories over three time intervals: $0.05 \leq t \leq 0.10$ s, $0.10 \leq t \leq 0.15$ s, and $0.15 \leq t \leq 0.20$ s. As shown in the figure, in the quiescent regions (e.g., $y \leq 0.05$ m), particles move downward with a settling velocity. This settling is caused by the particle density exceeding the liquid density. Above $y = 0.05$ m, the rising bubbles transport tracers upward and push tracers above the bubbles toward the free surface and lateral regions. The reconstructed start and end positions closely overlap their ground-truth counterparts. The reconstructed tracer trajectories and bubble outlines closely agree with those in the ground truth. Only a small number of reconstructed trajectories show a slight mismatch. The mismatch may be caused by fast tracer motion, limited temporal sampling, and the use of a constant nudging strength and a simplified correction model. In general, Fig. 6.3 shows that the proposed AOT-nudging solver can recover the Lagrangian tracer trajectories and bubble outlines despite using inertial tracers with a high Stokes number.

Figures 6.4 and 6.5 compare the liquid-phase velocity magnitude and velocity-gradient magnitude at $t = 0.2$ s, respectively. In the ground-truth solution, the two bubbles have coalesced and moved toward the free surface. A high-velocity region appears near the left side of the merged bubble, and a slender wake extends downward. The velocity-gradient field shows strong shear near the merged bubble and along the wake filament. The baseline simulation differs from these structures: the bubbles do not merge, the high-speed region is displaced, and the wake and gradient fields lose coherence. By contrast, the AOT-nudging reconstruction recovers the coalesced bubble shape, the high-velocity region, and the main wake structures. Some local smoothing remains in high-gradient regions due to reduced mesh resolution and sparse tracers. Nevertheless, the reconstructed fields are closer to the ground truth than the baseline simulation. This shows that assimilating volume-fraction observations together with inertial-particle observations improves both the liquid-phase velocity field and its gradient structures.

Figure 6.6 compares the vorticity field ω_z at $t = 0.2$ s, with tracer-particle locations overlaid. The particles are not uniformly distributed in the liquid domain. Fewer tracers are present near some high-vorticity structures. This is expected because inertial tracers have a finite response time and do not exactly follow rapid vortical motion. They are expelled from strong vortical cores and accumulate in lower-vorticity or strain-dominated regions. In addition, gravity-buoyancy imbalance causes particle settling in relatively quiescent regions. As a result, the particle observations provide non-uniform sampling of the liquid flow. Even with this local bias, the AOT-nudging reconstruction still captures the vortical

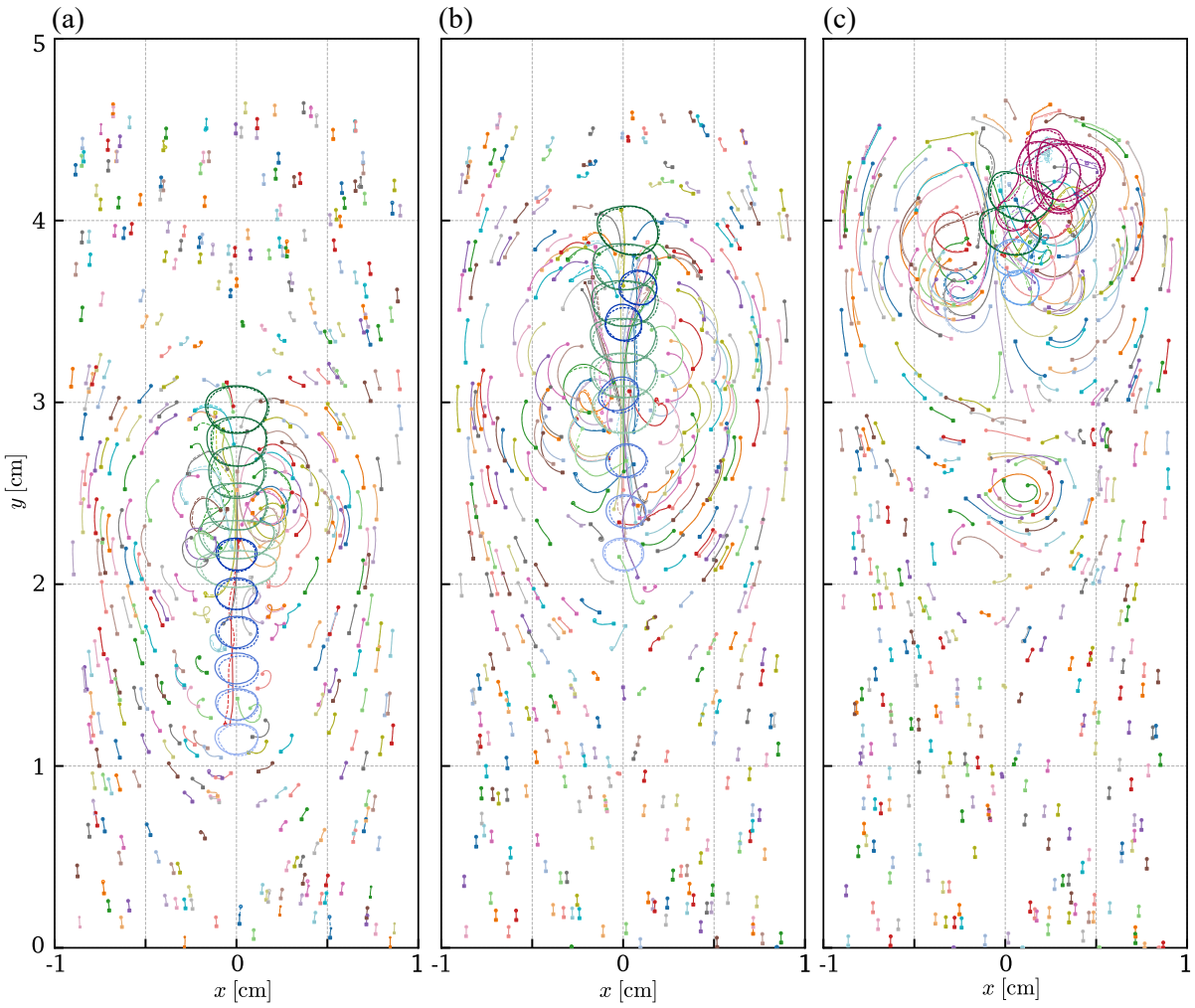


Figure 6.3: Comparison of ground-truth and reconstructed Lagrangian particle trajectories over three time intervals. Subfigures (a) – (c) show the trajectories over $0.05 \leq t \leq 0.10$ s, $0.10 \leq t \leq 0.15$ s, and $0.15 \leq t \leq 0.20$ s, respectively. Solid and dashed lines denote the ground-truth and reconstructed particle trajectories and bubbles, respectively. Circle and square markers represent the start and end of trajectories. The two bubbles are colored blue and green. When they merge, the merged bubble is shown in red. For illustration, 400 particles out of 800 are shown for clarity in each subfigure.

structures and tracer pathlines more accurately than the baseline simulation.

In summary, Figs. 6.3 – 6.6 show that the three-phase AOT-nudging framework can

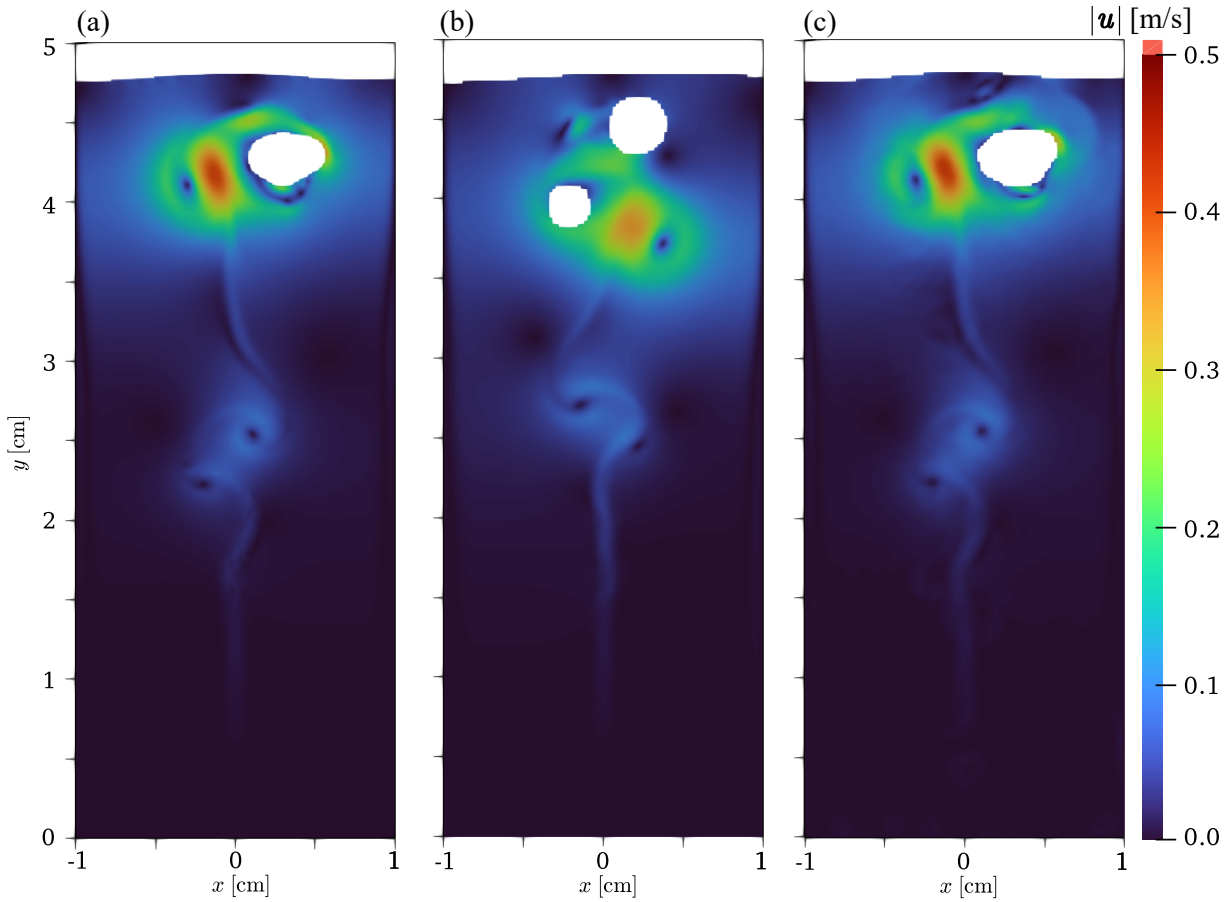


Figure 6.4: Comparison of liquid-phase velocity magnitude fields at $t = 0.2$ s. Subfigures (a) – (c) show the ground truth, the baseline simulation, and the three-phase AOT-nudging reconstruction, respectively.

be used to reconstruct the bubbly flow using inertial tracer particles. The results indicate that particle observations correct both individual particle trajectories and the bubble-driven liquid motion. The remaining discrepancies are reasonable because the tracers are discrete, sparse, and inertial rather than perfectly passive.

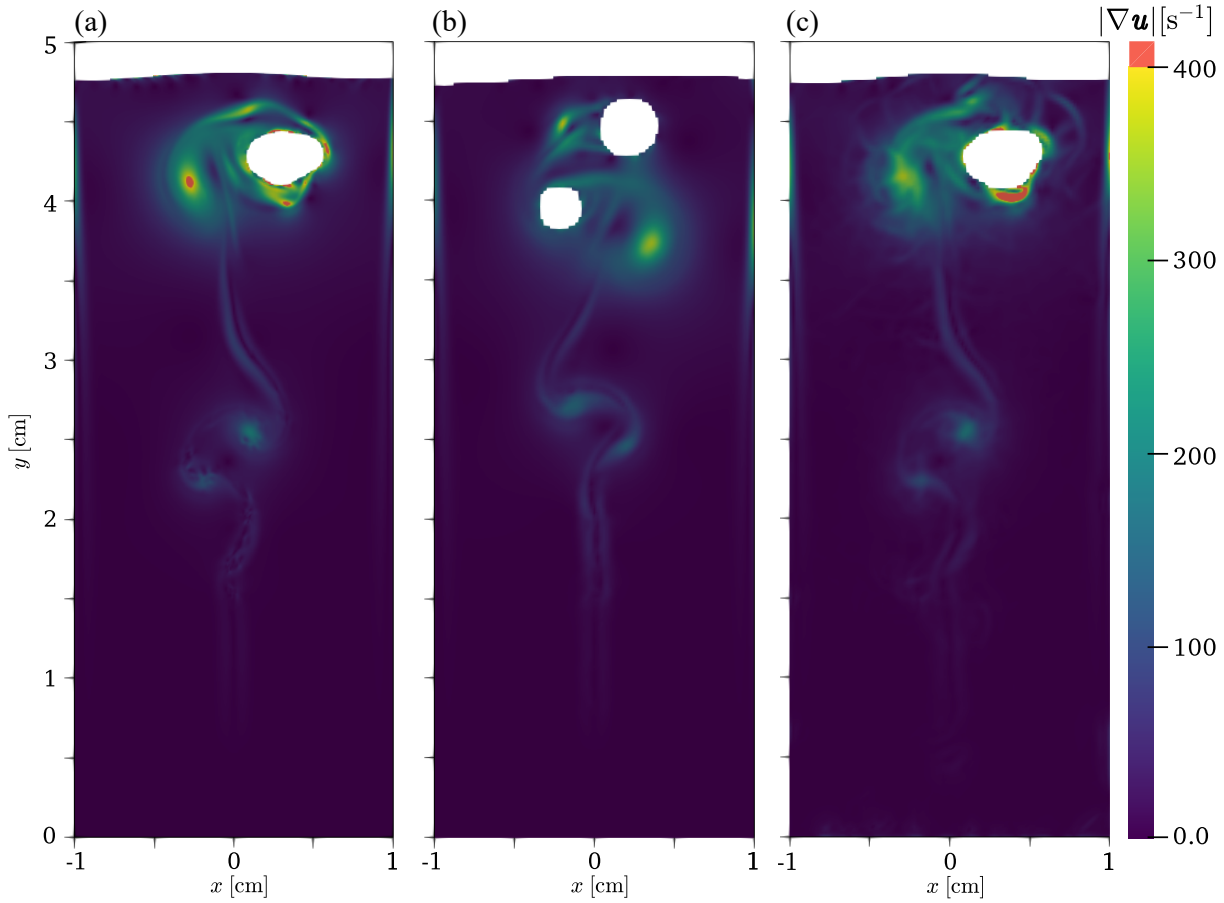


Figure 6.5: Comparison of liquid-phase velocity-gradient magnitude fields $|\nabla \mathbf{u}|$ at $t = 0.2$ s. Subfigures (a) – (c) show the ground truth, the baseline simulation, and the three-phase AOT-nudging reconstruction, respectively.

6.4 Conclusions

This chapter developed an AOT-nudging solver for bubbly flows with inertial particle tracking, extending the previous two-phase VoF-based AOT-nudging solver in Chap. 4 to a three-phase flow. While retaining the volume-fraction nudging for the gas-liquid interface, it adds the Lagrangian particle tracking, inertial particle correction, and AOT-nudging coupling to the solver discussed in Chap. 4.

For the Lagrangian particle tracking, particle positions are used as the primary observations. The simulated particles are transported by the reconstructed carrier flow. A

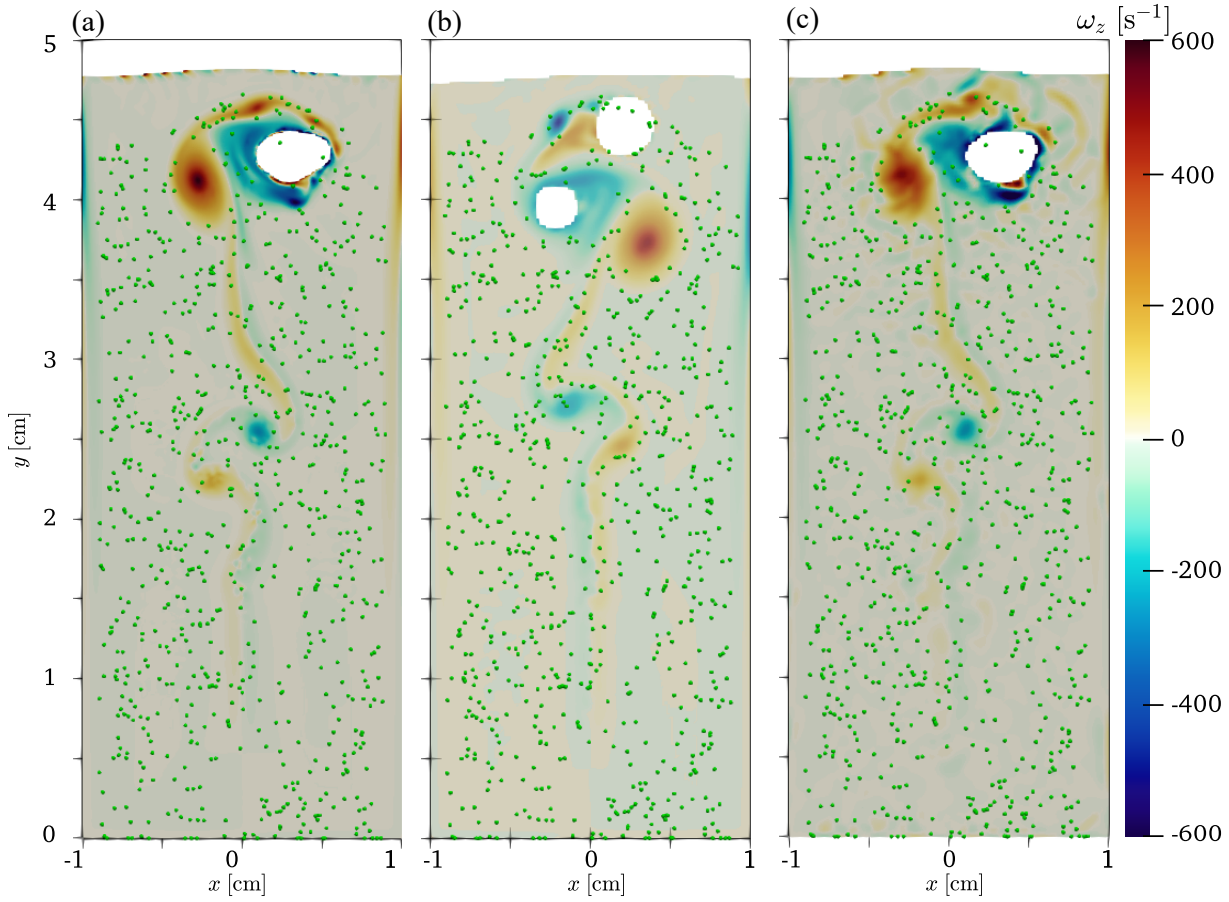


Figure 6.6: Comparison of vorticity fields ω_z at $t = 0.2$ s with tracer-particle locations overlaid. Subfigures (a) – (c) show the ground truth, the baseline simulation, and the three-phase AOT-nudging reconstruction, respectively.

particle-level nudging force is applied to reduce the mismatch between the observed and reconstructed trajectories. This correction drives the simulated particle trajectories toward the observed trajectories. Therefore, the Lagrangian observations provide direct constraints on particle transport in the liquid phase.

For the inertial-particle correction, the particle positions are first used to estimate particle kinematics (e.g., velocity and acceleration). Then, a particle-response model is used to infer the liquid-phase velocity from the observed particle kinematics. This step accounts for the finite particle response time before the particle data are used in the momentum nudging.

For the AOT-nudging coupling, the particle observations affect the reconstruction through two pathways. From a Lagrangian perspective, they directly nudge the simulated particle trajectories toward the observed trajectories. From the Eulerian perspective, the observed particle kinematics are used to infer liquid-phase velocity observations. In turn, the liquid-phase flow advects the reconstructed inertial particles.

The validation results based on a bubble-rising flow with $\mathrm{St} = 1$ tracers show that this coupled strategy can reconstruct the three-phase flow. The reconstructed particle trajectories, liquid-phase velocity, and differential flow quantities (e.g., velocity gradients and vorticity) are all in good agreement with the ground truth.

If the bubbles are sufficiently small and their slip relative to the surrounding liquid is negligible, their motion may also be used as Lagrangian tracers of the surrounding liquid flow. In this case, additional solid tracers, such as plastic or glass particles, would no longer be required. The three-phase flow-reconstruction problem could be reduced to a two-phase system.

Chapter 7

Conclusions and Future Work

7.1 Conclusions

This thesis developed and validated a data assimilation (DA) framework for bubbly-flow reconstruction. The DA method used in this thesis is the Azouani–Olson–Titi (AOT) nudging algorithm [292]. The AOT-nudging algorithm can combine experimental observations with numerical simulations to estimate a flow state that is more accurate and complete than either experiments or simulations alone. To achieve DA, AOT-nudging introduces feedback terms into the governing equations as artificial source terms. These terms penalize the discrepancy between the *interpolated* numerical solution and the *interpolated* observations. Compared with conventional nudging, Kalman filters, and variational methods, AOT-nudging is a lightweight, efficient, and sequential DA method without compromising accuracy. It does not require a large global inverse problem or an ensemble of repeated simulations. Its unique interpolation operation not only resolves the mismatch between the sparse observations and the dense mesh, but also guarantees the convergence towards the ground truth in many dissipative systems.

In this work, the observations are obtained from image-based measurements. They include liquid-phase kinematic observations from image velocimetry, such as PIV or LPT, and gas–liquid interface observations from bubble images. The image-velocimetry observations correct the surrounding liquid motion, while the bubble-image observations constrain the volume-fraction field and interface evolution. The numerical simulation is based on the Volume-of-Fluid (VoF) method, performed in OpenFOAM. By combining experimental observations, numerical simulations, and data assimilation, the reconstructed solution is

continuously driven toward the observed state while remaining constrained by the governing equations.

The major contributions of this thesis are summarized as follows. First, a DA framework for bubbly-flow reconstruction is developed and validated. With this framework, sparse measurements can actively correct the simulation and reconstruct complete bubbly-flow fields. These fields include bubble kinematics, interface evolution, liquid-phase velocity, pressure, velocity gradients, and vorticity. In other words, a simulation and an experiment can be synchronized. Validation based on synthetic data shows that the proposed method improves the reconstruction of bubble motion and liquid-phase flow compared with a baseline simulation without DA. Experimental validation further illustrates that the solver can reconstruct temporally and spatially refined flow fields from image-based observations. These quantities are difficult to obtain directly from experiments alone and are also sensitive to initial conditions and numerical settings in simulations. These reconstructed local flow structures can be used to analyze bubble deformation, coalescence, and liquid-phase dynamics.

Second, a residual-based Uncertainty Quantification (UQ) framework for AOT-nudging reconstruction is developed and validated. AOT-nudging is a deterministic DA method. It does not provide an ensemble spread, posterior distribution, or confidence interval for the estimates. Therefore, uncertainty must be introduced as a separate diagnostic quantity. Starting from a generic observation-error model, point-wise uncertainty estimates were derived using the local observation–reconstruction mismatch underlying the AOT-nudging feedback and the prescribed measurement uncertainty, Taylor expansion, and triangle inequality. As a result, the reconstructed bubbly-flow fields are accompanied by local UQ, indicating the reconstruction quality.

Third, this thesis extended the AOT-nudging framework to three-phase bubbly flows containing inertial tracer particles. For particles with a finite Stokes number, the measured particle velocity is not exactly the liquid velocity. To address this issue, a particle-response model can infer the underlying liquid-phase velocity based on the tracer velocity and acceleration. The inferred liquid-phase velocities, observed particle trajectories, and bubble-interface observations are then incorporated into the coupled reconstruction. The validation results showed that this correction can faithfully reconstruct the kinematics and dynamics of bubbles, tracer particles, and the liquid-phase flow. This extension is relevant to practical experiments in which tracer inertia cannot be neglected.

Several supporting contributions were also made. First, this thesis provides numerical evidence that the AOT-nudging algorithm can be extended to bubbly flows. AOT-nudging has a rigorous theoretical foundation for some important dissipative dynamical systems.

However, its use in interface-resolved bubbly-flow reconstruction has been limited. The present work shows that AOT-nudging can be formulated and implemented in a VoF-based finite-volume solver for such problems. A rigorous convergence proof for the bubbly-flow system remains beyond the scope of this thesis. However, existing analyses for AOT-nudging in Bénard convection suggest that a similar proof may be attainable for bubbly flows, provided that the interface transport, surface tension, material properties, and phase coupling are treated appropriately. Nevertheless, the numerical results demonstrate stable and accurate reconstruction.

Second, this thesis analyzed the practical influence of key AOT-nudging parameters. The results show that the nudging strengths must be strong enough to correct the solution. However, excessively large strengths may cause numerical instability. In addition, a sufficiently high observation frequency is important. It limits the time available for nonlinear error growth between corrections. The mesh resolution has to be compatible with the nudging strength, the nudging frequency, and the physical properties of the flow. Mesh refinement alone does not necessarily improve reconstruction when the observation density, observation frequency, and nudging strengths are held fixed. These findings provide practical guidance for choosing parameters in future AOT-nudging bubbly-flow reconstructions.

Third, the experimental validation suggested that LPT observations may be more effective than PIV for the present reconstruction problem. The overlapping PIV interrogation window may over-smooth localized large velocity gradients, which are critical for bubble analysis. LPT retains particle-level Lagrangian information. In the experimental validation cases in this thesis, the LPT-based reconstruction better preserved localized high-speed flow features near bubbles and coalescence regions.

In summary, the results show that AOT-nudging is a practical, physics-constrained, and extensible framework for bubbly-flow reconstruction. The method can combine bubble images, PIV or LPT observations, and inertial-particle trajectories with a VoF-based finite-volume solver. It improves reconstruction accuracy relative to baseline simulations without DA. It also provides local uncertainty information. The framework offers a path toward realistic experimental multiphase-flow reconstruction from sparse and noisy observations.

7.2 Future Work

First, the nudging strategy can be further improved. The present solvers use prescribed nudging strengths. However, a fixed strength may not be optimal for all regions and all times. Future work could develop adaptive or uncertainty-weighted nudging gains. For example, stronger nudging could be applied where observations are reliable. Weaker nudging

could be used in regions with large measurement uncertainty or sparse observations. Such an adaptive strategy may improve robustness and reconstruction accuracy.

Second, the inertial-particle correction model can be further developed. The present work uses a simplified particle-response model to convert inertial particle kinematics into approximate fluid-velocity observations. Future studies could incorporate a more complete particle-force balance into the inertial-particle model, including added mass, pressure-gradient force, lift, and history effects. The method could also be extended to infer unknown particle properties directly from tracked trajectories. Examples include particle diameter and density. For denser particle suspensions, two-way coupling and particle–particle interactions should also be considered.

Third, the framework could be extended to three-dimensional high-speed multiphase flows, such as cavitation. In cavitation flows, tracer inertia and sparse measurements may limit the accuracy of image velocimetry. Cavitation is also challenging to simulate because of rapid interfacial motion, strong pressure variations, multiscale dynamics, and sensitivity to initial and boundary conditions. The proposed AOT-nudging framework is therefore promising for combining imperfect measurements with CFD to study cavitation flow in 3D.

Fourth, a possible convergence analysis of the AOT-nudging algorithm for bubbly flows could be developed based on a finite element method. The discontinuities in volume fraction, density, and viscosity could be treated directly using a discontinuous Galerkin (DG) method, in which element-wise discontinuities are handled through numerical fluxes. Within a variational weak-form framework, the AOT feedback terms could then be incorporated, and stability and error estimates could be derived using energy methods. Such an analysis may provide a mathematical bridge between existing AOT convergence theory and the present VoF implementation.

Lastly, the proposed framework may benefit both experimental researchers and CFD practitioners studying complex multiscale systems such as bioreactors and chemical reactors. For experimental studies, it can be used to recover flow information that is difficult to measure directly, such as local shear-stress distributions near bubbles during coalescence, breakup, and interactions with turbulence. For CFD studies, it can provide measurement-informed validation of numerical simulations. In the future, the framework could be further developed toward a physics-based digital twin for flow monitoring, prediction, and control.

References

[1] Heather MM Hill, Marielle S Kahn, Lucas J Brilliott, Briana M Roberts, Christie Gutierrez, and Stephanie Artz. Beluga (Delphinapterus leucas) bubble bursts: Surprise, protection, or play? *International Journal of Comparative Psychology*, 24(2), 2011.

[2] Ira Leifer and Ranjan Kumar Patro. The bubble mechanism for methane transport from the shallow sea bed to the surface: A review and sensitivity study. *Continental Shelf Research*, 22(16):2409–2428, 2002.

[3] Steven Emerson and Seth Bushinsky. The role of bubbles during air-sea gas exchange. *Journal of Geophysical Research: Oceans*, 121(6):4360–4376, 2016.

[4] Roger EA Arndt. Cavitation in fluid machinery and hydraulic structures. *Annual Review of Fluid Mechanics*, 13(1):273–326, 1981.

[5] George E Totten, Ying H Sun, Roland J Bishop Jr, and Xie Lin. Hydraulic system cavitation: A review. *SAE transactions*, pages 368–380, 1998.

[6] Francois Avellan. Introduction to cavitation in hydraulic machinery. In *Scientific Bulletin of the Politehnica University of Timisoara: Transactions on Mechanics*, 2004.

[7] KL De Graaf, PA Brandner, and Irene Penesis. Bubble dynamics of a seismic airgun. *Experimental Thermal and Fluid Science*, 55:228–238, 2014.

[8] KL De Graaf, Irene Penesis, and PA Brandner. Modelling of seismic airgun bubble dynamics and pressure field using the Gilmore equation with additional damping factors. *Ocean Engineering*, 76:32–39, 2014.

[9] Shuai Li, Devaraj van der Meer, A-Man Zhang, Andrea Prosperetti, and Detlef Lohse. Modelling large scale airgun-bubble dynamics with highly non-spherical features. *International Journal of Multiphase Flow*, 122:103143, 2020.

[10] Nitin Minocha, Jyeshtharaj Bhalchandra Joshi, Arun Kumar Nayak, and Pallipattu Krishnan Vijayan. 3D CFD simulation of passive decay heat removal system under boiling conditions: role of bubble sliding motion on inclined heated tubes. *Chemical Engineering Science*, 145:245–265, 2016.

[11] Qi Lu, Yu Liu, Jian Deng, Xiaowei Luo, Zhiyong Deng, and Zhengpeng Mi. Review of interdisciplinary heat transfer enhancement technology for nuclear reactor. *Annals of Nuclear Energy*, 159:108302, 2021.

[12] Andreas Poullikkas. Effects of two-phase liquid-gas flow on the performance of nuclear reactor cooling pumps. *Progress in Nuclear Energy*, 42(1):3–10, 2003.

[13] Sylvain Lefebvre, Jamal Chaouki, and Christophe Guy. Phase Mixing Modeling in Multiphase Reactors Containing Gas Bubble: a Review. *International Journal of Chemical Reactor Engineering*, 2(1), 2004.

[14] JJ Heijnen and K Van't Riet. Mass transfer, mixing and heat transfer phenomena in low viscosity bubble column reactors. *The Chemical Engineering Journal*, 28(2): B21–B42, 1984.

[15] Arsam Behkish, Zhuowu Men, Juan R Inga, and Badie I Morsi. Mass transfer characteristics in a large-scale slurry bubble column reactor with organic liquid mixtures. *Chemical Engineering Science*, 57(16):3307–3324, 2002.

[16] Junlian Yin, Jingjing Li, Hua Li, Wei Liu, and Dezhong Wang. Experimental study on the bubble generation characteristics for a venturi type bubble generator. *International Journal of Heat and Mass Transfer*, 91:218–224, 2015.

[17] Lynda Boubendir, Salah Chikh, and Lounes Tadrist. On the surface tension role in bubble growth and detachment in a micro-tube. *International Journal of Multiphase Flow*, 124:103196, 2020.

[18] Grant B Deane and M Dale Stokes. Scale dependence of bubble creation mechanisms in breaking waves. *Nature*, 418(6900):839–844, 2002.

[19] GK Batchelor. The stability of a large gas bubble rising through liquid. *Journal of Fluid Mechanics*, 184:399–422, 1987.

[20] Paul Bonnefis, David Fabre, and Jacques Magnaudet. When, how, and why the path of an air bubble rising in pure water becomes unstable. *Proceedings of the National Academy of Sciences*, 120(11):e2300897120, 2023.

[21] Yingjie Chang, Conrad Müller, Péter Kováts, Liejin Guo, and Katharina Zähringer. Hydrodynamics and shape reconstruction of single rising air bubbles in water using high-speed tomographic particle tracking velocimetry and 3D geometric reconstruction. *Experiments in Fluids*, 65(1):6, 2024.

[22] Ashik Ullah Mohammad Masuk, Ashwanth KR Salibindla, and Rui Ni. The orientational dynamics of deformable finite-sized bubbles in turbulence. *Journal of Fluid Mechanics*, 915:A79, 2021.

[23] Ashik Ullah Mohammad Masuk, Yinghe Qi, Ashwanth KR Salibindla, and Rui Ni. Towards a phenomenological model on the deformation and orientation dynamics of finite-sized bubbles in both quiescent and turbulent media. *Journal of Fluid Mechanics*, 920:A4, 2021.

[24] Rui Ni. Deformation and breakup of bubbles and drops in turbulence. *Annual Review of Fluid Mechanics*, 56(1):319–347, 2024.

[25] Ashik Ullah Mohammad Masuk, Ashwanth KR Salibindla, and Rui Ni. Simultaneous measurements of deforming Hinze-scale bubbles with surrounding turbulence. *Journal of Fluid Mechanics*, 910:A21, 2021.

[26] Ashik Ullah Mohammad Masuk, Ashwanth Salibindla, Shiyong Tan, and Rui Ni. V-ONSET (Vertical Octagonal Noncorrosive Stirred Energetic Turbulence): a vertical water tunnel with a large energy dissipation rate to study bubble/droplet deformation and breakup in strong turbulence. *Review of Scientific Instruments*, 90(8), 2019.

[27] Yinghe Qi, Shiyong Tan, Noah Corbitt, Carl Urbanik, Ashwanth KR Salibindla, and Rui Ni. Fragmentation in turbulence by small eddies. *Nature Communications*, 13 (1):469, 2022.

[28] Shijie Zhong and Rui Ni. On the breakup frequency of bubbles and droplets in turbulence: a compilation and evaluation of experimental data. *International Journal of Multiphase Flow*, 176:104842, 2024.

[29] Richard L Stover, Charles W Tobias, and Morton M Denn. Bubble coalescence dynamics. *AIChE Journal*, 43(10):2385–2392, 1997.

[30] Aman Zhang, Pengnan Sun, and Furen Ming. An SPH modeling of bubble rising and coalescing in three dimensions. *Computer Methods in Applied Mechanics and Engineering*, 294:189–209, 2015.

[31] Shiyong Tan, Shijie Zhong, Yinghe Qi, Xu Xu, and Rui Ni. Dynamics of bubble collision and coalescence in three-dimensional turbulent flows. *Journal of Fluid Mechanics*, 1020:A15, 2025.

[32] ST Thoroddsen, TG Etoh, and K Takehara. Experiments on bubble pinch-off. *Physics of Fluids*, 19(4), 2007.

[33] JC Burton, R Waldrep, and P Taborek. Scaling and instabilities in bubble pinch-off. *Physical Review Letters*, 94(18):184502, 2005.

[34] Raymond Bergmann, Devaraj van der Meer, Mark Stijnman, Marijn Sandtke, Andrea Prosperetti, and Detlef Lohse. Giant bubble pinch-off. *Physical Review Letters*, 96 (15):154505, 2006.

[35] Yinghe Qi, Ashik Ullah Mohammad Masuk, and Rui Ni. Towards a model of bubble breakup in turbulence through experimental constraints. *International Journal of Multiphase Flow*, 132:103397, 2020.

[36] Ashwanth KR Salibindla, Ashik Ullah Mohammad Masuk, and Rui Ni. Experimental investigation of the acceleration statistics and added-mass force of deformable bubbles in intense turbulence. *Journal of Fluid Mechanics*, 912:A50, 2021.

[37] Emil-Alexandru Brujan, Kester Nahen, Peter Schmidt, and Alfred Vogel. Dynamics of laser-induced cavitation bubbles near an elastic boundary. *Journal of Fluid Mechanics*, 433:251–281, 2001.

[38] A Vogel, Werner Lauterborn, and R Timm. Optical and acoustic investigations of the dynamics of laser-produced cavitation bubbles near a solid boundary. *Journal of Fluid Mechanics*, 206:299–338, 1989.

[39] CF Hung and JJ Hwangfu. Experimental study of the behaviour of mini-charge underwater explosion bubbles near different boundaries. *Journal of Fluid Mechanics*, 651:55–80, 2010.

[40] E Klaseboer, KC Hung, C Wang, CW Wang, BC Khoo, P Boyce, S Debono, and H Charlier. Experimental and numerical investigation of the dynamics of an underwater explosion bubble near a resilient/rigid structure. *Journal of Fluid Mechanics*, 537:387–413, 2005.

[41] John R Blake and DC Gibson. Cavitation bubbles near boundaries. *Annual Review of Fluid Mechanics*, 19(1):99–123, 1987.

[42] Xukun Luo, DJ Lee, Raymond Lau, Guoqiang Yang, and Liang-Shih Fan. Maximum stable bubble size and gas holdup in high-pressure slurry bubble columns. *AIChE Journal*, 45(4):665–680, 1999.

[43] JP Giovannettone, E Tsai, and John S Gulliver. Gas void ratio and bubble diameter inside a deep airlift reactor. *Chemical Engineering Journal*, 149(1-3):301–310, 2009.

[44] R Schäfer, C Merten, and GJET Eigenberger. Bubble size distributions in a bubble column reactor under industrial conditions. *Experimental Thermal and Fluid Science*, 26(6-7):595–604, 2002.

[45] Giorgio Besagni and Fabio Inzoli. Bubble size distributions and shapes in annular gap bubble column. *Experimental Thermal and Fluid Science*, 74:27–48, 2016.

[46] Harris Wong, CJ Radke, and S Morris. The motion of long bubbles in polygonal capillaries. Part 1. Thin films. *Journal of Fluid Mechanics*, 292:71–94, 1995.

[47] Harris Wong, CJ Radke, and S Morris. The motion of long bubbles in polygonal capillaries. Part 2. Drag, fluid pressure and fluid flow. *Journal of Fluid Mechanics*, 292:95–110, 1995.

[48] Reza Azadi, Jaime Wong, David Nobes, et al. Experimental and analytical investigation of meso-scale slug bubble dynamics in a square capillary channel. *Physics of Fluids*, 32(8), 2020.

[49] Reza Azadi and David S Nobes. Local flow dynamics in the motion of slug bubbles in a flowing mini square channel. *International Journal of Heat and Mass Transfer*, 178:121588, 2021.

[50] Milton S Plesset and Andrea Prosperetti. Bubble dynamics and cavitation. *Annual Review of Fluid Mechanics*, 9:145–185, 1977.

[51] Christopher E Brennen. *Cavitation and bubble dynamics*. Cambridge University Press, 2014.

[52] Christoph Brücker. Structure and dynamics of the wake of bubbles and its relevance for bubble interaction. *Physics of Fluids*, 11(7):1781–1796, 1999.

[53] Sheng-lin Yan, Xu-qing Wang, Li-tao Zhu, Xi-bao Zhang, and Zheng-hong Luo. Mechanisms and modeling of bubble dynamic behaviors and mass transfer under gravity: A review. *Chemical Engineering Science*, 277:118854, 2023.

[54] Y Sato, M Sadatomi, and K Sekoguchi. Momentum and heat transfer in two-phase bubble flow-I. Theory. *International Journal of Multiphase Flow*, 7(2):167–177, 1981.

[55] Akio Tomiyama, Isao Kataoka, Iztok Zun, and Tadashi Sakaguchi. Drag coefficients of single bubbles under normal and micro gravity conditions. *JSME International Journal Series B Fluids and Thermal Engineering*, 41(2):472–479, 1998.

[56] Mamoru Ishii and Novak Zuber. Drag coefficient and relative velocity in bubbly, droplet or particulate flows. *AIChE Journal*, 25(5):843–855, 1979.

[57] Dominique Legendre and Jacques Magnaudet. The lift force on a spherical bubble in a viscous linear shear flow. *Journal of Fluid Mechanics*, 368:81–126, 1998.

[58] Akio Tomiyama, Hidesada Tamai, Iztok Zun, and Shigeo Hosokawa. Transverse migration of single bubbles in simple shear flows. *Chemical Engineering Science*, 57 (11):1849–1858, 2002.

[59] S Aoyama, K Hayashi, S Hosokawa, D Lucas, and A Tomiyama. Lift force acting on single bubbles in linear shear flows. *International Journal of Multiphase Flow*, 96: 113–122, 2017.

[60] Hean Luo and Hallvard F Svendsen. Theoretical model for drop and bubble breakup in turbulent dispersions. *AIChE Journal*, 42(5):1225–1233, 1996.

[61] Michael J Prince and Harvey W Blanch. Bubble coalescence and break-up in air-sparged bubble columns. *AIChE Journal*, 36(10):1485–1499, 1990.

[62] Carlos Martínez-Bazán, Jose L Montañes, and Juan C Lasheras. On the breakup of an air bubble injected into a fully developed turbulent flow. Part 1. Breakup frequency. *Journal of Fluid Mechanics*, 401:157–182, 1999.

[63] Yixiang Liao, Roland Rzehak, Dirk Lucas, and Eckhard Krepper. Baseline closure model for dispersed bubbly flow: Bubble coalescence and breakup. *Chemical Engineering Science*, 122:336–349, 2015.

[64] Timothy O Oolman and Harvey W Blanch. Bubble coalescence in air-sparged bioreactors. *Biotechnology and Bioengineering*, 28(4):578–584, 1986.

[65] Jieun Yeo and Hyungmin Park. Bubble–bubble interactions in two-dimensional bubble-chain flows. *International Journal of Multiphase Flow*, 171:104665, 2024.

[66] Yuchen Song, Yalan Qian, Tingting Zhang, Junlian Yin, and Dezhong Wang. Simultaneous measurements of bubble deformation and breakup with surrounding liquid-phase flow. *Experiments in Fluids*, 63(5):83, 2022.

[67] Deify Law, Francine Battaglia, and Theodore J Heindel. Model validation for low and high superficial gas velocity bubble column flows. *Chemical Engineering Science*, 63(18):4605–4616, 2008.

[68] Tian Ma, Hendrik Hessenkemper, Dirk Lucas, and Andrew D Bragg. An experimental study on the multiscale properties of turbulence in bubble-laden flows. *Journal of Fluid Mechanics*, 936:A42, 2022.

[69] Roland Rzehak, Manuel Krauß, Péter Kováts, and Katharina Zähringer. Fluid dynamics in a bubble column: New experiments and simulations. *International Journal of Multiphase Flow*, 89:299–312, 2017.

[70] Ege Ertekin, John M Kavanagh, David F Fletcher, and Dale D McClure. Validation studies to assist in the development of scale and system independent CFD models for industrial bubble columns. *Chemical Engineering Research and Design*, 171:1–12, 2021.

[71] Yann Mezui, Martin Obligado, and Alain Cartellier. Buoyancy-driven bubbly flows: scaling of velocities in bubble columns operated in the heterogeneous regime. *Journal of Fluid Mechanics*, 952:A10, 2022.

[72] Hugo A Jakobsen, Bente H Sannæs, Sverre Grevskott, and Hallvard F Svendsen. Modeling of vertical bubble-driven flows. *Industrial & Engineering Chemistry Research*, 36(10):4052–4074, 1997.

[73] Markus Raffel, Christian E Willert, Fulvio Scarano, Christian J Kähler, Steve T Wereley, Jürgen Kompenhans, et al. PIV uncertainty and measurement accuracy. *Particle Image Velocimetry: A Practical Guide*, pages 203–241, 2018.

[74] Dana Dabiri and Charles Pecora. *Particle tracking velocimetry*. IOP Publishing Bristol, 2020.

[75] Andrea Sciacchitano. Uncertainty quantification in particle image velocimetry. *Measurement Science and Technology*, 30(9):092001, 2019.

[76] Henk Kaarle Versteeg and Weeratunge Malalasekera. *An introduction to computational fluid dynamics: the finite volume method*. Pearson Education, 2007.

[77] Gretar Tryggvason, Sadegh Dabiri, Bahman Aboulhasanzadeh, and Jiacai Lu. Multiscale considerations in direct numerical simulations of multiphase flows. *Physics of Fluids*, 25(3), 2013.

[78] Roland Rzehak, Thomas Ziegenhein, Sebastian Kriebitzsch, Eckhard Krepper, and Dirk Lucas. Unified modeling of bubbly flows in pipes, bubble columns, and airlift columns. *Chemical Engineering Science*, 157:147–158, 2017.

[79] Alessio Innocenti, Alice Jaccod, Stéphane Popinet, and Sergio Chibbaro. Direct numerical simulation of bubble-induced turbulence. *Journal of Fluid Mechanics*, 918:A23, 2021.

[80] Yan Jin, RF Cavero, Christian Weiland, Marko Hoffmann, and Michael Schlüter. Effects of bubble-induced turbulence on interfacial species transport: A direct numerical simulation study. *Chemical Engineering Science*, 279:118934, 2023.

[81] Kazuyasu Sugiyama, Shu Takagi, and Yoichiro Matsumoto. Multi-scale analysis of bubbly flows. *Computer Methods in Applied Mechanics and Engineering*, 191(6-7): 689–704, 2001.

[82] Mamoru Ishii and Takashi Hibiki. *Thermo-fluid dynamics of two-phase flow*. Springer Science & Business Media, 2010.

[83] Mamoru Ishii. Thermo-fluid dynamic theory of two-phase flow. *NASA Sti/recon Technical Report A*, 75:29657, 1975.

[84] Mamoru Ishii. Two-fluid model for two-phase flow. *Multiphase Science and Technology*, 5(1-4), 1990.

[85] Francis H Harlow and J Eddie Welch. Numerical calculation of time-dependent viscous incompressible flow of fluid with free surface. *The Physics of Fluids*, 8(12): 2182–2189, 1965.

[86] BD Nichols, CW Hirt, and RS Hotchkiss. SOLA-VOF: A solution algorithm for transient fluid flow with multiple free boundaries. Technical report, Los Alamos National Lab.(LANL), Los Alamos, NM (United States), 1980.

[87] Cyril W Hirt and Billy D Nichols. Volume of fluid (VOF) method for the dynamics of free boundaries. *Journal of Computational Physics*, 39(1):201–225, 1981.

[88] Stanley Osher and James A Sethian. Fronts propagating with curvature-dependent speed: Algorithms based on Hamilton-Jacobi formulations. *Journal of Computational Physics*, 79(1):12–49, 1988.

[89] Salih Ozen Unverdi and Grétar Tryggvason. A front-tracking method for viscous, incompressible, multi-fluid flows. *Journal of Computational Physics*, 100(1):25–37, 1992.

[90] Giorgio Besagni, Nicolò Varallo, and Riccardo Mereu. Computational fluid dynamics modelling of two-phase bubble columns: A comprehensive review. *Fluids*, 8(3):91, 2023.

[91] Marco Colombo and Michael Fairweather. Influence of multiphase turbulence modelling on interfacial momentum transfer in two-fluid Eulerian-Eulerian CFD models of bubbly flows. *Chemical Engineering Science*, 195:968–984, 2019.

[92] Eckhard Krepper, Roland Rzehak, and Dirk Lucas. Validation of a closure model framework for turbulent bubbly two-phase flow in different flow situations. *Nuclear Engineering and Design*, 340:388–404, 2018.

[93] S Hänsch, I Evdokimov, F Schlegel, and D Lucas. A workflow for the sustainable development of closure models for bubbly flows. *Chemical Engineering Science*, 244: 116807, 2021.

[94] Han Bao, Jinyong Feng, Nam Dinh, and Hongbin Zhang. Computationally efficient CFD prediction of bubbly flow using physics-guided deep learning. *International Journal of Multiphase Flow*, 131:103378, 2020.

[95] Tarek Merabtene, Faroogh Garoosi, and Tew-Fik Mahdi. Numerical modeling of liquid spills from the damaged container and collision of two rising bubbles in partially filled enclosure using modified Volume-Of-Fluid (VOF) method. *Engineering Analysis with Boundary Elements*, 154:83–121, 2023.

[96] Faroogh Garoosi and Tew-Fik Mahdi. New benchmark problems for validation and verification of incompressible multi-fluid flows based on the improved Volume-Of-Fluid (VOF) method. *Colloids and Surfaces A: Physicochemical and Engineering Aspects*, 648:129313, 2022.

[97] Mark Asch, Marc Bocquet, and Maëlle Nodet. *Data assimilation: methods, algorithms, and applications*. SIAM, 2016.

[98] Kody Law, Andrew M Stuart, and Konstantinos C Zygalakis. *Data Assimilation: A Mathematical Introduction*, volume 62 of *Texts in Applied Mathematics*. Springer, Cham, 2015. doi: 10.1007/978-3-319-20325-6.

[99] Chuangxin He, Sen Li, and Yingzheng Liu. Data assimilation: new impetus in experimental fluid dynamics. *Experiments in Fluids*, 66(5):94, 2025.

[100] Alberto Carrassi, Marc Bocquet, Laurent Bertino, and Geir Evensen. Data assimilation in the geosciences: An overview of methods, issues, and perspectives. *Wiley Interdisciplinary Reviews: Climate Change*, 9(5):e535, 2018.

[101] Maryam Azhin, Pedro Silva-Aires, Khushaal Popli, Artin Afacan, Qi Liu, and Vinay Prasad. State Estimation of a Flotation Column using Fundamental Dynamic Models. *IFAC-PapersOnLine*, 55(21):108–113, 2022.

[102] Chen Wei, Jagadeeshwar L Tabjula, Jyotsna Sharma, and Yuanhang Chen. A novel data assimilation-based real-time state estimation method for gas influx profiling during riser gas events. *Journal of Energy Resources Technology*, 145(9):092901, 2023.

[103] Shungo Okamura and Kie Okabayashi. Twin experiments for data assimilation of cavitating flow around a hydrofoil. *International Journal of Multiphase Flow*, 188: 105201, 2025.

[104] Aoi Watanabe, Ryuhei Sato, Ikuya Kinefuchi, and Yasushi Shibuta. douka: A universal platform of data assimilation for materials modeling. *The Journal of Chemical Physics*, 163(11), 2025.

[105] Javad Eshraghi, Arezoo M Ardekani, and Pavlos P Vlachos. Data assimilation for modeling cavitation bubble dynamics. *Experiments in Fluids*, 62(5):90, 2021.

[106] Jean-Sebastien Spratt, Mauro Rodriguez, Kevin Schmidmayer, Spencer H Bryngelson, Jin Yang, Christian Franck, and Tim Colonius. Characterizing viscoelastic materials via ensemble-based data assimilation of bubble collapse observations. *Journal of the Mechanics and Physics of Solids*, 152:104455, 2021.

[107] Daizhou Wen, Wuguang Chen, Junlian Yin, Yuchen Song, Mingjun Ren, and Dezhong Wang. Overlapping bubble detection and tracking method based on convolutional neural network and kalman filter. *Chemical Engineering Science*, 263: 118059, 2022.

[108] Jun Man, Qiang Zheng, Laosheng Wu, and Lingzao Zeng. Adaptive multi-fidelity probabilistic collocation-based Kalman filter for subsurface flow data assimilation: numerical modeling and real-world experiment. *Stochastic Environmental Research and Risk Assessment*, 34(8):1135–1146, 2020.

[109] Meng Tang, Yimin Liu, and Louis J Durlofsky. Deep-learning-based surrogate flow modeling and geological parameterization for data assimilation in 3D subsurface flow. *Computer Methods in Applied Mechanics and Engineering*, 376:113636, 2021.

[110] Xiaocong Lyu, Wendong Wang, Denis Voskov, Piyang Liu, and Li Chen. Multi-scale modeling for multiphase flow and reactive mass transport in subsurface energy storage: A review. *Advances in Geo-Energy Research*, 15(3):245–260, 2025.

[111] Aseel Farhat, Evelyn Lunasin, and Edriss S Titi. Data assimilation algorithm for 3D Bénard convection in porous media employing only temperature measurements. *Journal of Mathematical Analysis and Applications*, 438(1):492–506, 2016.

[112] Ruoyu Hu, Sanjeeb Poudel, Feng Bao, and Sanghyun Lee. Ensemble score filter for data assimilation of two-phase flow models in porous media. *Journal of Computational Physics*, 544:114416, 2026. doi: 10.1016/j.jcp.2025.114416.

[113] Yaqing Gu and Dean S Oliver. An iterative ensemble Kalman filter for multiphase fluid flow data assimilation. *SPE Journal*, 12(04):438–446, 2007.

[114] Seungpil Jung, Kyungbook Lee, Changhyup Park, and Jonggeun Choe. Ensemble-based data assimilation in reservoir characterization: A review. *Energies*, 11(2):445, 2018.

[115] Yat Tin Chow, Wing Tat Leung, and Ali Pakzad. Continuous data assimilation for two-phase flow: analysis and simulations. *Journal of Computational Physics*, 466: 111395, 2022.

[116] Kristian Fossum, Trond Mannseth, and Andreas S Stordal. Assessment of multilevel ensemble-based data assimilation for reservoir history matching. *Computational Geosciences*, 24(1):217–239, 2020.

[117] Marco Ferrari, Arianna Bonzanini, Gianni Arioli, Pietro Poesio, et al. Estimation of flow rates and parameters in two-phase stratified and slug flow by an ensemble Kalman filter. In *12th International Conference on CFD in Oil & Gas, Metallurgical and Process Industries SINTEF, Trondheim, NORWAY*, pages 171–177, 2017.

[118] Douglas G Dommermuth, Christopher D Lewis, Vu H Tran, and Miguel A Valenciano. Direct simulations of wind-driven breaking ocean waves with data assimilation. *arXiv preprint arXiv:1410.0418*, 2014.

[119] Hans Ngodock, Matthew Carrier, Innocent Souopgui, Scott Smith, Paul Martin, Philip Muscarella, and Gregg Jacobs. On the direct assimilation of along-track sea-surface height observations into a free-surface ocean model using a weak constraints four-dimensional variational (4d-var) method. *Quarterly Journal of the Royal Meteorological Society*, 142(695):1160–1170, 2016.

[120] Liwen Yan, Linyuan Che, and Jing Li. Water wave reconstruction of full hydrodynamic models via data assimilation. *arXiv preprint arXiv:2510.14356*, 2025.

[121] Iain G Currie. *Fundamental mechanics of fluids*. CRC Press, 2016.

[122] Ronald J Adrian. Particle-imaging techniques for experimental fluid mechanics. *Annual Review of Fluid Mechanics*, 23(1):261–304, 1991.

[123] Markus Raffel, Christian E Willert, Jürgen Kompenhans, et al. *Particle image velocimetry: a practical guide*, volume 2. Springer, 1998.

[124] Ronald J Adrian. Twenty years of particle image velocimetry. *Experiments in Fluids*, 39(2):159–169, 2005.

[125] Ronald J Adrian and Jerry Westerweel. *Particle image velocimetry*. Cambridge University Press, 2011.

[126] MP Arroyo and CA Greated. Stereoscopic particle image velocimetry. *Measurement Science and Technology*, 2(12):1181–1186, 1991.

[127] AK Prasad and RJ Adrian. Stereoscopic particle image velocimetry applied to liquid flows. *Experiments in Fluids*, 15(1):49–60, 1993.

[128] Ajay K Prasad. Stereoscopic particle image velocimetry. *Experiments in Fluids*, 29 (2):103–116, 2000.

[129] Gerrit E Elsinga, Fulvio Scarano, Bernhard Wieneke, and Bas W van Oudheusden. Tomographic particle image velocimetry. *Experiments in Fluids*, 41(6):933–947, 2006.

[130] Callum Atkinson and Julio Soria. An efficient simultaneous reconstruction technique for tomographic particle image velocimetry. *Experiments in Fluids*, 47(4):553–568, 2009.

[131] Juan G Santiago, Steve T Wereley, Carl D Meinhart, DJ Beebe, and Ronald J Adrian. A particle image velocimetry system for microfluidics. *Experiments in Fluids*, 25(4): 316–319, 1998.

[132] Michael J Hargather, Michael J Lawson, Gary S Settles, and Leonard M Weinstein. Seedless velocimetry measurements by schlieren image velocimetry. *AIAA Journal*, 49(3):611–620, 2011.

[133] Yin Long, Anning Yan, Feng Liu, and Wanqiu Jiang. Single-shot schlieren image based density field reconstruction for supersonic flow by data-driven paradigm. *Physics of Fluids*, 37(8), 2025.

[134] Daniel Schanz, Sebastian Gesemann, and Andreas Schröder. Shake-The-Box: Lagrangian particle tracking at high particle image densities. *Experiments in Fluids*, 57(5):1–27, 2016.

[135] Shiyong Tan, Ashwanth Salibindla, Ashik Ullah Mohammad Masuk, and Rui Ni. Introducing OpenLPT: new method of removing ghost particles and high-concentration particle shadow tracking. *Experiments in Fluids*, 61(2):47, 2020.

[136] Mao Takeyama, Hitoshi Suto, and Yasuo Hattori. 3D3C rainbow particle tracking velocimetry: improving depth resolution and velocity vector acquisition rate by using color space for a multi-cycle rainbow pattern. *Journal of Visualization*, 27(6):1089–1102, 2024.

[137] Mao Takeyama, Kota Fujiwara, and Yasuo Hattori. Improvement in the number of velocity vector acquisitions using an in-picture tracking method for 3D3C rainbow particle tracking velocimetry. *Fluids*, 9(10):226, 2024.

[138] Mao Takeyama, Hideki Kikumoto, Yichen Wang, and Yasutomo Takakuwa. 3D3C Velocity Measurement Around a Cubic Building Model in a Wind Tunnel Using a Single-Camera Rainbow PTV Technique. *Japan Architectural Review*, 9(1):e70089, 2026.

[139] Mahyar Moaven, Abbishek Gururaj, Vrishank Raghav, and Brian Thurow. Improving depth uncertainty in plenoptic camera-based velocimetry. *Experiments in Fluids*, 65 (4):49, 2024.

[140] Mahyar Moaven, Abbishek Gururaj, Vrishank Raghav, and Brian Thurow. Adaptation and validation of physics-informed neural networks for rotating 3D velocimetry. *Experiments in Fluids*, 67(4):46, 2026.

[141] Cameron Tropea, Alexander L Yarin, John F Foss, et al. *Springer handbook of experimental fluid mechanics*, volume 1. Springer, 2007.

[142] Pijush K Kundu, Ira M Cohen, David R Dowling, and Jesse Capecelatro. *Fluid mechanics*. Elsevier, 2024.

[143] Mohammad S Saidi, M Rismanian, Masoud Monjezi, Mohsen Zendehbad, and S Fatehiboroujeni. Comparison between Lagrangian and Eulerian approaches in predicting motion of micron-sized particles in laminar flows. *Atmospheric Environment*, 89: 199–206, 2014.

[144] Randall J LeVeque. *Finite volume methods for hyperbolic problems*, volume 31. Cambridge University Press, 2002.

[145] Eleuterio F Toro. *Riemann solvers and numerical methods for fluid dynamics: a practical introduction*. Springer Science & Business Media, 2013.

[146] Bernhard Wieneke. Iterative reconstruction of volumetric particle distribution. *Measurement Science and Technology*, 24(2):024008, 2012.

[147] Xing Han and Kai Zhang. Lagrangian analysis of fluid transport in pulsatile post-stenotic flows. *Experimental Thermal and Fluid Science*, 161:111342, 2025.

[148] Mark D Jeronimo, Kai Zhang, and David E Rival. Direct Lagrangian measurements of particle residence time. *Experiments in Fluids*, 60:1–11, 2019.

[149] Kai Zhang and David E Rival. Direct Lagrangian method to characterize entrainment dynamics using particle residence time: a case study on a laminar separation bubble. *Experiments in Fluids*, 61(12):243, 2020.

[150] Melissa A Green, Clarence W Rowley, and George Haller. Detection of Lagrangian coherent structures in three-dimensional turbulence. *Journal of Fluid Mechanics*, 572:111–120, 2007.

[151] Giuseppe A Rosi, Andrew M Walker, and David E Rival. Lagrangian coherent structure identification using a Voronoi tessellation-based networking algorithm. *Experiments in Fluids*, 56:1–14, 2015.

[152] Yifei Yu, Pushpa Shrestha, Oscar Alvarez, Charles Nottage, and Chaoqun Liu. Correlation analysis among vorticity, Q method and Liutex. *Journal of Hydrodynamics*, 32(6):1207–1211, 2020.

[153] Yifei Yu, Pushpa Shrestha, Charles Nottage, and Chaoqun Liu. Principal coordinates and principal velocity gradient tensor decomposition. *Journal of Hydrodynamics*, 32 (3):441–453, 2020.

[154] Yifei Yu, Pushpa Shrestha, Oscar Alvarez, Charles Nottage, and Chaoqun Liu. Investigation of correlation between vorticity, Q, λci, λ2, Δ and Liutex. *Computers & Fluids*, 225:104977, 2021.

[155] Christian Cierpka, Benjamin Lütke, and Christian J Kähler. Higher order multi-frame particle tracking velocimetry. *Experiments in Fluids*, 54(5):1–12, 2013.

[156] Beat Lüthi. *Some aspects of strain, vorticity and material element dynamics as measured with 3D particle tracking velocimetry in a turbulent flow*. PhD thesis, ETH Zurich, 2002.

[157] Sebastian Gesemann, Florian Huhn, Daniel Schanz, and Andreas Schröder. From noisy particle tracks to velocity, acceleration and pressure fields using B-splines and penalties. In *18th International Symposium on Applications of Laser and Imaging Techniques to Fluid Mechanics, Lisbon, Portugal*, volume 4, 2016.

[158] Simone Ferrari and Lionel Rossi. Particle tracking velocimetry and accelerometry (PTVA) measurements applied to quasi-two-dimensional multi-scale flows. *Experiments in Fluids*, 44(6):873–886, 2008.

[159] Nadeem A Malik and Th Dracos. Lagrangian PTV in 3D flows. *Applied Scientific Research*, 51:161–166, 1993.

[160] Yi-sheng Gao, Jian-ming Liu, Yi-fei Yu, and Chaoqun Liu. A liutex based definition and identification of vortex core center lines. *Journal of Hydrodynamics*, 31(3):445–454, 2019.

[161] Chaoqun Liu and Yifei Yu. Mathematical foundation of liutex theory. *Journal of Hydrodynamics*, 34(6):981–993, 2022.

[162] Yifei Yu, Yi-qian Wang, and Chaoqun Liu. A letter for objective liutex. *Journal of Hydrodynamics*, 34(5):965–969, 2022.

[163] Jan FG Schneiders and Fulvio Scarano. Dense velocity reconstruction from tomographic PTV with material derivatives. *Experiments in Fluids*, 57:1–22, 2016.

[164] Young Jin Jeon, Markus Müller, and Dirk Michaelis. Fine scale reconstruction (VIC#) by implementing additional constraints and coarse-grid approximation into VIC+. *Experiments in Fluids*, 63(4):70, 2022.

[165] Gregory E Fasshauer. *Meshfree approximation methods with MATLAB*, volume 6. World Scientific, 2007.

[166] K Takehara and TG Etoh. Direct evaluation method of vorticity combined with PTV. In *Selected Papers from the 31st International Congress on High-Speed Imaging and Photonics*, volume 10328, pages 193–199. SPIE, 2017.

[167] Maxim Bobrov, Mikhail Hrebtov, Vladislav Ivashchenko, Rustam Mullyadzhanov, Alexander Seredkin, Mikhail Tokarev, Dinar Zaripov, Vladimir Dulin, and Dmitriy Markovich. Pressure evaluation from Lagrangian particle tracking data using a grid-free least-squares method. *Measurement Science and Technology*, 32(8):084014, 2021.

[168] Bengt Fornberg, Elisabeth Larsson, and Natasha Flyer. Stable computations with gaussian radial basis functions. *SIAM Journal on Scientific Computing*, 33(2):869–892, 2011.

[169] Elisabeth Larsson, Erik Lehto, Alfa Heryudono, and Bengt Fornberg. Stable computation of differentiation matrices and scattered node stencils based on Gaussian radial basis functions. *SIAM Journal on Scientific Computing*, 35(4):A2096–A2119, 2013.

[170] Pietro Sperotto, Sandra Pieraccini, and Miguel A Mendez. A meshless method to compute pressure fields from image velocimetry. *Measurement Science and Technology*, 33(9):094005, 2022.

[171] Lanyu Li and Zhao Pan. Three-dimensional time-resolved Lagrangian flow field reconstruction based on constrained least squares and stable radial basis function. *Experiments in Fluids*, 65(4):57, 2024.

[172] Manuel Ratz and Miguel A Mendez. A meshless and binless approach to compute statistics in 3D Ensemble PTV. *Experiments in Fluids*, 65(9):142, 2024.

[173] Damien Rigutto, Manuel Ratz, and Miguel A Mendez. A meshless data-tailored approach to compute statistics from scattered data with adaptive radial basis functions. *arXiv preprint arXiv:2511.20449*, 2025.

[174] Manuel Ratz, Alessandro Parente, and Miguel Alfonso Mendez. Meshless data-driven decompositions with RBF-based inner products. *Computers & Fluids*, page 107133, 2026.

[175] Bengt Fornberg and Grady Wright. Stable computation of multiquadric interpolants for all values of the shape parameter. *Computers & Mathematics with Applications*, 48(5-6):853–867, 2004.

[176] YM Lau, K Thiruvalluvan Sujatha, M Gaeini, NG Deen, and JAM Kuipers. Experimental study of the bubble size distribution in a pseudo-2D bubble column. *Chemical Engineering Science*, 98:203–211, 2013.

[177] K.T. Sujatha, B.G.J. Meeusen, J.A.M. Kuipers, and N.G. Deen. Experimental studies of bubbly flow in a pseudo-2D micro-structured bubble column reactor using digital image analysis. *Chemical Engineering Science*, 130:18–30, 2015.

[178] P. Spicka, M.M. Dias, and J.C.B. Lopes. Gas-liquid flow in a 2D column: Comparison between experimental data and CFD modelling. *Chemical Engineering Science*, 56 (21-22):6367–6383, 2001.

[179] Chong Zhang, Taotao Fu, Chunying Zhu, Shaokun Jiang, Youguang Ma, and Huai Z Li. Dynamics of bubble formation in highly viscous liquids in a flow-focusing device. *Chemical Engineering Science*, 172:278–285, 2017.

[180] Taotao Fu, Youguang Ma, Denis Funfschilling, Chunying Zhu, and Huai Z Li. Squeezing-to-dripping transition for bubble formation in a microfluidic T-junction. *Chemical Engineering Science*, 65(12):3739–3748, 2010.

[181] Christoph Meyer, Marko Hoffmann, and Michael Schlüter. Micro-PIV analysis of gas–liquid Taylor flow in a vertical oriented square shaped fluidic channel. *International Journal of Multiphase Flow*, 67:140–148, 2014.

[182] Wojciech Matusik, Chris Buehler, Ramesh Raskar, Steven J Gortler, and Leonard McMillan. Image-based visual hulls. In *Proceedings of the 27th annual conference on Computer graphics and interactive techniques*, pages 369–374, 2000.

[183] Aldo Laurentini. The visual hull concept for silhouette-based image understanding. *IEEE Transactions on Pattern Analysis and Machine Intelligence*, 16(2):150–162, 2002.

[184] D Adhikari and Ellen K Longmire. Visual hull method for tomographic PIV measurement of flow around moving objects. *Experiments in Fluids*, 53(4):943–964, 2012.

[185] Yucheng Fu and Yang Liu. 3D bubble reconstruction using multiple cameras and space carving method. *Measurement Science and Technology*, 29(7):075206, 2018.

[186] Ashik Ullah Mohammad Masuk, Ashwanth Salibindla, and Rui Ni. A robust virtual-camera 3D shape reconstruction of deforming bubbles/droplets with additional physical constraints. *International Journal of Multiphase Flow*, 120:103088, 2019.

[187] Ashwanth KR Salibindla, Ashik Ullah Mohammad Masuk, Shiyong Tan, and Rui Ni. Lift and drag coefficients of deformable bubbles in intense turbulence determined from bubble rise velocity. *Journal of Fluid Mechanics*, 894:A20, 2020.

[188] David Marr and Tomaso Poggio. Cooperative Computation of Stereo Disparity: A cooperative algorithm is derived for extracting disparity information from stereo image pairs. *Science*, 194(4262):283–287, 1976.

[189] Nalpantidis Lazaros, Georgios Christou Sirakoulis, and Antonios Gasteratos. Review of stereo vision algorithms: from software to hardware. *International Journal of Optomechatronics*, 2(4):435–462, 2008.

[190] Rostam Affendi Hamzah and Haidi Ibrahim. Literature survey on stereo vision disparity map algorithms. *Journal of Sensors*, 2016(1):8742920, 2016.

[191] Anne Jordt, Claudius Zelenka, Jens Schneider von Deimling, Reinhard Koch, and Kevin Köser. The bubble box: Towards an automated visual sensor for 3D analysis and characterization of marine gas release sites. *Sensors*, 15(12):30716–30735, 2015.

[192] Ting Xue, Liqun Qu, Zhaofeng Cao, and Tao Zhang. Three-dimensional feature parameters measurement of bubbles in gas–liquid two-phase flow based on virtual stereo vision. *Flow Measurement and Instrumentation*, 27:29–36, 2012.

[193] Tingting Zhang, Yalan Qian, Junlian Yin, Botao Zhang, and Dezhong Wang. Experimental study on 3D bubble shape evolution in swirl flow. *Experimental Thermal and Fluid Science*, 102:368–375, 2019.

[194] A Fujiwara, Y Danmoto, Koichi Hishida, and Masanobu Maeda. Bubble deformation and flow structure measured by double shadow images and PIV/LIF. *Experiments in Fluids*, 36(1):157–165, 2004.

[195] M Honkanen. Reconstruction of a three-dimensional bubble surface from high-speed orthogonal imaging of dilute bubbly flow. *WIT Trans Eng Sci*, 63:469–480, 2009.

[196] F Fischer and U Hampel. Ultra fast electron beam X-ray computed tomography for two-phase flow measurement. *Nuclear Engineering and Design*, 240(9):2254–2259, 2010.

[197] Alberto Aliseda and Theodore J Heindel. X-ray flow visualization in multiphase flows. *Annual Review of Fluid Mechanics*, 53(1):543–567, 2021.

[198] Adriaan BM Graas, Evert C Wagner, Tristan van Leeuwen, J Ruud van Ommen, K Joost Batenburg, Felix Lucka, and Luis M Portela. X-ray tomography for fully-3D time-resolved reconstruction of bubbling fluidized beds. *Powder Technology*, 434: 119269, 2024.

[199] Yuk Man Lau, Karolin Müller, Salar Azizi, and Markus Schubert. Voronoï analysis of bubbly flows via ultrafast X-ray tomographic imaging. *Experiments in Fluids*, 57 (3):35, 2016.

[200] Richard Gordon, Robert Bender, and Gabor T Herman. Algebraic reconstruction techniques (ART) for three-dimensional electron microscopy and X-ray photography. *Journal of Theoretical Biology*, 29(3):471–481, 1970.

[201] Gabor T Herman and Arnold Lent. Iterative reconstruction algorithms. *Computers in Biology and Medicine*, 6(4):273–294, 1976.

[202] Yuchen Song, Guangyuan Huang, Junlian Yin, and Dezhong Wang. Three-dimensional reconstruction of bubble geometry from single-perspective images based on ray tracing algorithm. *Measurement Science and Technology*, 36(1):016010, 2024.

[203] Chaoyue Gong, Yuchen Song, Guangyuan Huang, Wuguang Chen, Junlian Yin, and Dezhong Wang. BubDepth: A neural network approach to three-dimensional reconstruction of bubble geometry from single-view images. *International Journal of Multiphase Flow*, 152:104100, 2022.

[204] Li-Tao Zhu, Xi-Zhong Chen, Bo Ouyang, Wei-Cheng Yan, He Lei, Zhe Chen, and Zheng-Hong Luo. Review of machine learning for hydrodynamics, transport, and reactions in multiphase flows and reactors. *Industrial & Engineering Chemistry Research*, 61(28):9901–9949, 2022.

[205] Yewon Kim and Hyungmin Park. Deep learning-based automated and universal bubble detection and mask extraction in complex two-phase flows. *Scientific Reports*, 11(1):8940, 2021.

[206] Qianwen Wang, Xiaolu Li, Cangsu Xu, Tianhong Yan, and Yuntang Li. Bubble recognizing and tracking in a plate heat exchanger by using image processing and convolutional neural network. *International Journal of Multiphase Flow*, 138:103593, 2021.

[207] Tim Haas, Christian Schubert, Moritz Eickhoff, and Herbert Pfeifer. BubCNN: Bubble detection using Faster RCNN and shape regression network. *Chemical Engineering Science*, 216:115467, 2020.

[208] Igor Poletaev, Mikhail P Tokarev, and Konstantin S Pervunin. Bubble patterns recognition using neural networks: Application to the analysis of a two-phase bubbly jet. *International Journal of Multiphase Flow*, 126:103194, 2020.

[209] Evelyn N Wang, Shankar Devasenathipathy, Hao Lin, Carlos H Hidrovo, Juan G Santiago, Kenneth E Goodson, and Thomas W Kenny. A hybrid method for bubble geometry reconstruction in two-phase microchannels. *Experiments in Fluids*, 40(6): 847–858, 2006.

[210] Shiyong Tan, Shijie Zhong, and Rui Ni. 3D Lagrangian tracking of polydispersed bubbles at high image densities. *Experiments in Fluids*, 64(4):85, 2023.

[211] J Lelouvetel, T Tanaka, Y Sato, and K Hishida. Transport mechanisms of the turbulent energy cascade in upward/downward bubbly flows. *Journal of Fluid Mechanics*, 741:514–542, 2014.

[212] D Eskin, E Meretskaya, and A Vikhansky. A model of breakup of a rising bubble in a turbulent flow. *Chemical Engineering Science*, 226:115846, 2020.

[213] CD Ohl, A Tijink, and Andrea Prosperetti. The added mass of an expanding bubble. *Journal of Fluid Mechanics*, 482:271–290, 2003.

[214] Florent Ravelet, Catherine Colin, and Frédéric Risso. On the dynamics and breakup of a bubble rising in a turbulent flow. *Physics of Fluids*, 23(10), 2011.

[215] Yuchen Bian, Feng Dong, Weida Zhang, Hongyi Wang, Chao Tan, and Zhiqiang Zhang. 3D reconstruction of a single rising bubble in water using digital image processing and characteristic matrix. *Particuology*, 11(2):170–183, 2013.

[216] Mingming Wu and Morteza Gharib. Experimental studies on the shape and path of small air bubbles rising in clean water. *Physics of Fluids*, 14(7):L49–L52, 2002.

[217] Niels G Deen. *An experimental and computational study of fluid dynamics in gas-liquid chemical reactors*. PhD thesis, Aalborg University, 2001.

[218] Mário AR Talaia. Terminal velocity of a bubble rise in a liquid column. *World Academy of Science, Engineering and Technology*, 28:264–268, 2007.

[219] M Maldonado, JJ Quinn, CO Gomez, and JA Finch. An experimental study examining the relationship between bubble shape and rise velocity. *Chemical Engineering Science*, 98:7–11, 2013.

[220] Irfan Khan, Mingjun Wang, Yapei Zhang, Wenxi Tian, Guanghui Su, and Suizheng Qiu. Two-phase bubbly flow simulation using CFD method: A review of models for interfacial forces. *Progress in Nuclear Energy*, 125:103360, 2020.

[221] Wei Chen and Lifeng Zhang. Effects of interphase forces on multiphase flow and bubble distribution in continuous casting strands. *Metallurgical and Materials Transactions B*, 52(1):528–547, 2021.

[222] John Stewart Turner. *Buoyancy effects in fluids*. Cambridge University Press, 1979.

[223] Harald Ibach. *Physics of surfaces and interfaces*. Springer, 2006.

[224] Leiv Magne Siqveland and Svein Magne Skjæveland. Derivations of the Young-Laplace equation. *Capillarity*, 4(2):23–30, 2021.

[225] Roy J Kuffner. The measurement of dynamic surface tensions of solutions of slowly diffusing molecules by the maximum bubble pressure method. *Journal of Colloid Science*, 16(5):497–500, 1961.

[226] M Austin, BB Bright, and EA Simpson. The measurement of the dynamic surface tension of manoxol OT solutions for freshly formed surfaces. *Journal of Colloid and Interface Science*, 23(1):108–112, 1967.

[227] Karol J Mysels. The maximum bubble pressure method of measuring surface tension, revisited. *Colloids and Surfaces*, 43(2):241–262, 1990.

[228] VB Fainerman, R Miller, and P Joos. The measurement of dynamic surface tension by the maximum bubble pressure method. *Colloid and Polymer Science*, 272(6): 731–739, 1994.

[229] G Sridhar and J Katz. Drag and lift forces on microscopic bubbles entrained by a vortex. *Physics of Fluids*, 7(2):389–399, 1995.

[230] Jacques Magnaudet and Ian Eames. The motion of high-Reynolds-number bubbles in inhomogeneous flows. *Annual Review of Fluid Mechanics*, 32(1):659–708, 2000.

[231] George Keith Batchelor. *An introduction to fluid dynamics*. Cambridge University Press, 2000.

[232] Roland Clift, John R Grace, and Martin E Weber. *Bubbles, drops, and particles*. Courier Corporation, 2005.

[233] Jacques Magnaudet and Dominique Legendre. The viscous drag force on a spherical bubble with a time-dependent radius. *Physics of Fluids*, 10(3):550–554, 1998.

[234] Long Cu Ngo and Hyoung Gwon Choi. Evaluation of pressure and viscous drags of a rising bubble at small Reynolds numbers. *Journal of Mechanical Science and Technology*, 36(3):1303–1313, 2022.

[235] Ming Liu, Binbin Wang, and Lei Tan. Correlation of drag coefficient between rising bubbles in chain. *Physics of Fluids*, 34(4), 2022.

[236] I Ẑun. The transverse migration of bubbles influenced by walls in vertical bubbly flow. *International Journal of Multiphase Flow*, 6(6):583–588, 1980.

[237] D Lucas, H-M Prasser, and A Manera. Influence of the lift force on the stability of a bubble column. *Chemical Engineering Science*, 60(13):3609–3619, 2005.

[238] Niklas Hidman, Henrik Ström, Srdjan Sasic, and Gaetano Sardina. The lift force on deformable and freely moving bubbles in linear shear flows. *Journal of Fluid Mechanics*, 952:A34, 2022.

[239] A Biesheuvel and S Spoelstra. The added mass coefficient of a dispersion of spherical gas bubbles in liquid. *International Journal of Multiphase Flow*, 15(6):911–924, 1989.

[240] Ashok S Sangani, DZ Zhang, and Andrea Prosperetti. The added mass, Basset, and viscous drag coefficients in nondilute bubbly liquids undergoing small-amplitude oscillatory motion. *Physics of Fluids A: Fluid Dynamics*, 3(12):2955–2970, 1991.

[241] Alfred Barnard Basset. *A treatise on hydrodynamics: with numerous examples*, volume 2. Deighton, Bell and Company, 1888.

[242] Patricio A Moreno-Casas and Fabian A Bombardelli. Computation of the Basset force: recent advances and environmental flow applications. *Environmental Fluid Mechanics*, 16(1):193–208, 2016.

[243] Huiting Chen, Weitian Ding, Han Wei, Henrik Saxén, and Yaowei Yu. A coupled CFD-DEM study on the effect of Basset force aimed at the motion of a single bubble. *Materials*, 15(15):5461, 2022.

[244] Ralph Lindken and Wolfgang Merzkirch. Velocity measurements of liquid and gaseous phase for a system of bubbles rising in water. *Experiments in Fluids*, 29(Suppl 1): S194–S201, 2000.

[245] Ralph Lindken and Wolfgang Merzkirch. A novel PIV technique for measurements in multiphase flows and its application to two-phase bubbly flows. *Experiments in Fluids*, 33(6):814–825, 2002.

[246] S So, H Morikita, S Takagi, and Y Matsumoto. Laser Doppler velocimetry measurement of turbulent bubbly channel flow. *Experiments in Fluids*, 33(1):135–142, 2002.

[247] Ling-xin Zhang, Xin-sheng Cheng, Han Tu, Qi Gao, Xue-ming Shao, Xiang-Wei Liao, and Liang Zhao. Measurement of two-phase velocities in bubble flows using laser Doppler velocimetry. *Journal of Hydrodynamics*, 34(6):1134–1144, 2022.

[248] Guan Heng Yeoh and Jiyuan Tu. *Computational techniques for multiphase flows*. Butterworth-Heinemann, 2019.

[249] Donald A Drew and Stephen L Passman. *Theory of multicomponent fluids*, volume 135. Springer Science & Business Media, 2006.

[250] Said Elghobashi. On predicting particle-laden turbulent flows. *Applied Scientific Research*, 52(4):309–329, 1994.

[251] S Laın, D Bröder, M Sommerfeld, and MF Göz. Modelling hydrodynamics and turbulence in a bubble column using the Euler–Lagrange procedure. *International Journal of Multiphase Flow*, 28(8):1381–1407, 2002.

[252] Vivek V Buwa, Dhanannjay S Deo, and Vivek V Ranade. Eulerian–Lagrangian simulations of unsteady gas–liquid flows in bubble columns. *International Journal of Multiphase Flow*, 32(7):864–885, 2006.

[253] Gaetano Sardina, Klas Jareteg, Henrik Ström, and Srdjan Sasic. Assessing the ability of the Eulerian-Eulerian and the Eulerian-Lagrangian frameworks to capture meso-scale dynamics in bubbly flows. *Chemical Engineering Science*, 201:58–73, 2019.

[254] Vittorio E Badalassi, Hector D Ceniceros, and Sanjoy Banerjee. Computation of multiphase systems with phase field models. *Journal of Computational Physics*, 190 (2):371–397, 2003.

[255] Junseok Kim. Phase-field models for multi-component fluid flows. *Communications in Computational Physics*, 12(3):613–661, 2012.

[256] John W Cahn and John E Hilliard. Free energy of a nonuniform system. I. Interfacial free energy. *The Journal of Chemical Physics*, 28(2):258–267, 1958.

[257] Amy Novick-Cohen. The cahn–hilliard equation. *Handbook of differential equations: evolutionary equations*, 4:201–228, 2008.

[258] Samuel Miller Allen and John W Cahn. Ground state structures in ordered binary alloys with second neighbor interactions. *Acta Metallurgica*, 20(3):423–433, 1972.

[259] Samuel M Allen and John W Cahn. A correction to the ground state of FCC binary ordered alloys with first and second neighbor pairwise interactions. *Scripta Metallurgica*, 7(12):1261–1264, 1973.

[260] Grétar Tryggvason, Bernard Bunner, Asghar Esmaeeli, Damir Juric, N Al-Rawahi, W Tauber, Jaehoon Han, Selman Nas, and Y-J Jan. A front-tracking method for the computations of multiphase flow. *Journal of Computational Physics*, 169(2):708–759, 2001.

[261] Mark Sussman, Peter Smereka, and Stanley Osher. A level set approach for computing solutions to incompressible two-phase flow. *Journal of Computational Physics*, 114(1):146–159, 1994.

[262] Stanley Osher and Ronald P Fedkiw. Level set methods: an overview and some recent results. *Journal of Computational Physics*, 169(2):463–502, 2001.

[263] James A Sethian and Peter Smereka. Level set methods for fluid interfaces. *Annual Review of Fluid Mechanics*, 35(1):341–372, 2003.

[264] Douglas Enright, Ronald Fedkiw, Joel Ferziger, and Ian Mitchell. A hybrid particle level set method for improved interface capturing. *Journal of Computational Physics*, 183(1):83–116, 2002.

[265] Ruben Scardovelli and Stéphane Zaleski. Direct numerical simulation of free-surface and interfacial flow. *Annual Review of Fluid Mechanics*, 31(1):567–603, 1999.

[266] Holger Nobach and Eberhard Bodenschatz. Limitations of accuracy in PIV due to individual variations of particle image intensities. *Experiments in Fluids*, 47(1):27–38, 2009.

[267] Holger Nobach. Influence of individual variations of particle image intensities on high-resolution PIV. *Experiments in Fluids*, 50(4):919–927, 2011.

[268] PM Bardet, MA Andre, and DR Neal. Systematic timing errors in laser-based transit-time velocimetry. In *10th International Symposium on Particle Image Velocimetry (PIV13)*, Delft, The Netherlands, 2013.

[269] Philippe Courtier, E Andersson, W Heckley, D Vasiljevic, M Hamrud, A Hollingsworth, F Rabier, M Fisher, and J Pailleux. The ECMWF implementation of three-dimensional variational assimilation (3D-Var). I: Formulation. *Quarterly Journal of the Royal Meteorological Society*, 124(550):1783–1807, 1998.

[270] Erik Andersson, Jan Haseler, Per Undén, Philippe Courtier, Graeme Kelly, Drasko Vasiljevic, Cedo Brankovic, Catherine Gaffard, Anthony Hollingsworth, Christian Jakob, et al. The ECMWF implementation of three-dimensional variational assimilation (3D-Var). III: Experimental results. *Quarterly Journal of the Royal Meteorological Society*, 124(550):1831–1860, 1998.

[271] Michael Fisher and Erik Andersson. Developments in 4D-Var and Kalman filtering. Technical report, European Centre for Medium Range Weather Forecasts, 2001.

[272] Andrew C Lorenc and F Rawlins. Why does 4D-Var beat 3D-Var? *Quarterly Journal of the Royal Meteorological Society: A journal of the atmospheric sciences, applied meteorology and physical oceanography*, 131(613):3247–3257, 2005.

[273] Chuangxin He, Peng Wang, Hyung Jin Sung, Wenwu Zhou, Di Peng, and Yingzheng Liu. Enhancing modal synchronisation in wall-bounded turbulence via sequential variational data assimilation. *Journal of Fluid Mechanics*, 1032:A62, 2026.

[274] Rudolph Emil Kalman. A new approach to linear filtering and prediction problems. *Journal of Basic Engineering*, 82(1):35–45, 1960.

[275] Leonard A McGee and Stanley F Schmidt. Discovery of the Kalman filter as a practical tool for aerospace and industry. Technical report, National Aeronautics and Space Administration, 1985.

[276] Geir Evensen. Sequential data assimilation with a nonlinear quasi-geostrophic model using Monte Carlo methods to forecast error statistics. *Journal of Geophysical Research: Oceans*, 99(C5):10143–10162, 1994.

[277] Zhiwen Deng, Chuangxin He, Xin Wen, and Yingzheng Liu. Recovering turbulent flow field from local quantity measurement: turbulence modeling using ensemble-Kalman-filter-based data assimilation. *Journal of Visualization*, 21(6):1043–1063, 2018.

[278] François-Xavier Le Dimet and Olivier Talagrand. Variational algorithms for analysis and assimilation of meteorological observations: theoretical aspects. *Tellus A: Dynamic Meteorology and Oceanography*, 38(2):97–110, 1986.

[279] Andrew C Lorenc. Analysis methods for numerical weather prediction. *Quarterly Journal of the Royal Meteorological Society*, 112(474):1177–1194, 1986.

[280] Richard C Dorf and Robert H Bishop. *Modern Control Systems*. Pearson, 12 edition, 2011.

[281] David G Luenberger. Observing the state of a linear system. *IEEE Transactions on Military Electronics*, 8(2):74–80, 1964.

[282] Michael A Johnson and Mohammad H Moradi. *PID control*. Springer, 2005.

[283] Patricio Clark Di Leoni, Andrea Mazzino, and Luca Biferale. Synchronization to big data: Nudging the Navier-Stokes equations for data assimilation of turbulent flows. *Physical Review X*, 10(1):011023, 2020.

[284] Richard A Anthes. Data assimilation and initialization of hurricane prediction models. *Journal of Atmospheric Sciences*, 31(3):702–719, 1974.

[285] James E Hoke and Richard A Anthes. The initialization of numerical models by a dynamic-initialization technique. *Monthly Weather Review*, 104(12):1551–1556, 1976.

[286] Jacques Verron. Nudging satellite altimeter data into quasi-geostrophic ocean models. *Journal of Geophysical Research: Oceans*, 97(C5):7479–7491, 1992.

[287] Kim M Waldron, Jan Paegle, and John D Horel. Sensitivity of a spectrally filtered and nudged limited-area model to outer model options. *Monthly Weather Review*, 124(3):529–547, 1996.

[288] William C Skamarock, Joseph B Klemp, Jimy Dudhia, David O Gill, Zhiquan Liu, Judith Berner, Wei Wang, Jordan G Powers, Michael G Duda, Dale M Barker, et al. A description of the advanced research WRF version 4. *NCAR tech. note ncar/tn-556+ str*, 145, 2019.

[289] Patricio Clark Di Leoni, Andrea Mazzino, and Luca Biferale. Inferring flow parameters and turbulent configuration with physics-informed data assimilation and spectral nudging. *Physical Review Fluids*, 3(10):104604, 2018.

[290] Didier Auroux and Jacques Blum. Back and forth nudging algorithm for data assimilation problems. *Comptes Rendus Mathematique*, 340(12):873–878, 2005. ISSN 1631-073X.

[291] Abderrahim Azouani and Edriss S. Titi. Feedback control of nonlinear dissipative systems by finite determining parameters - A reaction-diffusion paradigm. *Evolution Equations and Control Theory*, 3(4):579–594, 2014.

[292] Abderrahim Azouani, Eric Olson, and Edriss S Titi. Continuous data assimilation using general interpolant observables. *Journal of Nonlinear Science*, 24:277–304, 2014.

[293] John Milnor. On the concept of attractor. *Communications in Mathematical Physics*, 99:177–195, 1985.

[294] Ciprian Foias, Michael S Jolly, Rostyslav Kravchenko, and Edriss S Titi. A unified approach to determining forms for the 2D Navier–Stokes equations-the general interpolants case. *Russian Mathematical Surveys*, 69(2):359, 2014.

[295] Aseel Farhat, Evelyn Lunasin, and Edriss S Titi. Abridged continuous data assimilation for the 2D Navier–Stokes equations utilizing measurements of only one component of the velocity field. *Journal of Mathematical Fluid Mechanics*, 18:1–23, 2016.

[296] Hakima Bessaih, Eric Olson, and Edriss S Titi. Continuous data assimilation with stochastically noisy data. *Nonlinearity*, 28(3):729, 2015.

[297] Emine Celik and Eric Olson. Data assimilation using time-delay nudging in the presence of Gaussian noise. *Journal of Nonlinear Science*, 33(6):110, 2023.

[298] Animikh Biswas, Zachary Bradshaw, and Michael S Jolly. Data Assimilation for the Navier–Stokes Equations Using Local Observables. *SIAM Journal on Applied Dynamical Systems*, 20(4):2174–2203, 2021.

[299] Ciprian Foias, Cecilia F Mondaini, and Edriss S Titi. A discrete data assimilation scheme for the solutions of the two-dimensional Navier–Stokes equations and their statistics. *SIAM Journal on Applied Dynamical Systems*, 15(4):2109–2142, 2016.

[300] Animikh Biswas and Randy Price. Continuous Data Assimilation for the Three-Dimensional Navier–Stokes Equations. *SIAM Journal on Mathematical Analysis*, 53 (6):6697–6723, 2021.

[301] Matthew Gardner, Adam Larios, Leo G Rebholz, Duygu Vargun, and Camille Zerfas. Continuous data assimilation applied to a velocity–vorticity formulation of the 2D Navier–Stokes equations. *Electronic Research Archive*, 29(3):2223–2247, 2021. doi: 10.3934/era.2020113.

[302] Animikh Biswas, Ciprian Foias, Cecilia F Mondaini, and Edriss S Titi. Downscaling data assimilation algorithm with applications to statistical solutions of the Navier–Stokes equations. In *Annales de l'Institut Henri Poincaré C, Analyse non linéaire*, volume 36, pages 295–326. Elsevier, 2019.

[303] Animikh Biswas and Vincent R Martinez. Higher-order synchronization for a data assimilation algorithm for the 2D Navier–Stokes equations. *Nonlinear Analysis: Real World Applications*, 35:132–157, 2017.

[304] Hussain A Ibdah, Cecilia F Mondaini, and Edriss S Titi. Fully discrete numerical schemes of a data assimilation algorithm: uniform-in-time error estimates. *IMA Journal of Numerical Analysis*, 40(4):2584–2625, 2020.

[305] Cecilia F Mondaini and Edriss S Titi. Uniform-in-time error estimates for the post-processing Galerkin method applied to a data assimilation algorithm. *SIAM Journal on Numerical Analysis*, 56(1):78–110, 2018.

[306] Bosco García-Archilla and Julia Novo. Error analysis of fully discrete mixed finite element data assimilation schemes for the Navier-Stokes equations. *Advances in Computational Mathematics*, 46(4):61, 2020.

[307] Bosco García-Archilla, Julia Novo, and Edriss S Titi. Uniform in Time Error Estimates for a Finite Element Method Applied to a Downscaling Data Assimilation Algorithm for the Navier–Stokes Equations. *SIAM Journal on Numerical Analysis*, 58(1):410–429, 2020.

[308] Emine Celik, Eric Olson, and Edriss S Titi. Spectral filtering of interpolant observables for a discrete-in-time downscaling data assimilation algorithm. *SIAM Journal on Applied Dynamical Systems*, 18(2):1118–1142, 2019.

[309] Adam Larios, Yuan Pei, and Collin Victor. The second-best way to do sparse-in-time continuous data assimilation: Improving convergence rates for the 2D and 3D Navier-Stokes equations. *arXiv preprint arXiv:2303.03495*, 2023.

[310] Débora AF Albanez, Helena J Nussenzveig Lopes, and Edriss S Titi. Continuous data assimilation for the three-dimensional Navier–Stokes-α model. *Asymptotic Analysis*, 97(1-2):139–164, 2016.

[311] Aseel Farhat, Evelyn Lunasin, and Edriss S Titi. A data assimilation algorithm: The paradigm of the 3D Leray-α model of turbulence. *Partial differential equations arising from physics and geometry*, 450:253–273, 2019.

[312] Michael S Jolly, Vincent R Martinez, and Edriss S Titi. A data assimilation algorithm for the subcritical surface quasi-geostrophic equation. *Advanced Nonlinear Studies*, 17(1):167–192, 2017.

[313] Michael S Jolly, Vincent R Martinez, Eric J Olson, and Edriss S Titi. Continuous data assimilation with blurred-in-time measurements of the surface quasi-geostrophic equation. *Chinese Annals of Mathematics, Series B*, 40(5):721–764, 2019.

[314] Aseel Farhat, Michael S Jolly, and Edriss S Titi. Continuous data assimilation for the 2D Bénard convection through velocity measurements alone. *Physica D: Nonlinear Phenomena*, 303:59–66, 2015.

[315] Aseel Farhat, Evelyn Lunasin, and Edriss S Titi. Continuous data assimilation for a 2D Bénard convection system through horizontal velocity measurements alone. *Journal of Nonlinear Science*, 27:1065–1087, 2017.

[316] Animikh Biswas, Joshua Hudson, Adam Larios, and Yuan Pei. Continuous data assimilation for the 2D magnetohydrodynamic equations using one component of the velocity and magnetic fields. *Asymptotic Analysis*, 108(1-2):1–43, 2018.

[317] Peter A Markowich, Edriss S Titi, and Saber Trabelsi. Continuous data assimilation for the three-dimensional Brinkman–Forchheimer-extended Darcy model. *Nonlinearity*, 29(4):1292, 2016.

[318] Markus Zauner, Vincent Mons, Olivier Marquet, and Benjamin Leclaire. Nudging-based data assimilation of the turbulent flow around a square cylinder. *Journal of Fluid Mechanics*, 937:A38, 2022.

[319] Adam Larios, Leo G Rebholz, and Camille Zerfas. Global in time stability and accuracy of IMEX-FEM data assimilation schemes for Navier–Stokes equations. *Computer Methods in Applied Mechanics and Engineering*, 345:1077–1093, 2019.

[320] Leo G Rebholz and Camille Zerfas. Simple and efficient continuous data assimilation of evolution equations via algebraic nudging. *Numerical Methods for Partial Differential Equations*, 37(3):2588–2612, 2021.

[321] Masakazu Gesho, Eric Olson, and Edriss S Titi. A computational study of a data assimilation algorithm for the two-dimensional Navier-Stokes equations. *Communications in Computational Physics*, 19(4):1094–1110, 2016.

[322] Trenton Franz, Adam Larios, and Collin Victor. The bleeps, the sweeps, and the creeps: convergence rates for dynamic observer patterns via data assimilation for the 2D Navier–Stokes equations. *Computer Methods in Applied Mechanics and Engineering*, 392:114673, 2022.

[323] Adam Larios and Collin Victor. Continuous Data Assimilation with a Moving Cluster of Data Points for a Reaction Diffusion Equation: A Computational Study. *Communications in Computational Physics*, 29(4):1273–1298, 2021.

[324] Ning Ning and Collin Victor. An Assessment of Ensemble Kalman Filter and Azouani-Olson-Titi Algorithms for Data Assimilation: A Comparative Study. *arXiv preprint arXiv:2407.17424*, 2024.

[325] Benjamin Pachev, Jared P Whitehead, and Shane A McQuarrie. Concurrent Multi-Parameter Learning Demonstrated on the Kuramoto–Sivashinsky Equation. *SIAM Journal on Scientific Computing*, 44(5):A2974–A2990, 2022.

[326] Adam Larios and Yuan Pei. Nonlinear continuous data assimilation. *Available at SSRN 4283518*, 2024.

[327] MU Altaf, ES Titi, T Gebrael, OM Knio, L Zhao, MF McCabe, and Ibrahim Hoteit. Downscaling the 2D Bénard convection equations using continuous data assimilation. *Computational Geosciences*, 21:393–410, 2017.

[328] Srinivas Desamsetti, Hari Prasad Dasari, Sabique Langodan, Edriss S Titi, Omar Knio, and Ibrahim Hoteit. Efficient dynamical downscaling of general circulation models using continuous data assimilation. *Quarterly Journal of the Royal Meteorological Society*, 145(724):3175–3194, 2019.

[329] Elizabeth Carlson, Luke P Van Roekel, Humberto C Godinez, Mark R Petersen, and Adam Larios. Exploring a new computationally efficient data assimilation algorithm for ocean models. *Authorea Preprints*, 2022.

[330] Yuan Pei. Continuous data assimilation for the 3D primitive equations of the ocean. *Communications on Pure and Applied Analysis*, 18(2):643–661, 2019. ISSN 1534-0392.

[331] Elizabeth Carlson, Joshua Hudson, and Adam Larios. Parameter recovery for the 2 dimensional Navier–Stokes equations via continuous data assimilation. *SIAM Journal on Scientific Computing*, 42(1):A250–A270, 2020.

[332] Elizabeth Carlson, Joshua Hudson, Adam Larios, Vincent R. Martinez, Eunice Ng, and Jared P. Whitehead. Dynamically learning the parameters of a chaotic system using partial observations. *Discrete and Continuous Dynamical Systems*, 42(8):3809–3839, 2022. ISSN 1078-0947.

[333] Camille Zerfas, Leo G Rebholz, Michael Schneier, and Traian Iliescu. Continuous data assimilation reduced order models of fluid flow. *Computer Methods in Applied Mechanics and Engineering*, 357:112596, 2019.

[334] Harbir Antil, Rainald Löhner, and Randy Price. Data assimilation with deep neural nets informed by nudging. In *Reduction, Approximation, Machine Learning, Surrogates, Emulators and Simulators: RAMSES*, pages 17–41. Springer, 2024.

[335] Aseel Farhat, Evelyn Lunasin, and Edriss S Titi. On the Charney conjecture of data assimilation employing temperature measurements alone: the paradigm of 3D planetary geostrophic model. *Mathematics of Climate and Weather Forecasting*, 2 (1), 2016.

[336] Hermann Schlichting and Klaus Gersten. *Boundary-layer theory*. Springer, 2016.

[337] Francis Patton Bretherton. The motion of long bubbles in tubes. *Journal of Fluid Mechanics*, 10(2):166–188, 1961.

[338] Ufuk Olgac and Metin Muradoglu. Effects of surfactant on liquid film thickness in the bretherton problem. *International Journal of Multiphase Flow*, 48:58–70, 2013.

[339] Jerome A Neufeld. Bubbling forth on thin films. *Journal of Fluid Mechanics*, 1000: F1, 2024.

[340] Fred Fairbrother and Alfred E Stubbs. 119. studies in electro-endosmosis. part vi. the "bubble-tube" method of measurement. *Journal of the Chemical Society (Resumed)*, pages 527–529, 1935.

[341] David G Lowe. Distinctive image features from scale-invariant keypoints. *International Journal of Computer Vision*, 60(2):91–110, 2004.

[342] Farzad Forughi. PIV: A Particle Image Velocimetry Code in Python and MATLAB. GitHub repository, 2024. URL https://github.com/forughi/PIV. Open-source software, GNU GPL v3.0; accessed July 3, 2026.

[343] Thomas Janke, R Schwarze, and K Bauer. Part2Track: A MATLAB package for double frame and time resolved particle tracking velocimetry. *SoftwareX*, 11:100413, 2020.

[344] Edriss S Titi and Collin Victor. On the inadequacy of nudging data assimilation algorithms for non-dissipative systems. *Discrete and Continuous Dynamical Systems - Series S*, 26:477–507, 2026. doi: 10.3934/dcdss.2025151.

[345] T Abel Engh and Metall Nilmani. Bubbling at high flow rates in inviscid and viscous liquids (slags). *Metallurgical Transactions B*, 19:83–94, 1988.

[346] JK Walters and JF Davidson. The initial motion of a gas bubble formed in an inviscid liquid. *Journal of Fluid Mechanics*, 17(3):321–336, 1963.

[347] Kazuki Maeda, Masanobu Date, Kazuyasu Sugiyama, Shu Takagi, and Yoichiro Matsumoto. Viscid–inviscid interactions of pairwise bubbles in a turbulent channel flow and their implications for bubble clustering. *Journal of Fluid Mechanics*, 919:A30, 2021.

[348] Henry G Weller, Gavin Tabor, Hrvoje Jasak, and Christer Fureby. A tensorial approach to computational continuum mechanics using object-oriented techniques. *Computers in Physics*, 12(6):620–631, 1998.

[349] Raad I Issa. Solution of the implicitly discretised fluid flow equations by operator-splitting. *Journal of Computational Physics*, 62(1):40–65, 1986.

[350] Suhas V Patankar and D Brian Spalding. A calculation procedure for heat, mass and momentum transfer in three-dimensional parabolic flows. In *Numerical prediction of flow, heat transfer, turbulence and combustion*, pages 54–73. Elsevier, 1983.

[351] Suhas Patankar. *Numerical heat transfer and fluid flow*. CRC Press, 2018.

[352] Christopher J Greenshields and Henry G Weller. *Notes on Computational Fluid Dynamics: General Principles*. CFD Direct Ltd, Reading, UK, 2022.

[353] Jay P Boris and David L Book. Flux-corrected transport. I. SHASTA, a fluid transport algorithm that works. *Journal of Computational Physics*, 11(1):38–69, 1973.

[354] Steven T Zalesak. Fully multidimensional flux-corrected transport algorithms for fluids. *Journal of Computational Physics*, 31(3):335–362, 1979.

[355] Dominique Legendre, Roberto Zenit, and J Rodrigo Velez-Cordero. On the deformation of gas bubbles in liquids. *Physics of Fluids*, 24(4), 2012.

[356] John R Grace. Shapes and velocities of single drops and bubbles moving freely through immiscible liquids. *Trans. Inst. Chem. Eng.*, 54:167–173, 1976.

[357] Dahya Bhaga and ME Weber. Bubbles in viscous liquids: shapes, wakes and velocities. *Journal of Fluid Mechanics*, 105:61–85, 1981.

[358] OpenFOAM Foundation. OpenFOAM 2.3.0: Multiphase Modelling, feb 2014. URL https://openfoam.org/release/2-3-0/multiphase/. Accessed July 9, 2026.

[359] OpenCFD Ltd. Breaking of a Dam. OpenFOAM User Guide, 2026. Accessed July 9, 2026.

[360] Bjarke Eltard Larsen, David R. Fuhrman, and Johan Roenby. Performance of interfoam on the simulation of progressive waves. *Coastal Engineering Journal*, 61(3): 380–400, 2019. doi: 10.1080/21664250.2019.1609713.

[361] Jared S Cox, Kenneth S Brentner, and Christopher L Rumsey. Computation of vortex shedding and radiated sound for a circular cylinder: subcritical to transcritical reynolds numbers. *Theoretical and Computational Fluid Dynamics*, 12(4):233–253, 1998.

[362] Philip G Saffman. Vortex dynamics. In *Theoretical Approaches to Turbulence*, pages 263–277. Springer, 1992.

[363] Jinsong Hua, Jan F Stene, and Ping Lin. Numerical simulation of 3d bubbles rising in viscous liquids using a front tracking method. *Journal of Computational Physics*, 227(6):3358–3382, 2008.

[364] W Dijkhuizen, I Roghair, M Van Sint Annaland, and JAM Kuipers. Dns of gas bubbles behaviour using an improved 3d front tracking model—drag force on isolated bubbles and comparison with experiments. *Chemical Engineering Science*, 65(4): 1415–1426, 2010.

[365] Ivo Roghair, Julián Martínez Mercado, Martin Van Sint Annaland, Hans Kuipers, Chao Sun, and Detlef Lohse. Energy spectra and bubble velocity distributions in pseudo-turbulence: Numerical simulations vs. experiments. *International Journal of Multiphase Flow*, 37(9):1093–1098, 2011.

[366] Aurore Loisy, Aurore Naso, and Peter D. M. Spelt. Buoyancy-driven bubbly flows: Ordered and free rise at small and intermediate volume fraction. *Journal of Fluid Mechanics*, 816:94–141, 2017. doi: 10.1017/jfm.2017.64.

[367] Andrea Cioncolini and Mirco Magnini. Shapes and rise velocities of single bubbles in a confined annular channel: Experiments and numerical simulations. *Fluids*, 6(12): 437, 2021. doi: 10.3390/fluids6120437.

[368] Raghav Mundhra, Rajaram Lakkaraju, Prasanta Kumar Das, Maksim A Pakhomov, and Pavel D Lobanov. Effect of wall proximity and surface tension on a single bubble rising near a vertical wall. *Water*, 15(8):1567, 2023.

[369] Harry Nyquist. Certain topics in telegraph transmission theory. *Transactions of the American Institute of Electrical Engineers*, 47(2):617–644, 1928.

[370] Hélène Lange, Patricia Taillandier, and Jean-Pierre Riba. Effect of high shear stress on microbial viability. *Journal of Chemical Technology & Biotechnology: International Research in Process, Environmental & Clean Technology*, 76(5):501–505, 2001.

[371] F Garcia-Ochoa, E Gomez, A Alcon, and VE Santos. The effect of hydrodynamic stress on the growth of xanthomonas campestris cultures in a stirred and sparged tank bioreactor. *Bioprocess and Biosystems Engineering*, 36(7):911–925, 2013.

[372] Benjamin H Timmins, Brandon W Wilson, Barton L Smith, and Pavlos P Vlachos. A method for automatic estimation of instantaneous local uncertainty in particle image velocimetry measurements. *Experiments in Fluids*, 53(4):1133–1147, 2012.

[373] John J Charonko and Pavlos P Vlachos. Estimation of uncertainty bounds for individual particle image velocimetry measurements from cross-correlation peak ratio. *Measurement Science and Technology*, 24(6):065301, 2013.

[374] Zhenyu Xue, John J Charonko, and Pavlos P Vlachos. Particle image velocimetry correlation signal-to-noise ratio metrics and measurement uncertainty quantification. *Measurement Science and Technology*, 25(11):115301, 2014.

[375] Zhenyu Xue, John J Charonko, and Pavlos P Vlachos. Particle image pattern mutual information and uncertainty estimation for particle image velocimetry. *Measurement Science and Technology*, 26(7):074001, 2015.

[376] Andrea Sciacchitano, Bernhard Wieneke, and Fulvio Scarano. PIV uncertainty quantification by image matching. *Measurement Science and Technology*, 24(4):045302, 2013.

[377] Bernhard Wieneke. PIV uncertainty quantification from correlation statistics. *Measurement Science and Technology*, 26(7):074002, 2015.

[378] Sayantan Bhattacharya, John J Charonko, and Pavlos P Vlachos. Particle image velocimetry (PIV) uncertainty quantification using moment of correlation (MC) plane. *Measurement Science and Technology*, 29(11):115301, 2018.

[379] Sayantan Bhattacharya and Pavlos P Vlachos. Volumetric particle tracking velocimetry (PTV) uncertainty quantification. *Experiments in Fluids*, 61(9):197, 2020.

[380] Thomas Janke and Dirk Michaelis. Uncertainty quantification for PTV/LPT data and adaptive track filtering. In *14th international symposium on particle image velocimetry*, volume 1, 2021.

[381] Yang Liu, Chengqi Wang, Yalan Qian, and Xiaodong Sun. Uncertainty analysis of PIV measurements in bubbly flows considering sampling and bubble effects with ray optics modeling. *Nuclear Engineering and Design*, 364:110677, 2020.

[382] O Marfaing, M Guingo, J Laviéville, S Mimouni, E Baglietto, N Lubchenko, B Magolan, R Sugrue, and BT Nadiga. Comparison and uncertainty quantification of two-fluid models for bubbly flows with NEPTUNE_CFD and STAR-CCM+. *Nuclear Engineering and Design*, 337:1–16, 2018.

[383] Yang Liu, Nam T Dinh, Ralph C Smith, and Xiaodong Sun. Uncertainty quantification of two-phase flow and boiling heat transfer simulations through a data-driven

modular Bayesian approach. *International Journal of Heat and Mass Transfer*, 138: 1096–1116, 2019.

[384] Yang Liu, Xiaodong Sun, and Nam T Dinh. Validation and uncertainty quantification of multiphase-CFD solvers: A data-driven Bayesian framework supported by high-resolution experiments. *Nuclear Engineering and Design*, 354:110200, 2019.

[385] Yang Liu, Nam Dinh, Xiaodong Sun, and Rui Hu. Uncertainty quantification for multiphase computational fluid dynamics closure relations with a physics-informed bayesian approach. *Nuclear Technology*, 209(12):2002–2015, 2023.

[386] Martin R Maxey and James J Riley. Equation of motion for a small rigid sphere in a nonuniform flow. *The Physics of Fluids*, 26(4):883–889, 1983.

[387] Renée Gatignol. The Faxén formulae for a rigid particle in an unsteady non-uniform Stokes flow. *Journal de Mécanique Théorique et Appliquée*, 2(2):143–160, 1983.

[388] Renwei Mei. Velocity fidelity of flow tracer particles. *Experiments in Fluids*, 22(1): 1–13, 1996.

[389] Adrian Melling. Tracer particles and seeding for particle image velocimetry. *Measurement Science and Technology*, 8(12):1406–1416, 1997.

[390] David Engler Faleiros, Marthijn Tuinstra, Andrea Sciacchitano, and Fulvio Scarano. The slip velocity of nearly neutrally buoyant tracers for large-scale PIV. *Experiments in Fluids*, 62(9):186, 2021.

[391] S Ghaemi, A Schmidt-Ott, and F Scarano. Nanostructured tracers for laser-based diagnostics in high-speed flows. *Measurement Science and Technology*, 21(10):105403, 2010.

[392] D Ragni, F Schrijer, BW Van Oudheusden, and F Scarano. Particle tracer response across shocks measured by PIV. *Experiments in Fluids*, 50(1):53–64, 2011.

[393] Johannes Bosbach, Matthias Kühn, and Claus Wagner. Large scale particle image velocimetry with helium filled soap bubbles. *Experiments in Fluids*, 46(3):539–547, 2009.

[394] Fulvio Scarano, Sina Ghaemi, Giuseppe Carlo Alp Caridi, Johannes Bosbach, Uwe Dierksheide, and Andrea Sciacchitano. On the use of helium-filled soap bubbles for large-scale tomographic PIV in wind tunnel experiments. *Experiments in Fluids*, 56 (2):42, 2015.

[395] David Engler Faleiros, Marthijn Tuinstra, Andrea Sciacchitano, and Fulvio Scarano. Helium-filled soap bubbles tracing fidelity in wall-bounded turbulence. *Experiments in Fluids*, 59(3):56, 2018.

[396] Fang Chen, Hong Liu, Zifeng Yang, and Hui Hu. Tracking characteristics of tracer particles for PIV measurements in supersonic flows. *Chinese Journal of Aeronautics*, 30(2):577–585, 2017.

[397] Ross A Burns, Heeseok Koo, Venkatramanan Raman, and Noel T Clemens. Improved large-eddy simulation validation methodology: application to supersonic inlet/isolator flow. *AIAA Journal*, 53(4):817–831, 2015.

[398] Fabio JWA Martins, Jonas Kirchmann, Andreas Kronenburg, and Frank Beyrau. Quantification and mitigation of PIV bias errors caused by intermittent particle seeding and particle lag by means of large eddy simulations. *Measurement Science and Technology*, 32(10):104006, 2021.

[399] Matthew T Aultman, Kevin Disotell, and Lian Duan. The effect of particle lag on statistics of hypersonic turbulent boundary layers subject to pressure gradients. In *AIAA SCITECH 2022 Forum*, page 1062, 2022.

[400] Shunsuke Koike, Hidemi Takahashi, Koichi Tanaka, Mitsutomo Hirota, Kenichi Takita, and Goro Masuya. Correction method for particle velocimetry data based on the Stokes drag law. *AIAA Journal*, 45(11):2770–2777, 2007.

[401] Dilip Kalagotla, Daniel Cuppoletti, Paul Orkwis, Kevin Hernandez-Lichtl, Jonas Gustavsson, and Rajan Kumar. Deep-learning-based particle inertia bias corrector for shock-dominated PIV data. *Experiments in Fluids*, 67(5):57, 2026.

[402] Ke Zhou, Jiaqi Li, Jiarong Hong, and Samuel J Grauer. Stochastic particle advection velocimetry (SPAV): theory, simulations, and proof-of-concept experiments. *Measurement Science and Technology*, 34(6):065302, 2023.

[403] Ke Zhou and Samuel J Grauer. Flow reconstruction and particle characterization from inertial Lagrangian tracks. *arXiv preprint arXiv:2311.09076*, 2023.

[404] Ke Zhou and Samuel J Grauer. On the joint estimation of flow fields and particle properties from Lagrangian data. *Journal of Fluid Mechanics*, 1041:A5, 2026. doi: 10.1017/jfm.2026.11913.

[405] Francesco Romanò. Reconstructing the fluid flow by tracking of large particles. *Physical Review Fluids*, 4(10):104301, 2019.

[406] Efstathios E Michaelides. Review—The transient equation of motion for particles, bubbles, and droplets. *Journal of Fluids Engineering*, 119(2):233–247, 1997. doi: 10.1115/1.2819127.

[407] L Schiller and A Naumann. A drag coefficient correlation. *Zeit. Ver. Deutsch. Ing.*, 77:318–320, 1933.

[408] Donald A Drew. Mathematical modeling of two-phase flow. Technical report, Wisconsin Univ-Madison Mathematics Research Center, 1982.

[409] Tim R Auton, Julian Charles Roland Hunt, and M Prud'Homme. The force exerted on a body in inviscid unsteady non-uniform rotational flow. *Journal of Fluid Mechanics*, 197:241–257, 1988.

[410] Philip Geoffrey Saffman. The lift on a small sphere in a slow shear flow. *Journal of Fluid Mechanics*, 22(2):385–400, 1965.

[411] Renwei Mei. An approximate expression for the shear lift force on a spherical particle at finite Reynolds number. *International Journal of Multiphase Flow*, 18(1):145–147, 1992.

[412] Christopher E Brennen. *Fundamentals of multiphase flow*. Cambridge University Press, 2005.

[413] John Happel and Howard Brenner. *Low Reynolds number hydrodynamics: with special applications to particulate media*. Springer Science & Business Media, 2012.

[414] Jeremiah U Brackbill, Douglas B Kothe, and Charles Zemach. A continuum method for modeling surface tension. *Journal of Computational Physics*, 100(2):335–354, 1992.

APPENDICES

Appendix A

Volume-of-Fluid Method

The governing equations for incompressible VoF-based bubbly flows are:

$$\begin{aligned} \nabla \cdot \boldsymbol{u} &= 0, \\ \frac{\partial(\rho \boldsymbol{u})}{\partial t} + \nabla \cdot (\rho \boldsymbol{u}\boldsymbol{u}) &= -\nabla p + \nabla \cdot \boldsymbol{\tau} + \boldsymbol{f}_{\text{ten}} + \boldsymbol{f}_{\text{grv}}, \\ \frac{\partial \alpha}{\partial t} + \nabla \cdot (\alpha \boldsymbol{u}) &= 0, \end{aligned} \tag{A.1}$$

where $\boldsymbol{u}$ is the velocity field shared by both phases, t is the time, p is the pressure, α is the volume fraction of the continuous phase ($\alpha = 1$ in liquid, $\alpha = 0$ in gas). The mixture fluid properties, i.e., density and dynamic viscosity, are computed by volume fraction weighted averaging:

$$\begin{aligned} \rho &= \rho_{\text{l}}\alpha + \rho_{\text{g}}(1-\alpha), \\ \mu &= \mu_{\text{l}}\alpha + \mu_{\text{g}}(1-\alpha), \end{aligned}$$

where the subscripts $[\cdot]_{\text{l}}$ and $[\cdot]_{\text{g}}$ denote the liquid and gas, respectively. For a Newtonian fluid, the viscous stress tensor is

$$\boldsymbol{\tau} = \mu \left[\nabla \boldsymbol{u} + (\nabla \boldsymbol{u})^{\intercal}\right] - \frac{2}{3}\mu(\nabla \cdot \boldsymbol{u})\mathbf{I},$$

which simplifies to $\boldsymbol{\tau} = \mu[\nabla \boldsymbol{u} + (\nabla \boldsymbol{u})^{\intercal}]$ for incompressible flows. $\mathbf{I}$ is the identity tensor. The surface tension force $\boldsymbol{f}_{\text{ten}}$ is modeled using the Continuum Surface Force (CSF) approach [414]:

$$\boldsymbol{f}_{\text{ten}} = \sigma\kappa\nabla\alpha, \qquad \kappa = -\nabla \cdot \left(\frac{\nabla\alpha}{\|\nabla\alpha\|}\right),$$

where σ is the surface tension coefficient, and κ is the local interface curvature. $\boldsymbol{f}_{\text{grv}}$ is the gravity per unit volume.

Several numerical treatments are introduced in A.1 to improve stability and interface resolution. First, an artificial compression term is added to the phase-fraction transport equation to counteract numerical diffusion and maintain a sharp interface:

$$\frac{\partial \alpha}{\partial t} + \nabla \cdot (\alpha \boldsymbol{u}) + \nabla \cdot [\boldsymbol{u}_{\text{rc}} \alpha (1 - \alpha)] = 0,$$

where $\boldsymbol{u}_{\text{rc}}$ is a relative compression velocity aligned with the interface normal. Because the factor $\alpha(1 - \alpha)$ is nonzero only near the interface, the compression acts locally and helps preserve interface sharpness.

Second, a modified pressure variable p_{rgh} is introduced to remove hydrostatic pressure effects:

$$p_{\text{rgh}} = p - \rho \boldsymbol{g} \cdot \boldsymbol{h},$$

where $\boldsymbol{h}$ is the position vector, and $\boldsymbol{g}$ is the gravitational acceleration vector. The modified pressure simplifies boundary condition treatment and avoids artificial pressure jumps at non-vertical fluid interfaces. Therefore, the momentum equation is

$$\frac{\partial (\rho \boldsymbol{u})}{\partial t} + \nabla \cdot (\rho \boldsymbol{u}\boldsymbol{u}) = -\nabla p_{\text{rgh}} + \nabla \cdot \boldsymbol{\tau} + \sigma \kappa \nabla \alpha - \boldsymbol{g} \cdot \boldsymbol{h} \nabla \rho. \tag{A.2}$$

Third, due to non-uniform μ, the divergence of the viscous stress tensor is split into:

$$\nabla \cdot \boldsymbol{\tau} = \nabla \cdot (\mu \nabla \boldsymbol{u}) + \nabla \mu \cdot \nabla \boldsymbol{u}. \tag{A.3}$$

The first term on the right-hand side (RHS) in (A.3) has a Laplacian operator and is discretized implicitly in `interFoam`, while the second term on the RHS in (A.3) is explicitly discretized. Based on (A.2) and (A.3), the momentum equation becomes

$$\frac{\partial (\rho \boldsymbol{u})}{\partial t} + \nabla \cdot (\rho \boldsymbol{u}\boldsymbol{u}) = -\nabla p_{\text{rgh}} + \nabla \cdot (\mu \nabla \boldsymbol{u}) + \nabla \boldsymbol{u} \cdot \nabla \mu + \sigma \kappa \nabla \alpha - \boldsymbol{g} \cdot \boldsymbol{h} \nabla \rho.$$

Appendix B

PIMPLE Algorithm

This appendix summarizes the pressure–velocity coupling procedure used in the present solver. After the phase-fraction equation has been advanced and the mixture properties have been updated, the momentum and pressure fields are solved through the standard PIMPLE algorithm [349–352] in OpenFOAM [348]. Within each time step, the algorithm consists of a momentum predictor, a pressure Poisson equation, a flux correction, and a momentum correction. These steps are repeated within the outer loop until the prescribed convergence criteria or iteration limits are reached. More details about the PIMPLE algorithm can be found in [348–352].

First, the momentum predictor is solved for the intermediate velocity field $\mathbf{U}^*$ using the latest available pressure field, namely $p_{\mathrm{rgh}}^{\mathrm{n}}$ at the beginning of the time step or the most recent pressure from the previous outer iteration:

$$\mathrm{A}_{u,\mathrm{P}}^{\mathrm{n}}\,\mathbf{U}_{\mathrm{P}}^{*} \;=\; -\sum_{\mathrm{N}\in\mathcal{N}(\mathrm{P})} \mathrm{A}_{u,\mathrm{N}}^{\mathrm{n}}\,\mathbf{U}_{\mathrm{N}}^{*} \;+\; \mathrm{S}_{u,\mathrm{P}}^{\mathrm{n}} \;-\; \nabla p_{\mathrm{rgh},\mathrm{P}}^{\mathrm{n}}.$$

Here, $\mathcal{N}(\mathrm{P})$ denotes the set of neighboring cells of cell P. The subscripts $(\cdot)_{\mathrm{P}}$ and $(\cdot)_{\mathrm{N}}$ represent quantities evaluated at cell P and its neighboring cells, respectively. The superscript $(\cdot)^{\mathrm{n}}$ is the current time step, while the superscript $(\cdot)^*$ denotes the predicted quantity within the current pressure–velocity iteration. The coefficient $\mathrm{A}_{u,\mathrm{P}}^{\mathrm{n}}$ is the diagonal coefficient of the discretized momentum equation, and $\mathrm{A}_{u,\mathrm{N}}^{\mathrm{n}}$ are the corresponding off-diagonal neighbor coefficients. These coefficients collect the temporal, convective, and diffusive contributions formed with the updated mixture properties (e.g., ρ^*, μ^*). The source term $\mathrm{S}_{u,\mathrm{P}}^{\mathrm{n}}$ contains the explicit contributions from body forces, surface tension, and the AOT-nudging source term. The predicted field $\mathbf{U}^*$ does not satisfy the continuity equation.

Next, a pressure Poisson equation is assembled and solved using the predicted field:

$$\nabla\cdot\left(\frac{1}{\mathrm{A}^{\mathrm{n}}_{u}}\nabla p^{*}_{\mathrm{rgh}}\right) \;=\; \nabla\cdot\,\mathbf{HbyA}^{*}, \qquad \mathbf{HbyA}^{*}_{\mathrm{P}} \;=\; \frac{-\sum \mathrm{A}^{\mathrm{n}}_{u,\mathrm{N}}\,\mathbf{U}^{*}_{\mathrm{N}} + \mathrm{S}^{\mathrm{n}}_{u,\mathrm{P}}}{\mathrm{A}^{\mathrm{n}}_{u,\mathrm{P}}}.$$

Here, p^{*}_{rgh} is the modified pressure within the current iteration, and $\mathbf{HbyA}^{*}_{\mathrm{P}}$ is the predicted cell-centered velocity-like quantity obtained by dividing the non-pressure part of the momentum equation by the diagonal coefficient. The notation $\mathrm{A}^{\mathrm{n}}_{u}$ without a cell index denotes the diagonal momentum-coefficient field over the whole mesh. The quantity $\mathbf{HbyA}^{*}$ is first assembled at cell centers and then interpolated to faces when evaluating the divergence operator. Non-orthogonal corrections are treated in the standard finite-volume manner.

After the pressure equation is solved, the face fluxes are corrected so that they are consistent with the updated pressure field:

$$\phi^{**}_{\mathrm{fc}} \;=\; (\mathbf{HbyA}^{*}_{\mathrm{fc}}\cdot\mathbf{S}_{\mathrm{fc}}) \;-\; \left(\frac{1}{\mathrm{A}^{\mathrm{n}}_{u}}\nabla p^{*}_{\mathrm{rgh}}\right)_{\mathrm{fc}}\cdot\mathbf{S}_{\mathrm{fc}}.$$

Here, the subscript $(\cdot)_{\mathrm{fc}}$ denotes a quantity evaluated at a face, and $\mathbf{S}_{\mathrm{fc}}$ is the face-area vector. The magnitude of $\mathbf{S}_{\mathrm{fc}}$ is the face area, and its direction is the outward unit-normal direction. The quantity ϕ^{**}_{fc} is the corrected face flux after the pressure update. The superscript $(\cdot)^{**}$ denotes the corrected quantity after pressure correction. Note that ϕ^{**}_{fc} is the quantity that enforces discrete mass conservation and couples the corrected pressure field to the face-based transport operations in the solver. Furthermore, the corrected face fluxes satisfy the solenoidal constraint in the finite-volume sense.

The cell-centered velocity field is then updated through the momentum correction step:

$$\mathbf{U}^{**}_{\mathrm{P}} \;=\; \mathbf{HbyA}^{*}_{\mathrm{P}} \;-\; \frac{1}{\mathrm{A}^{\mathrm{n}}_{u,\mathrm{P}}}\,(\nabla p^{*}_{\mathrm{rgh}})_{\mathrm{P}},$$

where $(\nabla p^{*}_{\mathrm{rgh}})_{\mathrm{P}}$ is the cell-centered pressure gradient reconstructed from the face values. This step replaces the predicted field $\mathbf{U}^{*}$ with the corrected field $\mathbf{U}^{**}$, which is consistent with the updated pressure and corrected fluxes.

Lastly, pressure and velocity are under-relaxed in the usual PIMPLE manner, the residuals are updated, and the correction loop is repeated until the prescribed tolerances are satisfied or the maximum number of iterations is reached. Within one time step, the explicit AOT-nudging source terms and the refreshed mixture properties (e.g., $\rho^{*}, \mu^{*}, \kappa^{*}$) are held fixed during the inner pressure–velocity corrections. Therefore, the PIMPLE loop provides the pressure–velocity coupling framework through which the updated mixture properties and AOT-nudging feedback are incorporated into the solver.

Appendix C

Derivation of Particle Response Time

Consider a small spherical particle moving in a fluid. The particle has diameter d_p, density ρ_p, volume $V_\mathrm{p} = \pi d_\mathrm{p}^3/6$, and mass $m_\mathrm{p} = \rho_\mathrm{p} V_\mathrm{p} = \rho_\mathrm{p} \pi d_\mathrm{p}^3/6$. Let $\boldsymbol{u}_\mathrm{p}$ be the particle velocity, and let $\boldsymbol{u}_\mathrm{f}$ be the local undisturbed carrier-fluid velocity at the particle position. The slip velocity is

$$\boldsymbol{u}_\mathrm{slip} = \boldsymbol{u}_\mathrm{f} - \boldsymbol{u}_\mathrm{p}.$$

For a small spherical particle in the creeping-flow regime, the drag force is given by Stokes' law:

$$\boldsymbol{F}_D = 3\pi\mu_\mathrm{f} d_\mathrm{p} \left(\boldsymbol{u}_\mathrm{f} - \boldsymbol{u}_\mathrm{p}\right),$$

where μ_f is the dynamic viscosity of the carrier fluid.

If drag is the dominant hydrodynamic force, Newton's second law gives

$$m_\mathrm{p} \frac{d\boldsymbol{u}_\mathrm{p}}{dt} = 3\pi\mu_\mathrm{f} d_\mathrm{p} \left(\boldsymbol{u}_\mathrm{f} - \boldsymbol{u}_\mathrm{p}\right). \tag{C.1}$$

Substituting $m_\mathrm{p} = \rho_\mathrm{p}\pi d_\mathrm{p}^3/6$ into (C.1) gives

$$\rho_\mathrm{p} \frac{\pi d_\mathrm{p}^3}{6} \frac{d\boldsymbol{u}_\mathrm{p}}{dt} = 3\pi\mu_\mathrm{f} d_\mathrm{p} \left(\boldsymbol{u}_\mathrm{f} - \boldsymbol{u}_\mathrm{p}\right). \tag{C.2}$$

Simplifying (C.2) gives

$$\frac{d\boldsymbol{u}_\mathrm{p}}{dt} = \frac{18\mu_\mathrm{f}}{\rho_\mathrm{p} d_\mathrm{p}^2} \left(\boldsymbol{u}_\mathrm{f} - \boldsymbol{u}_\mathrm{p}\right).$$

This equation can be written as

$$\frac{d\boldsymbol{u}_\mathrm{p}}{dt} = \frac{1}{\tau_\mathrm{p}} \left(\boldsymbol{u}_\mathrm{f} - \boldsymbol{u}_\mathrm{p} \right),$$

where

$$\tau_\mathrm{p} = \frac{\rho_\mathrm{p} d_\mathrm{p}^2}{18 \mu_\mathrm{f}}.$$

Therefore, τ_p can be interpreted as the characteristic time scale over which the particle velocity relaxes toward the local fluid velocity.

It should be noted that this expression is derived under the Stokes-drag assumption, which is strictly valid for $\mathrm{Re}_\mathrm{p} \ll 1$. For particles at finite Reynolds numbers, the effective response may differ because of nonlinear drag. In this thesis, τ_p is therefore used as a characteristic first-order response time in the inertial-particle correction model.